Year : 2023

Periphyton development in recently-deglaciated floodplains: from physical habitat constraints to ecosystem engineering

Roncoroni Matteo

Roncoroni Matteo, 2023, Periphyton development in recently-deglaciated floodplains: from physical habitat constraints to ecosystem engineering

Originally published at : Thesis, University of Lausanne

Posted at the University of Lausanne Open Archive http://serval.unil.ch
Document URN : urn:nbn:ch:serval-BIB_B48778F39E377

UNIL | Université de Lausanne

FACULTÉ DES GEOSCIENCES ET DE L'ENVIRONNEMENT

INSTITUTE OF EARTH SURFACE DYNAMICS

Periphyton development in recently-deglaciated floodplains: from physical habitat constraints to ecosystem engineering

THÈSE DE DOCTORAT

présentée à la

Faculté des Géosciences et de l'environnement
de l'Université de Lausanne

pour l'obtention du grade de

Docteur en Sciences de l'Environnement

par

Matteo Roncoroni
B.Sc., M.Sc., Université de Lausanne, Suisse

Directeur de thèse
Prof. Dr. Stuart Nicholas Lane

Co-directeur de thèse
Prof. Dr. Tom Jan Battin

Jury

Prof. Dr. Marie-Elodie Perga
Dr. Nathalie Chèvre
Dr. Christopher Robinson
Prof. Dr. Patrice Carbonneau

LAUSANNE
(Mai 2023)

UNIL | Université de Lausanne
Faculté des géosciences et de l'environnement
bâtiment Géopolis bureau 4631

IMPRIMATUR

Vu le rapport présenté par le jury d'examen, composé de

Présidente de la séance publique :	Mme la Professeure Marie-Elodie Perga
Présidente du colloque :	Mme la Professeure Marie-Elodie Perga
Directeur de thèse :	M. le Professeur Stuart Lane
Co-directeur de thèse :	M. le Professeur Tom Battin
Experte interne :	Mme la Docteure Nathalie Chèvre
Expert externe :	M. le Professeur Patrice Carbonneau
Expert externe :	M. le Professeur Christopher Robinson

Le Doyen de la Faculté des géosciences et de l'environnement autorise l'impression de la thèse de

Monsieur Matteo RONCORONI

Titulaire d'un
Master en Géomorphologie de montagne
de l'Université de Lausanne

intitulée

PERIPHYTON DEVELOPMENT IN RECENTLY-DEGLACIATED FLOODPLAINS: FROM PHYSICAL HABITAT CONSTRAINTS TO ECOSYSTEM ENGINEERING

Lausanne, le 12 juin 2023

Pour le Doyen de la Faculté des géosciences et de l'environnement

Professeure Marie-Elodie Perga

To my beloved Mom, Augusta Roncoroni (1954 – 2018)

Acknowledgements

This doctoral dissertation is the result of years of teamwork, fruitful collaborations and extraordinary supervisions; I would like to sincerely thank the following people:

Prof. Dr. Stuart Lane, my thesis director. Thanks for your unconditional help and availability over these long years of thesis (and before, during my Bachelor and Master thesis). Over the years, you have given me so much, so much more than I could give you back. I am grateful to you for making me grow as a researcher and for sharing your passion and dedication to science. Last but not least, you are an amazing person.

Prof. Dr. Tom Battin, my thesis co-director. Thanks for your help and availability whenever I needed it. I knew nothing about biofilms before this thesis, but I have benefited from your knowledge and passion allowing me to explore an extremely interesting and intriguing topic.

My colleagues at AlpWISE. Thanks for your help and availability, but most of all for sharing wonderful moments with me. It has been a pleasure working with you and I am proud to call you friends.

Dr. Aurélien Ballu. Thanks for your help, for always being available and sharing your technical and scientific knowledge. I owe you a lot.

The student assistants. Thanks for your help in collecting the data in Otemma. Your help was essential.

My colleagues at IDYST for the fruitful discussions and wonderful times spent together during these years.

The people at the River Ecosystems Laboratory, for your help and the moments spent on the field together.

My friends. Thank you for the moments we have spent together and the support you have given me. I am proud to have friends like you.

Jessica. Thanks for your support, for always believing in me, and for the wonderful years we have spent together.

My family. Thanks for your support and help all these years. For always believing in me. For the opportunities you have given me. I will be eternally grateful to you. Grazie!

Mamma, this thesis is for you. It is because of you that I have this passion for rivers. It is mostly thanks to you that I have come this far. Grazie!

Balerna, May 2023

Matteo Roncoroni

Summary

The rapid recession of glaciers is exposing large surfaces to the development of embryonic ecosystems. Such ecosystems are often dominated by stream biofilms, including periphyton. These have been proven to be highly adaptable and effective in colonizing new environments. In practice, however, the colonization of new stream systems is made difficult by the harshness of glacial stream systems, which receive a high proportion of glacially-fed and destructive (i.e., high shear stresses, loaded in sediments, etc.) water. Traditionally, the ecological functioning of glacial stream systems has been associated with the time since deglaciation, i.e. the distance from the glacier terminus, and to windows of opportunity in which the environmental conditions are more favorable to the development of periphyton. These two paradigms still hold today, but they might be less applicable due to the rapidity with which floodplains are being exposed by glacier retreat. This scientific gap motivates this research.

This thesis decrypts the periphyton stream habitat of recently deglaciated floodplains, and in parallel investigates the potential role of periphyton in promoting primary succession through ecosystem engineering. The focus is on the floodplain of the Otemma Glacier (Switzerland) where a set of different methodological and analytical approaches are deployed. The thesis presents framework for high frequency (daily-scale), high resolution (cm-scale) mapping of the presence of periphyton at the floodplain scale using Uncrewed Airborne Vehicles (UAVs). This approach reveals that periphyton may be detected and subsequently mapped through the combination of drone-derived visible band ratios and logistic regression analysis.

These data are then used to determine the spatial organization and temporal dynamics of periphyton in order to establish how their development, maintenance and destruction is linked to the physical environment. Periphyton development requires access to water, which must be available at the surface, as glacial sediments are poor at water retention. However, whilst water determines where periphyton could grow, where periphyton is found in practice is mostly governed by habitat stability, and the latter can be of short or long duration. When stability is of short duration, it is commonly related to the morphodynamics of the glacial stream, and particularly to the evolution of the stream braids. When stability is of long duration, it is related to clear-water tributaries that flow over terraces that have been disconnected from the main active and braided floodplain. In such stable channels and during the melt-season, periphyton can reach a potentially perennial state, provided that sufficient water is available. If this condition is met, periphyton likely modify the properties of the streambed.

To understand these processes further, a series of in situ flume experiments were undertaken in the forefield of the Otemma glacier and reproducing the conditions found in stable tributaries. The ways in which periphyton modify stream bed morphology, water infiltration and near bed hydraulics was monitored. This research demonstrated the functional role of periphyton as ecosystem engineers, showing how periphyton development reduces the vertical infiltration of water by clogging sediment interstices, causes the river-bed to be smoother and simultaneously reduces the

intensity of turbulence and the turbulence-related processes responsible for sediment transport.

The results of this thesis show that disturbances in proglacial braidplains are not spatially homogenous, and if conditions of both stability and access to water are guaranteed throughout the melt-season periphyton may thrive. These conditions allow periphyton to develop substantially, covering large surfaces and for long periods of time. The perennial development has the result of engineering the streambed of tributary channels, and ultimately promoting primary succession, primarily by maintaining the water at the surface.

Résumé

Le recul rapide des glaciers expose de grandes surfaces au développement d'écosystèmes embryonnaires. Ces écosystèmes sont souvent dominés par les biofilms, notamment par les périphytons. Ces derniers se sont avérés très adaptables et efficaces pour coloniser de nouveaux environnements. En pratique, la colonisation de nouveaux cours d'eau est rendue difficile par la forte proportion d'eau glaciaire et de sédiments qui y sont présents. Traditionnellement, le fonctionnement écologique d'un cours d'eau glaciaire est défini par le temps qui sépare ce dernier de sa création au moment de la fonte du glacier et aussi à des fenêtres d'opportunités où les conditions environnementales sont moins sévères. Ces deux paradigmes sont toujours valables aujourd'hui, mais ils pourraient être moins pertinents en raison de la rapidité avec laquelle le retrait des glaciers expose les plaines alluviales. Ce fait doit amener une nouvelle approche scientifique, c'est ce qui motive cette recherche.

Cette thèse décrit l'habitat des périphytons de ces nouvelles plaines alluviales jusqu'alors recouvertes par des glaciers. En parallèle, elle étudie le rôle potentiel des périphytons en tant qu'ingénieurs des écosystèmes et leur rôle dans la promotion de la succession primaire. Plusieurs approches méthodologiques et analytiques ont été menées dans la plaine alluviale du glacier d'Otemma (Suisse). La thèse présente une méthode pour la cartographie à haute fréquence temporelle et à haute résolution spatiale de la présence des périphytons à l'échelle de la plaine alluviale en utilisant des drones (UAV). Cette nouvelle approche révèle que les périphytons peuvent être détectés et ensuite cartographiés par l'analyse conjointe d'images capturées par des drones (spectre visible) et de régressions logistiques. Ces données sont ensuite utilisées pour déterminer l'organisation spatiale et la dynamique temporelle des périphytons afin d'établir comment leur développement et leur disparition sont liés aux conditions environnementales.

Le développement des périphytons nécessite un accès à l'eau, qui doit être disponible à la surface. Cependant, alors que l'eau détermine où ils peuvent apparaître, les périphytons se développent préférablement dans les zones où l'habitat bénéficie d'une certaine stabilité, qui peut être de courte ou de longue durée. Lorsque la stabilité est de courte durée, elle est généralement liée à la morphodynamique du cours d'eau glaciaire et en particulier à l'évolution des méandres du cours d'eau. Lorsqu'en revanche elle est de longue durée, elle est liée aux affluents d'eau claire qui s'écoulent sur des terrasses qui ont été déconnectées de la principale plaine alluviale active et tressée. Dans ces canaux stables et pendant la saison de fonte, les périphytons peuvent s'établir de manière pérenne, à condition qu'il y ait suffisamment d'eau. Si cette condition est remplie, la présence des périphytons entraine une modification des propriétés du lit du cours d'eau.

Pour mieux comprendre ces processus, une série d'expériences *in situ* a été entreprise près du glacier d'Otemma, imitant les conditions rencontrées dans les tributaires stables. La façon dont les périphytons modifient la morphologie du lit du cours d'eau, l'infiltration de l'eau et les caractéristiques de l'écoulement proche du fond du lit ont été particulièrement étudiées. Cette recherche a démontré le rôle majeur des

périphytons dans le fonctionnement de l’écosystème, en montrant comment leur développement réduit l'infiltration verticale de l'eau en colmatant les interstices entre les sédiments. Les périphytons rendent également le lit plus lisse, ce qui modifie les composantes hydrauliques près du fond.

Les résultats de cette thèse mettent en évidence que les perturbations ne sont pas spatialement homogènes et que si les conditions de stabilité et d'accès à l'eau sont garanties tout au long de la saison de fonte les périphytons peuvent prospérer dans les plaines alluviales glaciaires. Ces conditions permettent aux périphytons de se développer de manière significative, en couvrant de grandes surfaces et pendant de longues périodes. Cette prospérité a pour conséquence de modifier le lit des chenaux des tributaires et, en définitive, de favoriser la succession primaire, principalement en maintenant l'eau à la surface grâce à l’imperméabilisation du lit.

Table of contents

List of Figures

List of Tables

Nomenclature

Acronyms

3D	Three-dimensional
ADV	Acoustic Doppler Velocimeter
AlpWISE	Alpine Water, Ice, Sediment and Ecology
CH1903	Swiss geographic coordinate system
CH1903+	Swiss geographic coordinate system
DEM	Digital Elevation Model
DN	Digital Number
DoD	DEMs of Difference
EPFL	Swiss Federal Institute of Technology, Lausanne
EPS	Extracellular Polymeric Substances
ETHZ	Swiss Federal Institute of Technology, Zürich
FA	Flume A
FB	Flume B
GCP	Ground Control Point
GIS	Geographic Information System
GPU	Graphics Processing Unit
GPS	Global Positioning System
JD	Julian Day
LoD	Limit of Detection
MCC	Matthews Correlation Coefficient
MVS	Multiview Stereo
OoD	Occupations of Difference
PhD	Doctor of Philosophy
PIF	Pseudo-Invariant-Feature
PVC	Polyvinyl Chloride
RAM	Random Access Memory
RGB	Red-Green-Blue
RMSE	Root Mean Square Error
SSC	Suspended Sediment Concentration
SfM	Structure-from-Motion
TKE	Turbulent Kinetic Energy
UAV	Uncrewed Aerial Vehicle
UV	Ultraviolet

Roman symbols

B_c	Braiding Index
cm	Centimeter
Fr	Froude number
g	Gravitational constant
Gb	Gigabyte
Ghz	Gigahertz
k	Turbulent Kinetic Energy
k_g	Constant
m	Meter
mm	Millimeter
R^2	Coefficient of determination

Re	Reynolds number
T	Transformation matrix (Nortek Vectrino)
T or t	Time
u	Horizontal velocity
v	Horizontal velocity
w	Vertical velocity
$\bar{x}$	Mean of variable

Greek symbols

λ	Expected maximum
τ_o	Bed shear stress
τ_{oc}	Critical bed shear stress
σ	Standard deviation

Chapter 1: Introduction

1.1 Thesis overview and structure

This PhD thesis focuses on the development of periphyton in recently-deglaciated floodplains. It attempts to understand how the physical habitat of glacial floodplains conditions the development of periphyton, and how in turn periphyton development promotes primary succession through ecosystem engineering. This PhD thesis is part of the wider, interdisciplinary, and synergistic project ENSEMBLE[1]. This project combines experts from different scientific domains (e.g., geomorphology, stream ecology, microbiology, etc.), and aims to understand why biofilms, including periphyton, are successful modes of life in glacial environments and how they contribute to the ontogeny of glacial floodplains. ENSEMBLE is a collaborative project involving four academic institutions: the University of Lausanne (UNIL), the Swiss Federal Institute of Technology of Lausanne (EPFL), the Swiss Federal Institute of Technology of Zürich (ETHZ) and the University of Luxemburg.

The thesis is built around four scientific papers, and it is structured as follows. This Chapter describes and justifies the thesis aims and associated research questions. It also provides an overview of the collaborations with fellow researchers and the resulting scientific outputs that are not explicitly examined in this thesis. Chapter 2 is a published literature review that proposes a conceptual model for the ontogeny of recently-deglaciated floodplains. Chapter 3 develops and assesses a method for periphyton mapping at high temporal and spatial resolutions. Chapter 4 aims to decrypt the relationship between periphyton development and physical habitat in a glacial floodplain, and to provide a better understanding of the ecological functioning of glacial stream systems. Chapter 5 seeks to develop an explanation of the patterns described in Chapter 4 through controlled *in situ* flume experiments. Chapter 6 synthesizes the research findings and considers perspectives for new frontiers in periphyton research. Chapter 7 concludes the thesis.

1.2 Scientific overview and PhD research questions

Glaciers are retreating worldwide (Moon, 2007). In the Alps they lost almost 50% of their surface between 1850 and 2000 (Zemp et al., 2006). This is creating spatially extensive proglacial environments where the switch from glacial to non-glacial conditions (Heckmann et al., 2016) has important ecological consequences. The latter are not only local but may extend some way further downstream even if the nature of these impacts remains poorly understood (Brown et al., 2007; Milner et al., 2009; Jacobsen et al., 2012; Hotaling et al., 2017).

[1] ENSEMBLE: *Elucidating the success of microbial biofilms and their implications for habitability and ecosystem evolution in glacial floodplain streams*. The ENSEMBLE project was supported by Swiss National Science Foundation Sinergia grant CRSII5_180241 ENSEMBLE awarded to T. J. Battin, S. N. Lane, M. Lever and P. Wilmes.

The terrain exposed by retreating glaciers will be colonized by new organisms (Chapin et al., 1994; Fastie, 1995; Kaufmann, 2001; Eichel, 2019). However, such systems can by highly unstable (Marren, 2005; Heckmann et al., 2016; Bakker et al., 2019) such that colonization might be difficult. Habitat instability in glacial forefields appears to be a preponderant factor in defining where, but also when, organisms such as periphyton can develop (Miller and Lane, 2019). Particularly in summer, high rates of reworking (Marren, 2005; Heckmann et al., 2016) caused by high meltwater and sediment supply rates (Milner and Petts, 1994; Nienow et al., 1998; Swift et al., 2005; Perolo et al., 2019) create continuous physical disturbances that may prevent new periphyton development or lead to the scour and burial of existing periphyton (Peterson, 1996; Biggs et al., 1998). In winter, disturbances are negligible given discharge attenuation (Malard et al., 1999; Maizels, 2002), but periphyton development rates should be lower given the snowpack (Uehlinger et al., 2010) and low levels of potential phototrophic activity. Hence, it is thought to be in the late spring and autumn when periphyton can proliferate in glacial floodplains (Uehlinger et al., 1998, 2002, 2010).

That said, however, glacial floodplains are also characterized by a heterogeneous assemblage of benthic habitats (Ward et al., 1998). This complexity results from the presence of tributary streams with less adverse environmental conditions (Ward et al., 1998; Uehlinger et al., 1998, Boix-Canadell et al., 2021), and by a wide range of disturbance frequencies within the most active floodplain system (Bakker et al., 2019). For instance, the classical model of proglacial margin response to a retreating glacier is erosion proximal to the glacier margin and deposition more distally. This commonly involves incision and terrace formation closer to the glacier and deposition and braiding in zones further downstream provided the valley setting (i.e., slope and width) allows it (Thompson and Jones, 1986; Thompson, 1988; Germanosky and Schumm, 1993; Marren and Toomath, 2013; 2014; Roussel et al., 2018). Terraces may be much more stable than active channel zones, i.e. where the stream is mostly braided (Maizels, 2002; Marren, 2005), and their presence and the tributaries that flow over them may explain why well-developed periphyton can be found in proglacial forefields even in summer when proglacial braidplains are most active (Miller and Lane, 2019). Thus, there is substantial opportunity for terraces to be hotspots for periphyton development. Terraces are one extreme however and between the more stable terrace zones and the zones of most frequent stream bed reworking there may be a range of times since the last disturbance (“landform ages”, Lane and Richards, 1997), and this may result in short and spatially-localised windows of opportunity that periphyton could exploit.

Such observations are complicated by the fact that low rates of disturbance do not necessarily mean that periphyton will develop, because water availability is also crucial (Rydgren et al., 2014). It is well known that glacial floodplains are supported by a complex set of different water sources (e.g., snow-melt, ice-melt, spring-fed, etc.) that vary in importance within the year (Malard et al., 1999; Ward et al., 1999; Müller et al., 2022). In addition, it is known that glaciogenic sediments are highly permeable and that surface water drains readily (Cooper, 1923; Matthews, 1992; Burga et al., 2010; Viles, 2012), becoming rapidly unavailable to organisms that require access to

it for their establishment and growth. This can be particularly problematic for some proglacial marginal zones, such as terraces, because they are disconnected from the main source of water during the summer, that is melt water. As access to water can be variable in space but also limited in time, where and when periphyton can develop within glacial forefields may also vary.

However, the feedbacks that follow periphyton development may limit such "drying" processes. For instance, it is thought that water can be maintained at the surface by periphyton (Miller and Lane, 2019), if their development leads to the clogging of streambed interstices (Ragusa et al., 1994; Cunningham et al., 1991; Thullner et al., 2002; Gette-Bouvarot et al., 2014; Caruso et al., 2017). If that is true, periphyton may have important impacts on floodplain habitability because water access is secured even during drier periods in areas where access to meltwater is not possible. It is also possible that periphyton increase sediment stability, as they do in other environments (Neumeier et al., 2006; Le Hir et al., 2007; Gerbersdorf et al., 2008a, b, 2009a, b; Vignaga et al., 2013; Fang et al., 2014; Thom et al., 2015; Pivato et al., 2019). Taken together, periphyton should increase the habitability of the benthic substrate, which (a) influences positively their own development; but (b) in decreasing sediment permeability and mobility, promote successional processes (Kaštovská et al., 2005; Zumsteg et al., 2012; Raab et al., 2012; Frey et al., 2013; Miller and Lane, 2019). In this sense, periphyton may have an important function as "ecosystem engineers" (Jones et al., 1994).

From this brief overview, it is logical to propose that periphyton play an important role in ecosystem development in recently-deglaciated terrains. Yet, periphyton have received surprisingly little attention. There are no systematic studies of where and when periphyton develop within melt-seasons in proglacial forefields. Linkages to habitat stability and water accessibility remain poorly quantified. There are almost no studies of how, and if, the development of periphyton feeds back into glacial forefield habitability through changes in surface drainage and bed sediment stability. Given this, the aims of my PhD thesis are (1) to quantify the dynamics and drivers of periphyton development in proglacial floodplains during the melt-season, and (2) if and subsequently how the development of periphyton promotes primary succession through ecosystem engineering. This PhD thesis addresses the following inter-related questions:

I. Where and when do periphyton develop in proglacial forefields during the melt-season?
II. How is periphyton development related to habitat stability, stream morphodynamics, and access to water spatially and temporally at the scale of a representative proglacial braid plain?
III. What are the mechanisms, rates and time-scales associated with these patterns and how does the development of periphyton feed back into glacial forefield habitability?

Four primary contributions to the scientific literature (Chapters 2 through 5) respond to these questions.

1.3 Thesis structure and research questions

Chapter 2 provides the overall scientific context of this thesis, and it serves as the foundation of the subsequent chapters by showing the importance of the research questions and associated hypotheses that are the focus of the thesis. To address the first research question, Chapter 3 presents a method for acquiring information on the spatio-temporal development of periphyton in an Alpine proglacial margin using very high resolution, drone-acquired imagery coupled with subsequent image processing and analysis. The derived information is then used in Chapter 4 to address the second research question concerning the relation of the spatio-temporal development of periphyton to physical habitat. This extensive analysis suggests the importance of water availability and sediment stability as a condition for perennial periphyton development. These findings then drive the design of a set of experiments in Chapter 5, which address the third research question concerning the mechanisms induced by periphyton development.

1.4 Study site

The study site of this thesis is the floodplain of the Otemma glacier (Figure 1; 45°56′04.9″N 7°24′46.1″E), which is located in Southwestern Switzerland. The floodplain is at an average altitude of 2450 m above sea level. It is approximately 900 m long and 150 m wide, and it is constrained by crystalline bedrock (metagranitoides and metagabbros), and steep slopes. The floodplain has formed since the early 2000s in response to the rapid (*c*. 50 m per year) retreat of the Otemma glacier (Mancini and Lane, 2020; Egli et al., 2021).

The floodplain is characterized by a well-developed braided glacial stream system, which drives high rates of morphodynamic activity during the melt season (Mancini and Lane, 2020). The floodplain is also drained by a number of hillslope-fed (i.e., krenal and rithral) channels that converge into the main glacially-fed stream (Müller et al., 2022). The ecosystem (i.e., pioneering plants, macroinvertebrates, biofilms, etc.) is therefore constrained to morphodynamically less active zones and channel-fed hillslope sources (Miller and Lane, 2019; Brandani et al., 2022).

These physical and hydrological characteristics make the floodplain of the Otemma glacier an exceptional natural laboratory for studying periphyton dynamics. The ecosystem is embryonic, and its development still dictated by the hydro- and morphodynamic behaviour of the floodplain. This combination allows for a proper investigation of how the environment constraints the development of periphyton, but also how periphyton act as ecosystem engineers.

The floodplain is remote and indeed virtually untouched by human interventions that may influence the embryonic ecosystem. Furthermore, the remoteness prevent crowds from visiting the proglacial margin, thereby limiting interference with data

collection and the running of the experiments. Finally, the AlpWISE[2] group has intensively studied the floodplain (and the Otemma glacier) since 2017, thereby producing remarkable scientific datasets and promoting scientific exchanges and collaborations.

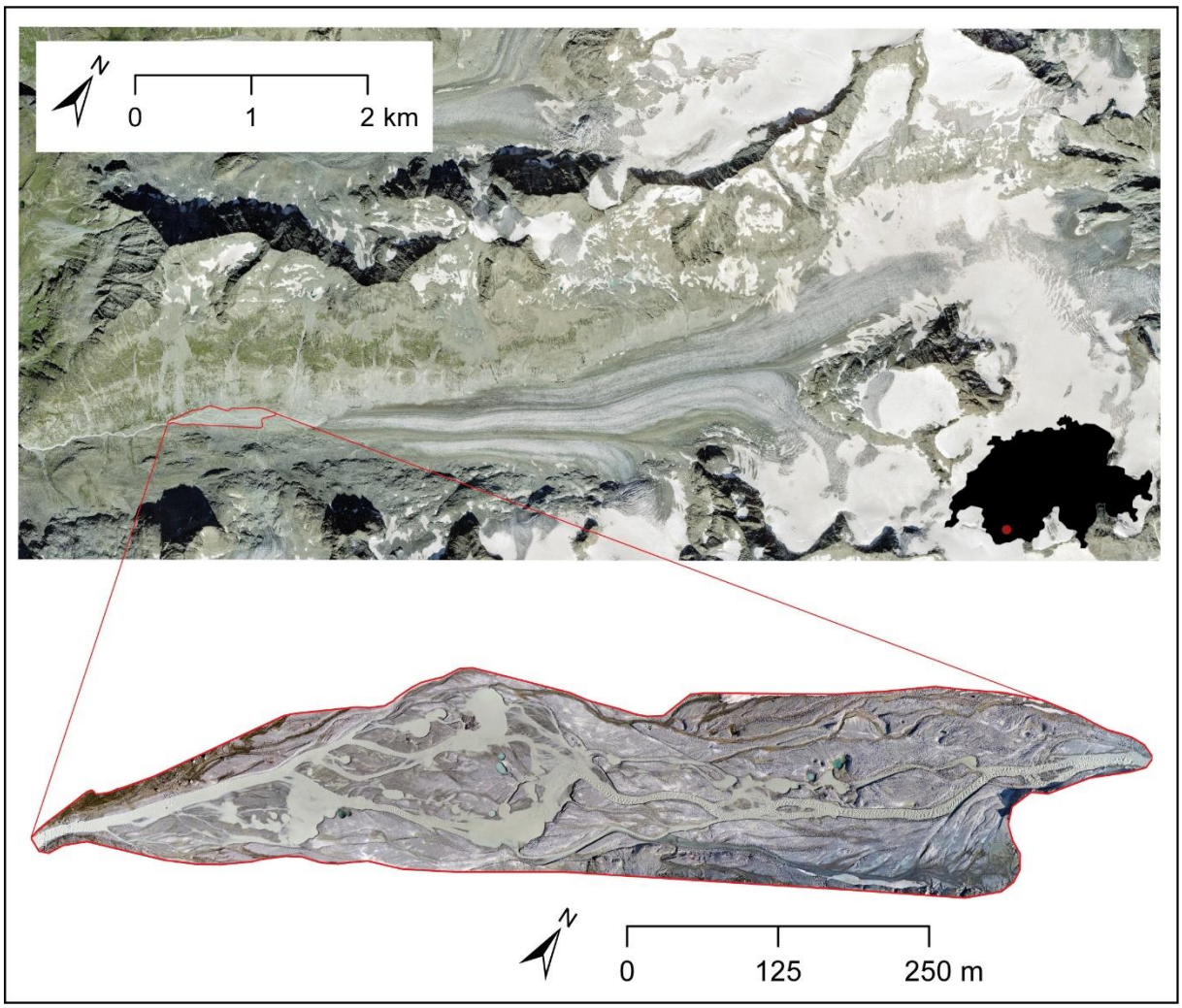

Figure 1: View of the headwaters of the Dranse de Bagnes (top image; ©Swisstopo) and zoom of the study zone, the floodplain of the Otemma glacier (bottom image).

1.5 Overview of the methodological approach

I address the three research questions with a set of different methodological approaches. The first research question attempts to define the spatio-temporal development of periphyton, with a particular focus upon the melt-season (Chapter 3). To do so, I collected high frequency (i.e., daily) drone imagery of the floodplain of the Otemma glacier, and I processed these images through rigorous Structure-from-Motion (SfM) Multiview Stereo (MVS) photogrammetry (Westoby et al., 2012; Fonstad et al., 2013; James et al., 2017, 2020; Lane et al., 2020). I then used the SfM-MVS derived orthomosaics to compute a set of visible band ratios (e.g., Tucker, 1979;

[2] The AlpWISE (ALPine Water, Ice, Sediment and Ecology) group is led by Prof. Dr. Stuart N. Lane, and is part of the Institute of Earth Surface Dynamics (University of Lausanne).

Kawashima and Nakatani, 1998; Gitelson et al., 2002; Saberioon et al., 2014) and to train logistic regression models to map periphyton presence in space and time.

The second question seeks to relate periphyton development to habitat stability, stream morphodynamics, and access to water (Chapter 4). Following Lane and Richards (1997) and Bakker et al. (2019), I first used the DEMs produced through SfM-MVS photogrammetry to characterize the events of streambed reworking (i.e., instability). Second, I used the orthomosaics to characterize the stream dynamics, and particularly the braiding intensity (Hong and Davies, 1979; Ashmore, 1988; Chew and Ashmore, 2001; Egozi and Ashmore, 2008) and the hydrological stability of non-glacial water sources. I then related these results with those of Chapter 3, and attempt to decrypt the physical habitat of periphyton.

The results of Chapter 4 likely provide the boundaries for answering the third research question, and hence to assess the potential feedbacks associated with periphyton development (Miller and Lane, 2019). To do so, I installed two outdoor flumes in the forefield of the Otemma glacier, and reproduced the environmental conditions suitable to periphyton development. During the running of the experiments, I followed the development of periphyton, and the evolution of the streambed with a set of different techniques. I collected daily imagery of the flumes for photogrammetric processing (Lane et al., 2001; Chandler et al., 2001; Butler et al., 2002; Kasprak et al., 2015; Morgan et al., 2017; Leduc et al., 2019), and subsequent analysis of the evolution of the bed (e.g., roughness). Concurrently, I investigated bio-clogging (Battin and Sengschmitt, 1998; Ibisch and Borchardt, 2002) by collecting daily data on the rate at which water infiltrates into the flume sediment matrix. Finally, I deployed an Acoustic Doppler Velocimeter (ADV) to collect the 3D flow velocities at the bottom of the flumes, and processed the 3D velocities to investigate the evolution of near-bed turbulent structures (e.g., Keylock et al., 2014).

1.6 Additional scientific collaborations and co-authored papers

During this PhD project, I have collaborated with a number of fellow PhD researchers, and have contributed to their projects (Table 1). The aim of this sub-chapter is to summarize my contributions to these projects that are not a primary part of the thesis presented in the following chapters.

During the summer of 2019, I participated in the main sampling campaign of the ENSEMBLE project. The campaign took place on the forefields of three Swiss glaciers; the Otemma, Valsorey, and Tschierva; and aimed to characterize the spatial patterns of benthic biofilm diversity. During this campaign, I was in charge of managing the drone surveys (i.e., image collection, image processing), and collecting the precise locations of the sampling points. In addition, I helped the ENSEMBLE team in collecting biofilm and sediment samples for laboratory analysis. The results of this campaign led to a scientific publication in *Frontiers in Microbiology* (Brandani et al., 2022).

During the summers of 2020 and 2021, I took part in intensive field campaigns of the AlpWISE group at the Otemma glacier. These campaigns aimed to investigate the morphological, hydrological, and sedimentological functioning of recently-deglaciated alpine forefields, and used the Otemma glacier forefield as a case study. During these campaigns, I helped manage and collect drone images. Later, together with D. Mancini, I led the image processing and production of high resolution and high quality Digital Elevation Models (DEMs) and orthoimages. The photogrammetric outputs were used in different publications that are undergoing peer review or are in production. In Müller et al. (in review), the DEMs and orthoimages were used to define the boundaries for a physically-based model of meltwater-groundwater interactions. In Mancini et al. (in prep*, a*), we used the DEMs and orthoimages for a statistical characterization of the streambed elevations (i.e., the bathymetry) of a braided and turbid glacial stream including a new method for when high turbidity meant the stream bed was not visible. In Mancini et al. (in review), the DEMs and orthoimages were used to assess the sedimentological evolution of the Otemma floodpain, and ultimately to investigate the morphodynamic shredding by such a system. Finally, I also helped the collection of seismic data to analyze the sediment export signal of a glacial braided stream system (Mancini et al., in prep*, b*).

Table 1: List of contributions

Brandani, J., Peter, H., Busi, S.B., Kohler, T.J., Fodelianakis, S., Ezzat, L., Michoud, G., Bourquin, M., Pramateftaki, P., Roncoroni, M., Lane, S.N. and Battin, T.J. (2022). Spatial patterns of benthic biofilm diversity among streams draining proglacial floodplains. *Frontiers in Microbiology*, *13*.
Müller, T., Roncoroni, M., Mancini, D., Lane, S.N. and Schaefli, B. (*in review*). Current and future role of meltwater-groundwater dynamics in a proglacial Alpine outwash plain. *EGUsphere*, *1-34*.
Mancini, D., Roncoroni, M. and Lane, S.N. (*in preparation, a*). UAV- SfM photogrammetry of braided river morphodynamics using heuristic representation of inundated zones.
Mancini, D., Nicholas, A., Roncoroni, M. and Lane, S.N. (*in preparation, b*). Morphodynamic shredding of subglacial export by proglacial forefield in a context of rapid glacier retreat.
Mancini, D., Dietze, M., Muller, T., Jenkin, M., Miesen, F., Roncoroni, M., Nicholas, A. and Lane, S.N. (*in review*). Rapid shredding of subglacial sediment export signal by proglacial forefields. *Geophysical Research Letters - Earth Surface*.

Chapter 2: Ecosystem engineers: biofilms and the ontogeny of glacier floodplain ecosystems

2.1 Chapter overview

This chapter reviews the existing knowledge of biofilm development, including periphyton, in glacial floodplains and its relationship with glacial stream morphodynamics. It also discusses the potential role of biofilms in promoting primary succession via ecosystem engineering, and it proposes a conceptual model for glacial floodplain ontogenesis. This chapter was published as a peer-review paper: Roncoroni, M., Brandani, J., Battin, T.J., and Lane, S.N. (2019). Ecosystem engineers: biofilms and the ontogeny of glacier floodplain ecosystems. *Wiley Interdisciplinary Reviews: Water*, *6*(6), e1390.

2.2 Ecosystem engineers: biofilms and the ontogeny of glacier floodplain ecosystems

2.2.1 Introduction

Some organisms have the capacity to transform ecosystems echoing ways engineers build, create, and modify their surrounding environment (Polvi and Sarneel, 2018). The term “ecosystem engineering,” commonly used in ecology, describes this phenomenon and takes place in diverse ecosystems involving potentially a multitude of organisms (Jones et al., 1994, 1997). In an introduction to ecosystem engineers in rivers, Polvi and Sarneel (2018) state that while the balance between hydraulic energy and sediment size and quantity influence the shape and function of streams, ecosystem engineers may considerably modify the functioning of aquatic and riparian ecosystems by changing streamflow characteristics. Freshwater ecosystem engineers can be found from headwaters downstream to estuaries, and in channels with different perimeter sedimentology (e.g., gravel, sand, and cohesive or coarse material), patterns (e.g., single-thread, braided), and morphodynamics. A stream's hydrological context may set constraints upon the growth and survival of ecosystem engineers in aquatic and riparian ecosystems (Bätz et al., 2015; Gurnell, 2014) and organisms will generally only engineer positive feedbacks where resources are available (e.g., trapping and stabilizing fine sediments) within those constraints (Moore, 2006).

The floodplains of glacier-fed rivers, characterized by a recent switch to phototrophic conditions and extensive deposits of glaciogenic sediment, are usually slow to revegetate (Hotaling et al., 2017). Altitude, and hence temperature, may be a factor restricting vegetation succession, but fundamentally, glaciogenic sediments are nutrient-poor and unstable. Although conceptual models of vegetation succession in glacial forefields are well-developed (see review in Miller and Lane, 2019) the early stages of ontogenesis, and notably the role played by microbial life in driving related processes, is very poorly understood. Freshwater biofilms can develop rapidly and are implicated in multiple ecosystem processes (Battin et al., 2003, 2016) and, because of

the profound impacts that they can have upon resource availability, they are candidate ecosystem engineers. In this review, we focus upon freshwater stream benthic biofilms, as potential ecosystem engineers (Gerbersdorf et al., 2008a, b, 2009a, b) with a particular focus on the early ontogeny of glacial floodplain ecosystems following glacier retreat. Biofilms have received less focus compared to more visible organisms such as beavers, mussels, and snails (Gurnell, 2014), and thus their engineering capacity is less well documented (Polvi and Sarneel, 2018). The aim of this paper is to review the role of biofilms as ecosystem engineers in streams and to develop a conceptual model for the relevance of microbial biofilms for glacial floodplain ecosystem ontogeny.

Table 2: Key definitions

Autogenic	Autogenic engineers are organisms that change their surrounding environment through their own living or dead tissues, such as vegetation that increases river bank stability through its own biological structure.
Allogenic	Allogenic engineers are organisms that change their surrounding environment through the transformation of materials from one state to another, such as beavers that build wooden dams by cutting living trees.
Intentional engineering	Intentional modification of the surrounding environment to benefit from it (e.g., nest digging by salmonids).
Unintentional engineering	Unintentional modification of the surrounding environment that does not provide direct feedbacks to the engineer, but it can have positive or negative impacts upon other organisms.
Extracellular polymeric substances (EPS)	Biomolecules binding cells to each other and to solid materials mainly composed of polysaccharides and proteins.
Prokaryotes	Unicellular organisms lacking internal membrane-bound structure without a distinct nucleus.
Lysed cells	Cells affected by the breakdown of membrane due to virial, enzymatic or osmotic processes compromising its integrity.
Stoichiometric homeostasis	Property of an organism to keep its biomass element ratio relatively stable independently of its substrate.
Roughness	Roughness describes the loss of energy experienced by the flowing water due to the friction against the streambed and/or banks. Related to channel morphology (e.g., grain size, grain angle, etc.), it influences hydraulic components such as flow velocities, turbulence and particle motion, as well as the ecological setting of the benthic substratum.
Critical shear stress	The critical shear stress (τ_{oc}) is the threshold from which particles can be mobilized. Below this threshold, resisting forces (e.g., e.g. gravity) keep grains on the streambed; above this threshold, moving forces initiate particle movement. Hence, particle movement begins only when the shear stress (τ_o) exerted by water on the grains is greater than the critical shear stress defined by properties of the streambed
Ontogeny	In biology, ontogeny refers to development of an organism, an anatomical part or a behavioral trait through time. In this paper, we refer to the ecological development of glacial floodplains. In particular, we refer to the way in which life develops in these environments by converting barren, hostile and water-limited soils to fertile and water retaining ones (i.e., morphogenesis of a rocky environment).

2.2.2 Ecosystem engineering: key concepts

2.2.2.1 The concept of ecosystem engineering

Almost three decades ago, two new terms emerged in ecology: “ecosystem engineering” and “ecosystem engineers” (Jones et al., 1994; Lawton and Jones, 1993). The former describes the act of engineering an ecosystem, while the latter describes how organisms act as engineers (Jones et al., 1994). The notion of ecosystem engineering and engineers in rivers and streams has been reviewed by Moore (2006) and more recently by Polvi and Sarneel (2018) and so only a short summary is provided here.

Jones et al. (1994) described ecosystem engineers as “*organisms that directly or indirectly modulate the availability of resources* […] *to other species, by causing physical state changes in biotic and abiotic materials*” (Jones et al., 1994, p. 374). Jones et al. (1994, 1997) also introduced a key distinction between ecosystem engineers: autogenic versus allogenic. Autogenic engineers modify the surrounding environment through their own living or dead tissue (Jones et al., 1994; Polvi and Sarneel, 2018). Allogenic engineers change the environment through the transformation of materials from one state to another (Jones et al., 1994, 1997). As an example, vegetation (e.g., willows) plays an important role in the riparian zone (Gurnell and Petts, 2002) by stabilizing sediments and leading to the creation of more stable habitats like islands (Gurnell, 2014), as well as increasing bank stability (Simon and Collison, 2002). Hence, riparian plants are autogenic engineers as it is their own root system that increases the resistance of river banks to erosion. In contrast, caddisfly larvae build nets that reduce sediment erodibility by increasing the critical shear stress and hence resistance to sediment entrainment (Cardinale et al., 2004; Johnson et al., 2009; Statzner et al., 1999). They are allogenic engineers as it is material made by the larvae that increases the resistance of gravels to erosion by water. The distinction between autogenic and allogenic engineers is not fixed; allogenic engineers can also have autogenic effects, and vice versa (Jones et al., 1994), sometimes simultaneously. For instance, *Salix* autogenically increases the stability of river banks but allogenically changes depositional processes and can influence soil formation (Bätz et al., 2015).

Ecosystem engineering is not concerned with direct provision of resources (e.g., as part of a food chain) (Jones et al., 1994, 1997). For instance, predator–prey relationships between fish, such as salmonids, and macroinvertebrates, such as stoneflies (Soluk and Richardson, 1997), are not engineering because prey simply provides food to predators. Rather, ecosystem engineers effectively manage resources; either intentionally or unintentionally. The former describes the traits (“extended phenotypes”; see Dawkins, 1982) that an organism possesses that allows intentional transformation of its environment (e.g., when a beaver explicitly builds a dam or the female salmon digs a redd) (Jones et al., 1994, 1997). The latter describes the traces that have been left incidentally by organisms but which “manage” the environment for others (e.g., woody debris in the stream) (Jones et al., 1994, 1997).

Whether or not ecosystem engineering is intentional or unintentional, it is thought to occur in all ecosystems (Jones et al., 1994) and the majority of, if not all, organisms are capable of doing it (Jones et al., 1994, 1997; Wright and Jones, 2004).

Jones et al.'s statements about the ubiquity of ecosystem engineering opened a scientific debate about the usefulness of the terms “ecosystem engineering” and “ecosystem engineer”; what use is such terms if they apply everywhere and to all things (Reichman and Seabloom, 2002a, 2002b)? Ecosystem engineering needs to be distinguished in terms of scale and magnitude of impacts and not simply based upon a functional definition regarding how an organism engineers. Hence, we consider both functions and scale/magnitude effects. Hastings et al. (2007) noted that ecosystem engineering impacts can be either small or large, both in size and in time, and are related to the size and lifespan of the engineer itself. Impacts should be important and visible at large scales for organisms to be true engineers of ecosystems (Hastings et al., 2007). Intentional engineering may seem to be more important than unintentional, but this is not necessarily the case. For instance, large woody debris, which is unintentional engineering, can substantially impact salmonid populations (House and Boehne, 1986; Zika and Peter, 2002).

2.2.2.2 Stream ecosystem engineering: a matter of scale

The physical processes that drive rivers and the ways in which rivers in turn erode and deposit sediment to make landscapes have been identified at scales from the subdaily to millions of years (Schumm and Lichty, 1965). Such processes not only produce spatio-temporal variation in the landscapes we see but also create the habitat templates upon which life develops and also the constraints to which life must adapt (e.g., flow regime, accommodation space, perturbation frequency, microclimate, etc.). At the same time, and still poorly understood, organisms can modify stream ecosystems (Moore, 2006; Polvi and Sarneel, 2018) through ecosystem engineering. Not all organisms have similar engineering impacts on streams, and these effects depend upon the engineers themselves (Hastings et al., 2007). Ecosystem engineering has tended to focus on visible impacts (e.g., beaver dams) made by large organisms (Gerbersdorf et al., 2009b) but scaling stream ecosystem engineers based on their size is not forcibly correct for three reasons.

First, within-organism size variations may be important and bigger individuals may have bigger engineering effects. For instance, in relation to brown trout (*Salmo trutta*) redds, bigger females produce bigger redds (Crisp and Carling, 1989). Redd construction, by sorting sediments, decreases streambed erodibility by increasing the critical shear stress for sediment transport (Montgomery et al., 1996). Thus, bigger female trout have bigger engineering effects on the streambed compared with smaller females.

Second, scale depends upon your point of view. Depending on the chosen geomorphological scale (e.g., watershed vs. pool-riffle sequence) ecosystem engineering can lead to substantial differences in apparent impacts. For instance,

vegetation might have a greater stabilization potential compared to caddisflies at the overall watershed level, whereas for a given streambed surface caddisflies might have greater potential. Hence, the smaller the scale, the more important smaller organisms become.

Third, there is an important relationship between engineering magnitude and the number of organisms taking part in the engineering effort, and this association is generally positive and may be more than additive. This is because it is the assemblage of organisms that multiply the engineering potential of any individual organism (Boogert et al., 2006). Consider for example microorganisms (e.g., microbes); individually they are not able to stabilize sediments; in communities (biofilms) they may have remarkable stabilization effects (Section 2.2.3.2).

2.2.3 Stream biofilms as ecosystem engineers

2.2.3.1 Biofilms: an introduction

Biofilms dominate microbial life in most aquatic ecosystems (Flemming and Würtz, 2019) and particularly in streams (Battin et al., 2016). Biofilms are surface-attached microbial communities that dwell in a matrix composed of extracellular polymeric substances (EPS). Several properties emerge from the biofilm mode of life that underpin its ecological success (Flemming et al., 2016). The spatial organization of microbial life within a matrix induces the establishment of physical and chemical gradients that provide habitat diversity and hence increases biodiversity. The biofilm matrix also facilitates the sorption of solutes and resource capture, stimulating biotic interactions and protecting from erosion, grazing, and UV radiation, for instance.

Benthic biofilms in streams are highly diverse, including taxa from all three domains of life (i.e., archaea, bacteria, and eukaryotes) (Battin et al., 2016; Bengtsson et al., 2018) and even abundant and diverse viruses (M. Bekliz, personal communication). Prokaryotes and algae (mostly diatoms) rapidly colonize sedimentary surfaces where, after an initial adhesion phase, growth triggers a succession that often involves bacteria that are typical biofilm formers (Niederdorfer et al., 2016). As this succession proceeds, niches can develop within the nascent biofilm, which fosters its biodiversity (Jackson et al., 2001) (Figure 2).

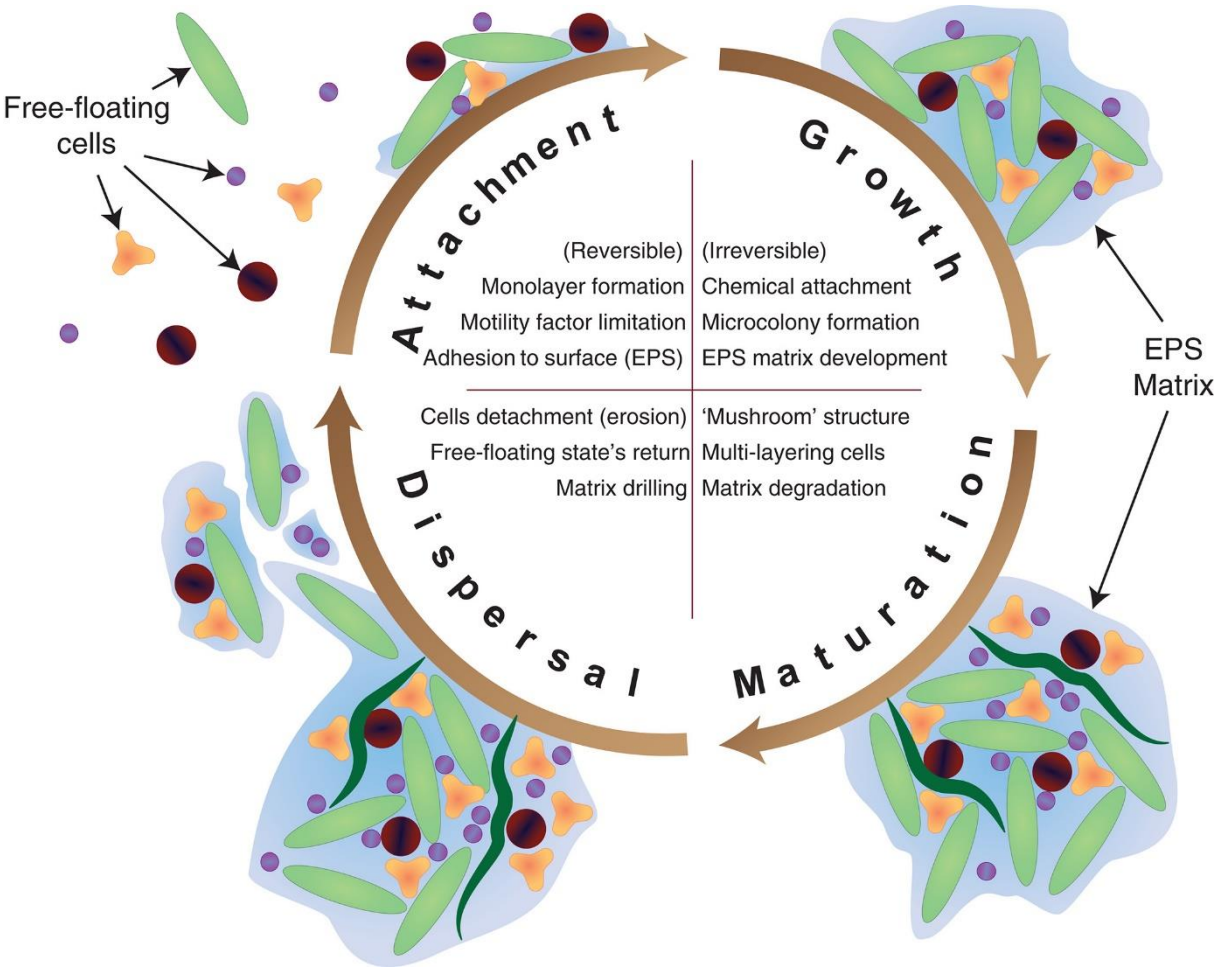

Figure 2: Biofilm development stages. From planktonic phase, microbes deposit and attach on the surface and start producing extracellular polymeric substances (EPS). With the secretion of EPS substances, the biofilm enters its growth stage and microcolonies are formed. When the biofilm matures, it may reach a "mushroom" structure where slough of biofilm will later be affected by erosion forces and dispersal. This dispersal stage will link together local communities and form biofilm metacommunities.

Depending on local hydraulics and sediment size distribution, benthic biofilms form complex and dynamic physical structures, including ridges or filamentous streamers (in the centimeter range) that float in water (Flemming and Wingender, 2010). The physical structure of biofilms is critical for mass transfer and related microbial processes including the uptake and metabolism of organic compounds (e.g., Battin et al., 2003; Singer et al., 2010). It is the combination of the very large reactive surface, high biodiversity, and continuous exposure to the flow of stream water and associated solutes that make biofilms so important for stream ecosystem processes. For instance, they are the major sites of ecosystem metabolism (i.e., gross primary production and respiration) and therefore of nutrient and carbon cycling in streams (Battin et al., 2016; Demars, 2018). As such, they also form the basis of the food web in numerous streams.

A critical aspect of biofilms is the matrix, extracellular material in which biofilms cells are embedded, acting as a protection for organisms (Flemming et al., 2016). The matrix is also recognized to store all available material from lysed cells and to capture

from the water phase both dissolved and particulate nutrients to make them available as nutrient and energy sources (Flemming and Wingender, 2010). EPS are the principal constituents of this matrix and are responsible for the biofilm's internal structure, surface attachment, and cohesion by maintaining cells in close proximity leading to strong cell-to-cell interactions (Flemming and Wingender, 2010). EPS differ between biofilms in terms of nutrient availability, community composition, hydrologic forces, and temperature. In their review, Flemming and Wingender (2010) describe the functions of EPS bacterial biofilms. These include functions such as adhesion, aggregation, cohesion of biofilms, sorption of inorganic ions, enzymatic activity, nutrient source, and water retention. It is thus possible to understand how the matrix can affect the mode of life of a given biofilm.

2.2.3.2 Biostabilization of sediments by biofilms

The hypothesis that biofilms cause biostabilization was suggested early in the 1930s by Carter (1932, 1933a, 1933b), but it was only quantitatively confirmed in the 1970s (Holland et al., 1974; Neumann et al., 1970; Scoffin, 1970). Traditionally, sediment transport has been seen as a physical process (Le Hir et al., 2007), related to channel hydraulics (e.g., Shields, 1936). However, in natural ecosystems, sediment transport processes can be altered by biotic influences (Flemming, 2002). This process is known as “biostabilization,” where organisms decrease the susceptibility of sediment to erosion (Paterson and Daborn, 1991).

Particle movement in streams starts when bed shear stress τ_o exceeds a certain threshold, the critical bed shear stress τ_{oc} (e.g., Fang et al., 2014; Leopold et al., 1964; Richards, 1982). It is now recognized that biofilms tend to increase τ_{oc} (Fang et al., 2014; Neumeier et al., 2006; Pivato et al., 2019). EPS are the major driver of increased cohesion and stability of sediments (Dade et al., 1990; de Boer, 1981; Grant and Gust, 1987; Paterson, 1989, 1994). Following Tolhurst et al. (2002), EPS involve sediment stabilization by either physical binding (apparent cohesion) or molecular electrochemical interactions (chemical cohesion).

It is also known that the biofilms modify bed morphology, so changing bed roughness, influencing near-bed velocities and ultimately impacting sediment transport (Van Rijn, 2007). Biofilms may themselves have a morphology and, as a result, they may increase (Flemming et al., 2007) or reduce (Fang et al., 2014) bed roughness. Biofilms can increase the roughness by developing free-flowing “fluffy” morphologies (e.g., free flowing streamers) that are easily erodible along with the uppermost sediment layers even at low flows (Flemming et al, 2007). On the other hand, biofilms can also reduce bed roughness by developing smoother mats, which reduce the shear stress available to transport the particles (Fang et al., 2014). However, this can also reduce the energy losses at the surface, change shear stress partitioning, and ultimately increase the component of shear stress available to entrain and transport sediment. Bed-smoothing (e.g., by introduction of finer sediments) has been shown to lead to bed destabilization (An et al., 2019; Wilcock et al., 2001) independent of any increases in critical shear stress. Whilst biofilms may increase resistance to motion,

their impact on shear stress partitioning may also increase the shear stress available for transport, which results in an increase of the susceptibility of the bed to being eroded. Thus, the bed stabilization provided by biofilms is a function of the balance between the forces that increase sediment cohesion and hence resistance to erosion and the forces that tend to erode them, both external (e.g., shear stress) and internal to the biofilms (e.g., fluffy morphologies, smoothed mats).

Whether or not biofilms stabilize sediments, it appears that this process is particle size dependent, and proportionally more important for finer particles. For instance, Statzner et al. (1999) found that benthic microalgae and their biofilms are able to stabilize sand particles, that is, those finer than 2 mm. The fact that biofilm stabilization is potentially particle size dependent, and greater for finer sediments, perhaps explains why there has been more focus on marine environments (e.g., tidal flats) than on freshwater environments (Fang et al., 2014). Freshwater environments can have coarser bed sediment but many coastal environments are depositional, composed of terrestrially derived material that has been sorted by rivers and streams, such that most material is finer.

Biostabilization also appears to be more efficient in saltwater than in freshwater because of ion concentrations related to seawater chemical properties (Gerbersdorf and Wieprecht, 2015; Spears et al., 2008). It has been shown (Flemming and Wingender, 2010) that biostabilization could be enhanced by a surplus of cations, such as in saltwater, that helps to create strong electrochemical bridges between the EPS and the sediments. For instance, Stal (2003) and Flemming et al. (2007) found that an increase in Ca^{2+} (and in general of all divalent cations) has the consequence of increasing the binding forces between the matrix and the sediments resulting in greater biostabilization.

To investigate the role of biofilms in stabilizing sediments, the analysis of shear stress and/or critical shear stress is common. Grant and Gust (1987) investigated the role of purple sulfur bacterial mats in stabilizing marine sediments, and they tested their hypothesis in laboratory flumes with samples collected directly on a South Florida beach. By increasing flume discharge (i.e., increasing τ_o) until the erosion threshold was reached, they demonstrated that colonized sediments have a τ_{oc} up to five times higher compared with sterile sediments (Grant and Gust, 1987). Similar results were recorded by Tolhurst et al. (2002) who found a 3.7 times increase in τ_{oc}. In their experiments, they used cohesive sediments from a Scottish estuary and a variable amount of commercially extracted EPS (Tolhurst et al., 2002), which mimics the natural increase of EPS following biofilm growth but without the need to wait for natural biofilm growth.

Neumeier et al. (2006) simulated diatom biofilm growth for a tidal environment in a laboratory flume in a 28-day experiment. They reported a 10-fold increase in τ_oc for sediments colonized by a well-developed biofilm (after 28 days of colonization) compared with abiotic sediments (Neumeier et al., 2006). In two 5-week experiments using small glass beads and biofilms sampled in a Scottish estuary, Gerbersdorf et al. (2008a) and Gerbersdorf et al. (2009b) found that τ_{oc} was up to 3.6 and 10.8 times

higher respectively compared with abiotic controls. The difference between these two increases was explained by the use of bacteria only in the former experiment and by the use of a mixture of bacteria and diatoms in the latter experiment (Gerbersdorf et al., 2009b). Gerbersdorf et al. (2009b) stated that one possible reason for this increase was synergistic interactions between diatoms and bacteria, with the former profiting from the exudates of the latter and vice versa.

Vignaga (2012) investigated biostabilization by freshwater cyanobacteria using experimental flumes, different particle sizes (1, 1.2, and 2.2 mm) and different growth periods (up to 10 weeks of colonization). Results showed the greatest biostabilization after 4 weeks with a maximum increase of τ_{oc} of 43% for particles of 1 mm, 35% for particles of 2.2 mm, and 30% for particles of 1.2 mm (Vignaga, 2012). This confirms the above-mentioned hypothesis that the impact of biofilms is likely to be greater for finer sediment. Thom et al. (2015), in 4–8-week experiments using flumes, riverine water, and glass beads of 0.1 and 0.2 mm showed a maximum increase of stability of almost 10 times compared with an abiotic reference (τ_{oc} = 0.23 N/m^2) (Thom et al., 2015).

Thom et al. (2015) also found that biostabilization is a seasonally driven phenomenon; the increase of τ_{oc} changes through the year. Sediment stability was just 1–1.5 times τ_{oc} for late autumn conditions, 3 times τ_{oc} for summer conditions, and at maximum (10 times) for spring conditions (Thom et al., 2015). Schmidt et al. (2016) also found a maximum increase of sediment stability with spring conditions and a minimum with autumn conditions. Seasonality has also been recorded in tidal environments (e.g., Amos et al., 2004; Widdows et al., 2000).

Pivato et al. (2019) showed that during winter and early spring biofilm growth was limited by low sediment temperatures and light availability. The low growth rate results in less developed winter biofilms (low biomass) incapable of stabilizing sediment because the mat was not developed enough to significantly increase the shear stress (Pivato et al., 2019). However, when meteorological and environmental conditions (e.g., light availability and sediment temperature) were suitable, the biofilm was able to mature rapidly and to provide effective biostabilization because the mat was developed enough to support higher shear stress (Pivato et al., 2019).

Other studies have considered the role of disturbance, here referred as an increase in the shear stress that could lead to bed destabilization and subsequent biofilm detachment, in conditioning how biofilms influence biostabilization. Mariotti and Fagherazzi (2012) modeled biofilms impacts under different disturbance scenarios in tidal environments. In their first scenario, strong but infrequent disturbances were applied to the biofilm, in the second, weak and infrequent disturbances were applied, while in the third weak (of the same magnitude of scenario 2) weak and frequent disturbances were applied. In the first case, biofilm biomass and τ_{oc} increased until the occurrence of the disturbance, which systematically destroyed the biofilm and restarted the cycle. In the second case, disturbances were neither large enough nor frequent enough to have a negative impact on the biofilm, which increased in both biomass and τ_{oc} until an equilibrium state was reached, defined here as the point in which biomass

and critical shear stress values fluctuate around a steady mean value. In the third case, frequent weak disturbances destroyed the biofilm progressively. From the last two scenarios, it appears that biofilm biostabilization is also a function of biofilm growth history (Mariotti and Fagherazzi, 2012). In similar projects, Yallop et al. (1994), Valentine et al. (2014), and Chen et al. (2017, 2019) for tidal environments and Thom et al. (2015) for riverine systems found that shorter growth periods lead to reduced stabilization effects, while long periods allow for stronger stability resulting in an increased ability to support greater shear stresses.

Chen et al. (2017) proposed also that the role of EPS in stabilizing sediment is not only a surficial phenomenon, and they argued that EPS can penetrate into sediment beds allowing for a deeper impact of biostabilization. In fact, they showed that after the failure of the surficial biofilm layer, the sediment stability still remained in place (Chen et al., 2017).

In summary, biofilms have the capacity to increase the critical shear stress of sediments, in particular by producing viscoelastic EPS. With increasing biostabilization, biofilms construct their own niche and may enhance the habitability of an otherwise unstable sedimentary environment. With better habitability, biofilms may proliferate resulting in greater EPS production and increased sediment stability, and so on until they are scoured or disintegrate. Hence, by changing the sediment state from unconsolidated to consolidated, biofilms act as allogenic engineers and this is done intentionally. Therefore, we propose the biostabilization of sedimentary environments as another important emergent property of the biofilm mode of life in streams, but whose importance is likely to be context specific (e.g., more important for fine sediments than coarse sediments).

2.2.3.3 Fertilization of sediments by biofilms

The mineral surfaces of stream sediments are typically devoid of significant amounts of organic substances. Dissolved molecules can sorb to the mineral surfaces thereby forming organomineral complexes (Aufdenkampe et al., 2011), which are typically thought to be protected from metabolism and hence of minor relevance for ecological processes (Rothman and Forney, 2008). As microbial biofilms colonize and accumulate on these mineral surfaces, they change the chemical stoichiometry of the sedimentary environment. Several processes are involved in this chemical shift. The adhesion of bacterial cells to minerals enriches their surface in nitrogen (N) and phosphorus (P) relative to carbon (C). This is because the C:N and C:P ratio of bacterial cells typically varies from 4 to 8 and 10 to 80, respectively (Hall et al., 2011). Microbial in origin, EPS are biopolymers that not only contain polysaccharides, but also DNA and a large variety of proteins as well (Flemming et al., 2007). As cells start proliferating and producing EPS they add organic carbon to the mineral matrix. Depending on the contribution of extracellular DNA and proteins to the EPS, the build-up of a biofilm matrix further enriches the mineral environment in P and N. As cells decay within the biofilms, their organic constituents are released to the matrix where they are transiently protected from loss through water flow, for instance. The exudation

of storage compounds by algae to maintain stoichiometric homeostasis during peak photosynthesis or shortly thereafter further contributes to chemical enrichment with the biofilm matrix. It is the close spatial proximity between the transient storage of reactive solutes and active cells that facilitates the remineralization and elemental cycling within biofilms (Battin et al., 2003). At the same time, the EPS matrix easily scavenges solutes from the streamwater owing to its very large surface area and chemical surface properties (Flemming et al., 2016; Freeman and Lock, 1995). As the biofilm matrix is enriched by EPS secretion and other chemical processes, more dissolved molecules sorb on mineral surfaces. This process is thus claimed to fertilize the biofilm's surrounding environment (Flemming and Wingender, 2010).

We argue therefore that the enrichment in nutrients by microorganisms and aided by the biofilm matrix acts as a fertilizer of an otherwise nutrient-poor mineral matrix. This is analogous to the soil build-up during primary vegetation succession. In streams, this process may gain relevance with concomitant biostabilization. In fact, it would be the latter that provides a time scale for microbial biofilms to accumulate and to recycle nutrients, and thereby fertilize the sediments. This is why we propose that biofilms act as allogenic engineers that alter the environment through material transformation (Jones et al., 1994). The resources resulting from this engineering become available for other microorganisms, but also for macroinvertebrates and potentially for plant seedlings as well. Fertilization can be understood as an intentional engineering process with a positive feedback on all microorganisms composing the biofilm matrix. In fact, nutrient enrichment within the sedimentary environment facilitates biofilm proliferation and further enhances nutrient stripping from the stream water.

2.2.4 Biofilms, ecosystem engineering and the ontogeny of glacial floodplains

2.2.4.1 Glacial floodplains and streams: highly dynamic environments

Glacial floodplains are highly dynamic environments experiencing continuous morphological change (Heckmann et al., 2016; Marren, 2005). Stream braiding is common in these environments (Maizels, 2002; Marren, 2005), and is controlled by both allogenic and autogenic factors (Ashworth and Ferguson, 1986). The system is externally influenced by discharge and sediment delivery. These combine with the extant morphology to determine spatial patterns of flow velocity and shear stress, as well as the sediment available for transport (Ashworth and Ferguson, 1986). Internally, shear stress partitioning and sediment availability regulate sediment transport. The latter shape channel morphology; and may sort sediment on the streambed, so changing bed roughness and velocity distributions and consequently the shear stresses (Ashworth and Ferguson, 1986). Bed sediment sorting will also change τ_{oc}. Thus, external factors control the internal ones and vice versa.

Discharge in glaciated river basins, and consequently in glacial forefields, has substantial variations both daily and yearly (Maizels, 2002; Marren, 2005), and it is usually charged with sediment in the form of bedload or suspended load (Gurnell,

1987; Milner and Petts, 1994). Daily or diurnal flow changes interact with stream bathymetry to drive rapid increases and then decreases in bed shear stress and hence sediment supply and sediment transport. Runoff can be produced by snowmelt or ice melt. Because the majority of ice melt is produced at the glacier surface (Nienow et al., 1998), ice melt is driven primarily by solar radiation, temperature, and wind speed (see Fountain, 1996; Nienow et al., 1998; Swift et al., 2005). Annually, discharge is strongly bound with radiation and temperature variations (Lane and Nienow, 2019; Maizels, 2002). Discharge is low in winter (Maizels, 2002; Malard et al., 1999) because the air temperature is below the melting point of ice. During late spring and summer, solar radiation becomes more intense and temperatures rise, and the daily flow maxima and variability increase due to snowpack melt (Nienow et al., 1998). As snow cover tends both to slow melt and to buffer melt water delivery to the stream, as long as the basin remains significantly snow covered, flow maxima tend to be damped and base flows maintained (Lane and Nienow, 2019). However, as snow melt occurs and the snow line retreats up a glacier, ice melt begins. As ice has a lower albedo than snow, melt rates are higher and as ice has a much lower porosity that snow, buffering and hence flow attenuation are reduced. Thus, peak flows become bigger and baseflows become smaller (Lane and Nienow, 2019; Malard et al., 1999; Nienow et al., 1998; Swift et al., 2005) through the melt season. By the end of the summer, falling incoming solar radiation causes glacier melt and so peak discharge to decrease but diurnal discharge variation is maintained. By late autumn, discharge approaches the winter minima (Maizels, 2002).

This variability in discharge is also coupled to strong variability in both suspended load and bedload. In glacial forefields, sediment sources may be either glacial or periglacial. The latter can be important, although this does depend on the degree of valley sidewall to proglacial stream coupling, which may be limited by alluvial fan formation (Lane et al., 2017). Over annual to decadal timescales glacial sediment sources are predominantly related to subglacial sediment evacuation by glacier melt. Measurements close to glacier margins (Mao et al., 2019) show distinct timescales of variation in suspended sediment concentration (SSC)-discharge relations. At the daily timescale (Clifford et al., 1995; Perolo et al., 2019), clockwise hysteresis can result because discharge forces shear stress to rise above the critical value needed for bed sediment transport and subglacial bed-accumulated fines are released. These become exhausted during the day, leading to lower concentrations on the falling limb. Superimposed on such daily timescales there may be a seasonal evolution. As sediment evacuation from glaciers falls to almost zero through winter, but at least some glacial erosion (due to ice deformation) may continue, there may be subglacial sediment accumulation during winter and early spring. This is evacuated and progressively exhausted through the melt season such that the degree of daily clockwise hysteresis may reduce (Clifford et al., 1995; Hodgkins, 1996; Mao and Carrillo, 2017; Riihimaki et al., 2005; Stott et al., 2014). It may also reduce due to the development of more channelized subglacial streams which reduce meltwater access to the bed of the glacier where sediment has accumulated and hence reduces sediment supply (Gimbert et al., 2016; Kulessa et al., 2008; Mair et al., 2002; Nienow et al., 1998; Swift et al., 2002).

Bedload is more difficult to measure and so it is less well known (Mao et al., 2019). Glacial streams are thought to be bedload dominated (Alley et al., 1997). Evidence points to some similarities with suspended sediment dynamics. Bedload transport appears to be controlled by discharge magnitude and variability. Perolo et al. (2019) showed how late season bedload export from an Alpine valley glacier switched on during the day and off during the night in response to variation in discharge and hence shear stress, leading to clockwise bedload transport hysteresis at the daily timescale. Using a hydraulic model for the whole melt season, they showed that bedload transport capacity was higher when the intensity of diurnal discharge fluctuation was greater because bedload responded as a nonlinear function of discharge over a critical value. Such changes in capacity may not be reflected in actual transport because, as with suspended sediment, there may be exhaustion effects at both the daily timescale but also at the seasonal timescale. However, such processes have rarely been studied.

The regular rise and fall of stream discharge, and hence bed shear stress, results in rates of morphodynamic change that are elevated as compared with nonglacial streams. Provided there is enough lateral accommodation space, high rates of sediment supply coupled to discharges that frequently exceed the threshold at which sediments start to move, lead to braided channel patterns. This may be reinforced by relatively low rates of ecosystem engineering due to vegetation, given climate conditions. Channel reworking rates have been shown to be a function of combined discharge and sediment supply variability (Lane et al., 1996) and give rise to a complex template of channels, submerged bedforms and exposed gravel bars (Germanoski and Schumm, 1993). Due to data collection challenges there are no studies that have quantified reworking rates at high frequency over an entire melt season. Bakker et al. (2019) presented data for a 3-week period, calculating bedload transport from measured erosion and deposition patterns. Figure 3 shows how bedload transport (and hence erosion and deposition) occurs over a number of different timescales and that during their 3 week study there was no part of the river occupied by water that was not reworked. This is of particular importance for biofilm development as rates of disturbance are so high that it is only likely to be in the early and late summer, when channel reworking rates fall, that there will be enough stability for biofilm development.

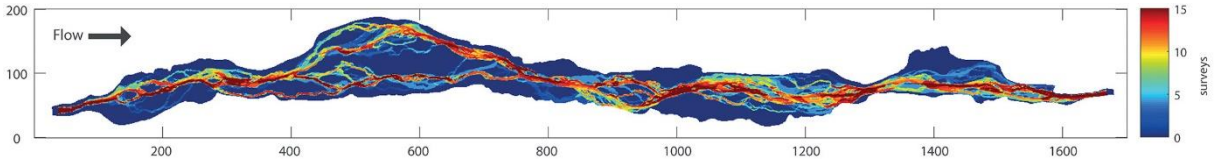

Figure 3: Transport frequency in an Alpine braided system showing the frequency of disturbances for 15 surveys of a river over a 21-day period (after Bakker et al., 2019). The x- and y-scales are given in meters.

Away from the morphodynamically active zone, zones that were previously active may become stable and allow vegetation succession (Figure 4). These are commonly on terraces, where incision of the active zone has reduced inundation and hence sediment transport and channel change frequency (Germanoski and Schumm, 1993; Marren, 2002; Marren and Toomath, 2013, 2014; Roussel et al., 2018;

Thompson, 1988; Thompson and Jones, 1986). Terrace formation depends upon the balance between sediment supply and sediment transport capacity (and hence glacier melt). With glacier recession, there is evidence (Cordier et al., 2017; de Winter et al., 2012; Roussel et al., 2018) that sediment supply does not keep up with capacity. The result is typically incision in front of retreating glacier margins, which provides sediment necessary for downstream aggradation (incision-aggradation, Marren, 2002; Beylich et al., 2009; Marren and Toomath, 2014; Roussel et al., 2018), although the extent to which this happens depends on valley slope and on whether or not proglacial lakes form that can disconnect downstream sediment delivery (Bogen et al., 2015). But, conditions have been observed where supply can keep up with capacity increases and aggradation is observed throughout the forefield (Curran et al., 2017). In flume experiments, Germanoski and Schumm (1993) showed that channel patterns associated with incision-aggradation are nearly always braided in aggradational zones, but may be braided or straight in incision zones, depending on incision rate; incising reaches invariably produce terraces, but higher incision rates are needed for a straight channel.

Given the apparent importance of more stable zones in supporting biofilm development (see Miller and Lane, 2019 and also Figures 4 and 6), this terrace formation is important. However, it is unlikely to be sufficient for biofilm development and vegetation succession. Glaciogenic deposits are typically extremely well drained and terraces, higher than the morphodynamically active river may be hydrologically stressed. To support ecological processes and succession, including biofilm development, water accessibility remains crucial (Rydgren et al., 2014) which implies that terraces need to be hydrologically connected, whether to surface water or groundwater (Miller and Lane, 2019). This makes ecosystem processes very dependent upon water sources besides those derived from the morphodynamically active stream itself, especially as incision is likely to have decoupled such terraces from groundwater supply by the mainstream. Such terraces are more likely to be dependent on snow-melt fed or spring-fed streams supplying water from the hillslopes (e.g., Malard et al., 1999; Ward et al., 1999) or larger-scale groundwater transfers. Snow-melt sources also tend to be seasonally variable (Malard et al., 1999) and evidence (Malard et al., 1999) suggests that in summertime terraces are supported by the hillslope-derived groundwater.

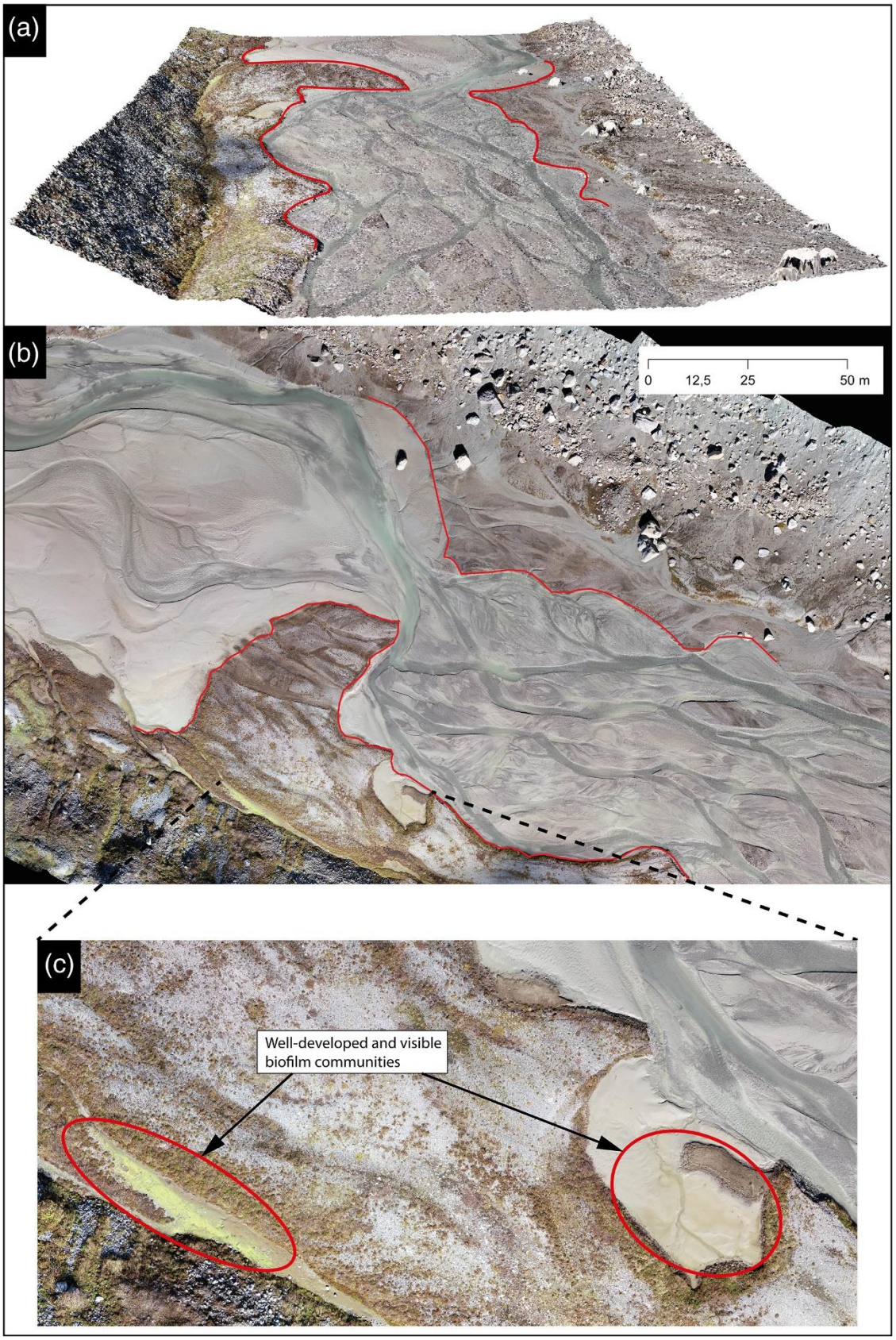

Figure 4: The Valsorey floodplain (Valais, Switzerland) in October 2018. The floodplain shows clearly primary succession patterns, which are confined to terraces (red lines mark the edges) on both sides of the river that are not reworked by the main braidplain (a,b). Well-developed and visible biofilm communities tend to be restricted to channels located on terraces (c) because disturbances are not too frequent to destroy the mats.

2.2.4.2 Proposed model of biofilms in glacier floodplain ecosystem ontogeny

2.2.4.2.1 From theory to reality

Previous sections showed how biofilms can act both as biostabilizators and fertilizers. In an ideal ecosystem, with the absence of abiotic disturbances both fertilization and biostabilization effects will increase with time (Figure 5a). The more stable the sediments are, the more biofilms will expand, grow and stabilize (Figure 2), and the more these effects will extend laterally to surrounding areas. The more nutrients captured within the biofilm matrix, the more enzymes will be produced, biofilm growth enhanced, and fertilization increased. These two processes should be complementary to one another and create a positive feedback loop that represents the first of the two types of ecosystem engineering identified above.

In theory, sediment fertilization allows microorganism and small plants to grow, and roots will enhance the stabilization of these sediments. Biostabilization should enhance fertilization by making biofilms and sediments less sensitive to erosion and by allowing the biofilm to store nutrients within its matrix and in sediments. This is the second type of bioengineering identified above. However, glacier-fed streams are continuously exposed to high-flow induced disturbances that may counter the potential effects of biostabilization. There are also questions that are yet unresolved regarding the extent to which biostabilization can really increase τ_{oc} sufficiently. The typical magnitude of the increases in τ_{oc} reported for the fine sediments typical of tidal environments are much lower than the magnitudes of the τ_{oc} values reported for the sediments, gravels, and coarser (e.g., 100–150 N/m^2) typical of glacial floodplain material. Thus, the biostabilization effects may be variable spatially, more important where there is sandy or silty material, which itself is more easily erodible and less likely to be stable.

2.2.4.2.2 Active floodplain

As highlighted in Section 2.2.4.1, stream dynamics continuously shape and reshape glacial forefields. This reworking may be seasonal, with periods of higher and lower rates of reworking that follow glacial hydrological and sediment supply regimes. Four periods can be identified and related to potential biofilm ecosystem engineering, namely summer, autumn, winter, and spring (Figure 5b). These periods do not map onto normal (e.g., astronomical or meteorological) definitions of the seasons and will vary substantially from year to year: for instance, at altitudes of 2000 m or higher, snowmelt in the glacial forefield may start as early as May or as late as early July depending on altitude and orientation (and hence shading); similarly, permanent snowfall in winter may occur as early as late September or as late as early December.

Summer experiences the highest discharges because of ice melt (Nienow et al., 1998). Additionally, summertime has intense diurnal flow variations (Lane and Nienow, 2019; Nienow et al., 1998; Swift et al., 2005). The increase in peak daily discharge and in the intensity of diurnal discharge variation through the melt season, which also drives

high rates of sediment delivery (Perolo et al., 2019), leads to the morphodynamically most active period. Not only may such activity erode the sediments to which biofilms are bound, the high sediment transport rate (Milner and Petts, 1994), and flow shear stresses (Cullis et al., 2014) may scour biofilms from bed sediments. Because disturbances are frequent, biofilms cannot fully develop and they cannot impact stream habitability. The time between two subsequent disturbances is too short to allow biofilms to reach a state of maturity (Thom et al., 2015). Thus, during the summer, biofilm development tends to be restricted to morphodynamically inactive zones (e.g., terraces; see below) and then limited by access to other resources, notably water.

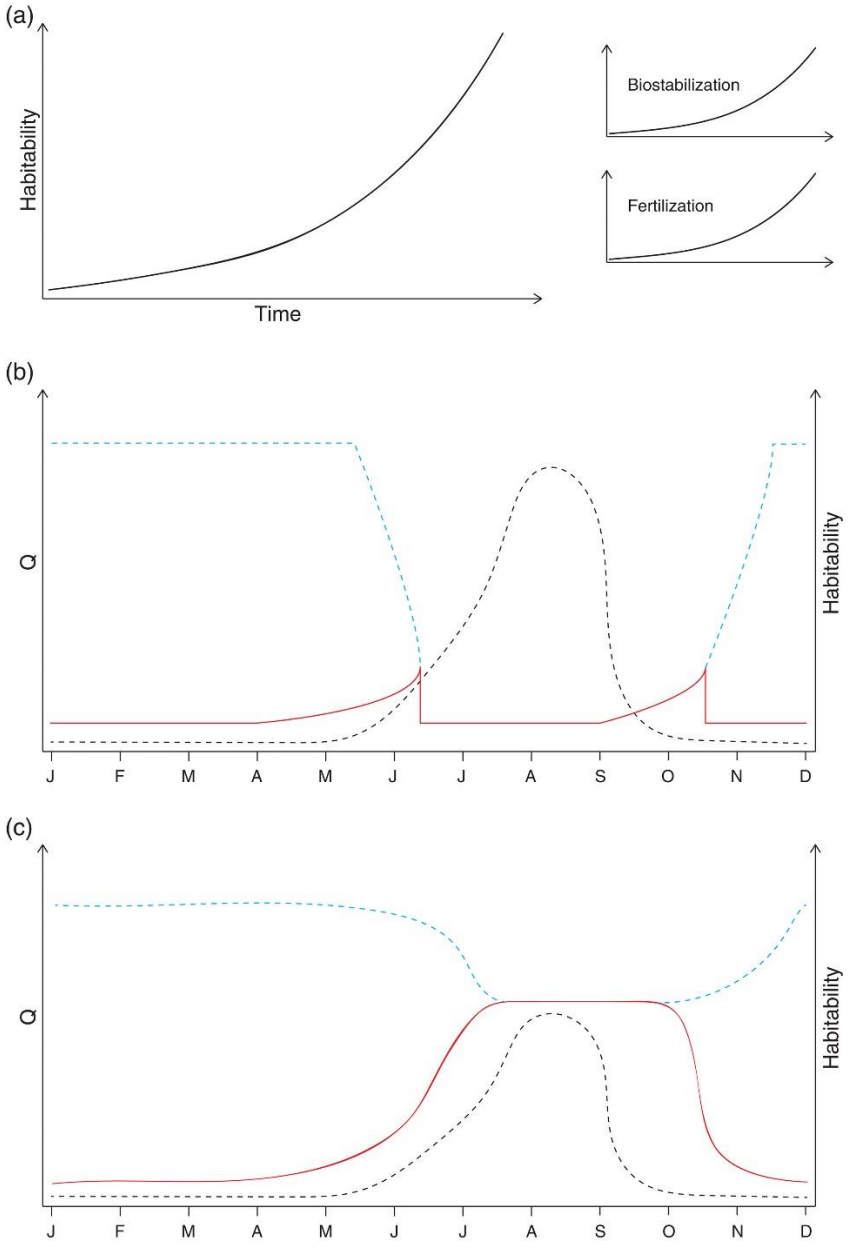

Figure 5: (a) Ideal model where disturbances do not occur during biofilm development leading to an exponential increase of habitability; (b) conceptual model of the variation in habitability in relation with stream discharge (Q) in the active floodplain. The black dashed line is the discharge (Q), the solid red line is the habitability, the blue dashed line represents the case in which habitability is increased during the winter time; (c) Conceptual model of the variation in habitability in relation with stream discharge (Q) in the abandoned channels.

When autumn approaches, from late August onwards, temperatures drop as does the discharge due to reduced melt. Although flow variation is commonly still important (Lane and Nienow, 2019), peak flows are commonly reduced and the rate of morphodynamic change falls. As a result, the size of the morphodynamically active zone contracts (Malard et al., 1999). Less-incised channels receive less discharge compared with well-incised ones where the bulk water flows preferentially, resulting in lower shear stress and greater probability that flow depth is less than the euphotic depth and solar radiation can reach the stream bed. Provided such channels are stable, biofilms may develop and increase habitability because irreversible attachment and EPS secretion is possible (Stoodley et al., 2002). Whether or not this has a positive feedback on stability of such streams is not yet known. The increase in habitability continues until the first significant snow which pauses photosynthesis. The latter may also be reduced by the progressive reduction in solar radiation exacerbated in Alpine valleys due to relief-driven effects on shading. We know little about how photosynthetic activity evolves as a function of time in such streams during the transition from late summer through autumn to early winter.

In winter, and even if there are almost no disturbances, we predict that biofilms cannot increase the habitability of the forefields, mainly because of the absence of light, which precludes phototrophic activity. This impedes the provision of energy for other organisms (Lavandier and Décamps, 1984), and given the nutrient depleted nature of glacier forefields (Bardgett et al., 2007; Bardgett and Walker, 2004), there should be few opportunities for chemotrophs to develop. That said, however, some chemotrophic activity could develop during winter if biofilms have accumulated sufficient nutrients in autumn to sustain their metabolic needs when light is no longer available. Coupled with longer periods of stability and appropriate water supply by groundwater (Malard et al., 1999), this should lead biofilms to reach a sufficient state of maturity, able to increase the habitability to its theoretical maximum. This hypothesis is relevant and is one reason why potential consumers of biofilms, such as macroinvertebrate communities, reach their maximum richness during winter in Alpine streams (Gabbud et al., 2019).

In spring, solar radiation and temperature rise leading to snowmelt. The presence of snow in the basin may attenuate runoff significantly leading to low diurnal flow fluctuations (Lane and Nienow, 2019) with relatively high base flows. Runoff is typically lower in terms of SSCs, until glacier melt starts. Provided discharges are not sufficient enough to cause τ_{oc} to be exceeded, low levels of morphodynamic activity should reduce disturbance which, coupled with high solar radiation intensity once the snowpack disappears, produces ideal conditions for biofilms to increase habitability. We might expect some spatial variability in this process, with the less incised channels being more morphodynamically stable. This “window of opportunity” begins to close as the melt season progresses, diurnal discharge variation becomes more intense, and rates of morphodynamic change increase. Whether or not this increase in habitability has any longer term effect is a moot point as it depends on the extent to which subsequent morphodynamic activity destroys biofilm communities.

2.2.4.2.3 Lateral gradients

As noted above, because of the potential for continuous reworking of the active floodplain, it is the abandoned channels located on terraces where it is most likely that biofilms will lead to a long-term increase in habitability. Such channels are likely to be only very rarely (if ever) inundated by the main stream due to the associated elevation differences. For instance, in the Glacier d'Otemma (Valais, Switzerland), Miller and Lane (2019) found that ~1 m height difference separated the active plain from one terrace on which very developed biofilms were observed (Figure 6) and this surface could not be inundated even at the highest discharges measured. Given their less disturbed nature, abandoned channels on terraces should support biofilm development and so ecosystem engineering (Figures 5c and 6). Moisture cannot be guaranteed, but may be supported by groundwater (Malard et al., 1999), by hillslope-derived flows, or by the positive feedbacks following biofilm development, which reduces vertical infiltration of water (Miller and Lane, 2019).

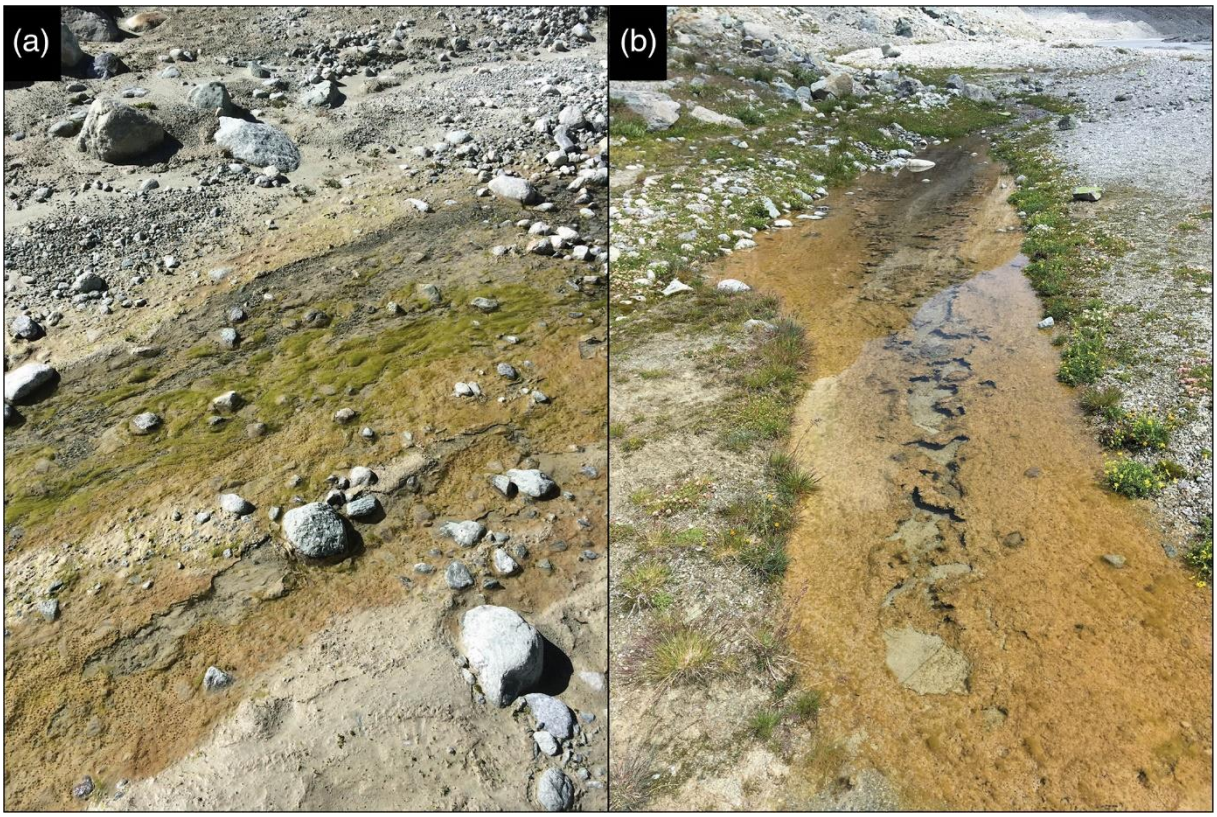

Figure 6: (a) Biofilm formation in a stream on a terrace in the Val d'Otemma, Valais, Switzerland; (b) a biofilm mat that has formed in a stream in the Val d'Otemma supplied with hillslope-sourced groundwater showing successional colonization of the channel margin by vegetation. The stream is on a terrace about 1 m above the morphodynamically active channel. Note to the right there are stable bar surfaces, also on the terrace, but largely void of primary production due to severe moisture limitations related to well-drained glaciogenic sediments.

In summer water sourced from groundwater and hillslopes will not scour biofilm to a significant degree. Disturbances are small in magnitude and the time between two of them may be long. Hence, biofilms can grow, reach a state of maturity and increase the local habitability to greater levels as compared with the active floodplain. The

feedbacks triggered by fertilization and biostabilization can propagate into vegetation succession with evidence that certain plants (i.e., debris vegetation), such as *Saxifraga aizodes*, *Trifolium badium*, *Poa alpina*, and *Festuca* sp., colonize preferentially near channel zones where biofilms create a perched water table (Figure 6b). The only process that can counter this development is lateral erosion of terraces by migration of the morphodynamically active zone.

In autumn, habitability falls progressively as solar radiation reduces until there is a permanent snow cover and with habitability eventually dropping to winter levels. With the onset of permanent snow cover, the environment should become more suitable for chemotrophs that might profit from nutrients that accumulated before snowfall. During winter, predictions made for the active floodplain should apply to channels located on terraces. In spring, the behavior is similar to that explained in the active floodplain, but the habitability reaches greater levels.

In summary, as terraces are sites of low disturbance magnitude and frequency, they may allow for ecosystem engineering by biofilms provided that there is sufficient moisture available, commonly related to non-glacial runoff and groundwater. Here we have identified an important additional engineering effect of biofilms in glacial floodplains, which is the effect of biofilms on drainage (Figure 6b), crucially important for vegetation establishment (Rydgren et al., 2014) given the ease of drainage of glaciogenic sediments. In that sense, it is plausible that after glacier recession (the surfaces of Figure 6 were still covered by ice in the mid 1990s) and terrace formation, biofilms have played a crucial role in maintaining water at the surface and allowing vegetation to develop progressively in the years after terrace formation. This is of particular interest given that pioneering vegetation has not been able to develop in other proximal zones of the Otemma forefield over the last 30 years, and it has been shown (e.g., Burga et al., 2010) that the first plants can appear as few as 10 years after deglaciation. Indeed, it is possible that the effects of biofilms on drainage may be significantly greater than the effects of biofilms on stabilization of sediment, given the size of the glaciogenic sediments that have to be stabilized. These observations emphasize a need to test hypotheses regarding biostabilization and drainage impacts of biofilms in glacial environments, and to include studies of groundwater in such analyses.

2.2.4.2.4 Longitudinal effects

These latitudinal effects need to be put into context. The glacial signals of colder water, discharge variation, and sediment supply will all attenuate with distance downstream from a glacier (e.g., Burgherr et al., 2002; Füreder, 1999; Milner and Petts, 1994; Uehlinger et al., 2003). Thus, there is likely to be a progressive reduction in the constraints on biofilm development that results in enhanced biofilm presence, greater rates of biofilm development, and increasing habitability. This has been demonstrated for macroinvertebrates by showing that moving away from the glacier snout (i.e., downstream) results in the increase of species richness and diversity (Finn et al., 2010).

We might conceptualize this as some kind of cusp model: as these constraints reduce downstream, there may be some sort of threshold at which the positive feedbacks that follow from biofilm development become sufficiently strong that they can support vegetation succession. The ecosystem engineering effects that then follow from this succession then start to create more stable zones, more capable of retaining water, where biofilm-driven habitability can increase further.

2.2.4.2.5 How can biofilm promote the ontogeny of glacial floodplains?

The above model suggests a need to think critically about the idea that biofilms are simple agents of habitability in glacial floodplains. As discussed above, there is no evidence of an exponential growth in habitability with time. At the same time, there is no evidence to believe that in the active floodplain biofilms can develop enough to promote habitability. By contrast, it appears that in abandoned and less disturbed channels, notably on terraces, the habitability can increase to a favorable point, which means that biofilms can grow up and increase their ecosystem engineering effects. Visual observations (Figures 4c and 6) and research (Miller and Lane, 2019) confirm that vegetation develops along channels. One might think that this is a result of the presence of flowing water. However, we argue that this view might be limited by the nature of these creeks that tend to dry out gradually during the summer (e.g., Malard et al., 1999), both by infiltration and exhaustion of solid water sources (i.e., the snow pack); a phenomenon that should reduce the development of vegetation. Thus, biofilms may be important in determining where vegetation can develop (Figure 6; Miller and Lane, 2019). Additionally, biofilms should increase the amount of soil nutrients available for plants to grow (Ciccazzo et al., 2016; Kaštovská et al., 2005; Schulz et al., 2013), which further explains why terraces are not fully covered by vegetation (see the upper-right part of Figure 6b). This effect may be a lateral one related to terraces but also a longitudinal one due to the attenuation described above.

Figure 7 proposes a model for the ontogeny of glacial floodplain ecosystems in relation to biofilms. At the very beginning, the floodplain has a fully developed braided system, where biofilms do not develop because of the high rate of disturbances (Figure 6a). As mentioned above, there could be some biofilm development in less incised channels during autumn and spring, but this phenomenon is ephemeral and systematically reset by stream dynamics in summer.

As the floodplain evolves, some surfaces are eroded and terraces form (e.g., Thompson and Jones, 1986), becoming disconnected from the main active plain (Figure 7b). Because these abandoned channels are no longer heavily perturbed by stream dynamics, biofilms are able to develop. The water needed to sustain biofilm development is provided mainly by hillslope groundwater (Malard et al., 1999), which is also thermally less variable (Ward, 1994), less turbid and enriched in nutrients (Brown et al., 2007). These conditions allow biofilms to trigger their engineering feedbacks, in which biostabilization increases fertilization, and vice versa. These feedbacks drive an increase of the organic matter content of sediments (Miller and Lane, 2019), promoting primary succession (Ciccazzo et al., 2016; Raab et al., 2012)

(Figure 7c). Additionally, biofilms can also promote moisture retention by reducing the permeability of channel beds (Miller and Lane, 2019; Figure 6), which reduces loss of water through drainage. This is of importance due to the low permeability of glaciogenic sediment (Burga et al., 2010). The additional engineering effect can be important for maintaining soil moisture if groundwater availability is reduced. Hence, by maintaining water at the surface of channels, biofilms can self-sustain their growth but also promote vegetation succession. Such a phenomenon has been recorded in Glacier d'Otemma forefield, where vegetation seems to grow preferentially along the impermeabilized channels (Figure 6b, Miller and Lane, 2019).

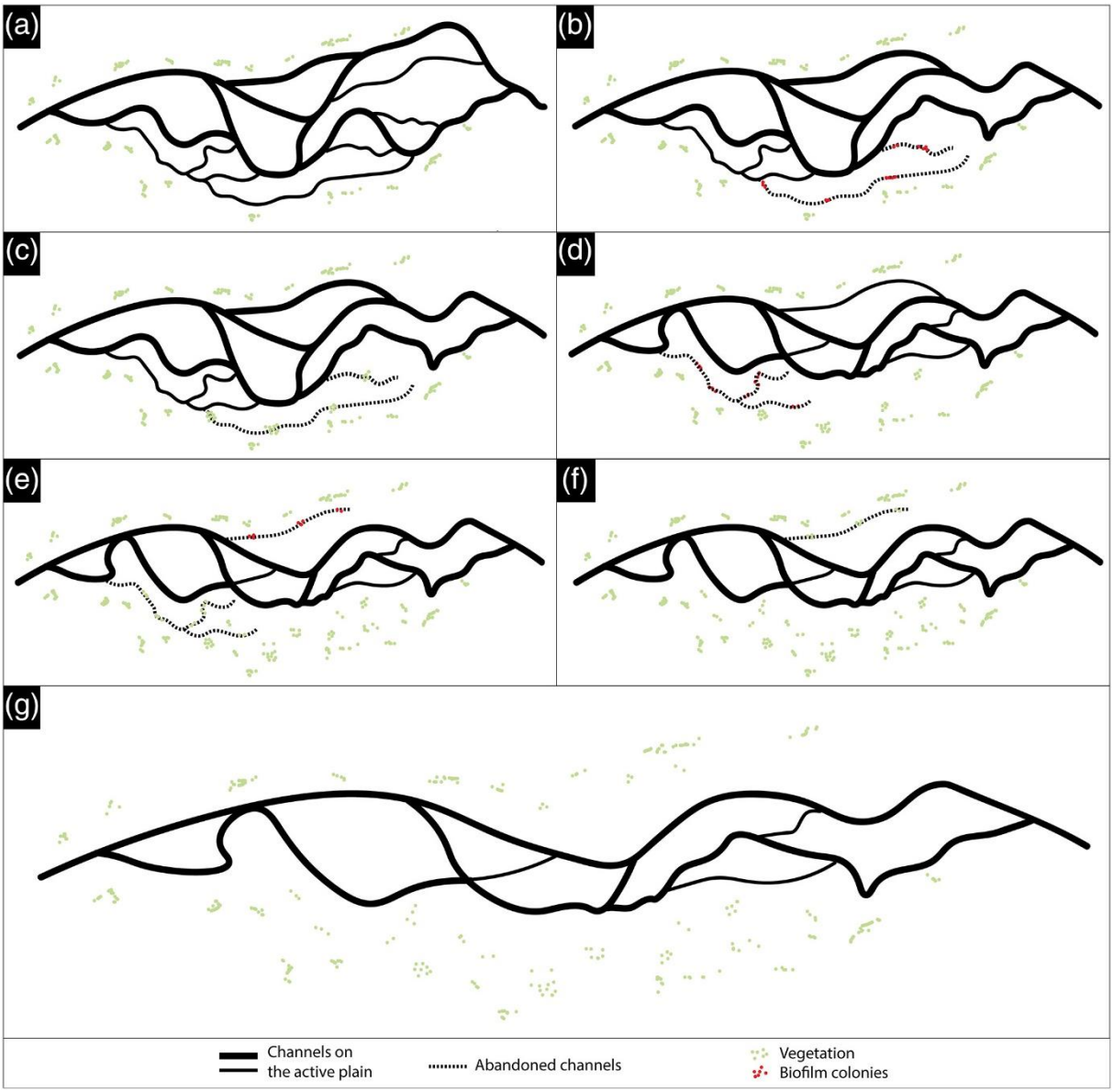

Figure 7: Floodplain ontogeny. (a) Floodplain at time$_{t0}$ biofilm is no longer developed; (b) Floodplain at time t_1 biofilm is developing and coalescing in bigger colonies in abandoned channels, commonly on terraces; (c) floodplain at time t_2. There is vegetation where there were biofilms; (d) floodplain at time t_3. Biofilms develop in the new abandoned channels; (e) floodplain at time t_4. New branches are now disconnected; (f) floodplain at time t_5. There is vegetation where were biofilms; (g) floodplain at time t_6. Vegetation has colonized more floodplain space.

As the floodplain evolves, new surfaces are created by terrace formation, which increases the space for biofilm engineering and vegetation development (Figure 7d–f). Theoretically, these processes lead to a decrease of the accommodation space of the braided system. Incision will then create new terraces, further reducing the accommodation space for active braiding and leading to the formation of a more straight single channel (Germanoski and Schumm, 1993). This process may be aided by glacier recession which increases the distance available for the attenuation of glacier flow, sediment and temperature signals.

This overall ecological process is triggered because microbial biofilms not only have the ability to uptake nutrients but also to store them within the biofilm matrix. Overtime, these available nutrients will also be stored in the surrounding soil environment (Kaštovská et al., 2005; Schmidt et al., 2008; Schulz et al., 2013), leading to an enrichment of soil with phosphorous, carbon and nitrogen. Soil enrichment may take some time to occur (already in the first 4 years after deglaciation; Schmidt et al., 2008), however it is a crucial step for glacier floodplain fertilization and succession. By adding nutrients to the soil, biofilms modify soil nutrient content allowing successional processes (Frey et al., 2013; Kaštovská et al., 2005; Miller and Lane, 2019; Raab et al., 2012; Zumsteg et al., 2012). Again, this process provides positive feedbacks where biofilm growth leads to more nutrient storage in soil, enhanced sediment stabilization and greater moisture retention. With stabilization and soil enrichment, succession and vegetation development will occur (already in the first 10 years after deglaciation; Burga et al., 2010), further reinforcing the stabilization of sediment and biofilm growth. As architects of soils, microbes are responsible for bedrock material weathering, the source of nutrients in vegetation free sites, potential surface biostabilization and important changes in near surface hydrology (Schulz et al., 2013).

As mentioned by Miller and Lane (2019), the roles of biofilms and vegetation should not be seen separately; they must be linked because the former interact with the latter and vice versa. Our model predicts that biofilms have a primordial role in fertilizing the substrate of abandoned channels on fluvial terraces, making other resources (notably water) available and possibly stabilizing sediment. As vegetation develops, the system becomes more stable, as well as more enriched in organic matter. Our model predicts also that the habitability provided by biofilms reduces as winter comes.

2.2.5 Conclusion

This review paper has highlighted how biofilms may engineer the environment through fertilization and biostabilization, and there are no reasons to exclude them from a list of potential ecosystem engineers just because their engineering is not as visible as that of other organisms or because of their relative small size compared with other ecosystem engineers. Furthermore, it has been argued that it is not accurate to evaluate biostabilization without accounting for fertilization, and vice versa, because they both interact together; and that the effects of biofilms on the biostabilization of glaciogenic deposits have not been proved. This is particularly important in scientific

terms because it brings together scientists from different domains, such as geomorphology, microbiology and geochemistry.

We also proposed a model for glacial floodplain ecosystem ontogeny that accounts for the engineering effects of biofilms by showing that biofilms are a means of promoting ecological succession in abandoned channels. Their pioneering role allows vegetation to install because conditions become less harsh. As a result, vegetation becomes ecologically relevant. For this reason, it is important to look at the entire successional process instead of looking at a single biological community. It is probably better to consider ecological succession as an extended organism; it is not the single organism (e.g., biofilms and vegetation) that can explain why barren soils become prone to life and then colonized, but the organic whole (i.e., extended organism) acting at each stage. Hence, we argue that it can be erroneous to evaluate the process of ecological succession by investigating one single stage or one single community, because each stage relies on the previous one and each community has synergies with another, and so on. This is the reason why the role of biofilms in ecological succession in deglaciated terrain should be considered as an extended ecosystem engineer that modifies the environment with the ultimate goal to transform it from a hostile one to a livable one.

That said, this model raises a number of questions that need to be investigated. First, we know very little about the biostabilization effects of biofilms in these kinds of environments. Second, we need to consider the timescales of ecosystem succession in relation to the timescales of biofilm development and their engineering effects. Third, we need to validate the latitudinal and longitudinal impacts of biofilms and how these influence ecosystem succession holistically over decadal timescales. Fourth, we need to consider whether vegetation can develop without biofilm engineering in these environments. Finally, we need to look at biofilms at the annual timescale and not just the spring or summer timescale. We need to understand what happens under snow to habitability, for instance. We need to monitor stream morphodynamics continually in parallel with the continuous monitoring of biofilm development and their ecosystem engineering functions. Through such intensive study, we may develop a much better understanding of the ecosystem engineering of biofilms in glacier floodplain ecosystems.

2.3 Chapter summary

The chapter has summarized constraints on the development of biofilms, including periphyton, that are present in glacial floodplains, and proposes a conceptual model for glacial floodplain ontogenesis. It hypothesizes that although the environment of glacial floodplain is harsh during the melt season, some zones of geomorphic stability (i.e., terraces) exist, and if they are sustained by water, they may support periphyton development. If that is the case, periphyton may modify streambed properties by decreasing the susceptibility of the substrate to being eroded, by reducing the water vertical infiltration, and by fertilizing sediment matrices. Modification of the streambed properties is thought to feed back into periphyton development, but

most importantly into pioneer vegetation. The consequence of this feedback is that the floodplain is likely to become vegetated faster (as compared to the classic chronosequence concept), and consequently more stable and less braided.

This chapter opens up a number of critical research questions (see Chapter 1.2) that need to be addressed in order to validate the hypothesis discussed throughout this section, and summarized in the previous paragraph. First, there is the need to define where and when periphyton develop during the melt-season (Chapter 3). This definition then allows quantification habitat stability, stream morphodynamics and access to water shape the habitat of periphyton at the floodplain scale (Chapter 4). These spatial patterns suggest underlying controls on where periphyton may develop, which requires experimental testing to confirm them (Chapter 5).

3. Chapter 3: Centimeter-scale mapping of phototrophic biofilms in glacial forefields using visible band ratios and UAV imagery

3.1 Chapter overview

This chapter presents high spatial (centimeter-scale) and high temporal (daily) quantification of the presence of phototrophic biofilms during the melt-season in a recently-deglaciated alpine glacial floodplain. By combining drone imagery, Structure-from-Motion Multi-View-Stereo photogrammetry, visible band ratios and logistic regressions, the chapter attempts to answer the first research question of this PhD thesis, that is "where and when do periphyton develop in proglacial forefields during the melt-season?". At the end of this Chapter we explain why we move from considering biofilms to considering periphyton in subsequent Chapters. This Chapter is published as: Roncoroni, M., Mancini, D., Kohler, T.J., Miesen, F., Gianini, M., Battin, T.J., and Lane, S.N. (2022). Centimeter-scale mapping of phototrophic biofilms in glacial forefields using visible band ratios and UAV imagery. *International Journal of Remote Sensing*, *43*(13), 4723-4757.

3.2 Centimeter-scale mapping of phototrophic biofilms in glacial forefields using visible band ratios and UAV imagery

3.2.1 Introduction

Biofilms are surface-attached microbial communities (Costerton et al., 1995) encapsulated in an extracellular polymeric matrix (Flemming and Wingender, 2010). The biofilm mode of life has been shown to be ubiquitous and highly adapted to primary colonization in aquatic environments (Flemming and Wuertz, 2019). In streams and rivers, benthic biofilms are involved in ecosystem processes (Battin et al., 2003, 2016) including nutrient uptake and recycling and carbon fluxes, and serve as the base of the food web. Biofilms may also stabilize fine sediments (Neumeier et al., 2006; Gerbersdorf et al., 2009a; Fang et al. 2014; Gerbersdorf and Wieprecht, 2015), even at large spatial scales (e.g. in estuaries; Brückner et al., 2021), thereby reducing vertical infiltration and supporting plant development in water-stressed environments (Miller and Lane, 2019; Roncoroni et al., 2019). Accordingly, several papers have argued that benthic biofilms should be included in the list of ecosystem engineers (*sensu* Jones et al., 1994) due to their capacity for modifying the physical state of biotic and/or abiotic materials for the benefit of other organisms (Gerbersdorf et al., 2008b; Gerbersdorf et al., 2009b; Roncoroni et al., 2019).

In recent years, research has mapped benthic biofilms to understand their spatial distributions (e.g., Méléder et al., 2003) and/or to determine their biomass (e.g., Combe et al., 2005). This is often possible due to the different spectral signatures of benthic biofilms, including photosynthetically active pigments (e.g., chlorophyll-a), compared to uncolonized substrates (Benyoucef et al., 2014; Salvatore et al., 2020). Such studies usually involve satellite or airborne imagery, which is excellent for large

spatial scales and can provide a wide range of spectral information (e.g., by using multi- and hyper-spectral sensors).

For example, Méléder et al. (2003) mapped the presence of benthic biofilms for Bourgneuf Bay (France) between 1986 and 1998 with the Normalized Difference Vegetation Index (NDVI; Tucker, 1979) calculated from multi-spectral satellite imagery. The authors found that biofilms had a specific NDVI range that allows discrimination from the uncolonized substrata but also from macro-algae. In the same way, Benyoucef et al. (2014) investigated the inter-annual distribution of benthic biofilms in the Loire estuary (France) between 1991 and 2009 and found that the NDVI derived from multi-spectral imagery was efficient for mapping purposes at the large scale. Both studies reported that the spatial resolution of their imagery (typically 20 × 20 m) was too coarse to measure high-resolution spatial variations in biofilm distribution, which may extend down to the centimetre-scale (Méléder et al., 2003; Benyoucef et al., 2014). More recently, Salvatore et al. (2020) and Power et al. (2020) used high-resolution satellite-based NDVI to identify the inter-annual and intra-seasonal distribution of photosynthetically active biofilms in the Fryxell basin, Antarctica. Both studies confirmed the efficiency of the NDVI in mapping biofilms, and Power et al. (2020) went even further by estimating the microbial mat biomass of the Fryxell basin.

Combe et al. (2005) estimated biofilm biomass and mapped biofilm distribution within Bourgneuf Bay using airborne hyper-spectral imagery. These authors found that this produced more reliable results than the multi-spectral imagery used by Méléder et al. (2003), primarily due to the increased spectral resolution of the sensor. Kazemipour et al. (2012) and Launeau et al. (2018) used hyper-spectral data to discriminate the main assemblages of benthic biofilms (e.g., diatom, cyanobacteria, etc.), and their biomass, from the hyper-spectral datasets of Bourgneuf Bay. In both studies, discrimination was possible due to prior knowledge of the spectral response of the key biofilm assemblages (Kazemipour et al., 2012; Launeau et al., 2018).

The use of airborne sensors in the previous studies, rather than satellites, produced high spatial resolution datasets ranging from 5 × 5 m in Combe et al. (2005) to 0.7x0.7 m in Launeau et al. (2018). However, such spatial resolutions were at the expense of temporal ones, and in Combe et al. (2005), Kazemipour et al. (2012) and Launeau et al. (2018), the study zones were imaged only once or twice. In the presence of sharp environmental gradients, a higher spatial resolution may be a critical requirement. Indeed, higher resolution datasets, although sometimes more limited in spatial extent, may reduce the occurrence of spectral mixing (see Bioucas-Dias et al., 2013) and improve mapping accuracy and precision.

In stream studies, there is the need for sub-metre resolution datasets to appreciate stream processes (e.g., Carbonneau et al., 2004; Marcus and Fonstad, 2008; Woodget et al., 2015; Woodget and Austrums, 2017). Here, habitat gradients can occur over just a few centimetres to metres such as in actively braiding rivers. Here, the environments most conducive to biofilm development are commonly more stable secondary channels that may be only a few metres or less in width. Therein,

centimetre-resolution data may be desirable and/or necessary because abiotic or biotic features can occur in or vary within very few centimetres of the channel.

Although spatial resolution is typically sensor-quality dependent, it is also controlled by the difference in elevation between the sensor and the ground (Westoby et al., 2012). Hence, high spatial resolution can be achieved either by using very expensive sensors like those on board satellites/aircrafts or by decreasing the distance between the target areas and the sensor themselves. To date, sensor technology has advanced to a point where miniaturized multi- or even hyper-spectral surveys may be carried out by an uncrewed aerial vehicle (UAV), yielding wide-ranging spectral information at unprecedented spatial and temporal resolutions. For instance, Harrison et al. (2020) used an UAV to collect hyper-spectral information for a 275-m-long reach of the American River in California (USA) and, amongst other techniques, used a biofilm-related chlorophyll-a map at 0.15 m resolution as a proxy to detect fall-run Chinook salmon (*Oncorhynchus tshawytscha*) spawning grounds. To our knowledge, benthic biofilm distribution and/or biomass has never been estimated from UAV-based multi-spectral imagery, and studies involving those sensors have focused upon algal bloom studies (see Kislik et al., 2018), trophic state monitoring (Su and Chou, 2015), and aquatic vegetation mapping (Chabot et al., 2018; Song and Park, 2020; Taddia et al., 2020).

In this study, we assess the extent to which low-cost UAVs with integrated RGB cameras can be a cost-effective alternative to multi- or hyper-spectral devices in mapping benthic biofilm distributions in extreme environments such as glacial forefields where very high (cm) spatial and high (daily to weekly) temporal resolution is required. Although RGB sensors have a very low spectral resolution (the three visible bands, namely, red, green and blue), it should be possible to map benthic biofilms in shallow and clear channels based on these bands as compared to the un-colonized substrata (Benyoucef et al., 2014). This is partially confirmed by the studies of Xu et al. (2018) who were able to map green algal tides with visible band ratios, Flynn and Chapra (2014) who mapped submerged vegetation with statistical analysis of RGB images, and by Kislik et al. (2020) that mapped filamentous algae by applying a supervised classification to their RGB images. The use of low-cost UAVs allows the costs of repeated mapping to be lowered and the financial consequences of sensor loss to be reduced.

We test the use of UAV-based and high-frequency RGB image acquisition with Structure-from-Motion Multiview-Stereo (SfM-MVS) photogrammetry (Westoby et al., 2012; Fonstad et al., 2013; Tamminga et al., 2015; Woodget et al., 2015; James et al., 2017, 2020; Dietrich, 2017; Roncoroni and Lane, 2019; Lane et al., 2020) to generate a high-resolution orthomosaic time series over a 5-month period of an Alpine glacier forefield characterized by a well-developed and heterogeneous stream ecosystem. We assess the performances of orthomosaic-derived visible band ratios and logistic models in mapping benthic biofilm distributions at high spatial and temporal resolutions. Aware that visible bands and ratios between them have limited capabilities in segmenting features based on their spectral response, we demonstrate that when

basic mapping, but at high frequency, is necessary there is no need for expensive sensors.

3.2.2 Methods

3.2.2.1 Study site

The forefield of the Glacier d'Otemma is situated in Val de Bagnes (Valais, Switzerland) (Figure 8). The forefield has formed since the early 2000s in response to retreat of the Glacier d'Otemma, which has retreated at an average of 50 m per year (Mancini and Lane, 2020). The resultant fluvial braidplain is approximately 900 m long and 150 m wide and characterized by a well-developed floodplain drained by a complex and heterogeneous kryal, krenal and rhithral stream system. The braidplain is active and continuously reworked during the melt-season (Mancini and Lane, 2020), typically constraining pioneer vegetation and benthic biofilms to the right-side terraces until rates of morphodynamic activity decline in the autumn.

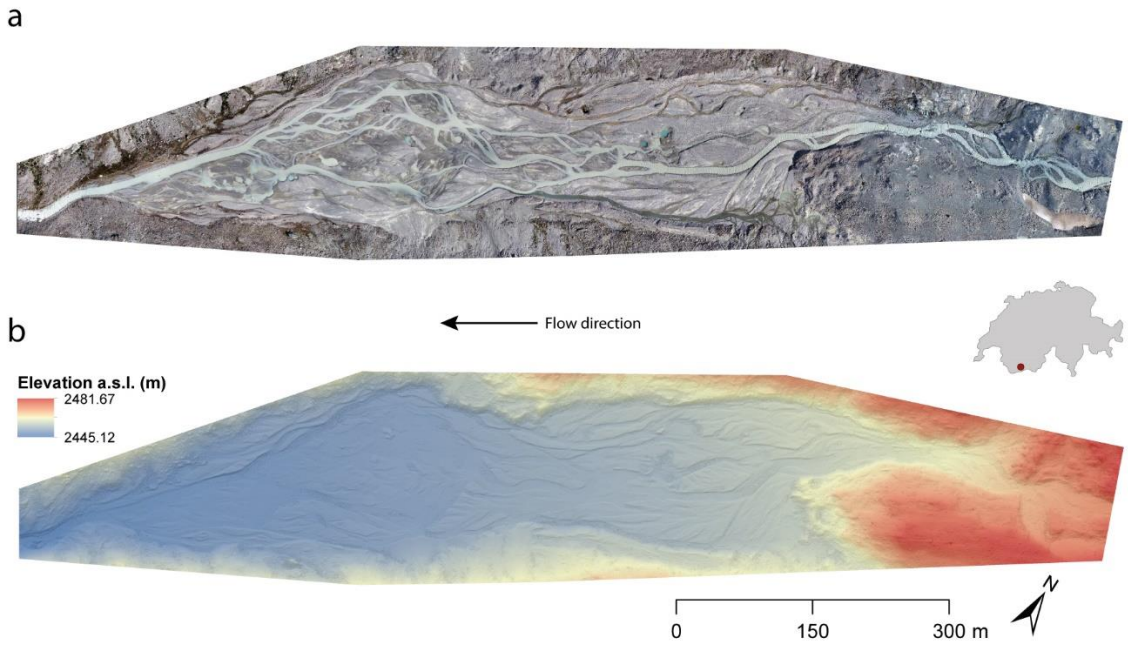

Figure 8: Forefield of the Glacier d'Otemma (Valais, Switzerland); Orthomosaic (a) and digital elevation model (b) of the study zone.

3.2.2.2 Image and ground control point acquisition

RGB imagery was collected from late June to early September 2020 on 52 non-consecutive days with an additional acquisition date in November 2020. To collect the images, we deployed a DJI Phantom 4 Pro quadcopter, which is a well-established UAV platform in SfM-MVS photogrammetric studies (James et al., 2020). Relatively low-cost and low-weight, the quadcopter allows for pre-programmed flight missions due to its incorporated GPS. The integrated RGB camera has a 20 megapixel sensor, mechanical shutter, nominal 8.8 mm focal length, and stores images in both JPEG and RAW formats.

The forefield was imaged once or twice per day. Diurnal discharge variation related to the melt pattern of the glacier causes extensive inundation of the braidplain during the afternoon and evening. Therefore, we focused on the early morning flights (acquired from 06h30 onwards) for biofilm mapping. We used the freeware Pix4Dcapture (v. 4.8.0) to manage flight missions and geometries, and automatically collect images in JPEG format. Flight geometries were designed to produce high-precision datasets free of systematic error DEMs (following James et al. 2020) for further analyses of the forefield. Each set of flights was composed of: i) four grids with the camera looking at nadir (90°), image overlap set at 80% and a flight elevation of 80 m; and ii) 7 circular missions with the camera taking off-nadir and centre-looking pictures every 6° of the circles and flight elevation of 60 m. To ensure continuous mapping, singular grids intersected with each other. Each flight session took roughly 3.5 hours to complete and was composed of about 2'000 JPEG images. Geometries, flight path dimensions, and camera positions are shown in Figure 9a.

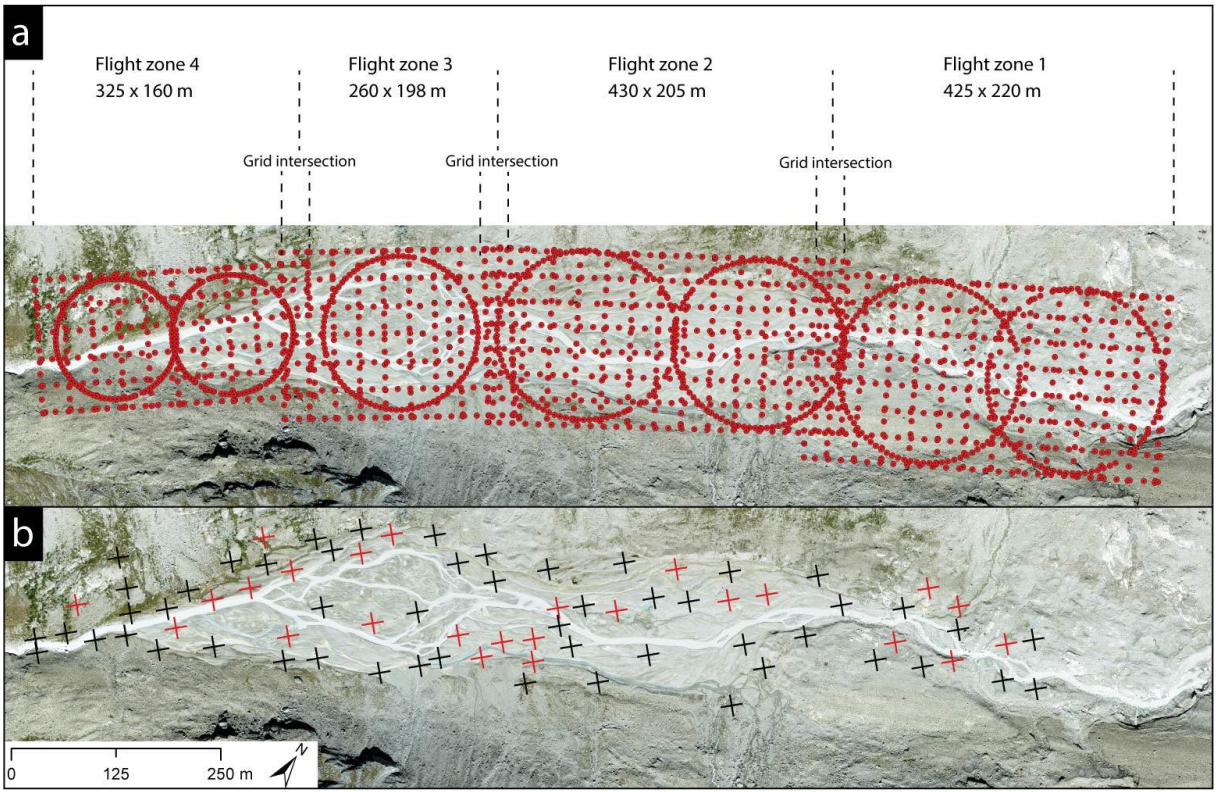

Figure 9: a) Flight geometries, camera positions and flight path dimensions. Image acquisition started at Flight zone 1, and take-off points were kept the same or similar throughout the season. b) Ground control point locations. Black GCPs were used in processing, while red GCPs were discarded after the Monte Carlo analysis. Orthomosaic ©swisstopo.

In SfM-MVS photogrammetry, at least three well-scattered Ground Control Points (GCPs) are needed to scale, rotate and orientate DEMs and orthomosaics to a real-world coordinate system (Fonstad et al., 2013; Woodget et al., 2015). However, research has shown that GCPs are needed to improve the solution of the collinearity equations and to reduce the occurrence of systematic deformations in DEMs. The number of points needed is dependent on the spatial extent of the study site (James and Robson, 2014; James et al., 2017, 2020). We fixed 77 GCPs across the zone of

interest (Figure 9b). We measured the GCPs at the beginning and end of the season with a differential GPS (dGPS) Trimble R10, and collected their absolute coordinates in the Swiss coordinate system CH1903+ to a precision of better than ±0.01 m in the horizontal and ±0.02 m in the vertical. The dGPS base station was located at the end of the floodplain and on the top of a bedrock hill to maximize the radio communication between the base and the rover. The base was corrected into the CH1903+ coordinate system using the fixed monitoring Swiss Federal Office for Topography provided via SwiPOS©.

3.2.2.3 Image processing and orthomosaic generation

The SfM-MVS photogrammetric processing was undertaken with Agisoft Metashape (v. 1.5.5) run on a dedicated workstation equipped with an AMD Ryzen 12-core processor (3.80 Ghz), 64 Gb RAM, and a GeForce RTX 2080 (8 Gb) graphic card allowing for GPU acceleration. To ensure strong (i.e., free of systematic deformations), reliable and replicable SfM-MVS photogrammetric processing within the totality of the datasets we followed the framework of James et al. (2017; 2020). Initially, we aligned the images of the first dataset (26 June 2020) to generate a sparse point cloud. We then explored how the different camera internal parameters (e.g., focal length, four radial and tangential distortion coefficients, principal point offsets, etc.) in the bundle adjustment influenced the 3D re-shaping of the sparse point cloud. To do so, we first used a Monte Carlo framework (James et al., 2017) in which different sets of camera internal parameters, so-called camera models (Table 3), were evaluated within the bundle adjustments by using a variable selection (but always 50%) of GCPs and 11 prescribed GCP accuracies (Table 3). Specifically, for each camera model investigated, we ran 1100 bundle adjustments, corresponding to 100 adjustments with 100 GCP combinations for each prescribed GCP accuracy.

Table 3: Summary of the parameters used within the Monte Carlo framework. We evaluated eight camera models found in classic SfM-MVS papers (James et al., 2017, 2020), where: f is the focal length, Kn is a radial distortion parameter, Pn is a decentring distortion parameter, Cx and Cy are principal point offset, Bn is an affinity and orthogonality parameter. The prescribed GCP accuracies (m) were chosen to cover a wide range of accuracies, from centimetres to metres, and refer to accuracies we may expect for each GCP.

Camera internal parameters (i.e., camera models)	**Reference**
Model 1: f, K1	(James et al., 2020)
Model 2: f, K1, P2	(James et al., 2020)
Model 3: f, Cx, Cy, B1, B2, K1, K2, K3, P1, P2	(James et al., 2020)
Model 4. f, Cx, Cy, B1, B2, K1, K2, K3, P1	(James et al., 2020)
Model 5: f, Cx, Cy, K1, K2, K3	(James et al., 2017)
Model 6: f, Cx, Cy, K1, K2, K3, P1, P2	(James et al., 2017)
Model 7: f, Cx, Cy, B1, B2, K1, K2, K3, K4, P1, P2	(James et al., 2017)
Model 8: f	(James et al., 2017)
Prescribed GCP accuracies (m) tested within the bundle adjustments	
0.001, 0.002, 0.005, 0.01, 0.02, 0.05, 0.10, 0.20, 0.50, 1.00, 2.00	
Percentage of GCPs used within the bundle adjustments	
10, 20, 30, 40, 50, 60, 70, 80, 90	

Based on the results of the Monte Carlo simulations, model 3, which includes focal length, principal point offset (Cx, Cy), affinity and orthogonality parameters (B1, B2), radial (K1, K2, K3) and decentring (P1, P2) distortions, delivered point clouds with the lowest probability of producing systematic errors even with the highest prescribed GCP accuracies. Second, for each camera model (Table 3) and by using the whole GCP population, we reconstructed (namely tie) point covariance maps (James et al., 2020) to detect visually systematic deformations in the point clouds. These maps showed the agreement between the tie point positions, and we found that model 3 delivered point clouds without any spatial structure related to the presence of systematic deformation.

We then assessed the quality of the GCPs by using model 3 in 900 bundle adjustments, but varying the percentage of GCPs (Table 3) used in each bundle adjustment (James et al., 2017). Based on the Monte Carlo results, the RMSE of the XYZ components stabilized at 0.02 m corresponding to the use of 60% of the GCP (n = 46) into the bundle adjustment. However, the best 46 GCPs were not spatially well distributed, hence why we retained 52 GCPs (68%) and discarded the 25 GCPs showing the highest vertical/horizontal errors (Figure 9b).

The chosen camera model and GCPs were applied in the processing of the remaining datasets (n = 53). In addition to this, each sparse point cloud was inspected before the bundle adjustment: i) to remove tie points seen by two images only, ii) to remove poorly positioned tie points (e.g., beneath the reconstructed surface), and iii) to remove images having fewer than 1000 projections in the tie points and error greater than 1 pixel (following James et al., 2020). With our workstation configuration and step-wise procedure, it took roughly 8 h per dataset to produce results with minimal 3D and optical distortions, fully georeferenced DEMs at 20 cm, and orthomosaics at 5 cm spatial resolutions.

3.2.2.4 Orthomosaic normalization

Multi-temporal images are often difficult to compare due to non-scene dependent changes, such as in sensor or illumination conditions (Schott et al., 1988; Du et al., 2002; Song and Woodcock, 2003; Liu et al., 2007; Bao et al., 2012). In our case, the sensor was the same throughout the field season (i.e., DJI Phantom 4 Pro's camera), but illumination changed during image acquisition because of differences in cloud coverage or sun position (both within the same dataset and between datasets).

The easiest way to deal with this problem is to have a dataset-specific image calibration based on individual scenes. Ideally, it would be possible to use one or a subset of scenes to produce a general classification rule that could be applied to all scenes. This requires that each orthomosaic must have similar signatures, in our case requiring that pixels composing non-biotic features (e.g., rocks, sand) should reflect the same quantity (i.e., digital numbers) of red, green, and blue bands throughout the measurement period. This is particularly important when a common logistic model (i.e., reference) is applied to a visible band ratio. To achieve this, we tested scene-to-scene

normalization (Schroeder et al., 2006) using a relative radiometric normalization, the Pseudo-Invariant-Feature (PIF) method. This method aims to correct each image to a reference by applying a linear model on pixels that should not have experienced any reflectivity change between the two acquisitions (Schott, et al., 1988; Du et al., 2002; Bao et al., 2012). Typically, PIFs are artificial objects (e.g., roofs, roads, etc.) that do not show seasonal or biological activity with almost constant reflectivity through time (Schott et al., 1988).

In our study area, there was a lack of artificial objects, and the only ones suitable for a traditional PIF normalization were the GCPs scattered on the floodplain, which were black and yellow and large enough to allow for single pixel picking. We visually inspected the set of orthomosaics, and we selected 45 single pixels within the eight clearest GCPs. Furthermore, we sampled an additional 37 single pixels of pure and constant-through-time dry sand and/or sediment to complete the PIF population ($n = 82$). After several attempts, we found that 82 PIFs provided a good trade-off between normalization quality and processing time. We also decided to use single pixels instead of averaging groups because of the important sub-decimetre variation in pixel colours. To cope with changes in light conditions and sun position, through the summer, we divided the dataset into three sub-datasets: i) Group 1, consisting of 19 datasets spanning from 26 June to 19 July 2020, using 14 July as a reference; ii) Group 2, consisting of 22 datasets spanning from 21 July to 21 August 2020, using 26 July as a reference; and iii) Group 3, consisting of 11 datasets spanning from 23 August to 13 September 2020, using 14 July as a reference. Group 3 shared the same reference as Group 1, although it is temporally distant because we noted that 14 July had good normalization performances on the images of the third group. The orthomosaic of 5 November 2020 was treated separately and called Group 4, and due to snow coverage, no correction was applied.

Within each group and on a band-by-band basis, we regressed linearly the digital numbers of the reference PIFs against the digital numbers of the PIFs of each orthomosaic to be normalized. We then applied the three linear models to the totality of the pixels composing the single-band (red, green, and blue) orthomosaics to ultimately obtain radiometric normalized bands. We assessed the quality of the normalizations by evaluating the root mean square error (RMSE) of pixel digital numbers before the normalization and after as compared with the relevant reference image, as well as by visually inspecting how the histograms changed after applying the linear models.

The orthomosaic normalization was performed through a Matlab (R2018a) routine. Even though PIF normalization should allow transferability of calibration models for biofilm mapping, we decided to also compare results with i) the non-normalized but group sorted orthomosaics and ii) a scene-by-scene calibration model.

3.2.2.5 Visible band ratios, logistic models, and probability maps

The non-normalized individual scenes and the normalized bands were used to compute visible band ratios, which have the advantage of summarizing the information of the three visible bands into one. Such ratios have been widely used in vegetation detection or crop studies since the 1970s (e.g., Tucker, 1979; Woebbecke et al., 1995; Kawashima and Nakatani, 1998; Meyer et al., 1998; Adamsen et al., 1999; Louhaichi et al., 2001; Gitelson et al., 2002; Meyer and Neto, 2008; Saberioon et al., 2014), but also in aquatic studies (Xu et al., 2018). Here, we computed eight band ratios (Table 4) and tested their performances in mapping biofilms.

Table 4: Band ratios tested for benthic biofilm. R, G, and B are non-normalized digital numbers (i.e. R, G, and B ranging from 0 to 255); r, g, b are normalized digital numbers (i.e. R, G, and B ranging from 0 to 1).

Name	**Acronym**	**Formula**	**Source**
Chromatic Coordinates of Red	RCC	R/(R+G+B)	Woebbecke *et al*., 1995
Normalized Green-Red Difference Index	NGRD	(g-r)((g+r)	Tucker, 1979
Excess Red Vegetation Index	ExR	1.4*r-g	Mao *et al*., 2003
Excess Green Vegetation Index	ExG	2*g-r-b	Woebbecke *et al*., 1995
Green Leaf Index	GLI	((G-R)+(G-B))/(G+R+G+B)	Louhauchi *et al*., 2001
Visible Atmospherically Resistant Index	VARI	(G-R)/(G+R-B)	Gitelson *et al*., 2002
Kawashima and Nakatani Index	KANA	(R-B)/(R+B)	Kawashima and Nakatani, 1998
Red Green Ratio Index	RGRI	R/G	Saberioon *et al*., 2014

To classify the orthomosaics into biofilm distributions across the whole floodplain, we first developed training/calibration and validation datasets for each orthomosaic. These datasets were based upon the selection of 150 sites at the single pixel level that were biofilms and covering the range principal colour assemblages present on the floodplain (i.e., red-brown and green). The site selection was straightforward because “glacial” biofilms have a distinctive colour compared to the dry or wet un-colonized substrata (e.g., grey), and this was clearly distinguishable on the orthomosaics at the spatial resolutions we were using. An additional 150 sites were selected across the floodplain to account for the un-colonized substrata. This was the calibration dataset. We then selected another set of sites (n = 300, 50% biofilm), using the same criteria but with no overlap with the calibration dataset. The biofilm mapping was then based upon training logistical models using the calibration dataset.

The outcome of the logistic model was a probability of biofilm being present. For validation, we converted the probability (0 to 1) into binary values (0 or 1) by assigning 0 (not biofilm) to sites with probability <0.5 and 1 (biofilm) to sites with probability >0.5. These predictions were combined with the validation to provide confusion matrices (i.e., true positive/negative vs. false positive/negative) and hence to assess model performance by comparing prediction accuracies, precisions, recalls, F-scores, and Matthews Correlation Coefficients (MCC) (Chicco and Jurman, 2020).

The logistic models were applied in two ways. First, to understand the optimal choice of logistic regression model type (Table 4) we applied each type to the reference images (14 July for Groups 1/3 and 20 July for Group 2) and the November image (Group 4). Second, having identified an ideal model type, we trained a scene-by-scene model for each date to be our reference probability map dataset. This made use of calibration data and validation data particular to each scene. This approach is labor-intensive, but it avoids the need to make assumptions about the temporal stability of the logistical models derived, and no normalization is required. We call these the reference datasets. Finally, we applied the calibrated logistic models selected for the two reference images to both the raw and the normalized orthomosaics according to the group each orthomosaic was in. Moving to calibration based upon a small number of references significantly reduces workloads, but makes the analysis more dependent on the reliability of normalization.

We produced three first probability map datasets: i) single – with a different calibration model for each scene, the single datasets; ii) raw – using the Group 1/3 and Group 2 reference calibration models and applied to non-normalized imagery; and iii) normalized – as per (ii) but using normalized imagery. All logistic regressions, validations, statistics and probability maps were performed in Matlab (R2018a).

3.2.2.6 Micro-topography shadow modelling

The effect of the floodplain micro-topography on shading and hence on the probability map quality was also investigated. We avoided exploring the shadowing effect of the surrounding peaks because, when present, it only affected the very upstream part of the study zone. We also did not develop a physically based treatment of the shadowing effect caused by clouds because of a lack of cloud cover data to include in a model. The micro-topography shadowing effect was, to varying degrees, always present and it was caused either by large boulders or by steep river banks. Normalization could not correct for this.

We modelled the micro-topography shadow by applying to our DEMs a potential solar radiation model (Kumar et al., 1997). The model accounts for the acquisition time and date (in our case the start and end of each UAV survey), the local topography using our DEMs, and latitude of the study zone, and it models the potential solar radiation in W/m^2 received during the selected period. Shadows were easily identified due to their low solar radiation, and subsequently masked binarily to exclude those pixels from being mapped in our probability maps. A new set of probabilistic maps was generated from the previous three datasets, and they are called single-shadow, raw-shadow, and normalized-shadow.

3.2.2.7 Occupation maps and noise assessment

Each scene produced a map showing the probability of biofilm occurrence. To understand how biofilms develop through time, we calculated the cumulative presence (in days) of biofilm in each pixel of the study zone, which we call an occupation map.

In doing so, we excluded the probability map of November because of the significant time since the last summer acquisition date (September 13). To produce the occupation maps, we firstly converted the pixel probability in binary classification by assigning 0 to pixels with probability <0.5 and 1 to pixels with probability >0.5. We then multiplied each binary map by a scalar representing the time-lag between two given acquisition dates (i.e., time-lag: $[(T - T_{n-1})/2 + (T_{n+1} - T)/2]$), and finally summed up the results to obtain the occupation (0–80 days) that biofilm was present in each pixel. Occupation calculations were performed in Matlab (R2018a), but maps were then exported in ascii-format and converted into a suitable format (.tiff) for ArcMap (v. 10.5.1). In the GIS environment, we masked the study zone to exclude the vegetated edges, the sparse pioneer species across the floodplain, and the GCPs.

These occupation maps are of significance for understanding biofilms because the duration of occupation likely influences the duration and intensity of ecosystem engineering that the biofilm can perform. Thus, to understand how sensitive occupation maps are to normalization and shadow correction, we take the single scene accumulation map without shadow correction as a reference. We then compare the generated maps: i) using the single scenes, shadow corrected; ii) the reference models applied to the raw scenes, shadow uncorrected and corrected; and iii) the reference models applied to the normalized scenes, shadow uncorrected and corrected to this reference. We call these comparisons Occupations of Difference (OoD).

We also attempted to calculate noise in the occupation maps. First, in this kind of environment, biofilms may form rapidly, over the order of days, but also be destroyed rapidly such as by a lateral shift in the river channel. This would produce a run of time periods where biofilm are present followed by, if destroyed, a run of time periods where biofilms are absent until conditions again allow biofilm development. Noise would then interrupt these runs until, in the ultimate extreme, the biofilm present-absent time series is completely random. To assess this, we undertook a runs test to lower the probability for each pixel, that an occupation map is based upon non-randomly distributed presence-absence through time. The lower the p-value the less a pixel is affected by noise and the more likely that the occupation is reflecting true biofilm growth and destruction. We call this the occupancy noise map and we calculated it for single, raw, and normalized datasets with and without shadow.

We then created a new set of occupation maps in which we used the occupancy noise maps to exclude occupation pixels that had less than 95% ($p < 0.05$) probability of reflecting true biofilm dynamics in a given dataset.

3.2.3 Results

3.2.3.1 Identification of logistic regression model type

3.2.3.1.1 Groups 1 and 3

The band ratios derived from the orthomosaic for 14 July 2020 were used to train 8 logistic models. The NGRD-, ExG-, GLI-, VARI-, and RGRI-derived models struggled to find a substantial separation between pixels with or without biofilms (see Supplementary Material SM4). The ExR-derived model behaved slightly better compared to the previous ones, whilst the RCC-, and KANA-derived models were able to find a more consistent spectral separation (see Supplementary Material SM4).

Table 5 shows the validation results based upon sites not used to train these previous models. Not surprisingly, models with a poor separation between biotic and abiotic pixel values during training underperformed (e.g., ExG and GLI, Table 5). To differing degrees, RCC, NGRD, ExR, VARI, and RGRI performed well when validated, but KANA produced the best validation results and was therefore selected as the model to map biofilm distributions for groups 1 and 3.

Table 5: Logistic regression coefficients and performances of the selected index-derived binary classifications for groups 1 and 3.

	β0	**β1**	**Accuracy**	**Precision**	**Recall**	**F1**	**MCC**
RCC	-129.13	361.94	0.98	0.99	0.97	0.98	0.97
NGRD	-4.36	-168.65	0.89	0.93	0.84	0.88	0.85
ExR	-35.83	221.51	0.94	0.96	0.91	0.94	0.92
ExG	-0.30	35.64	0.69	0.70	0.68	0.69	0.47
GLI	-0.30	47.87	0.69	0.70	0.68	0.69	0.47
VARI	-4.05	-88.96	0.86	0.91	0.80	0.85	0.80
KANA	-8.12	107.63	0.98	0.99	0.97	0.98	0.98
RGRI	-84.34	80.06	0.89	0.93	0.84	0.88	0.85

3.2.3.1.2 Group 2

The eight models trained for 26 July did not significantly differ from the models of groups 1 and 3 (see Supplementary Material SM5). Findings between groups are consistent: NGRD-, ExG-, GLI-, VARI-, and RGRI-derived models were again not able to substantially separate biotic and abiotic pixels. The ExR-derived model was slightly better, but the RCC- and KANA-derived models were the best at finding the natural boundaries between abiotic and biotic pixels (see Supplementary Material SM5).

As expected, the validation (Table 6) results for 26 July followed those for 14 July. The ExG- and GLI-derived models underperformed compared to the others, while the NGRD, VARI, and RGRI models were overall acceptable. The ExR-derived model was excellent, but still slightly worse than the RCC- and KANA-derived models. The

RCC- and KANA-derived models showed equal performances, but we selected the KANA model to be consistent with groups 1 and 3.

Table 6: Logistic regression coefficients and performances of the selected index-derived binary classifications for group 2.

	β0	β1	Accuracy	Precision	Recall	F1	MCC
RCC	-528.58	1447.96	0.99	0.97	1.00	0.99	0.97
NGRD	-3.38	-99.10	0.95	0.91	0.99	0.95	0.91
ExR	-28.27	163.54	0.98	0.97	1.00	0.98	0.97
ExG	-2.04	87.34	0.86	0.94	0.77	0.85	0.81
GLI	-2.06	118.35	0.86	0.94	0.77	0.85	0.81
VARI	-2.88	-53.27	0.91	0.86	0.99	0.92	0.84
KANA	-27.84	280.36	0.99	0.97	1.00	0.99	0.97
RGRI	-49.29	46.01	0.96	0.93	0.99	0.96	0.92

3.2.3.1.3 Group 4

Overall, the models for the November mosaic behaved in a similar way to the July datasets, with the NGRD-, ExG-, GLI-, VARI-, and RGRI-derived models still being unable to find a substantial boundary between abiotic and biotic pixels. ExR-, RCC-, and KANA-derived models found more obvious separations (see SM6).

Validation results (Table 7) did not differ significantly from July results, with ExG- and GLI-derived models having the lowest performances within the band ratios. NGRD-, VARI-, and RGRI-derived models performed slightly better in comparison with the July datasets, while the KANA-derived model performed slightly worse. In this case, the RCC models had a better performance compared to the KANA model, but the difference was small (1% in recall); therefore, we kept the KANA-derived model as with the previous groups such that our methodology is consistent.

Table 7: Performances of the selected index-derived binary classifications for group 4.

	β0	β1	Accuracy	Precision	Recall	F1	MCC
RCC	-61.54	171.01	0.98	0.99	0.98	0.98	0.98
NGRD	-1.85	-96.32	0.98	0.99	0.97	0.98	0.97
ExR	-18.76	120.81	0.98	0.99	0.97	0.98	0.97
ExG	-2.25	39.01	0.74	0.73	0.77	0.75	0.55
GLI	-2.28	53.68	0.74	0.73	0.77	0.75	0.55
VARI	-1.79	-58.11	0.98	0.99	0.97	0.98	0.97
KANA	-6.48	60.42	0.98	0.99	0.97	0.98	0.98
RGRI	-46.01	44.21	0.98	0.99	0.97	0.98	0.97

Based on these results, the KANA-derived model was selected as the type of logistical regression for the subsequent analyses.

3.2.3.2 Orthomosaic normalization

Figure 10 shows the digital number RMSE by band for each non-reference orthomosaic, both before and after normalization and in comparison with the relevant reference one (14 July for Group 1 and Group 3 datasets; 26 July for Group 2 datasets). The normalization behaved similarly between the bands.

Group 1 (26 June to 19 July or Julian day 178 to 201) showed a generalized important RMSE reduction, particularly on the red ($\bar{x}$=-28.8%; σ=12.9) and blue ($\bar{x}$=-32.5%; σ=±15.6) bands as compared to the green one ($\bar{x}$=-24%; σ=±10.2). Group 2 (21 July to 21 August or Julian day 203 to 234) had a tendency towards improvement (red band: $\bar{x}$=-13.2%; σ=±10.6; green band: $\bar{x}$=-13.6%; σ=±9.7; blue band: $\bar{x}$=-19.9%; σ=±14.5), but RMSE reduction was variable within the orthomosaics. Dates closer to the group 2 to 3 transition profited from a RMSE reduction through the normalization, but RMSEs still remained high (especially within the blue band). Dates closer to the group 1 to 2 transition had lower RMSEs before the normalization, and only a limited improvement was observed afterwards. Group 3 (23 August to 13 September or Julian day 236 to 256) had RMSEs <20 DNs before normalization (except 3 August), and the normalization was not particularly effective and the RMSE reduction was generally small. We observed a RMSE reduction of 14.3% (σ=±12.5) for the red band, of 9.3% (σ=±8.3) for the green band and of 9.9% (σ=±8.3) for the blue band.

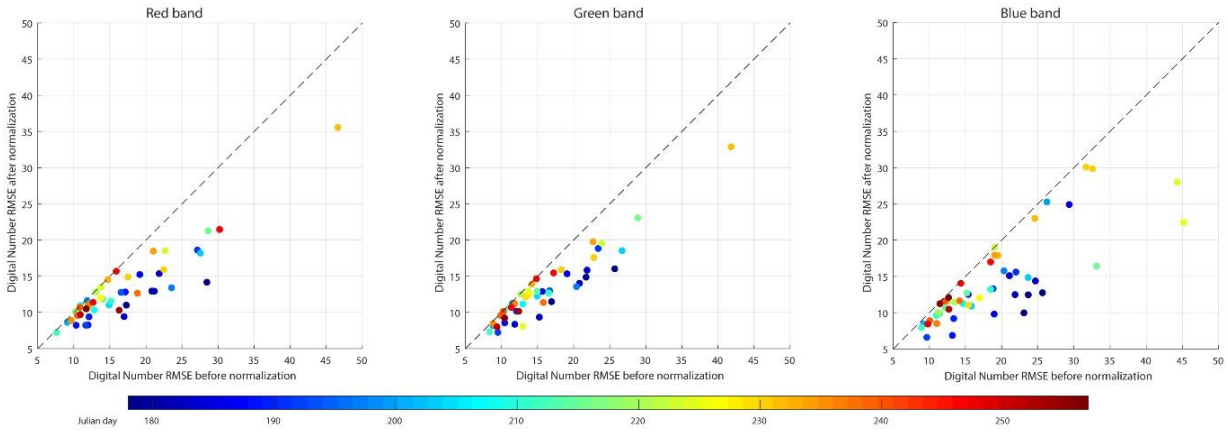

Figure 10: Digital Numbers (DNs) related RMSE of the pixels composing the non-reference images before and after normalization in comparison with their relevant reference orthomosaics for the red band, the green band and the blue band. Dates are in Julian days.

The generalized RMSE reductions resulted from applying the specific band-by-band linear models to normalize the DNs of the non-reference orthomosaics such that they are closer to those of the reference ones. In some cases, however, the RMSEs did not decrease to low magnitudes or decreased differently between the bands, and this translated into poorly normalized orthomosaics. The orthomosaic of 19 August (Figure 11) is an example of a poor normalization. The PIF points of the red and green bands were highly dispersed (resulting in poor R^2) and most of them deviated towards the brighter side of the colour tone (i.e. left of the 1:1 line) before applying the models. As expected, their corresponding models sat on the brighter side of the colour tone (y-intercepts of >50 and slopes of roughly 0.8). The blue band was slightly better and the

PIF points less dispersed ($R^2 = 0.9$). The blue model had better y-intercept and slope compared to the previous two bands, but tones with DNs >125 were translated into brighter tones whilst tones with DNs <125 into darker ones. The poor models then translated into a poorly normalized orthomosaic (Figure 11b), with an unnatural colour grading and very different as compared to the reference image. This is also visible from the histogram of the normalized orthomosaic (Figure 11b), with the blue band that lost some information while the red and green bands gained counts in the bright tail of the histogram. Overall, the orthomosaic was brighter and green tones were enhanced.

The 7 July orthomosaic (Figure 12) is, in contrast, an example of a good normalization. The band-related RMSE magnitudness were low before the normalization (±10–13 DNs) and the PIF points well-aligned. The linear models showed high R2, slopes of 0.9 and y-intercepts ranging from 19.21 to 24.29 (Figure 12a). Such slopes and y-intercepts enhanced the brightness of the bands, slightly attenuating the dark tones. As a response, the left tail of the histogram (i.e. the darker tones) of the normalized orthomosaic (Figure 12) was reduced, eventually resembling the master histogram.

An example of an excellent PIF normalization is shown for 30 July (Figure 13). Compared to the previous two orthomosaics, in this case the band RMSE magnitudes were already low (<9 DNs) before the normalization and the PIF points were well aligned. As a result, the linear models had very high R2, slopes close to 1 and y-intercepts close to 0 (Figure 13a). For these reasons, the application of such models should have provided the best normalization possible for this orthomosaic (Figure 13b), even though pre-normalization differences were already very low. A comprehensive summary of the normalization performances, including slopes and y-intercepts for each model, can be found in the supplementary (SM1, 2 and 3) information for this paper.

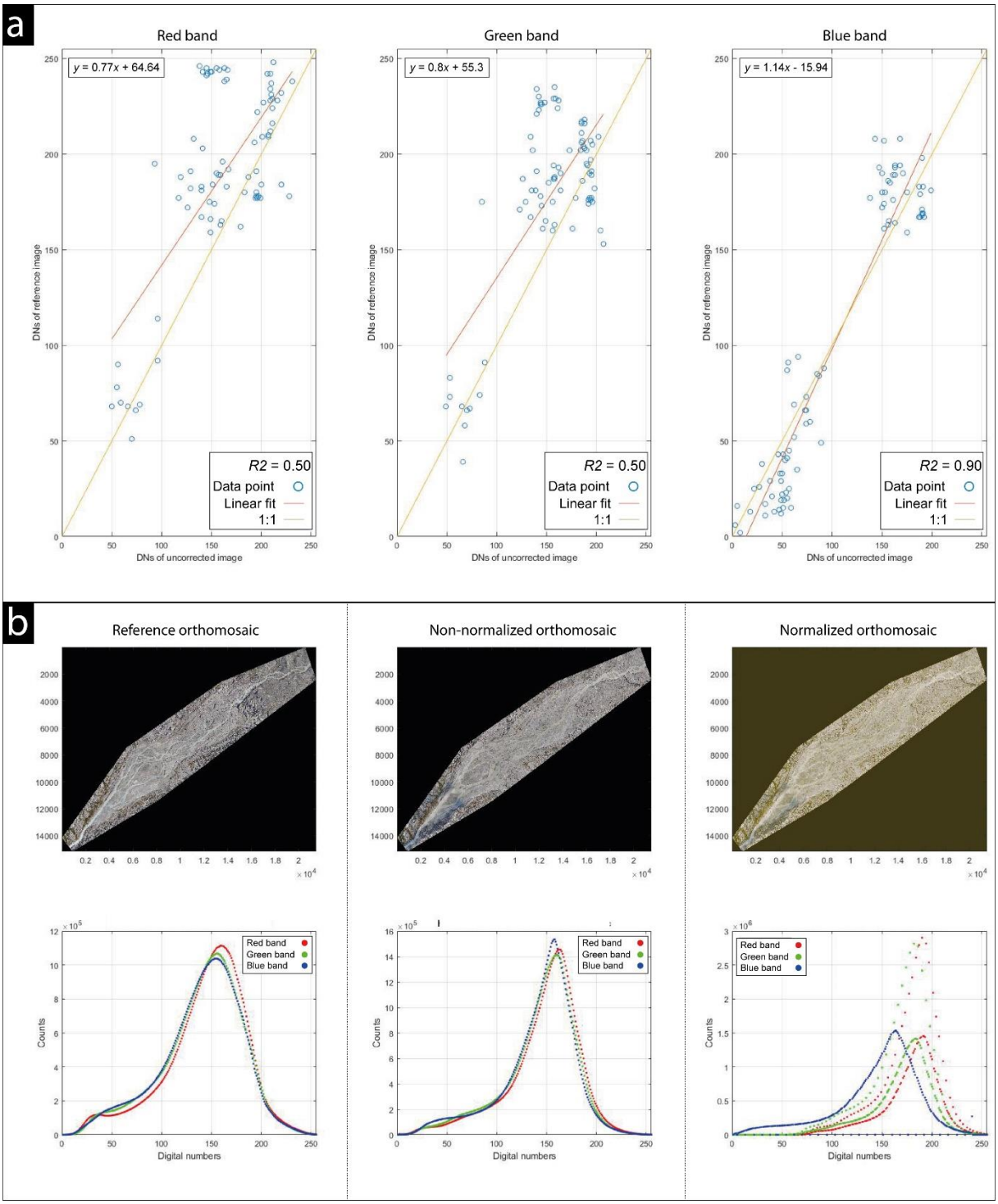

Figure 11: Example (19 August, Group 2) of a poor PIF normalization. a) Linear models and corresponding R2; b) Comparison between reference image (26 July), non-normalized orthomosaic (non-reference) and normalized one.

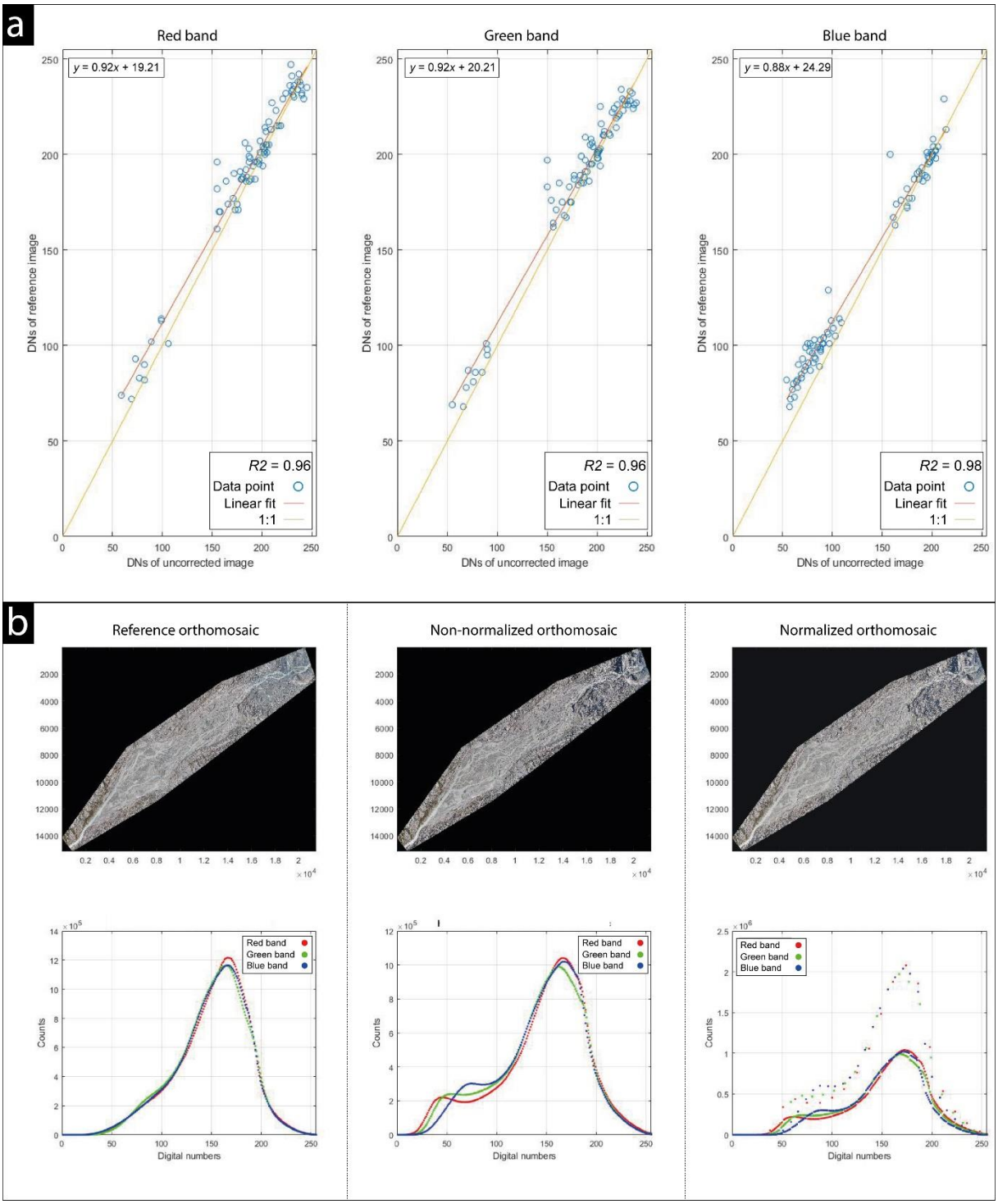

Figure 12: Example (7 July, Group 1) of a good PIF normalization. a) Linear models and corresponding R2; b) Comparison between reference image (i.e. 14 July), non-normalized orthomosaic (non-reference) and normalized one.

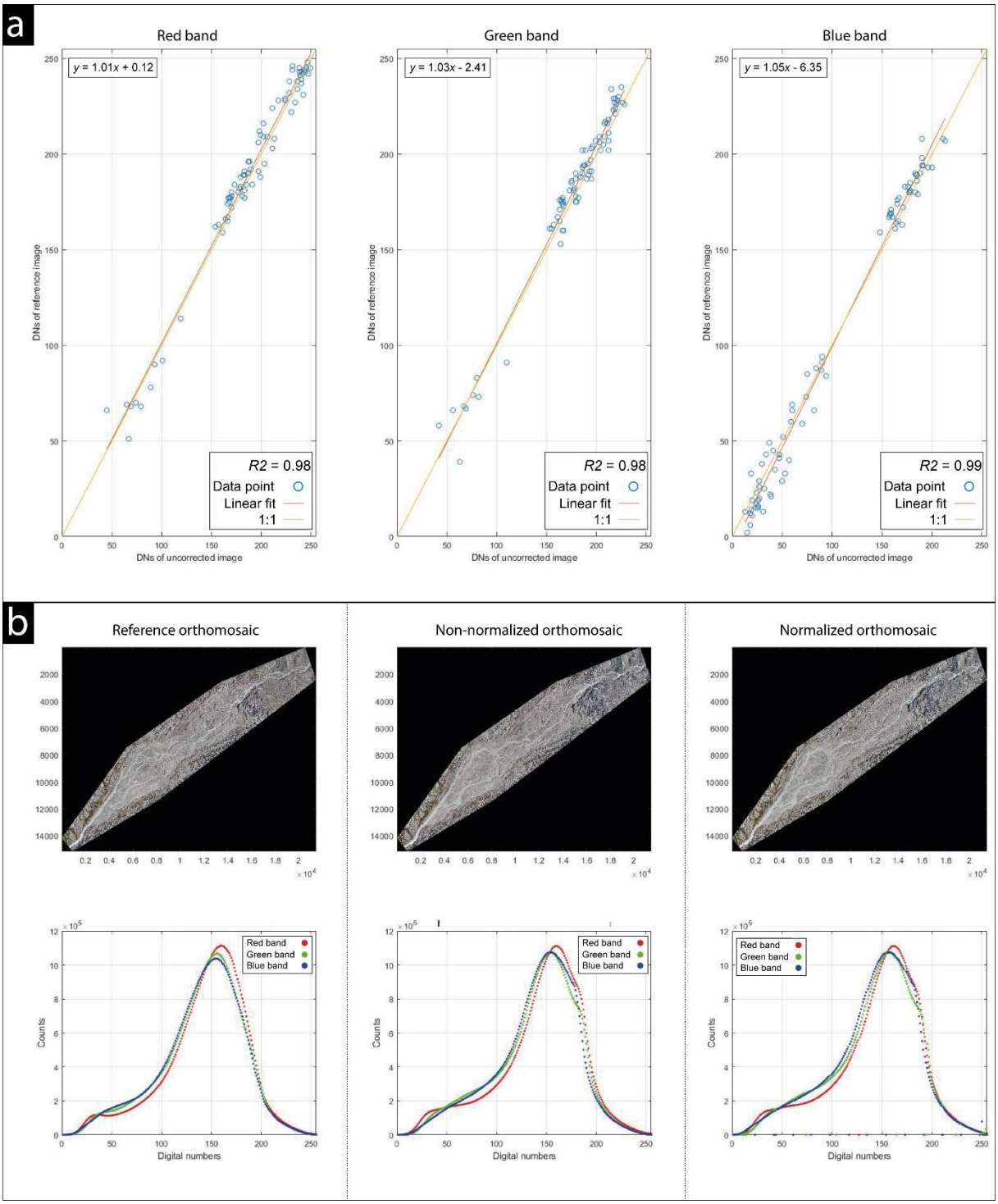

Figure 13: Example (30 July, Group 2) of an excellent PIF normalization. a) Linear models and corresponding R2; b) Comparison between reference image (i.e. 26 July), non-normalized orthomosaic before correction and normalized one.

3.2.3.3 Quantitative evaluation of the PIF normalization

We compared the performances of the PIF normalization models (i.e., normalized) with the performances of the raw mosaics (Figure 14a). We also evaluated the normalized (Figure 14b) and raw (Figure 14c) mosaics in comparison to the single calibrations.

Overall, using the reference models (14 July 2026 July) on the raw and normalized mosaics for other dates produced good results (Figure 14a). Surprisingly, the raw datasets had a substantially better performance than the normalized ones. Performance deterioration was more severe in Group 2 as compared to the less divergent Groups 1 and 3. When compared to the single models, the normalized dataset (Figure 14b) had a clearly poorer performance, and this was accentuated in Group 1 and notably Group 2, reflecting the difficulties encountered during the PIF normalization. The raw datasets (Figure 14c) were more similar to the single models, and even better in some cases. Interestingly, Group 2 datasets produced better results, reflecting again that normalization could lead to model deterioration.

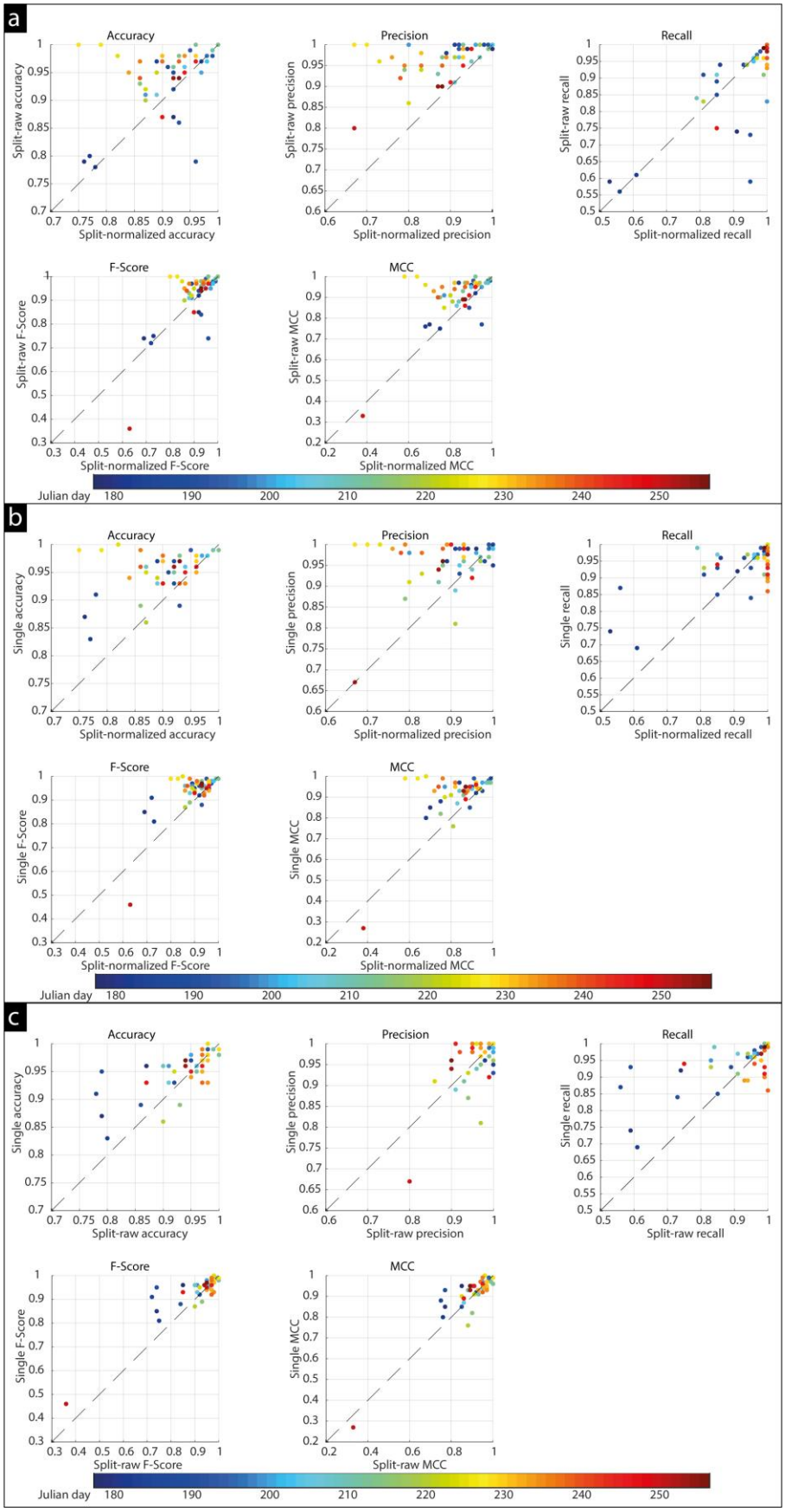

Figure 14: a) Comparison between normalized and raw performances, b) normalized and single performances, and c) raw and single performances.

3.2.3.4 Shadow model

An example of the micro-topography model and the subsequent biofilm presence/absence masking is presented in Figure 15. Moving water in glacial channels often created artefacts in the DEMs, and those in turn created micro-relief at the resolution we used, and hence shadows. Unlike true micro-topography shadows, such zones had a minimal effect on the shadow masks, since they were located on the surface of moving glacial water, i.e. where biofilms did not develop. Biofilm probability maps were binarized (Figure 15d) before being used as input in the occupation map calculations, but we also explored how biofilm presence/absence changed if micro-topography shadow areas were excluded from being mapped (Figure 15e). True micro-topography shadows were typically restricted to banks and boulders (Figure 15c). Removing micro-topography caused shadows did indeed remove zones mapped as biofilms. However, there were also some examples of micro-relief where biofilms were present in zones of shadow, notably around small boulders.

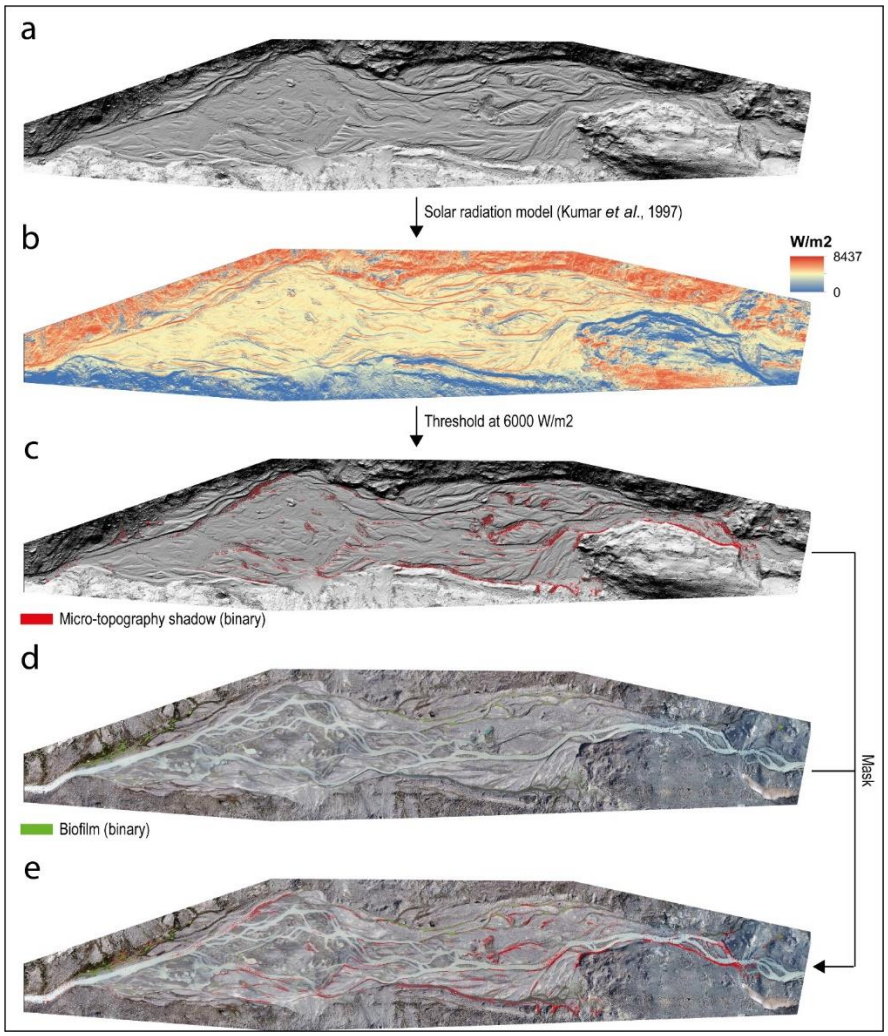

Figure 15: Example of the applied micro-topography shadow model to a binary presence/absence biofilm map from 14 July: a) Hillshaded DEM, b) modelled solar radiation, c) micro-topography shadow, binarized at 6000 W/m^2, d) presence/absence of biofilm (input of the occupation map), and e) presence/absence of biofilm masked by micro-topography shadows. Binarized micro-topography model and biofilm presence/absence were masked to exclude the edges.

3.2.3.5 Evaluation of the resultant biofilm maps

Occupation maps for the single, raw and normalized, with and without accounting for micro-topography shadow, are shown in Figure 15. Qualitatively, results tend to agree among themselves, with the highest cumulative presence of biofilms in channels located on the edges of the topographic right-side of the braidplain.

The use of the single and single-shadow probability datasets (Figure 16a, b) produced clusters of biofilm occupation that were very similar to each other, and only marginal differences were visible, most of which were located on the transitions between steep banks that created micro-topography shadows and water surfaces. Single pixels with an occupation range of 1 to 10 were present but widely distributed, found especially in the centre-part of the floodplain, and were likely to be noise. Results of the raw and raw-shadow derived occupations maps (Figure 16c, d) did not significantly differ from the single and single-shadow ones, although in both scenarios there were fewer pixels within the 1 to 10 day range in the centre-part of the braidplain. Similarly to the single datasets, micro-topography shadow removal did not substantially modify clusters of biofilm occupation. When occupation was calculated with the normalized datasets (with and without shadows; Figure 16e, f), significant biofilm presence over periods of 1–10 days was detected even in the active braidplain. This was not the case for the single datasets (Figure 16a, b) and the raw ones (Figure 16c, d), suggesting the presence of systematic mapping errors (i.e. spectral confusion plus noise) in the normalized probability maps.

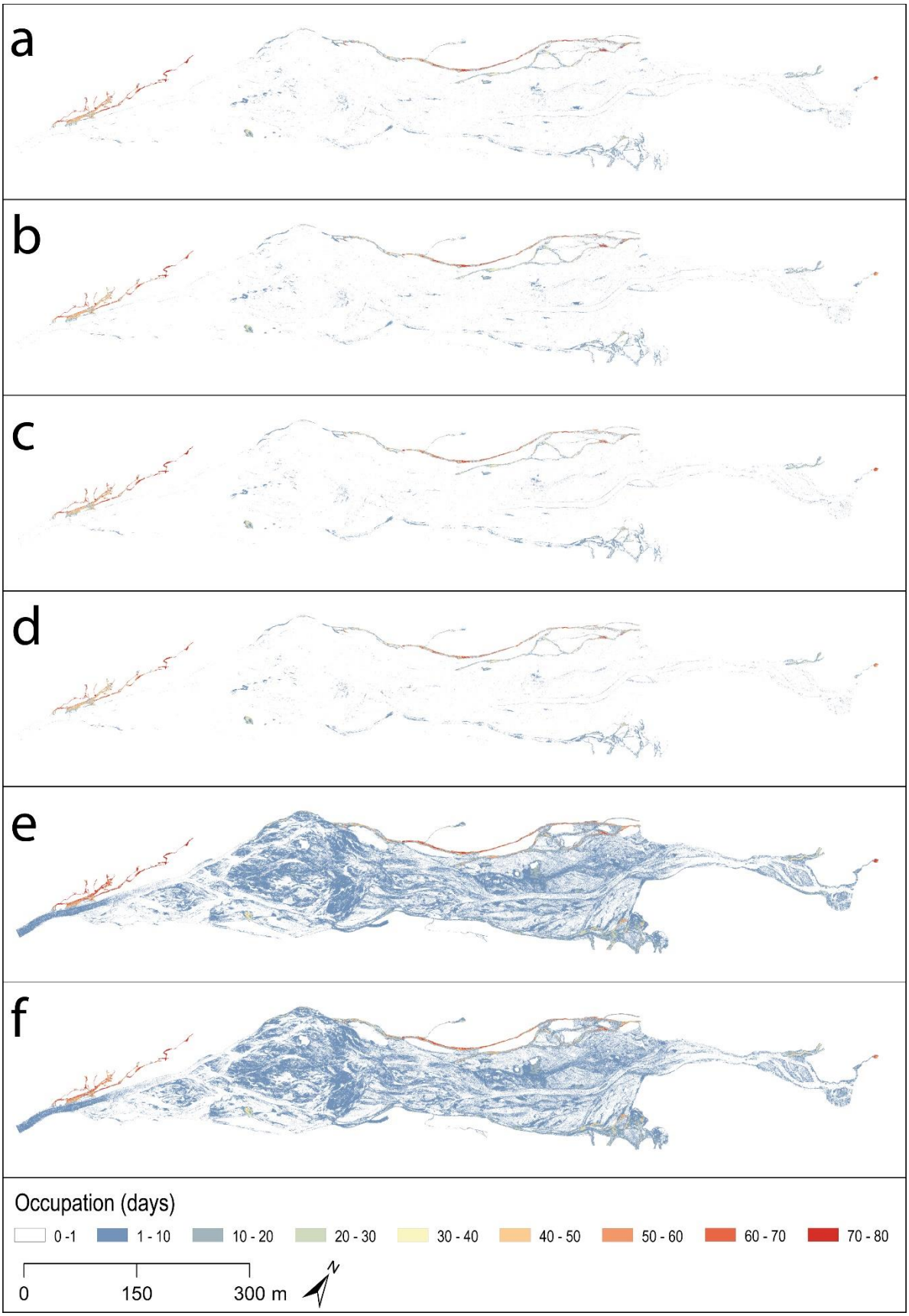

Figure 16: Occupation (in days) of biofilms on the floodplain of the Glacier d'Otemma during the period 26 June to 13 September 2020. Occupation calculated from a) the single dataset, b) the single-shadow dataset, c) the raw dataset, d) the raw-shadow dataset, e) the normalized dataset, and f) the normalized-shadow dataset.

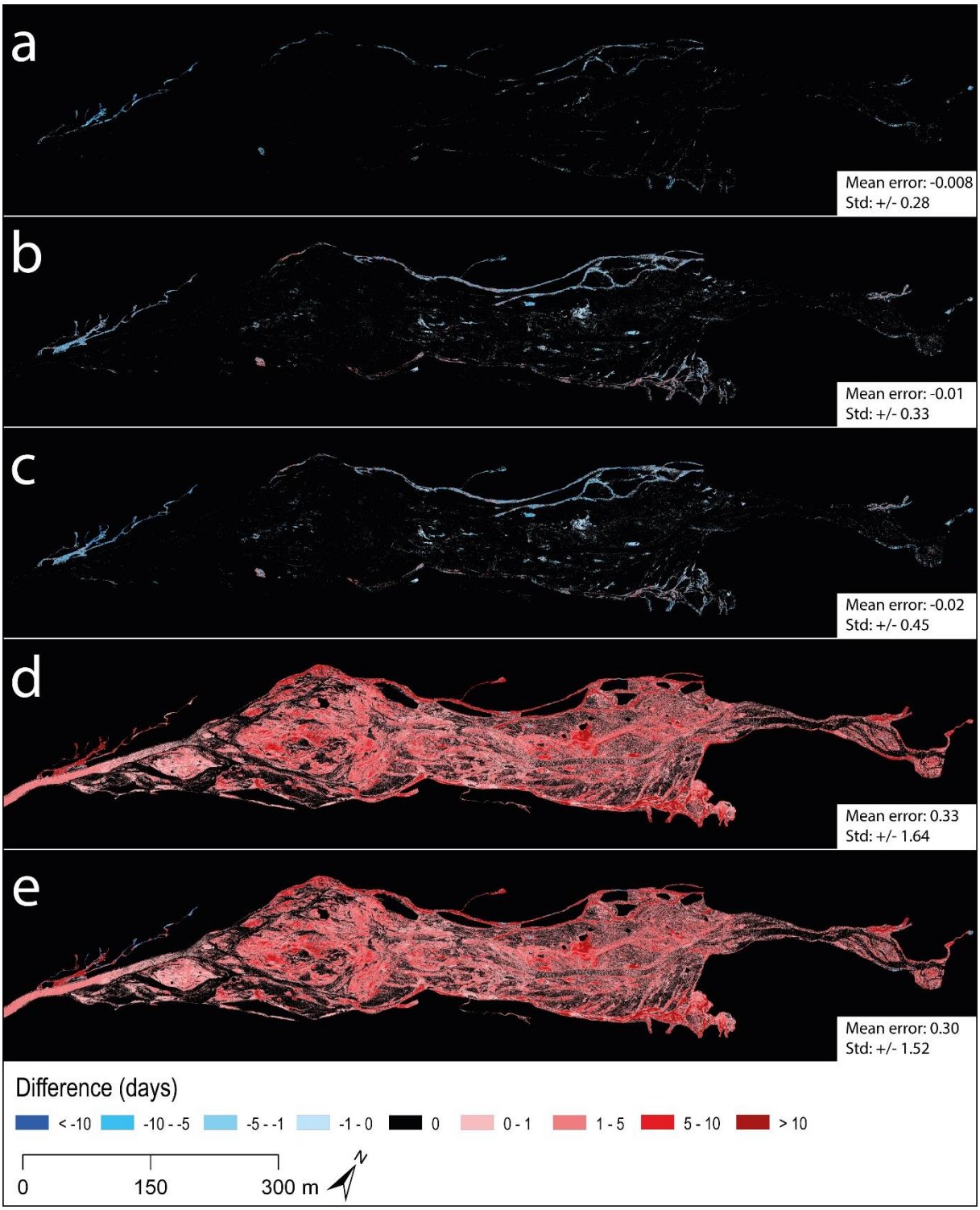

Figure 17: Occupations of Difference (OoD): a) Single-shadow minus single, b) raw minus single, c) raw-shadow minus single, d) normalized minus single, and e) normalized-shadow minus single.

Comparison between single and single-shadow Occupation of Difference (OoD) maps (Figure 17a) showed that the single-shadow map gave slightly lower occupation (mean difference: −0.008 days) as compared to the single map, and some noise was successfully removed from the upstream half of the floodplain. However, the right-side channels of the single-shadow occupation map showed anomalously lower reduced

occupation (mostly within the −5 day range) that resulted from the exclusion of pixels affected by micro-topography shadow, though those pixels were actually biofilm. Comparison between the raw occupation and single occupation maps with no shadow correction (Figure 17b) showed more heterogeneous differences, although the mean difference was still negative (−0.01). The centre-part of the braidplain had less noise, but there was either under- or over-estimation of occupation days in the side channels, both on the left and right sides of the braidplain. This result suggested that when applied to different dates the reference models (i.e. 14 July for groups 1 and 3, and 26 July for Group 2) were either too weak, creating over-estimation, or too strong, creating under-estimation. The OoD maps with the raw-shadow dataset (Figure 17c) were similar to that of the raw dataset (Figure 17b), but the mean difference was slightly higher, suggesting that micro-topography shadow masking had a stronger impact. Not surprisingly, the normalized occupation-related OoDs (Figure 17d, e) showed systematic overestimation across the whole floodplain suggesting that the reference models were typically too weak such that many non-biofilm pixels (e.g. wet sediments) were mapped as being biofilms due to pixel values greater than the 0.5 selected threshold.

3.2.3.6 Occupancy noise maps and p-value corrected occupation maps

The probability maps show those zones where the time-series of occupancy/non-occupancy is systematic ($p < 0.05$) and random ($p > 0.05$), the latter indicating possible noise (Figure 18). The single (Figure 18a, b) and raw (Figure 18c, d) scenarios showed similar results: i) single pixels (or small clusters) in the centre-part of the floodplain that may have a high total occupancy, but this occupancy is random and so likely to be noisy, and ii) zones in the side channels that also appeared to have some random occupancy. The normalized scenarios (Figure 18e, f) confirmed results in Section 3.2.3.5, with biofilm occupancy in the active braidplain being random and over-estimated.

We then used the occupancy noise maps to exclude pixels with $p > 0.05$ from being considered biofilm pixels in the occupation map calculations. A new set of occupation maps was generated (Figure 19). Most of the salt and pepper noise was successfully removed from the single and raw scenarios (Figure 19a–d) using this criterion. The overall biofilm extent mapped previously (Figure 16) was preserved in the new maps, although there was a generalized reduction of the biofilm extent at a threshold p-value = 0.05. Though such a threshold might be too strong, it produced maps where biofilm presence had a 95% probability of reflecting true biofilm dynamics. The normalized scenarios (Figure 19e, f) experienced the most important changes, with noise and systematic bias removed in large quantities from the new occupation maps, although some clusters and single pixels are still present. However, the overall extent resembled that of the more precise single and raw datasets (with and without shadow), with channels on the edges mapping the highest cumulative presence of biofilms.

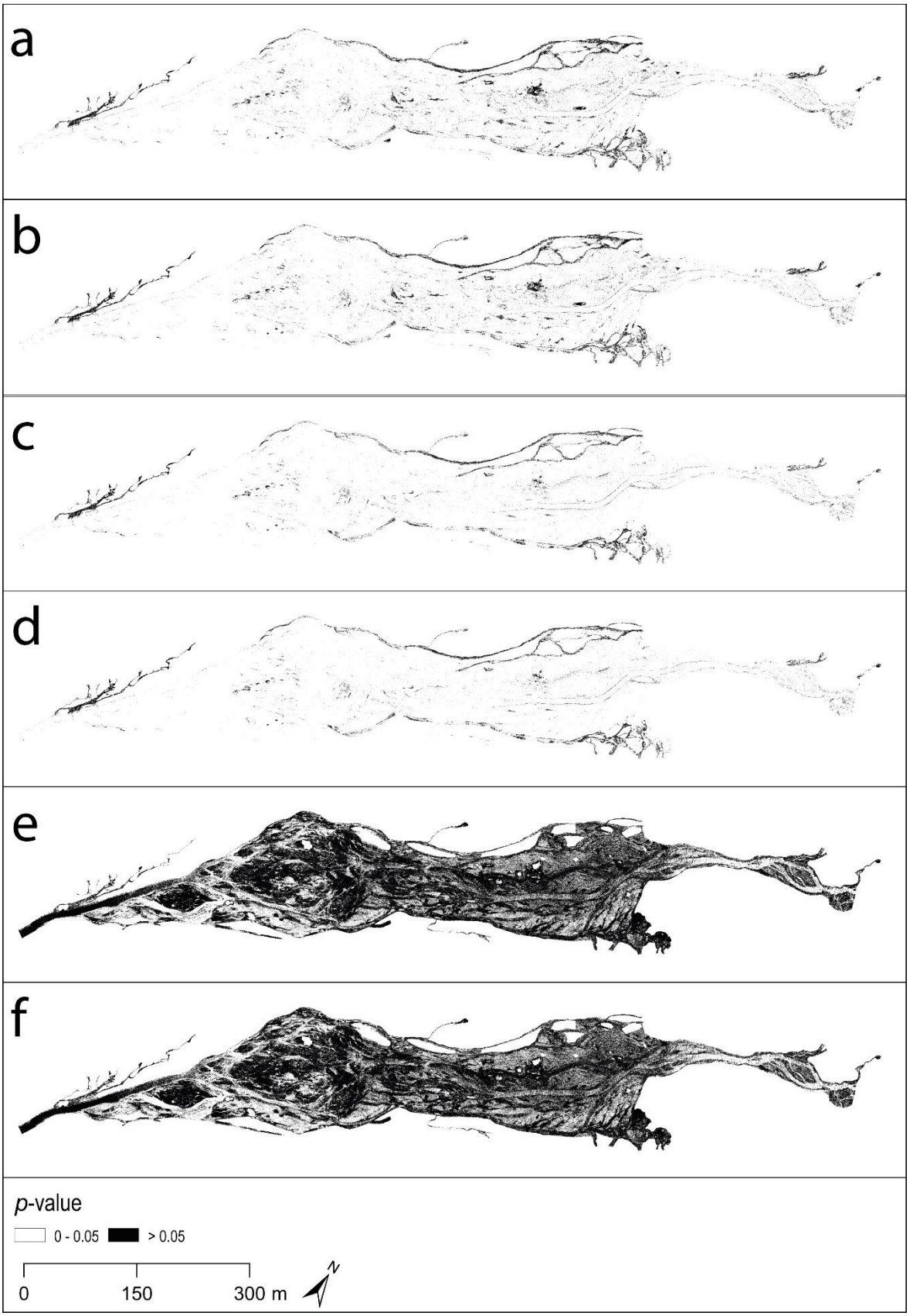

Figure 18: Maps of the probability that the time-series of occupation or non-occupation by biofilm is non-random ($p < 0.05$): a) the single dataset, b) the single-shadow dataset, c) the raw dataset, d) the raw-shadow dataset, e) the normalized dataset, and f) the normalized-shadow dataset.

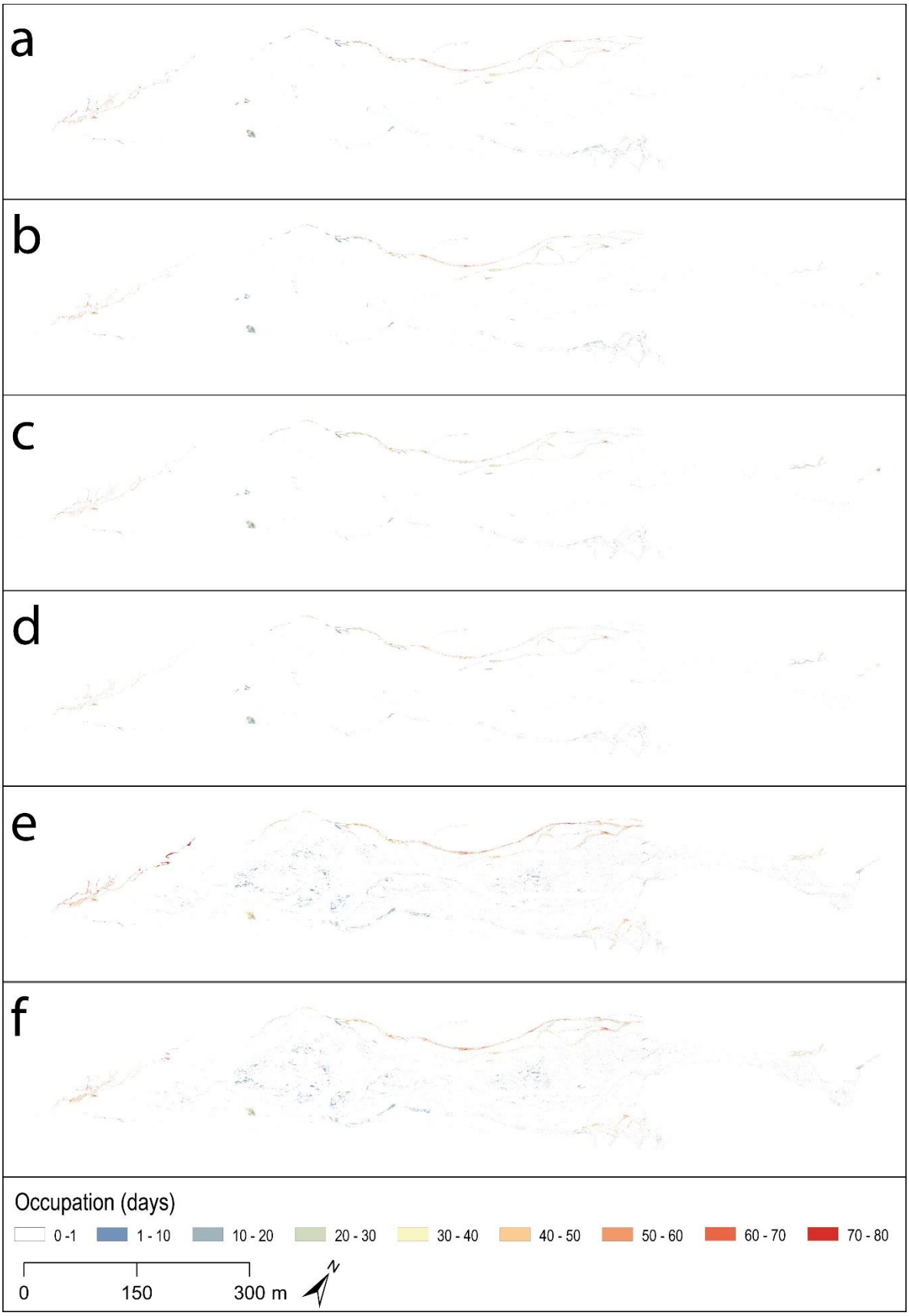

Figure 19: Occupation (in days) corrected for p-value of biofilms on the floodplain of the Glacier d'Otemma during the period 26 June to 13 September 2020. Occupation calculated from a) the single dataset, b) the single-shadow dataset, c) the raw dataset, d) the raw-shadow dataset, e) the normalized dataset, and f) the normalized-shadow dataset.

3.2.3.7 Biofilm distribution in space and time

On the basis of the results in Section 3.2.3.6, we selected single corrected for p-value as the basis of the final biofilm maps. Being able to map the distribution of biofilms at the whole floodplain scale and at such a high temporal resolution allows investigation of the seasonal pattern of biofilm development. During the summer (Figure 20a) biofilms tend to develop in channels located on stable or less active zones. Our results demonstrate that occupation of biomass in the active floodplain is very uncommon during the melt-season, and most of the biomass accumulates in stable or less active channels that are disconnected from the destructive glacial braided stream. In November (Figure 20b), biofilm distributions appeared very different as compared to the summer, in fact pixels with high probabilities of being biofilms are found even in the active braidplain that during that time is occupied by a less destructive glacial stream. In more general terms, the distribution evolution shows that biofilms tend to develop in the channels located on stable zones from June through mid-September while they tend to migrate towards the main active floodplain from mid-September onwards (fall at such altitudes).

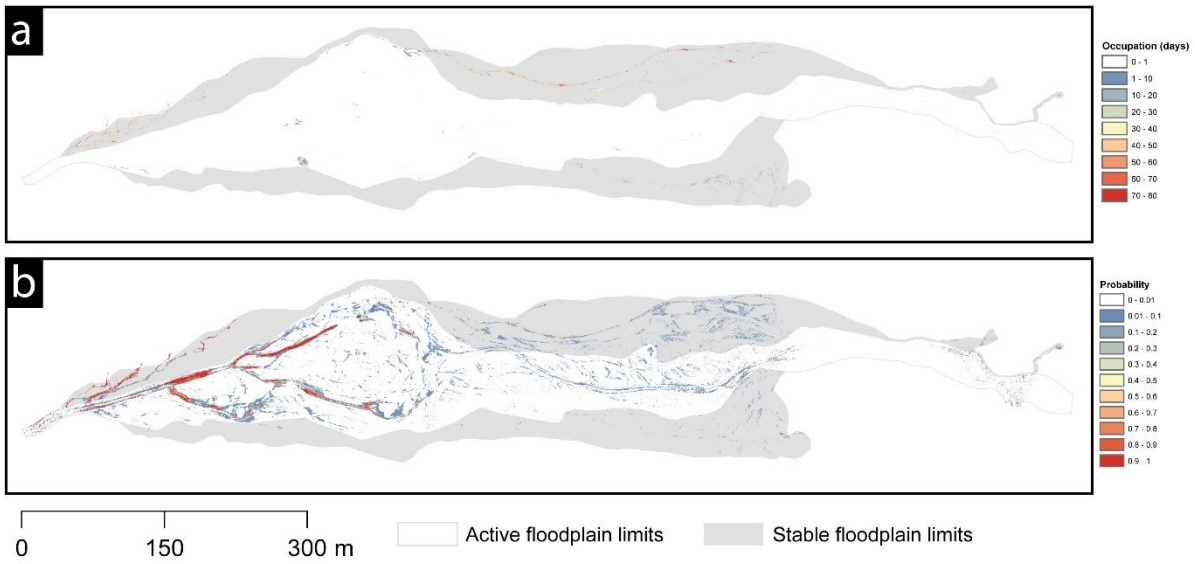

Figure 20: Seasonal distribution of biofilm on the floodplain of the Glacier d'Otemma. a) Biofilm occupation map (single and p-value corrected), from 26 June to 13 September; b) Probability map for the 5 November.

3.2.4 Discussion

3.2.4.1 Choice of logistic models

The choice of logistic models in this study produced very clear but different results. Within the band ratios and groups, the ExG and GLI significantly underperformed for the other indices analysed (Tables 5, 6 and 7). We assume that this finding is related to the nature of the benthic biofilms in the investigated forefield that were mainly reddish and/or brownish. In fact, both the ExG and GLI indices reduce the RGB information by using the green band as the principal component in the ratios

and this may have biased the detection of red or brown patches. For instance, the GLI index (Louhaichi et al., 2001) was developed to detect wheat leaves and stems that have typically high green DNs compared to red (and blue). The NGRD, VARI, and RGRI ratios produced better results as compared to the ExG and GLI indices (Tables 5, 6 and 7). Similar to the GLI and ExG indices, the green band is a central component of the NGRD, VARI, and RGRI ratios, though the red band is more important which may explain their superior performance. Interestingly, the NGRD, VARI and RGRI indices had performances equal to the EXR, RCC, and KANA indices in Group 4 (Table 7), but this could be explained by the presence of snow over the floodplain than created a very dichotomous situation where only snow-free channels had a different spectral signature compared to the rest of the floodplain. Overall, the ExR, RCC, and KANA indices gave the best results (Tables 5, 6 and 7). This may be explained by the central role of the red band in the calculations that matched with most of the biofilm pixels used in the training/validation process. The positive role of the red band is well known in vegetation studies. In fact, most vegetation indices use the red band combined with the near-infrared to map vegetation (Gitelson et al., 2002).

Finally, the KANA index (Kawashima and Nakatani, 1998) was selected for the mapping of phototrophic biofilms because it showed the overall best performance across the tests reported here. It has been shown (Kawashima and Nakatani, 1998; Gitelson et al., 2002) that the use of the blue band can have a beneficial effect when phototrophically active pigments must be detected. Kawashima and Nakatani (1998) noted that the blue band has a nearly constant response to chlorophyll-a content regardless of meteorological conditions, while red and green have negative correlation, and the use of blue as a base value (i.e., R-B) reduces the probability of having biased values. We therefore assume that the KANA index had generally better performances because of the presence of mostly reddish and/or brownish biofilms and the fact that the blue band attenuated the effects of changing light conditions.

3.2.4.2 Orthomosaic normalization and biofilm maps

Although as part of our study we undertook single scene-by-scene calibration, this is labour intensive. Hence, we tested the use of a smaller number of reference images to develop the calibrations. It has been shown that multi-temporal image comparison can be difficult due to non-scene dependent changes (Schott et al., 1988; Du et al., 2002; Song and Woodcock, 2003; Liu et al., 2007; Bao et al., 2012) that can affect the reflectivity of ground objects, and hence create inter-scene differences that are not related to the signal that is of interest. The goal of the PIF normalization was to homogenize the set of orthomosaics to resemble as much as possible our reference ones allowing the calibration of one single logistic model within each group: 14 July (groups 1 and 3), 26 July (Group 2) and 5 November (Group 4). The reference mosaics were converted into visible band ratios (Table 4) that have the advantage of reducing the RGB information to a point that is less sensitive to the solar radiation (Woebbecke et al., 1995; Kawashima and Nakatani, 1998; Cheng et al., 2001).

Despite a generalized RMSE reduction after the PIF normalization (Figure 10), the relative radiometric normalization method showed relatively mixed results whether considered in terms of the validation results (Figure 14) and the impacts on the occupation maps (Figures 16 and 17). Individual scenes had variable differences in their red, green and blue digital numbers before normalization and normalization was variable in the extent to which these differences could be reduced (Figure 10). Differences in the covariance of scene and reference digital numbers (compare Figures 11, 12 and 13) reflect this variable performance. We think it can be traced to three main reasons. First, it is preferable to select artificial PIFs (e.g., roofs, streets) to perform a radiometric normalization (Schott et al., 1988), but these only partially available here for the 55% of PIFs that were ground control points. These covered a restricted spectral range as they were black and yellow and were also distributed to optimize the SfM photogrammetric processing and not for the need of spectral normalization. Second, when shadows were present over the floodplain (e.g., Figure 11b), they modified the reflectivity of the ground and those PIFs occurring in a shadowed portion of the floodplain had very different values compared to those of the reference orthomosaics. This increased point dispersion in the model (e.g., Figure 11a). Shadows could only be corrected at the scale of the micro-topography due to unknown cloud cover. Third, it took 3.5 hours to image the complete floodplain, and when the floodplain was imaged was conditioned by the need to survey at low flows when as little of the floodplain as possible was inundated by turbid water. PIF normalization works well with satellites (Schott et al., 1988; Liu et al., 2007) that instantaneously image large areas, which by definition contain no spatial signature of temporally evolving light conditions. This is partly reflected in differences between groups. Group 1 contained data from close to the summer solstice when the survey had to be completed before the sun had risen above local mountains due to rapid water level rise mid-morning. Group 3 contained data at the end of the summer when the river stage rose later and so the flight could be undertaken in fully light conditions. Both had more homogeneous lighting and the normalization was needed less (Group 3, Figure 10) or was more effective (Group 1, Figure 10) than for Group 2. Commonly, during Group 2 image acquisition the floodplain went from being fully shaded to being fully exposed to sunlight.

The negative impacts of normalization were reflected in a general overestimation of biofilm extent as reflected in the occupation and OoD maps (Figures 16e, f and 17d, e). This was partly reflected in the validation statistics (Figure 14) which suggested very mixed results, even degrading statistics markedly and notably for the Group 2 data. The overestimation reflects the problem that re-assemblage of the single normalized bands into an RGB image can lead to a colour tone deterioration (Figure 11b), potentially caused by a new predominance of one of the three bands over the others. Here, the PIF normalization increased the DNs of our orthomosaics, then the index values and resulted in a generalized and systematic exceedance of the reference thresholds (i.e., 0.5 probability threshold) when occupation maps were generated. Notably, red DNs (e.g., wet sediments) became red dominated and so mapped as being biofilms.

This would question whether normalization of the sort used here was appropriate and perhaps suggests the need for a more physically based model-informed spectral correction (e.g., one that could be time-dependent when ambient lighting changes during data collection). The raw datasets were actually more consistent with the single image datasets. However, they had a tendency to underestimate biofilm extent (Figure 17b, c). This is likely because the reference thresholds from the logistic model were too strong for most of the dates such that less biofilm was detected when the reference 0.5-probability limit was applied.

The single image calibration models produced the cleanest probability and occupation maps (Figure 16a, b). This is not surprising as we trained a logistic model for each orthomosaic, resulting in models most suitable for the given situation (i.e. adapted threshold). They performed better in capturing the lighting characteristics of each scene provided there is reasonable lighting homogeneity within that scene. The reason for the multi-hour UAV flight time was to secure the high resolution needed to capture biofilm development for small scales over a large spatial extent. Thus, for these kinds of surveys, lighting is likely to be an issue and, at least until a more advanced normalization process is developed, it implies that more labour-intensive scene-specific calibration models are required.

We also evaluated the extent to which micro-topography shadows had an impact on our classifications. Micro-topography shadows were successfully detected and masked through segmentation of the potential solar radiation models (Kumar et al., 1997). The DEM resolution was sufficiently fine that in some cases moving surfaces (e.g. water) were mapped as having relief that created shadow (Figure 15c). Such artefacts occurred where biofilm either cannot develop or be visible due to the highly suspended sediment load. Although the shadow correction had a clearly beneficial effect on removing zones that were not biofilms, there were some zones where masking micro-topography shadows excluded also pixels that were likely to be true biofilms and the OoD between the single and single-shadow datasets (Figure 17a) demonstrated this. These were commonly related to pebbles and boulders located within and/or on the edges of channels that created shadowed pixels that were subsequently masked and excluded from calculation in the occupation maps. The positive contribution of the micro-topography models was limited to those pixels located on the transitions between steep banks and water surfaces that likely caused spectral confusion in our models.

Finally, the runs test provided a biologically informed statistical way to filter our occupations maps in which the pixels with p-value > 0.05 were discarded in occupation calculations. In the single and raw datasets (Figures 18a–d and Figure 19a–d), this might have excluded some pixels that were likely to reflect true biofilm dynamics (e.g., biofilms in side channels), but ensured that what was eventually mapped had a 95% probability of reflecting true dynamics (either presence, presence/destruction, or absence). The normalized dataset quality (Figure 19e, f) was enhanced as compared to previous results (Figure 16e, f), but some of the systematic bias caused by the normalization process was still present.

Our results suggested that phototrophic biofilms can be mapped through the combination of very low-cost UAVs and RGB cameras, but attention must be paid to lighting, hence the calibration of a scene-to-scene model (i.e., single) and using a biologically informed statistical feature appeared to be the most well suited for the range of conditions we encountered during the data collection.

3.2.4.3 Seasonal distribution of phototrophic biofilms and implications

Being able to map biofilm distributions and cumulative biofilm presence at high temporal and spatial resolutions provides important insights into benthic habitat functioning and how it responds to and co-evolves with external stressors. It is well known that glacial forefields are harsh environments due to their highly dynamic and unstable nature (Marren, 2005; Heckmann et al., 2016). Bakker et al., (2019) demonstrated that during the summer glacial streams continuously rework their accommodation spaces (i.e., floodplains) by erosion and deposition processes, resulting in low rates of environmental stability. This creates a disturbance-dominated regime that can influence biofilm development and/or survival, and is mainly controlled by the glacial-driven flow hydraulics. Bed load (i.e., bed instability) may impede biofilm development (Uehlinger et al., 1998, 2002, 2010 Rott et al., 2006), while high shear stresses may scour developed communities (Biggs and Close, 1989; Horner et al., 1990; Biggs and Thomsen, 1995; Cullis et al., 2014). The high suspended load may be responsible for biofilm abrasion (Horner and Welch, 1981; Horner et al., 1990; Francoeur and Biggs, 2006; Luce et al., 2010, 2013) but also limit the access to photosynthetically active radiation (Uehlinger et al., 2010). This explains why biofilm biomass is low during the melt-season (Uehlinger et al., 2002, 2010), but reaches two maxima during spring and fall, known as ‘windows of opportunity’ (see Uehlinger et al., 2002, 2010), because environmental conditions are less harsh (i.e., low discharge, low turbidity, and low or no bedload). From our maps (Figure 20), it is not possible to retrieve biofilm biomass directly, but our results tend to confirm the assumptions of Uehlinger and colleagues in relation to an autumn window. Biofilm presence was restricted to stable and water-fed terraces from June through late August. As the rate of morphodynamic change reduced from late August onwards, biofilm extent increased and presumably reached its highest mapped surface in November when the gelatinous dark-brown *Hydrurus foetidus* (Rott et al., 2006; Uehlinger et al., 2010) colonized extensive areas, including the turbid, most morphodynamically active main stream.

3.2.5 Conclusion

Here, we present a framework for mapping biofilm distributions by applying logistic regression to visible band ratios using UAV-based imagery processed using SfM-MVS photogrammetry. We demonstrated that with mapping at high frequency (daily) and spatial (cm) resolution, there is no need for expensive multi- or even hyper-spectral sensors in order to obtain valuable information on biofilm dynamics. Use of a suitable visible band ratio would be enough in most mapping scenarios due to the different colours of biofilms compared to the un-colonized substratum and these are retrievable in the visible range. We applied a basic linear normalization process to

normalize our orthomosaics. The effects of this were not conclusive and this was primarily because of non-homogeneous light conditions that caused considerable scatter in the training relations, but also meant that a linear correction was not always appropriate. A biologically-informed filter was particularly effective at removing points that would otherwise have been mapped as biofilms. Despite these issues, we were able to generate a time-series of distribution maps of an Alpine glacial floodplain that covers an entire melting season, from June to September. These maps will allow new insights on how biofilms develop and co-evolve in the harsh environment of a glacial forefield.

3.3 Chapter summary

The chapter developed and evaluated an approach for mapping phototrophic biofilms in glacial floodplains at high temporal and spatial resolutions. First, orthoimagery for an entire melt-season (plus one day in November) of the floodplain of the Otemma Glacier was produced. Second, the orthoimages were converted into visible band ratios that were applied to logistic regression models. This combination ultimately produced map in which pixels are defined by the number of days of periphyton occupation. An additional map, showing the presence of phototrophic biofilms in November is also produced.

In accordance with previous research (Miller and Lane, 2019; Roncoroni et al., 2019), the results show that phototrophic biofilms effectively developed during the melt-season, and this development is clearest in zones of high stability (i.e., terraces). This development therefore reflects the habitat heterogeneity of proglacial floodplains, and the importance of krenal and rhithral water sources (Ward et al., 1998). Away from these stable zones, development is rare, but reflects the spatial and temporal heterogeneity of disturbances (Bakker et al., 2019). Furthermore, these results show that in autumn development is mainly in the most active floodplain, reflecting the reduction in the number of disturbances and the presence of sufficient water for periphyton development. This further confirms the concept of windows of opportunity proposed by Uehlinger et al. (2002, 2010).

However, two important points emerged from this work. First, this approach was based upon the subjective selection of 300 sites (50% biofilm) for calibration and the subsequent selection of another 300 sites (50% biofilm) for validation. In automated classification techniques, it is common to have one single dataset, randomly split into two groups with one (i.e., the calibration) accounting for the 70/80% of the total population (Bishop and Nasrabadi, 2006). Furthermore, it is accepted that larger calibration/validation datasets (i.e., order of 1000s of calibration/validation points) lead to more reliable classifications (Ramezan et al., 2021). In contrast, the approach presented here was subjective, non-random and based upon a limited number of training/validation points that also were in spatial proximity, and therefore we could not exclude that the performances reported here were somehow inflated by the design of our calibration/validation datasets. Additionally, the chapter does not explore alternative band ratios to those already published in the literature and new approaches

to map the presence of phototrophic biofilms, and those could potentially provide better classification performances and require less work. This is an important weakness because the progress in machine learning techniques allow for the testing of multiple classification techniques (e.g., support-vector-machines, object-based classification, etc.) that could be more suitable, less labor-intensive and reliable in mapping phototrophic biofilms in these environments and independently of the changing light conditions. Some of these techniques have already been used in riverine studies (e.g., Carbonneau et al., 2020a, b), and these might have improved the overall quality of this chapter.

Second, this method provides data on biofilms that are visually identifiable on imagery. Subsequent attempts to relate the signatures reported in this Chapter to distributed measurement of Chlorophyll-*a* content suggest that the method does not map biofilms but one, albeit extremely important component of the biofilm family; periphyton. Strictly, this Chapter offers an extensive view of where and when periphyton develop in proglacial floodplains and subsequent Chapters switch to referring to periphyton.

This Chapter does not provide a full explanation of the reasons that drive periphyton development during the melt-season. Thus, Chapter 4 approaches this question via spatially extensive and zonal analyses; and Chapter 5 then seeks mechanistic understanding of these patterns.

Chapter 4: Decrypting the stream periphyton physical habitat of recently deglaciated floodplains

4.1 Chapter overview

The ability to map the presence of periphyton over an entire melt-season (Chapter 3) potentially allows quantification of how the environment of proglacial floodplains controls the spatio-temporal development of periphyton. Thus, this chapter decrypts the periphyton habitat, and to do so it combines the results of Chapter 3 with an analysis of the hydro- and morphodynamics of an Alpine proglacial floodplain system. Thus, this Chapter addresses the second question of this PhD thesis, which is "*how is periphyton development related to habitat stability, stream morphodynamics, and access to water spatially and temporally at the scale of a representative proglacial braid plain?*". This chapter is published as a peer-review paper: Roncoroni, M., Mancini, D., Miesen, F., Müller T., Gianini, M., Ouvry, B., Clémençon, M., Lardet, F., Battin, T.J., and Lane, S.N. (2023). Decrypting the stream periphyton physical habitat of recently deglaciated floodplains. *Science of the Total Environment*, 161374.

4.2 Decrypting the stream periphyton physical habitat of recently deglaciated floodplains

4.2.1 Introduction

The glacial floodplains that form downstream of Alpine glacier margins are known for being highly unstable during the melt season (Marren, 2005; Heckmann et al., 2016; Miller and Lane, 2019). Such instability is associated with high rates of both glacial melt and subglacial sediment supply (Nienow et al., 1998; Heckmann et al., 2016; Perolo et al., 2019) in the form of both bed and suspended loads (Gurnell, 1987; Milner and Petts, 1994; Swift et al., 2005). Due to its high turbidity, the solar radiation reaching the streambed is also attenuated (Boix Canadell et al., 2021). Thus, glacial water is harsh in ecological terms (Gabbud et al., 2019) and this has a significant strong impact on the organisms that inhabit such environments, likely limiting their development and survival (Milner and Petts, 1994).

Despite this unfavorable context, periphyton communities do develop in recently formed glacial floodplains. Uehlinger et al. (1998, 2002, 2010) noted that periphyton biomass is very low during the melt season because disturbance rates are high. Daily discharges are high, commonly high enough to cause shear stresses on the stream bed that exceed the critical shear stresses required for periphyton removal (Biggs and Close, 1989; Biggs et al., 1999; Francoeur and Biggs, 2006; Neumeier et al., 2006; Thom et al., 2015; Hoyle et al., 2017). The suspended load is also high, increasing the probability of abrasion of the periphyton mat (Horner and Welch, 1981; Horner et al., 1990; Francoeur and Biggs, 2006; Luce et al., 2010, 2013); and decreasing the solar radiation available to photosyntetically active microorganisms growing on the stream bed (Uehlinger et al., 2002, 2010). In this context, the time between two disturbances is often significantly shorter than the time needed for periphyton to develop (Thom et

al., 2015). However, glacial floodplains are heterogeneous and conditions may develop locally where stability is sufficient to allow periphyton to develop (Roncoroni et al., 2022), possibly aided by the ecosystem engineering provided by the periphyton themselves (Miller and Lane, 2019; Roncoroni et al., 2019).

Glacial floodplains are drained by a set of water sources, which are not limited to glacial sources alone (Malard et al., 1999; Ward et al., 1999; Müller et al., 2022); both krenal and rhithral sources may be present (Malard et al., 1999; Ward et al., 1999). These sources are less harsh as compared to glacial water due to their negligible turbidity and relative hydrological and thermal stability (Uehlinger et al., 1998; Boix Canadell et al., 2021). Provided that glacial water does not intrude into these channels during the melt season, krenal and rhithral sources offer more benign conditions and allow periphyton to develop (Uehlinger et al., 1998; Brandani et al., 2022). However, they are also prone to progressive drying during the melt season where they are dependent upon snow-melt as it becomes progressively exhausted.

Glacial floodplains are also characterized by zones of geomorphic stability that vary in space and time. Terraces are common in glacial floodplains (Germanoski and Schumm, 1993; Marren, 2002; Marren and Toomath, 2013, Marren and Toomath, 2014; Roussel et al., 2018), and are rarely if never inundated by glacial water (Roncoroni et al., 2019). The morphological disconnection from the more active floodplain makes terraces extremely stable yet prone to dry conditions if not connected to krenal and rhithral sources (Malard et al., 1999; Ward et al., 1999). Within the more active floodplain, stream braiding is common (Maizels, 2002; Marren, 2005) and likely results in a wider distribution of bed shear stresses and water depths (Bakker et al., 2019). Braiding intensity also evolves through time, and when it is high bedload tends to be reduced (Ashmore, 1988; Ashmore et al., 2011) or focused on a few very active channels where the bulk of water flows preferentially (Bertoldi et al., 2009; Egozi and Ashmore, 2009). This, in turn, has the result that some braids become less harsh for short periods time.

This review emphasizes that the development of periphyton during the melt season likely reflects the balance between the mosaic of heterogeneous yet-interconnected habitats and their stability within the glacial floodplain (Ward et al., 1998). In this paper, we present the first quantification of the spatio-temporal patterns of periphyton development; at high temporal (daily within glacial melt season) and spatial (cm scale) resolutions for an Alpine glacial floodplain system. We test the following hypotheses. First, we hypothesise that periphyton develop preferentially where stable krenal and rhithral water sources flow on terraces. The double condition of water availability and stability allows for longer growth periods because glacial water does not intrude into these channels, and prolonged conditions of water transparency and streambed stability are found simultaneously. Second and in agreement with the literature, we hypothesise a relationship between periphyton development and stability, but we extend the notion of stability to any streambed patch that is stable for long enough to allow for periphyton development. In this sense, we hypothesise that intense braiding likely favours the emergence of braids with more benign conditions (i.e., shallow water and low shear stress) that periphyton may colonize very rapidly. This

also extends to braids that have intermittent water supply, and are inundated only at high flows but do not experience substantial hydraulic disturbance. However, this colonization is likely of short duration due to a high probability of disturbance by active reworking of the channel. Finally, we hypothesise that periphyton development at the whole floodplain scale is the net result of the above-mentioned processes and reflects the spatially heterogeneous assemblage of disturbances in the most active portion of the floodplain and of the positive effect of the less destructive non-glacial water sources (e.g., krenal and rhithral) that may drain the most stable portions of the floodplain. This net result eventually defines where ecosystem engineering may occur (see Roncoroni et al., 2019).

4.2.2 Methods

4.2.2.1 Study site

The Otemma glacial floodplain (Figure 21. 1, 45°56′04.9″N 7°24′46.1″E) is located in the Val de Bagnes in Southwestern Switzerland. It has formed since the early 2000s in response to very rapid recession of the Otemma glacier (Egli et al., 2021) at an average rate of 50 m per year (Mancini and Lane, 2020). The floodplain, constrained upstream by crystalline bedrock and downstream and laterally by steeper slopes, is approximately 900 m long and 150 m wide. It includes kryal, krenal and rhithral water sources. The floodplain is highly dynamic during the melt-season (Mancini and Lane, 2020) restricting pioneer vegetation and stream periphyton development to surfaces with low rates of morphodynamic activity (Miller and Lane, 2019; Roncoroni et al., 2022; Brandani et al., 2022).

Our dataset is based upon high spatio-temporal resolution optical (i.e., red-green-blue (RGB) band) imagery acquired using a method developed and tested for periphyton mapping (Roncoroni et al., 2022).

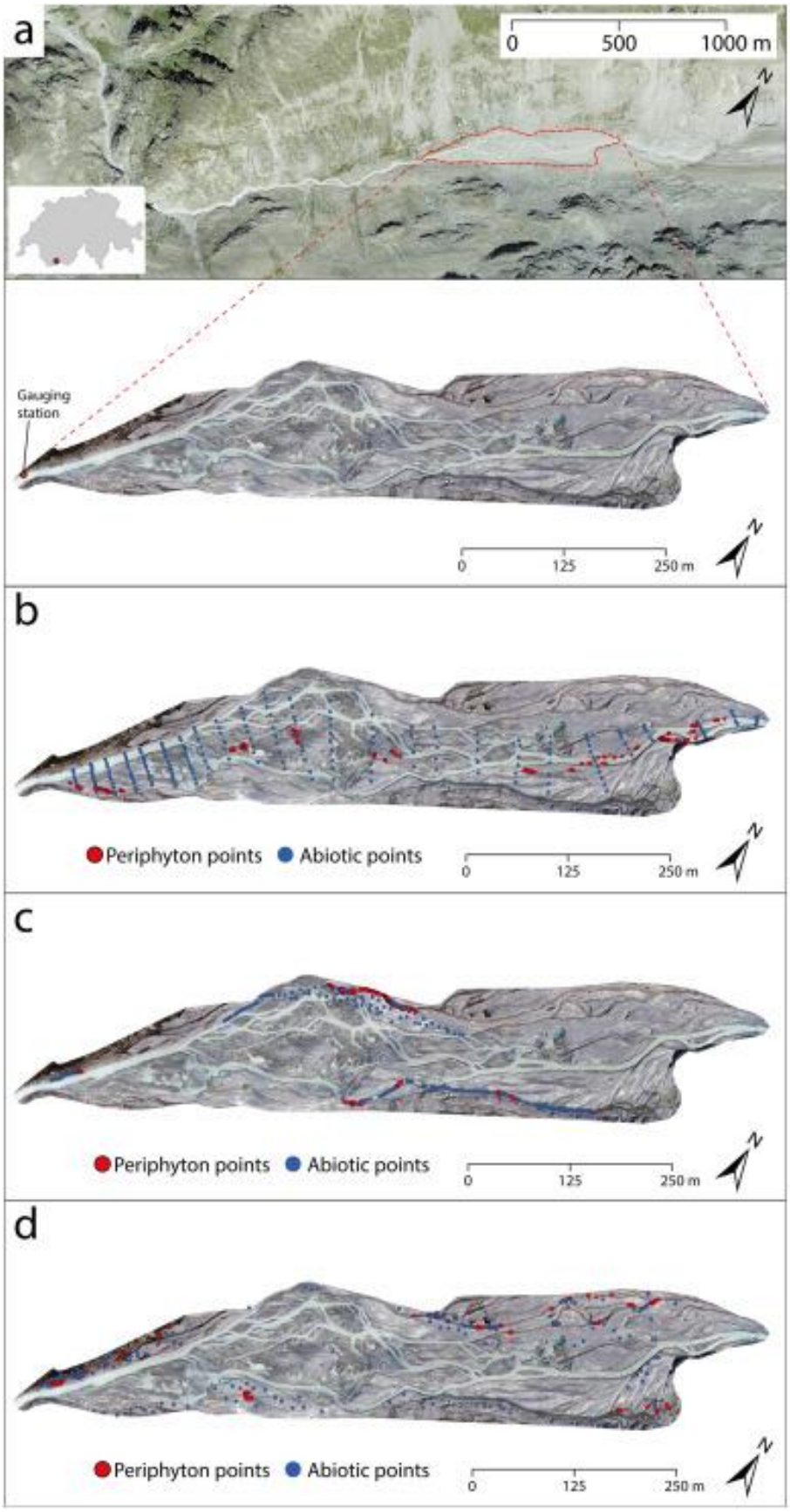

Figure 21: a) Headwaters of the Dranse de Bagnes (top view; orthomosaic ©Swisstopo) and zoom of the study zone (floodplain of the Otemma glacier, bottom view); b) Locations of the sampling points within the active floodplain; c) Locations of the sampling points within the buffer floodplain; d) Locations of the sampling points within the terrace zone.

4.2.2.2 Acquisition of images, ground control points, and Structure-from-Motion photogrammetric processing

We acquired RGB imagery of the floodplain on 52 non-consecutive days from late June to early September 2020. Images were collected with a DJI Phantom 4 Pro quadcopter, which is low cost, allows pre-programmed flight missions and has a camera of sufficient quality for Structure-from-Motion Multiview-Stereo (SfM-MVS) photogrammetric studies (James et al., 2020).

We flew the Uncrewed Aerial Vehicle (UAV) platform early in the morning (from 06 h30 onwards) to avoid extensive inundation of the floodplain, and used the freeware Pix4Dcapture (v. 4.8.0) to manage flight missions and image collection. Following James et al. (2020), we designed the flight missions to produce high precision and quality orthomosaics and Digital Elevation Models (DEMs). Images were collected in grids at 80 m above the ground with the camera looking at nadir (90°) and image overlap of 80 %. Additionally, we included off-nadir center-looking imagery by collecting images in circular missions at 60 m above the ground. We measured the position of 77 Ground Control Points (GCPs) with a differential GPS Trimble R10, with a known and corrected (using the fixed monitoring Swiss Federal Office for Topography provided via SwiPOS©) base station. GCP absolute position was collected in the Swiss coordinate system CH1903+.

We undertook the SfM-MVS photogrammetric processing in Agisoft Metashape (v. 1.5.5) and followed the framework of James et al. (2017, 2020) to ensure reliability and replicability within the datasets. To do so, we tested the camera internal parameters and GCP effectiveness in the bundle adjustment to lower the probability of producing datasets with systematic deformations (e.g., doming, datum shift). For the characteristics of our study site, our tests showed that the use of focal length, principal point offset (Cx, Cy), affinity and orthogonality parameters (B1, B2), radial (K1, K2, K3) and decentering (P1, P2) distortions within the bundle adjustment delivered the lowest probability of producing systematic deformations. Furthermore, the tests showed that 52 (68 %) out of 77 GCPs were sufficient to produce high quality 3D re-shaping and scaling of the point clouds (from which DEMs are then interpolated). We then exported DEMs at 20 cm and orthomosaics at 5 cm spatial resolutions. Further details can be found in Roncoroni et al. (2022).

4.2.2.3 Periphyton occupation map

We developed date-by-date calibration and validation datasets. Each dataset (i.e., training and validation) consisted of the coordinates of 300 pixels (n = 150 of pure periphyton; n = 150 of un-colonized substrata or turbid water). The pixel selection was based upon visual inspection of our orthomosaics, and this was possible due to the orthomosaic resolutions. Periphyton pixels were chosen to account for the different colour assumed by the periphyton at the time of image acquisition. Following tests (Roncoroni et al., 2022), we separeted each orthomosaic into single visible bands (red,

green and blue). We then calculated a visible band ratio, the KANA index (Kawashima and Nakatani, 1998):

$$KANA = (R - B) / (R + B) \quad [1]$$

where R and B are the intensities of the red and blue bands respectively. The KANA index has the advantage of accounting for the red band that has a beneficial effect in mapping vegetation (Gitelson et al., 2002) and the blue band that has a nearly constant response to chlorophyll-a (Kawashima and Nakatani, 1998). Once every orthomosaic was converted into the KANA index, we used the calibration pixels to train date-by-date logistic models. After model validation, we applied the logistic models to map phototrophic periphyton at the floodplain scale (Roncoroni et al., 2022).

We converted the probability maps into binary maps: pixels with a probability <0.5 were classified as not being periphyton whilst pixels with probability >0.5 as being periphyton. A preliminary occupation map, where each pixel corresponds to the days of periphyton occupation (0–80 days), was produced by summing up each binary map after having calculated its own time-lag compared to t_{n-1} and t_{n+1} (i.e., time-lag: $[(T - T_{n-1})/2 + (T_{n+1} - T)/2]$). We then assessed the noise in the occupation map by undertaking a runs test and excluded pixels with a probability <95 % (*p*-value < 0.05) of reflecting true periphyton dynamics (Roncoroni et al., 2022). Orthomosaic separations, visible band ratio calculations, logistic regressions, occupation maps and runs test were performed in Matlab (R2018a).

4.2.2.4 Submersion maps and geographical area segmentation

In a GIS environment (ArcMap, v. 10.5.1), we digitized the edges of the channels visible in each dataset (i.e., date) to allow determination of inundation extent at low discharge. Stacking each dataset allowed us to determine the number of days that each pixel in the floodplain was permanently inundated at low flow. Furthermore, this allowed calculation of braiding characteristics.

Following the channel segmentation of Ward et al. (1998), we then defined three geographical zones with distinctive hydrological properties. The first was defined as the active zone that was delimited by the maximum extent of glacially-fed water, but excluding zones with hillslope or ground-water derived clear water that was intermittently flooded by glacial-fed water. Within the active zone, as this was a braiding system, there was always the potential for inundation at high flow or morphodynamic change. However, there were areas in the active zone that during our study were morphologically more stable and other areas more dynamic. The second zone was one that had no incursion of glacier-derived water during the study period. This was primarily but not exclusively on low altitude (0.5 to 1 m) terraces and so we call this the terrace zone. The third zone was the buffer zone that effectively marked the interface between the active and terrace zones and included areas that contained intermittently clear and glacially-fed water.

To test for significant differences within the geographical areas of the floodplain (i.e., active, buffer, and stable), we finally performed a non-parametric Kruskal-Wallis.

4.2.2.5 Discharge time-series

At the downstream end of the floodplain (Figure 20), a gauging station site composed of (i) a Campbell CR200 datalogger with a CS451 pressure transducer and (ii) a Keller DCX-22AA-CTD logger and pressure transducer was installed. Continuous river stage measures were carried out during summer 2020, and here we use the data from June 26th to September 13th. Between July 19th and September 9th 2020, 21 discharge (m^3s^{-1}) measurements were derived from dye or salt (in the case of discharge lower than 0.5 m^3s^{-1}) tracings. These spot measurements were used to construct a stage-discharge relationship that was in turn used to provide a discharge time-series. The full details of these methods are provided in Müller et al. (2022).

4.2.2.6 Braiding index measures

Braiding indices were calculated using a channel count index that determines the number of channels (nc) in cross-sections (i) perpendicular to the main valley direction (Hong and Davies, 1979; Mosley, 1982; Ashmore, 1988; Chew and Ashmore, 2001; Egozi and Ashmore, 2008). We do not apply the Howard et al. (1970) requirement that cross-sections should be sufficiently far apart that no secondary channel is included in more than one cross-section. For n_s cross-sections, this gives a channel count braiding index (B_c) defined as

$$B_c = \frac{\sum_i^{n_s} n_c^i}{n_s} \quad [2]$$

4.2.2.7 Instability maps

We used the DEMs to produce an instability map that illustrates the number of days of instability (i.e., disturbances) in each pixel of the study site. This method was proposed by Lane and Richards (1997) and more recently by Bakker et al. (2019) to understand river-bed age, i.e. the time since the last stream reworking.

First, we calculated a set (n = 51) of limits of detection (LoD) which defines the magnitude of vertical change between two DEMs needed for 95 % confidence that the change is statistically significant given noise in the DEM data (see Supplementary material SM7). This is a standard practice in geomorphic change detection (Brasington et al., 2000, 2003; Lane et al., 2003; Milan et al., 2011; Bakker et al., 2019; Roncoroni and Lane, 2019; Mancini and Lane, 2020). In our case, we calculated a moving LoD (i.e., pairs of days, June 26th versus June 27th, June 27th versus June 28th) between any two DEMs at times T and T + 1 assuming that DEM errors are Gaussian and pairwise independent (in time);

$$LoD_{T,T+1} = \pm t[\sigma_T^2 + \sigma_{T+1}^2]^{0.5} \quad [3]$$

where t is the confidence interval (here 95 %, so t = 1.96), σ_T is the standard deviation of errors in DEM at time T.

Second, we calculated DEMs of Difference (DoD) by subtracting DEMs for each LoD to produce a set of DoDs (Brasington et al., 2000, 2003; Lane et al., 2003) and applied the associated LoD to identify significant changes.

Third, the thresholded DoDs were converted into binary change maps, in which we attributed 0 (i.e., stable) to elevation changes within the ±LoD range and 1 (i.e., change) to changes exceeding the ±LoD range. We then stuck the binary change maps by applying the time-lag scalar (i.e., time-lag: $[(T - T_{n-1})/2 + (T_{n+1} - T)/2]$) used in Sections 4.2.2.3 and 4.2.2.4, obtaining an instability map (0–80 days).

4.2.2.8 Periphyton point sampling and parameter extraction

On the occupation map and for each floodplain geographical area (i.e., stable, buffer, and active) we selected 400 periphyton and 200 non-periphyton (e.g., sediments, water) points (see Figure 21). The point coordinates were used to extract: (i) the percentage of time the point was occupied by periphyton; (ii) the percentage of time the point was unstable; (iii) the mean change in elevation from the closest glacial channel; (iv) the mean distance from the closest glacial channel; and (v) the percentage of time the point was submerged.

For the three habitats and on a date-by-date basis, we also extracted the daily periphyton presence/absence (0–1) from the periphyton binary maps and the submerged/dry (0–1) from the daily inundation maps.

Finally, for a general comparison of the three habitats, we also extracted the total number of pixels with at least one day of periphyton occupation.

4.2.3 Results

4.2.3.1 Occupation, submergence and instability

Within the active floodplain boundaries (Figure 22a), periphyton occupations were low (Figure 23a; Supplementary Material SM8), infrequent (Figure 23d), and spatially localized (Figure 22a). Meanwhile, 70.2 % of the active zone was submerged by glacial water for at least one day during summer 2020 (Supplementary Material SM9), with submergence rates generally high (Figure 23b), and a strongly braided and dynamic stream system (Figure 22b). Unstable surfaces were widespread across the active floodplain (Figure 22c), and 61.8 % of this area was reworked for at least one day during the summer (Supplementary Material SM9), although instability rates were rather low (Figure 23c; Supplementary Material SM8).

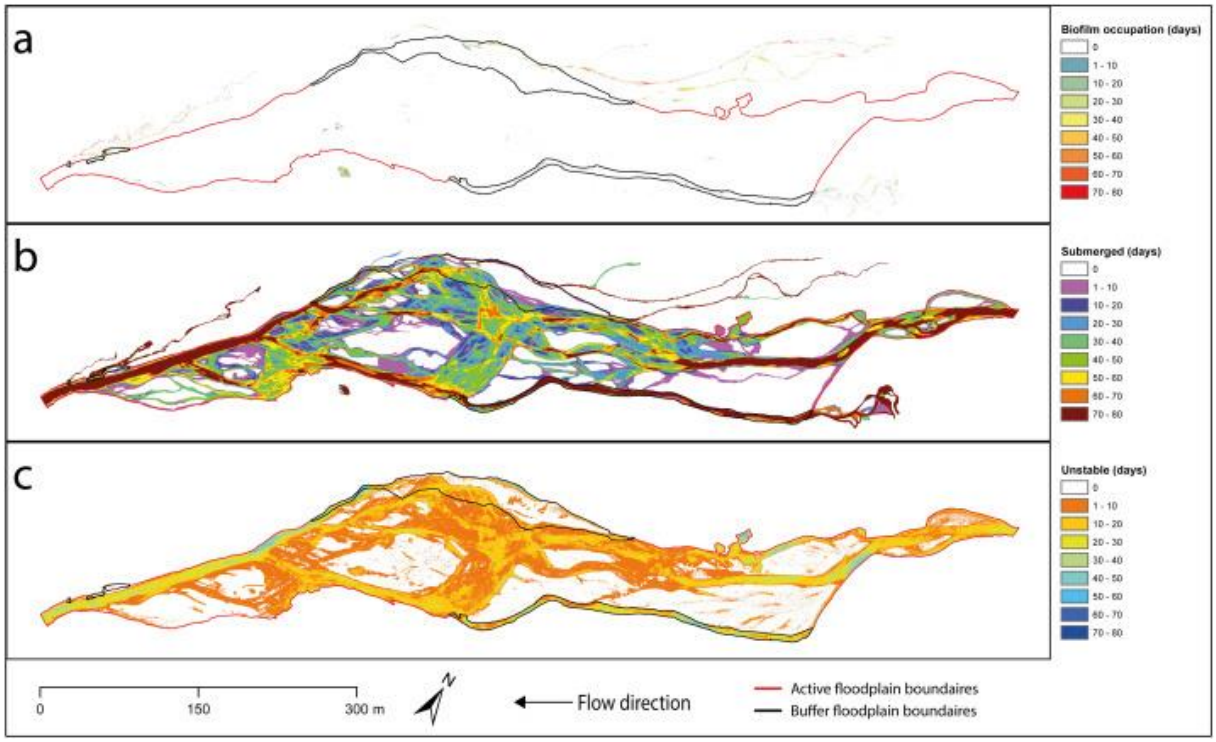

Figure 22: a) Periphyton occupation in number of days (see Roncoroni et al., 2022); b) Submergence in number of days; c) Instability in number of days. The interior of the black bounding boxes is the buffer zone; of the red bounding box the active zone (except for the buffer zone); and outside the red/black boxes the terrace zone.

Periphyton occupations in the buffer zone (Figure 22a) were higher than in the active zone (Figure 23a, d; Supplementary Material SM8), with buffer surfaces occupied by periphyton 30.9 % of time in average. 78.5 % of the buffer surface was submerged (either by glacial or clear water) for at least one day during the study period, with 75 % of this zone submerged for at least 1.9 % of the time (Figure 23b; Supplementary Material SM9). The higher submergence rates as compared to the active zone reflected the constant, yet stable, contribution of the clear water fed channels draining the buffer zone. Although occupations were high on average, the buffer zone was often unstable (Figures 22c and 23c; Supplementary Material SM8) and 73.7 % of the buffer zone experienced at least one disturbance episode during the study period.

The highest occupations were found in the terrace zone (Figures 22a and 23a, d), with periphyton occupying the streambeds 38.8 % of the time in average (Supplementary Material SM8). Periphyton locations were tied to channel locations, which covered 10 % of the terrace zones (Supplementary Material SM9). To put this into context, the terrace zones accounted for 72 % (713 m^2) of the periphyton coverage of the entire floodplain. The terrace zone was thus characterized by dry conditions (Figure 23b), but submerged areas when present were generally stable through time (Figures 22c and 23c; Supplementary Material SM8) and were not impacted by major disturbances (e.g. hillslope-originating mass movements) during the study period.

Finally, Kruskal-Wallis results showed significant differences among the geographical areas in response of occupation ($p < 0.001$), submergence ($p < 0.001$),

and instability ($p < 0.001$). These results suggested that zonation was appropriate and distinct biofilm habitats existed within the floodplain.

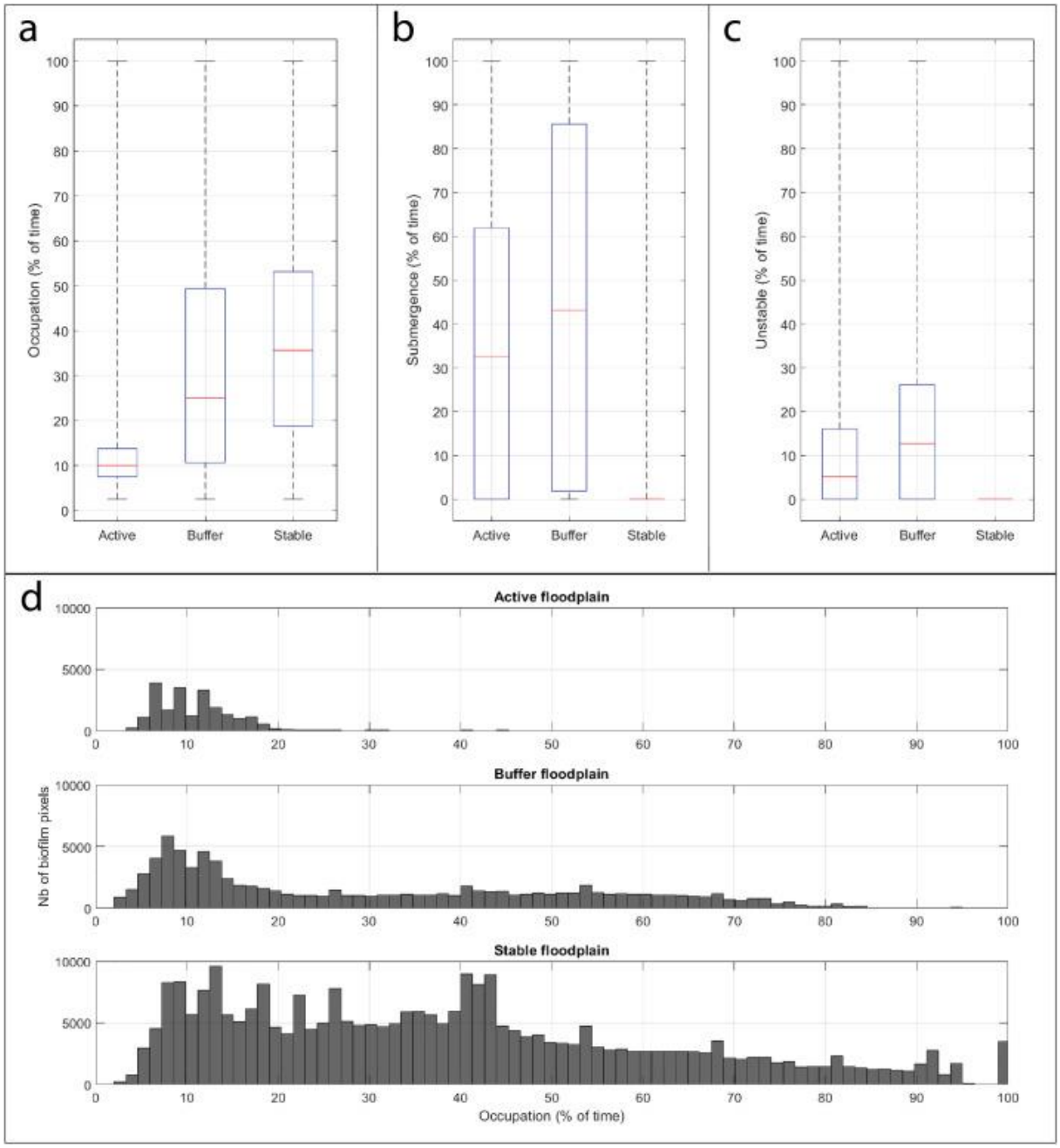

Figure 23: Comparison of a) the periphyton occupations (in % of time, 80 days is 100 %) between the geographical areas of the floodplain; b) the submergence (in % of time); and c) the instability (n % of time). d) Frequency of periphyton occupation (in % of time) for active, buffer, and stable zones. In 3a, 3b and 3c the whiskers define the data range and the box the 25 %, 50 % and 75 % percentiles.

4.2.3.2 Relationship between periphyton development and the physical habitat

Occupation was low (<20 % of the time) within the sampling point population of the active floodplain (Figure 24). In this zone, periphyton were commonly found in relatively stable surfaces that experienced stream reworking for <40 % of the melt-

season period (Figure 24a; Supplementary Material SM10). Nevertheless, the majority of the streambed occupied by periphyton occurred in areas that were unstable for <20 % of the time (Supplementary Material SM10). Not surprisingly, instability rates tended to increase submergence by glacially-fed water (Figure 24a). However, submergence of 40 to 70 % was also found to be beneficial for periphyton, but only when instability was simultaneously low (Figure 24b; Supplementary Material SM10).

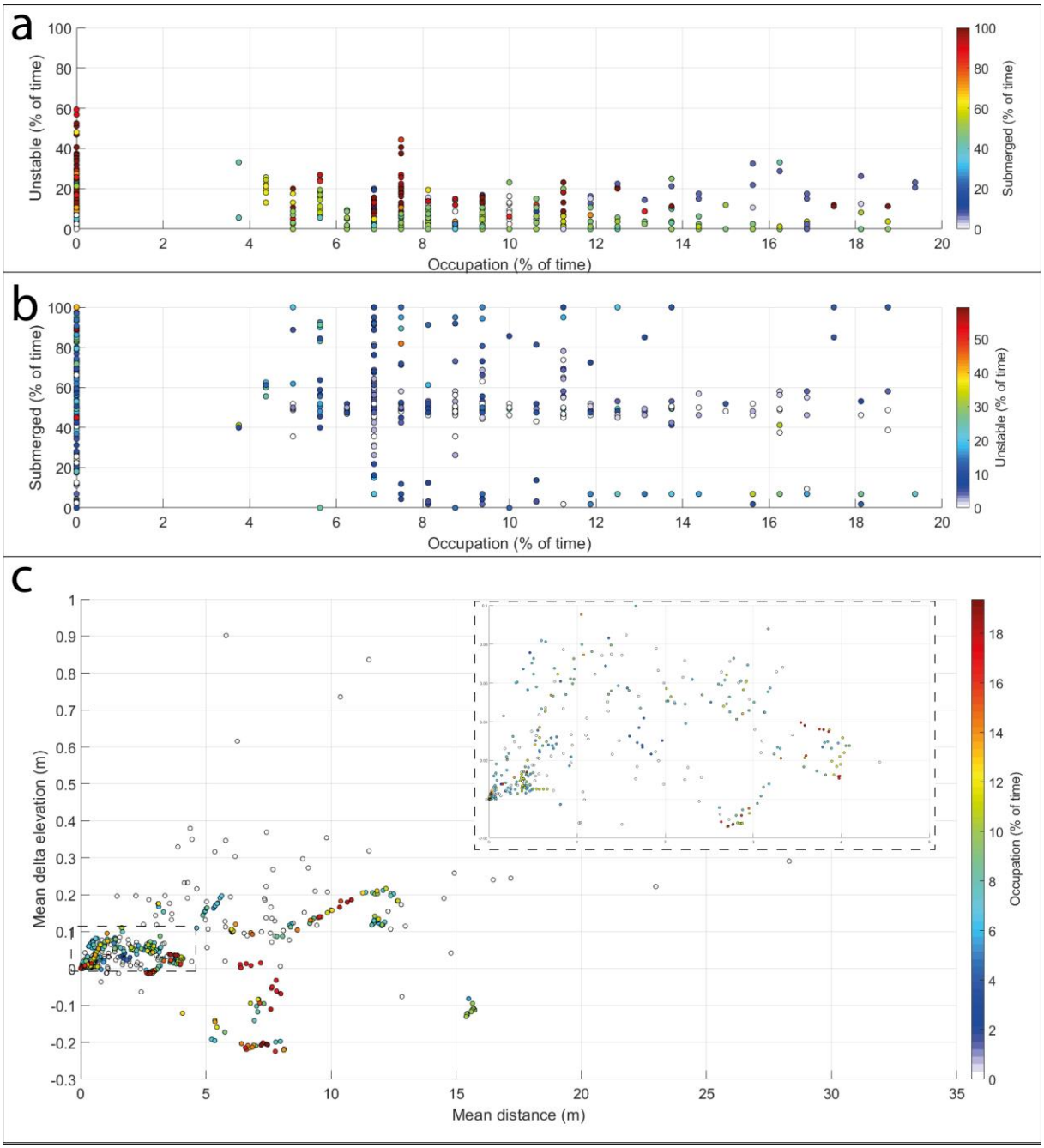

Figure 24: Relationships between a) instability, occupation and submergence, and b) submergence, occupation and instability for the active floodplain sampling points. c) Seasonal mean elevation difference and distance from the closest glacial channel.

The sampling points had relatively small elevation differences (−0.3–1 m), but were quite spread laterally (0–35 m) compared to the closest glacial channel (Figure 24c). However, most of the periphyton points had positive mean elevation differences

(0–0.1 m) but relatively little lateral distances compared to the closest glacial channel (0–5 m; Figure 24c). Periphyton likely used marginal channels that were cut off from the main active stream system and became dry at some point during the melt-season. On the other hand, unoccupied points (i.e., white dots with black outlines in Figure 24c) tended to be located at greater elevation differences (above 0.1 m) or greater distances (from 10 m), which suggest drier conditions due to the greater disconnection from glacial water.

In the buffer zone, unstable points typically had high submergence rates (Figure 25a). However, the highest submergence rates did not always lead to the highest instabilities (Figure 25b). Periphyton presence followed this trend and periphyton preferentially used the streambed patches that were more stable and also the most submerged (Figure 25a, b; Supplementary Material SM11), although cases in which periphyton developed on more unstable or drier surfaces existed.

The mean altitude differences between the sampling points and the closest glacial channels (Figure 25c) showed a clear dichotomy in the buffer floodplain. Unoccupied or low occupation points used lower altitudes (i.e., smaller elevation differences) while medium to high occupation points were found at greater altitudes compared to the closest glacial channel. This clear dichotomy was likely the result of glacial water flooding into the buffer zone, with lower surfaces being flooded more easily (so low or no occupations) and higher surfaces being rarely flooded (so medium or high occupations). Laterally, unoccupied patches were typically found closer to the glacial channels or far from them. In the first case, short lateral distances, coupled with small elevation differences, made glacial water intrusion easier and disturbances more frequent; in the second case greater lateral distances made glacial intrusion more rare resulting in drier conditions.

Glacial water intrusion in the buffer zone had a clear negative impact on periphyton occupation (Figure 26; Supplementary Material SM12). In fact, the highest occupations as well as the highest number of occupied points were found on surfaces that were rarely inundated by glacial water, but that were submerged by clear water most of the time. On the contrary, only a few periphyton points were found on surfaces that were also often flooded by glacial water.

Access to water was crucial on the terraces, and most of the periphyton points were found in channels with submergence rates >80 % (Figure 27a; Supplementary Material SM13). Those locations were identified across all elevation ranges and across all distances from the nearest glacial stream. On the other hand, unoccupied points were mostly found on dry surfaces (Supplementary Material SM13), that also had high altitudes compared to or were far from the closest glacial channel (Figure 27b), so that the floodplain water table was likely too low to provide water to the surface and sustain periphyton accrual. Compared to the active and buffer floodplains, our results suggest that periphyton development was only limited by water availability.

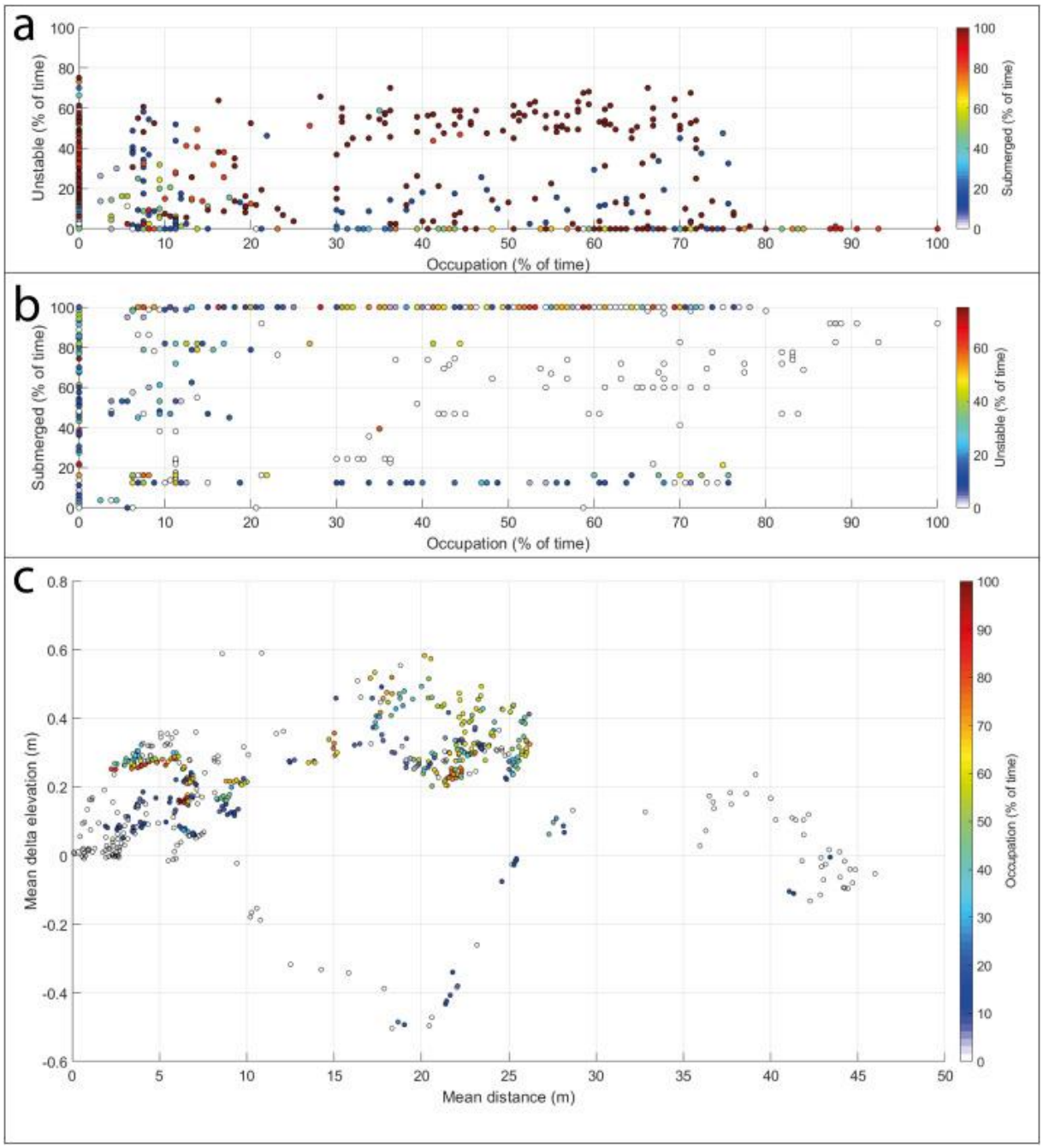

Figure 25: Relationships between a) instability, occupation and submergence, and b) submergence, occupation and instability for the buffer floodplain sampling points. c) Seasonal mean elevation difference and distance from the closest glacial channel.

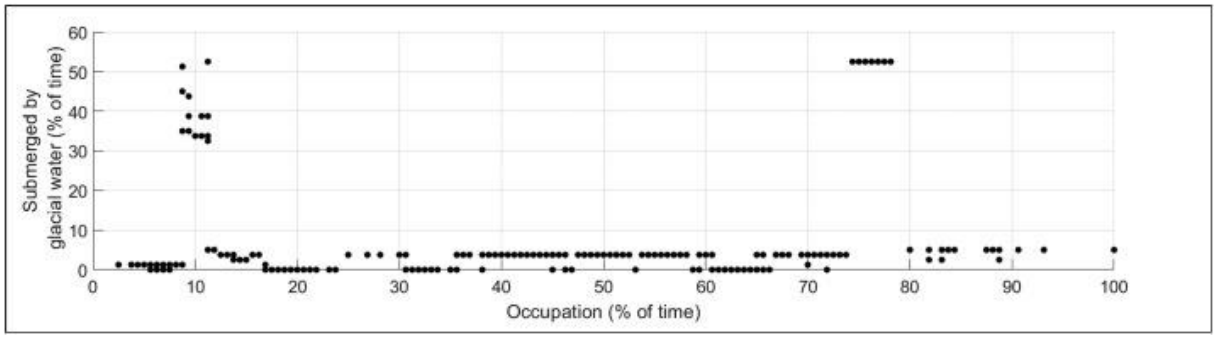

Figure 26: Influence of glacial water on periphyton occupation within the buffer zone.

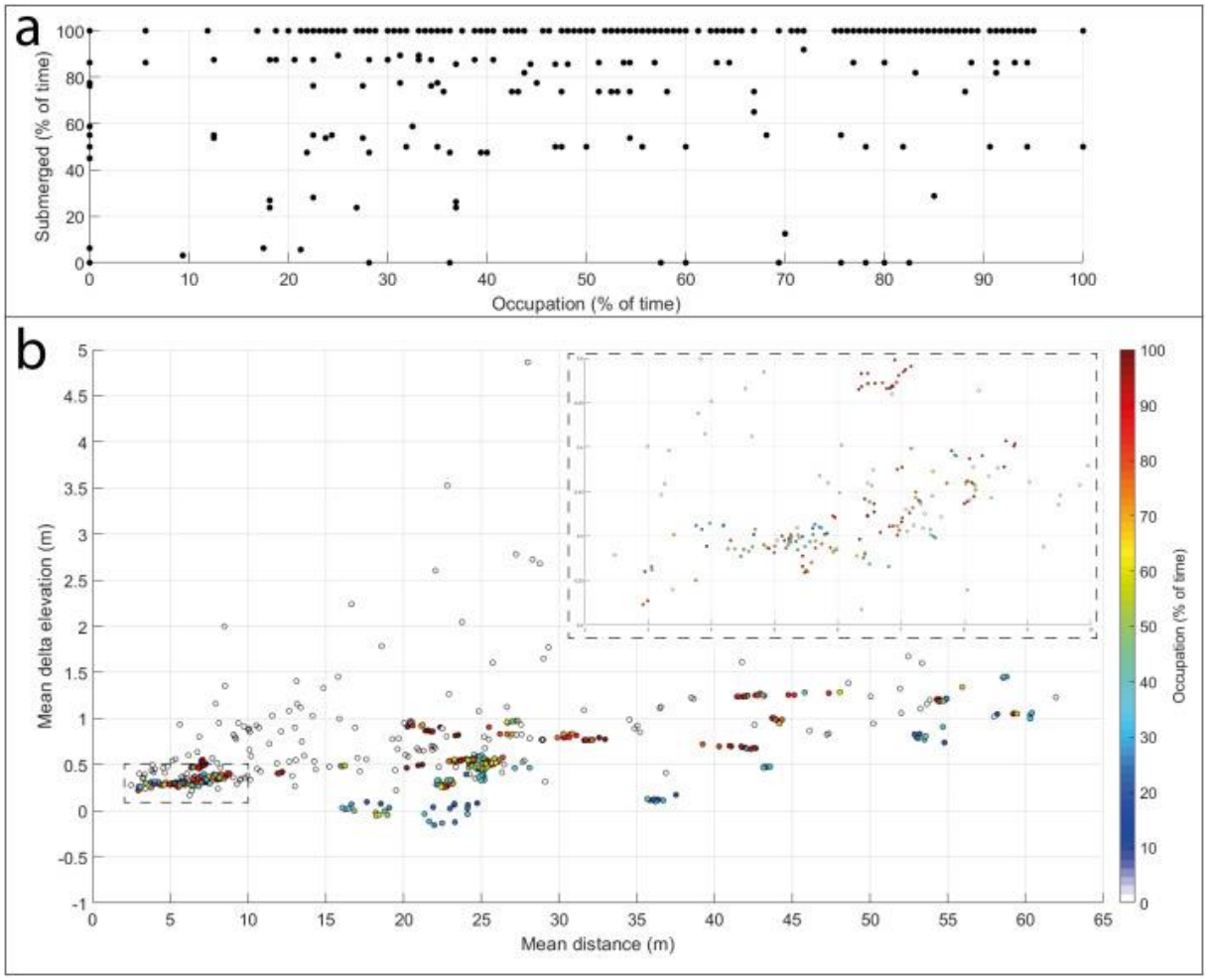

Figure 27: Relationships between a) submergence, occupation and instability for the terrace zone sampling points; b) seasonal mean elevation difference and distance from the closest glacial channel.

4.2.3.3 Temporally resolved periphyton physical habitat

We quantified the temporal evolution of periphyton presence/absence coupled with inundation data and in relation to the daily low/high discharge and braiding index over the entire 2020 melt-season (Figure 28).

Periphyton in the terrace zone (Figure 28a) had typically long periods of growth and survival, and some channel sections were already colonized before the 26th of June (or Julian Day, JD 178). It appeared that several periphyton locations (0–150) disappeared around the end of July (from JD 210); but returned from JD 220. Other periphyton locations (200–400) behaved in a similar way, but for different dates. There were streambed patches with periphyton that were not submerged by clear water during the drone surveys, suggesting daily fluctuations of the tributary water levels and the capability of periphyton to survive short periods of drought. It appeared that the terrace zones were not influenced by variations in the glacial daily low/high discharge (Figure 28d) even though channel desiccation events did occur around JD 223 when ice-melt slowed and discharge began to fall. This could potentially be traced to the

progressive exhaustion of ground-fed and high-altitude snowmelt water sources, which correlates with declining glacier melt.

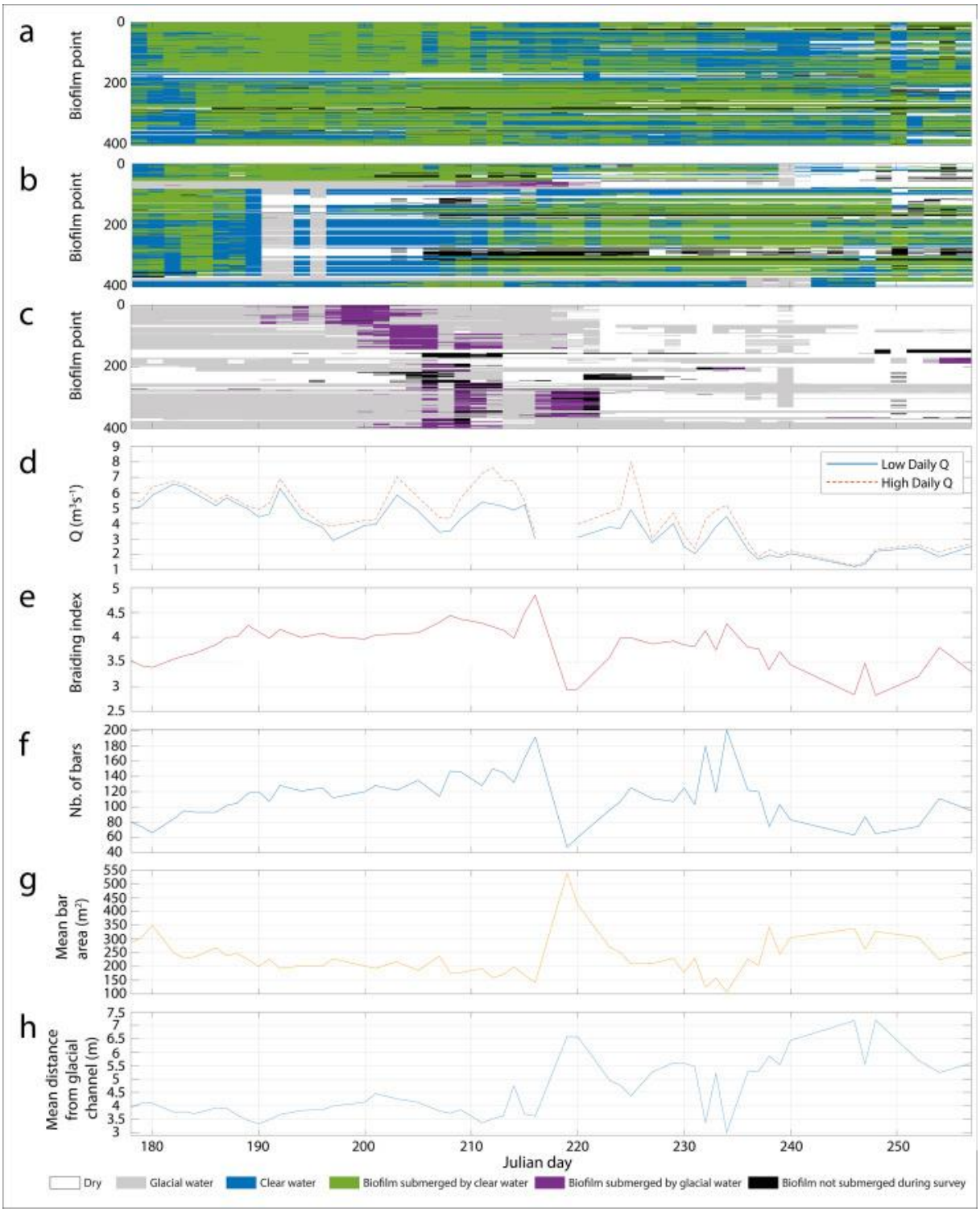

Figure 28: Temporally resolved peripyhton physical habitat within a) terrace, b) buffer and c) active zones; d) Daily low and high Qs (m^3s^{-1}); e) Braiding index; f) Number of bars; g) Mean bar area (m^2); and h) Average distance from bars to glacial channels (m).

The buffer zone (Figure 28b) was more complex compared to the terrace zone. Periphyton locations 0 to 25 lasted for about 60 days. Periphyton were then removed,

notably associated with the intrusion of glacier-originating water around JD 238. Locations 25 to 51 partially disappeared around JD 217 due to desiccation of the channel. Locations 80 to 360 suggested some disturbance by glacial water with the sudden disappearance of most of the periphyton locations around JD 186 and JD 188.

Though the locations were mapped as being clear water during the morning drone survey, we noted that glacial water flooded those surfaces during the daily peak flow events (Figure 28d). Locations 80 to 360 began to recover, notably from JD 210 onwards.

The active zone (Figure 28c) suggested a strong linkage between periphyton presence, glacial water and stream morphodynamics. At the beginning of the survey season (JD 178-190), discharge was high, so was the inundation extent, and braiding was minimal, resulting in wider channels with harsh conditions for periphyton. The majority of periphyton locations developed between JD 190 and JD 220, and all those locations shared the same patterns of accrual and removal by glacial water. Periphyton accrual usually happened after a drop in discharge whilst removal often happened after a discharge increment (Figure 28d). This gives the appearance of short windows of opportunity. During this period of development, the braiding intensity and the bar numbers were at their maximum (Figure 28e, f), whilst the mean bar areas and the average distances of the bars from the glacial channels at their lowest (Figure 8g, h). In this sense, the likelihood of having smaller, shallower, less harsh anabranches that supported periphyton development was higher. We also found periphyton that were not submerged during our low flow drone surveys (e.g., JD 202-225, Figure 28c), suggesting that periphyton were inundated at higher flows within the same day to the extent needed to sustain their development (Figure 28d), but such water was less destructive. Later in the season, from JD 220 onwards, the glacial stream system started to shrink (Figure 28h) turning the previously occupied channels dry and canalizing the bulk of melt-water in a smaller number of braids (Figure 28e). Periphyton development in the active zone stopped during this period.

4.2.4 Discussion

4.2.4.1 Physical environment and periphyton habitat

The physical environment of glacial floodplains is dynamic in summer (Marren, 2005; Heckmann et al., 2016; Bakker et al., 2019), limiting periphyton accrual (Milner and Petts, 1994; Uehlinger et al., 1998, 2002, 2010; Battin et al., 2004; Boix Canadell et al., 2021). Our results support these findings, but also highlight the spatio-temporal heterogeneity of hydraulic-related disturbances and the presence of suitable periphyton habitats beyond tributaries (i.e., krenal and rhithral) and terrace tributaries during the melt-season in summer.

Recently-deglaciated floodplains are drained by various water sources including kryal, krenal and rhithral (Malard et al., 1999; Ward et al., 1999) and shaped by different hydro-geomorphic features including stream braiding (Maizels, 2002; Marren, 2005)

and terraces (Germanoski and Schumm, 1993; Marren, 2002; Marren and Toomath, 2013, Marren and Toomath, 2014; Roussel et al., 2018). Accounting for these different hydrological and hydro-geomorphic features is indeed important when studying the ecological functioning of glacial floodplains. We segmented the floodplain of Otemma into three geographical zones and showed that these each had distinctive periphyton development patterns (Figures 22a and 28) which can be mapped onto both inundation characteristics (Figure 22b) and river instability (Figure 22c).

The importance of access to krenal and rhithral water was clear in our study site with periphyton on the stable terraces concentrated in channels constantly fed by adjacent hillslopes (hypothesis 1). Equally, despite extensive inundation in the active zone, this water was invariably turbid and periphyton only developed significantly where water was very shallow or in braids inundated only at high flows (hypothesis 2). In the active zone, where rates of floodplain reworking were highest (Figure 22c), periphyton were ephemeral (Figure 28c) with low occupation rates (Figure 23d), appearing in short windows when conditions were stable (hypothesis 2). We confirmed a link between these processes and the intensity of river braiding (Figure 28) (hypothesis 2) and in the active zone, windows of opportunity appeared when the river was most braided, so reducing the average distance to (glacial) water and increasing the likelihood that flows were shallow. These windows of opportunity were only of short duration (hypothesis 2; Figure 28c) because of the intensity of disturbance of the active zone (Figure 22c).

Within our study site, we characterize three zones with distinct periphyton dynamics. In the active zone, periphyton accrual is limited in space and time (Figures. 22a, 23a, d, 24 and 28c), and periphyton develop in short windows of opportunity linked to three processes: (i) access to glacial water; (ii) periods of stability; and hence (iii) stream morphodynamics. In the summer of 2020, access to glacial water passed through what appears to be an optimal window (Figure 28). At first, to JD190, inundation by glacial water at low flow was extensive, resulting in channels with harsh conditions due to the high amount of glacially-fed water distributed in a limited number of channels (Figure 28e). From JD 190 onwards, draining of the floodplain caused a rapid increase in bar numbers and area (Figure 28f, g), forming channels that were hydraulically less harsh (Ashmore, 1988; Ashmore et al., 2011), with increased streambed stability and likely shallower (Warburton and Davies, 1994) such that the phototrophically-active radiation could reach the channel bottom. Our results also show that periphyton developed on surfaces that were dry during low flows (Figure 28c), but likely submerged by water during high flows (Figure 28d) such that survival was guaranteed. In this sense, research has demonstrated, notably in Antarctica, that benthic periphyton can survive extended drought periods (McKnight et al., 2007) and remain photosynthetically-active in hours when re-submerged (Hawes and Howard-Williams, 1998). Later in the season (from JD 220), those periphyton areas were reworked such that periphyton eventually were removed. From JD 220 onwards, the river incised, braiding index and the number of bars fell (Figure 28e, f); these areas became almost permanently dry (Figure 28c), and progressively more distant from glacial water (Figure 28h). Periphyton development ceased even though stability increases during this period. Thus, periphyton presence in the active zone is related to

windows of opportunity in the active zone and associated with areas that are periodically and locally less harsh or intermittent and largely morphodynamically stable. As inundation tends towards being permanent so it is more likely to be deeper and faster flowing, slowing periphyton development and increasing the probability of its removal. The result is that there are zones present in the active floodplain that can support periphyton provided that there is some but not too much glacial water supply, but these are spatially-restricted and also dynamic as river morphodynamics can change locally how harsh the water is (water depth; bed shear stress) as well as the ease of access to that water. In the case reported here, a seasonal shift towards less braiding (Figure 28e) eventually increased the average distance from channels containing glacial water and for sites that were not permanently inundated periphyton presence largely ended (Figure 28c). The linkage to braiding implies that wider exogenic drivers of braiding intensity (notably the ratio glacier sediment supply to sediment transport capacity, a function of glacier melt rate) will in turn drive periphyton dynamics in the active zone.

The buffer zone represents one where there is progressively less glacial water intrusion but there is permanent non-glacial water supply. Unlike in the active channel, the permanent availability of clear water means that periphyton presence can approach being perennial (Figure 23b) although not throughout this zone. In the buffer zone, glacial water may intrude clear water channels, periphyton are impacted and their survival reduced (Figure 26) and this is likely due to sudden but sometimes short-lived changes in habitat conditions (i.e., from clear to glacial water) and increased streambed instability (Figure 25a, b). However, periphyton can recover (Figure 28b) within a relatively short time (Battin et al., 2003) if clear water flow resumes. Higher elevations compared to the closest glacial channels (Figure 25c) clearly host higher periphyton occupation in this zone because glacial water intrusion is less common, and probably less destructive. As these zones are more likely to have water, they may become hotspots for eventual primary vegetation succession as long as the magnitude and frequency of disturbance by the glacial stream remains low.

The terrace zone is unimpacted by glacial water. Terraces are common in glacial floodplains (Marren, 2002, 2005; Marren and Toomath, 2013, 2014; Roussel et al., 2018) due to systematic shifts in the balance between glacial sediment supply and sediment transport capacity. Terraces commonly form when capacity exceeds supply and this matters in terms of stability. The disconnection (Figure 27b) from the glacial stream leads to a stable habitat that is never (i.e., the case of summer 2020) or very rarely inundated by glacial water. In theory, the lack of access to glacial water becomes a limit and it makes periphyton colonization in this zone highly-dependent on snow-melt or groundwater-fed streams (Malard et al., 1999; Ward et al., 1999). Such water is substantially less harsh and periphyton development is enhanced due to water transparency and overall hydrological, hydraulic and thermal stability (Boix Canadell et al., 2021); but it is also spatially restricted leading to periphyton development that is localized (Figure 22a) to the streams that cross this zone. In such areas, we find the highest rates of periphyton coverage (Figure 23a, d) with the highest occupation days (Figure 22a; Roncoroni et al., 2022) compared to the buffer and active zones. Our results (Figure 28a) also suggest a periodic renewal of periphyton mats, followed by

rapid re-colonization of the streambed. That said, there are other potential disturbances to periphyton habitats in this zone. Progressive snow-melt decline, which may also cause a decline in shallow groundwater if it is also snow-melt fed, causes desiccation events to become more common from August onwards (Figure 28a), tracking the contraction of the stream system at the end of the melt-season (Malard et al., 1999). Roncoroni et al. (2022) found that the terraces of the Otemma glacier floodplain were almost dry during late autumn and periphyton were restricted to the active zone where disturbance had reduced (i.e., window of opportunity; Uehlinger et al., 2002, 2010) and glacial water had much lower suspended sediment concentrations and so was much less harsh.

4.2.4.2 Implications for ecosystem engineering

Our results further demonstrate the strong control of the physical habitat template on periphyton accrual, survival and removal. Water accessibility is central in supporting periphyton development (Rydgren et al., 2014), but large amounts of water lead to high shear stresses, notably from ice-melt, and so can become destructive. In this sense, the active zone has the highest annual water availability, but this water provides harsh and unstable conditions. Periods between two disturbances are often so short that periphyton cannot develop or reach a state of maturity (Thom et al., 2015). The negative effect of glacial water is accentuated in the buffer zone where more generalist periphyton are likely to develop. Glacial water intrusion in clear water channels results in sudden habitat changes that, depending on the length of the events, could lead to periphyton removal. Our results suggest that glacial water – and hence the associated high shear stresses, bed and suspended loads – shapes the ecological functioning of glacial floodplains by creating a disturbance-dominated regime that results in an ephemeralisation of the periphyton habitat. Active and buffer zones should indeed be regarded as ephemeral habitats, where periphyton may only develop in specific, short windows and zones of opportunity within the melt-season (hypothesis 3).

On the other hand, tributaries on disconnected terraces that are rarely if never inundated by glacial water should be considered as perennial habitats during the melt-season (hypothesis 3) due to higher algal biomass (Brandani et al., 2022) and long survival periods (Roncoroni et al., 2022). These perennial habitats are stable, drained by clear water (Boix Canadell et al., 2021) and are also enriched in dissolved organic matter (Brandani et al., 2022).

Different studies consider periphyton as ecosystem engineering agents (Gerbersdorf et al., 2008a, 2009b), even in glacial floodplains (Miller and Lane, 2019; Roncoroni et al., 2019). In glacial floodplains, benthic periphyton are thought to fertilize the nutrient-deprived glaciogenic sediments, maintain the water at the surface by creating an impermeable layer at the streambed surface and, to a smaller extent, stabilize streambed sediments (Miller and Lane, 2019; Roncoroni et al., 2019). Such engineering effects are supposed to promote primary succession and to explain patterns of succession that do not follow the chronosequences of Matthews (1992).

Our results suggest that ecosystem engineering likely only occurs in perennial habitats, which support long-term periphyton during the melt-season, also when vegetation can grow at such high altitudes. On the contrary, ephemeral habitats might hold the highest cumulative biomasses (especially during windows of opportunity; Uehlinger et al., 2002, 2010), but the positive feedbacks associated with periphyton growth are likely to reset on periodic bases without influencing positively vegetation development over the long-term.

4.2.5 Conclusions

In this paper, we decrypted the periphyton physical habitat in a recently deglaciated floodplain; and we did this at high temporal and spatial resolutions. We formulated three hypotheses: (i) the simultaneous presence of krenal and rhithral channels over terraces favours the development of periphyton in those zones; (ii) intense stream braiding creates short windows of opportunity; and (iii) periphyton development at the floodplain scale is the net result of the above-mentioned hypothesis and this result matters in terms of ecosystem engineering.

In agreement with the literature (Uehlinger et al., 1998; Ward et al., 1998), we highlighted the importance of krenal and rhithral channels as being hot spots for periphyton but we also demonstrated the importance of channel location. However, krenal and rhithral channels are hot spots only if they flow over terraces. If such channels flow at lower floodplain elevations, they are prone to be inundated by glacial water (i.e., the buffer zone) resulting in harmful effects for periphyton. We also demonstrated that stream morphodynamics (i.e., braiding) have the potential to create zones of ephemeral stability. We demonstrated that when braiding intensity is high, some braids become less harsh so that periphyton may rapidly develop. Equally, we demonstrated that such braids are rapidly cut off by stream dynamics, resulting in periodic periphyton reset. Finally, our results suggest that systematic variation in periphyton presence/absence is strongest laterally rather than longitudinally, and the role of periphyton in driving ecosystem succession following deglaciation is likely concentrated in hotspots where access to water is associated with non-glacial and thus non-harsh conditions, itself related to the heterogeneous assemblage of disturbances in space and time.

Although we find glacial floodplains with similar stream morphodynamics throughout the Alps, and beyond, our results are contextualised to a single system, the Otemma floodplain. We acknowledge this, and we highlight that a more comprehensive understanding of the periphyton physical habitat of recently deglaciated floodplains must require new studies in floodplains with different characteristics (e.g., slope, glacial extent, orientation, discharge, etc.).

4.3 Chapter summary

This Chapter provided a spatio-temporal quantification of the physical habitat of periphyton in recently-deglaciated Alpine floodplains. It decrypted the physical habitat

by combining the results of Chapter 3 with an analysis of the hydro- and morpho-dynamics of an Alpine proglacial floodplain system.

The results show that periphyton development in a proglacial floodplain is controlled by habitat stability, and water access. Furthermore, the results suggest that a proglacial margin can be divided into geographical zones (i.e., terrace, buffer, and active zones), each characterized by its own hydro- and morphodynamic features, and this is then reflected in zone-specific patterns of periphyton development. The terrace zone is the most stable area of the floodplain, and if drained by krenal-fed and rhithral-fed channels it is a hotspot for periphyton. Such channels are found in the buffer zone as well, but the lower elevations of this zone make those channel prone to glacial water intrusion and hence disturbances. Within the active zone, disturbances are common and periphyton development limited to periods when braiding is intense. In this zone, periphyton development remains ephemeral.

These results suggest there is a potential contribution of periphyton to ecosystem engineering. Miller and Lane (2019) and Chapter 2 suggested that periphyton may engineer the environment of proglacial floodplains, mainly by reducing the water vertical infiltration and the susceptibility of the substrate to being eroded. The results of this section demonstrate that terraces, if drained by krenal-fed and rhithral-fed channels, are hotspots for periphyton. Therefore, the positive feedback associated with periphyton, if that effectively exists, is likely to be restricted to those stable zones where periphyton can develop perennially during the growth season. What the Chapter has not been able to do is to provide mechanistic evidence of the rate and intensity of such processes. This is the goal of Chapter 5.

Chapter 5: Ecosystem engineering by periphyton in Alpine proglacial streams

5.1 Chapter overview

The findings of Chapter 4 emphasized that the investigation of the possible effects of ecosystem engineering should focus on the channels that drain terraces because they allow periphyton to reach a perennial state of development. This section therefore attempts to provide the first quantitative evidence of how periphyton engineer the environment of the terraced zones of glacial floodplains. The study is based on a set of outdoor flume experiments that were run on the vicinity of the forefield of the Glacier d'Otemma. The section attempts to answer the third question of this PhD thesis that is "*what are the mechanisms, rates and time-scales associated with these patterns and how does the development of periphyton feed back into glacial forefield habitability?*". Chapter 5 has been submitted to the journal *Earth Surface Processes and Landforms*, and it is currently in peer-review as: Roncoroni, M., Ballu, M., Selitaj, A., Mancini, D., Miesen, F., Aguet, M., Battin, T.J., Lane, S.N. (in review). Ecosystem engineering by periphyton in Alpine proglacial streams. *Earth Surface Processes and Landforms.*

5.2 Ecosystem engineering by periphyton in Alpine proglacial streams

5.2.1 Introduction

Stream periphyton are implicated in multiple ecosystem processes such as carbon fluxes and nutrient uptake/recycling (Battin et al., 2003a, 2016). Recently, they have been included as ecosystem engineers (Gerbersdorf et al., 2008a, 2009b; Roncoroni et al., 2019). Periphyton are thought to have three broad potential engineering impacts. First, they may stabilize sediments by increasing the critical bed shear stress T_{oc} required for sediment movement (Neumeier et al., 2006; Le Hir et al., 2007; Gerbersdorf et al., 2008b, 2009a; Vignaga et al., 2013; Fang et al., 2014; Thom et al., 2015; Pivato et al., 2019). The secretion of EPS leads to physical binding of and/or molecular electrochemical interactions between substrate grains (Grant and Gust, 1987; Dade et al., 1990; Tolhurst et al., 2002). This effect appears to be particle-size dependent, more effective for finer grains (Statzner et al., 1999) and a function of both seasonality (Widdows et al., 2000; Amos et al., 2004; Thom et al., 2015; Schmidt et al., 2016; Pivato et al., 2019), and periphyton growth history (Mariotti and Fagherazzi, 2012).

Second, periphyton may modify near bed hydrodynamics through their effects on the micro-morphology of the river bed surface (Nikora et al., 1997, 2002; Fang et al., 2014; Kazemifar et al., 2021). Periphyton development may decrease (Labiod et al., 2007) or increase (Nikora et al., 1997; Piqué et al., 2016) bed roughness, but also decrease porosity by filling particle pores (Kazemifar et al., 2021). Such phenomena could ultimately dampen, in the case of reduced roughness and porosity, or enhance, in the case of increased roughness, near-bed Reynolds shear stresses (Breugem et

al., 2006; Suga et al., 2010; Kazemifar et al., 2021). Decomposition of the Reynolds shear stress into bursting processes (i.e., outward interactions, ejections, inward interactions, and sweeps) (Nelson et al., 1995) may be important because. Bursting processes, and particularly sweep and ejection events, play an active role in sediment entrainment and transport (Thorne et al., 1989; Bennett and Best, 1995; Wu and Jiang, 2007; Paiement-Paradis et al., 2011; Mianaei and Keshavarzi, 2010; Dwivedi et al., 2011; Keylock et al., 2014). Periphyton development may either attenuate or enhance such processes and so impact particle movement and river- bed stability.

Changes in critical bed shear stress and turbulence intensity could may impact biostabilization. It appears that biostabilization is more efficient in marine/tidal environments (Spears et al., 2008; Flemming and Wingender, 2010; Gerbersdorf and Wieprecht, 2015). This is partly to the chemistry of seawater which aids cohesive processes but also due to finer sediment. Biostabilization has been documented in rivers (Thom et al., 2015; Schmidt et al., 2016), but the coarser sediment composition may limit periphyton contribution. To date, it has not been investigated extensively in proglacial margin streams.

The third engineering impact may occur in parallel to biostabilization. By binding particles with EPS and filling particle pores, periphyton may clog streambed interstices (Battin and Sengschmitt, 1999; Gette-Bouvarot et al., 2014). Bed clogging reduces hyporheic exchanges between the sediment surface and sub-surface interface (Ibisch and Borchardt, 2002). The result is reduced vertical hydraulic conductivity of the sediments and hence reduced vertical water infiltration (Ragusa et al., 1994; Cunningham et al., 1991; Thullner et al., 2002; Gette-Bouvarot et al., 2014; Caruso et al., 2017). This process may be particularly important in proglacial margins as glacial sediments are commonly well-drained (Cooper, 1923; Matthews, 1992; Burga et al., 2010; Viles, 2012). Recent work (Miller and Lane, 2019; Roncoroni et al., 2019) has argued that that periphyton may trigger a positive feedback in which their development promotes surface water retention so that pioneer vegetation can have a benefit.

As yet, there are no quantitative studies on the combined effects of periphyton development on biostabilization and infiltration in proglacial margins, despite reviews that suggest its potential importance (Miller and Lane, 2019; Roncoroni et al., 2019). We fill this gap by running a set of outdoor flume experiments that reproduce the conditions found in stable proglacial margins where biofilms can develop (Roncoroni et al., 2023). We test the following hypothesis. First, the streambed surficial morphology evolves in response to periphyton development. Grains are rapidly coated by biomass, the benthic interstices filled and the bed roughness reduced (H1a). If disturbances are introduced, we hypothesized that the bed tends to return to a pre-colonized situation, thus rougher (H1b). Second, the changes in bed roughness modify the turbulent structures in the near-bed layer, and the bursting events and the turbulent kinetic energy are likely reduced (H2a). The introduction of disturbances should change the near-bed hydraulics, as a response to the changes in bed roughness (H2b). Third, by filling the streambed interstices, periphyton reduces water vertical infiltration so that more water can be maintained more readily at the surface (H3a). However, we hypothesize that when disturbances are introduced, the periphyton effect on infiltration

is partly cancelled (H3b) and this is due to the changes in bed morphology induced by the dry conditions.

5.2.2 Methods

5.2.2.1 Flume and experiment setups

In order to consider periphyton development in the geographical setting of a natural proglacial margin, we installed two parallel flumes (Fig. 1a, FA and FB) in the vicinity of the forefield of the Otemma Glacier (45°56'04.9"N 7°24'46.1"E) We designed the flumes to mimic the hydraulic and environmental conditions of the tributaries found on the Otemma floodplain (Roncoroni et al., 2023) and without any kind of spatial scaling. In the experiments we wanted to reproduce conditions of water transparency, hydrological and thermal stability, depth, natural lighting, and slope. For the first part of the experiment, both flumes were run with identical conditions to assess reproducibility; they diverged for the second part of the experiment when artificial drying events were introduced into FA. The experiment lasted in full for 54 days from July 14 (JD195) to September 6 (JD249) 2021. In experiment FA after 28 days of constant discharge we introduced disturbances, desiccation events, comprising: (1) a single day of dry conditions, followed by two days of submergence; (2) two days of dry conditions, followed by 3 days of submergence; (3) three days of dry conditions, followed by six days of submergence; and (4) seven days of dry conditions, followed by two days of submergence. In experiment FB, no disturbance was introduced.

The flume structure and components were built in the field. We connected a tank (~1000 liters) to a hillslope tributary, and filled this tank solely by gravity. The tank had two security pipes intended to maintain a constant hydraulic head through time (Figure 29b, c). At the bottom of the tank we connected a T-shape pipe with two adjustable valves (one per flume; Figure 29a-c). The water was discharged into two attenuation tanks (Figure 29c) which reduced water turbulence at the flume entrances. Water entered two trapezoidal flumes made of polyvinyl chloride (PVC), and sustained by wooded supports and a metal scaffold. Additionally, each flume exterior was equipped with 10 wooden ground control points (GCPs) (Figure 29a) for photogrammetric purposes.

The flumes were 4 m long, and 0.3 m wide at the (Figure 29b, c). Longitudinally in each flume there were three sections; the first was 1 m long and aimed to allow for flow adaptation to the channels; the second was 2 m long. It has a PVC base that was 7 cm lower than the first section to create a sediment chamber. We packed the bed of each chamber with clean sediment sieved at 0.8-1.6 cm to a thickness of 7 cm. At the end of each chamber, three buried aluminum pipes (Ø 7 mm) collected water after vertical infiltration through the sediments for measuring the evolution in infiltration. The third section was 1 m long, and intended to avoid flow recirculation over the sediments due to the weirs at the downstream end of each flume (Figure 29d). The weir allowed water depth to be constant at ~11.5 cm through time in each flume. The discharge in

each flume was ~2 ls^{-1}. The overall slope of the flumes was set to 0°. An overview of the experiment initial conditions is presented in Table 8.

Table 8: Initial experiment conditions for both FA and FB.

Flow rate (l/s)	~2
Horizontal mean velocity (m/s)	0.05
Mean depth (m)	0.115
Bottom width (m)	0.3
Slope (°)	0
Reynolds number Re	4056.5
Froude number Fr	0.045
Grainsize range (cm)	0.8 – 1.6

5.2.2.2 Infiltration measurements

We collected the water flowing out of the aluminum pipes (Figure 29c) every day at 8:00 am for FA (except when the flume was dry), and at 8:15 am for FB. For both flumes, we recorded the time to fill a 500ml bottle, weighed the content with a high precision scale, and repeated the procedure 10 times to reduce measuring bias. The daily infiltration rate was obtained by averaging the 10 measures.

5.2.2.3 Photogrammetry and DEM correction

We collected daily images of the flumes for photogrammetric analysis. We used a DSLR Sony Alpha 7 III camera equipped with a Sigma Art 50mm F1.8 lens. Image acquisition took place in the afternoon to get the most homogenous light conditions, and produced an average of 300 pictures (JPEG format) per flume per date of acquisition. The images were acquired manually by the operator who moved along the flume sides several times to ensure sufficient lateral and frontal overlap. The pictures were taken with F-stop set to 11, shutter speed set to 1/1000, ISO set to between 16000 and 20000, and a wide automatic focus. In addition to the pictures, we acquired the absolute position of 20 GCPs (10 per flume, see Figure 29a) with a differential GPS Trimble R10. GCPs were collected to rotate, scale, and translate the photogrammetric products into a real world coordinate system (i.e., CH1903 LV03) and to aid in reducing systematic deformations (Chandler et al., 2001; Butler et al., 2002; Leduc et al., 2019; James et al., 2017, 2020).

The images were processed through Structure-from-Motion Multi-View-Stereo (SfM-MVS) photogrammetry (e.g., Westoby et al., 2012, James and Robson, 2014; James et al., 2017, 2020). We processed the images in Agisoft Metashape (v. 1.5.5) run on a dedicated workstation equipped with an AMD Ryzen 12-core processor (3.80 Ghz), 64 Gb RAM, and a GeForce RTX 2080 (8 Gb) graphic card. For each set of flume images, the processing was divided into three stages. First, we aligned the images by setting the key point and tie point limits to 40’000 and 4’000 respectively. We then cleaned the sparse point cloud by removing erroneous 3D points (James et al., 2020). Second, we included the GCPs and re-fitted the 3D surface through a bundle adjustment that accounted for focal length, principal point offset (Cx, Cy), radial (K1,

K2, K3) and decentering (P1, P2) distortions. Third, we generated a dense point cloud (ultra-high quality and mild depth filtering), and then interpolated a DEM to 0.0005 m.

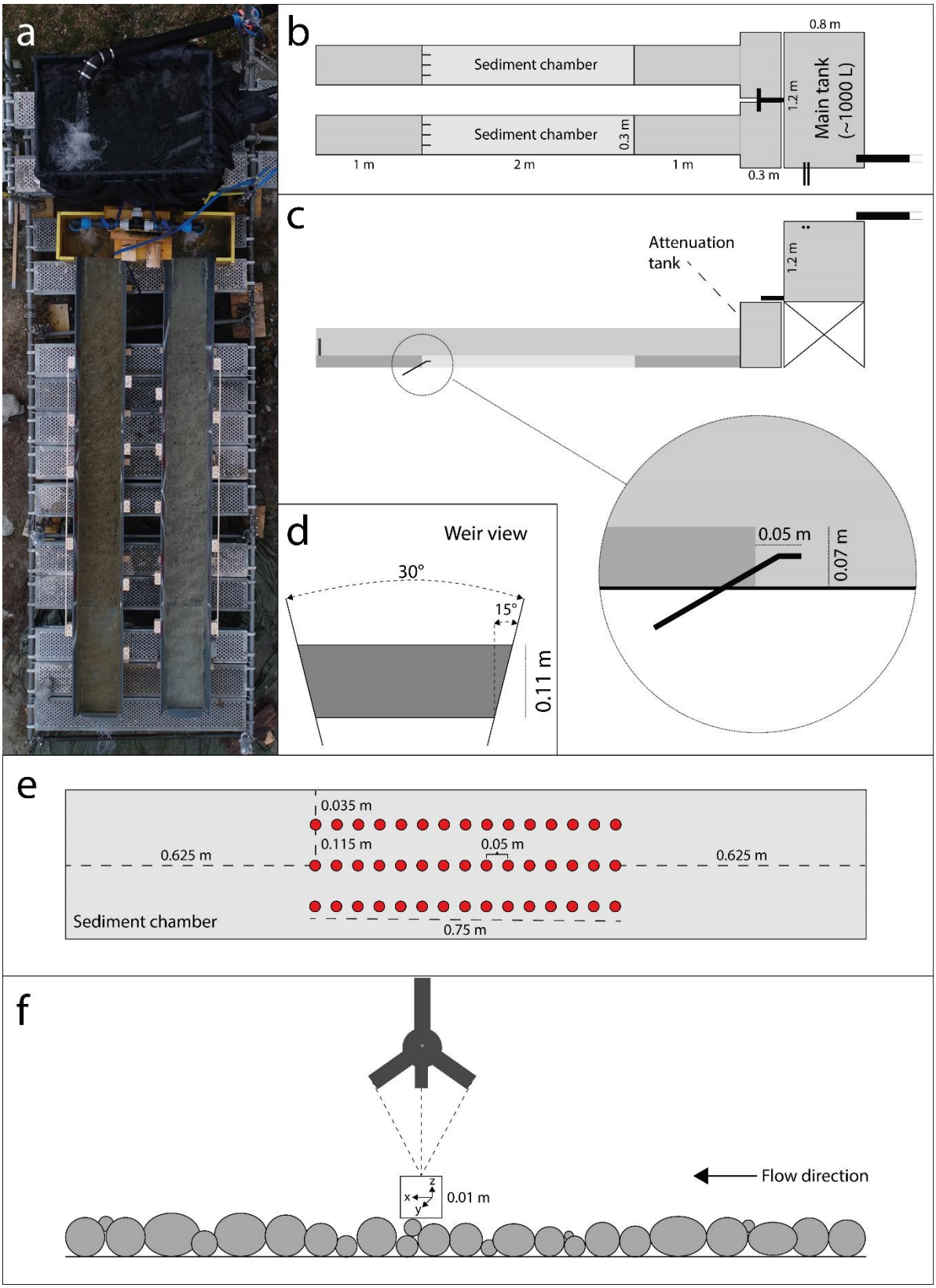

Figure 29: Flume experiment setup. a) Aerial image of the flume setup; b) Top-view; c) Lateral view, and zoom of the grasping pipe; d) Weir view; e) ADV sampling locations; f) ADV measurement domain.

Obtaining independent validation data was a challenge at the resolution of this study in a field-based experiment. As we were interested in comparing DEMs through time, we therefore decided to make use of the fact that the dry, non-sediment zones of the flume should not change through time and compare every DEM to an initial reference DEM (acquired on July 15 or JD196, for both flumes). For each flume, we selected 200 checkpoints and extracted their elevations. The error was calculated by subtracting the DEM elevations from the reference DEM elevations. We computed the mean error and standard deviation of errors, and we plotted those values in respect of the X and Y coordinates. Our results suggested low-magnitude systematic deformations in the form of doming (see James and Robson, 2014). Similarly to Bakker et al. (2019) and Mancini and Lane (2020), we attempted to model the deformation, and subsequently remove it. Here, we applied a quadratic polynomial model to the X and Y coordinates. We did this in Matlab (R2021b). This produced a date and flume specific correction DEM that was then removed from the original DEM to obtain a DEM free of systematic deformation. We assessed the quality of the correction with 200 additional checkpoints.

As the DEMs were impacted by the effect of refraction at the air-water interface (Fryer and Kniest, 1985; Westaway et al., 2000, 2001; Woodget et al., 2015; Dietrich, 2017) we performed a bathymetric correction following Westaway et al. (2000, 2001). We interpolated the water surface elevations via a linear interpolation in GIS (ArcMap v.10.5.1). In Matlab (R2021b), we subtracted the DEM elevations from the water surface elevations obtaining the apparent depths. The apparent depths were multiplied by the refractive index of water (here 1.337, Harvey et al., 1998), and true depths calculated. The quality of the bathymetric correction was assessed by comparing the depths of a further 68 checkpoints with the reference.

5.2.2.4 DEM analysis

After correction, we had 38 DEMs for FA and 39 for FB. We analyzed our DEMs to gain insights into roughness evolution and benthic interstice filling through time. In Matlab (R2021b), we used a linear polynomial surface fit to detrend our DEMs and remove planar bedforms (Bertin et al., 2017), and extracted the DEM portion for the sediment chambers. We calculated the standard deviation of bed elevations (i.e., surface roughness; Aberle and Smart, 2003; Smart et al., 2004) by using a moving window of 100 pixels (i.e. 0.0025 m^2). This window was designed to be about 2 to 4 times the mean grain diameter and to pick up changes in surface roughness at the scale of small grain clusters. For each DEM (i.e., date), we then averaged the windowed standard deviations to obtain the mean roughness at the sediment chamber scale. Finally, we investigated the filling of benthic interstices by quantifying the elevation lows, considering the 90^{th} percentile and the 85^{th} and 95^{th} percentile range of DEMs.

5.2.2.5 Hydraulic data collection, processing and analysis

We investigated the evolution of the near-bed hydraulics of FA and FB. We tracked the hydraulics of FA for 12 dates (from JD197 to JD238), and FB for 13 dates (from JD197 to JD245). We collected the 3D components of the flow velocities with an Acoustic Doppler Velocimeter (ADV), the Nortket Vectrino (VCN9421), supported by a sliding aluminum structure that allowed us to relocate the ADV precisely within the flumes. We sampled the 3D velocities of 45 points (Figure 29e), and we did this for the near-bed layer at 1 cm from the flume bottom (Figure 29f). The sampling points were divided in three parallel lines (15 points each), located at the center of the sediment chamber and sufficiently away from the flume walls to avoid wall hydraulic interference (Figure 29e). Each sampling point was measured for 60 seconds at a sampling rate of 25 Hz. The data were stored in .dat format, and subsequently treated and analyzed in Matlab (R2021b).

ADV time-series commonly contain two types of noise that have to be removed in order to obtain reliable estimates; those caused by Doppler noise; and those caused by aliasing (Cea et al., 2007). Research has shown that these effects tend to be greatest in the velocity components in the plane tangential to the ADV axis, in situations that are more turbulent, and in the presence of air bubbles (Nikora and Goring, 1998). They lead to inflated estimates of turbulence parameters (such as turbulent kinetic energy) and modify the power spectrum notably at higher frequencies (Cea et al., 2007). The most extreme manifestation of their effects is isolated spikes in velocity time-series. Visual interpretation suggested that spikes were occasionally present. Thus, we undertook spike removal. This was based upon Goring and Nikora (2002) and Cea et al. (2007). The first derivation of a velocity signal enhances high frequency components (Cea et al., 2007) and may suggest physically implausible flow accelerations and decelerations. Goring and Nikora (2002) proposed that the maximum acceleration/deceleration should be of the same order of magnitude as gravity acceleration, g and that an acceleration/deceleration criterion could be used to identify implausible instantaneous velocity values or spikes. Acceleration for velocity component x at time *i* ($a_{x,i}$) is defined as:

$$a_{x,i} = \frac{u_{x,i} - u_{x,i-1}}{\Delta t} \quad [4]$$

where $u_{x,i}$ is the instantaneous velocity at time *t*. Goring and Nikora (2002) then identified as a spike for point in the time-series that satisfied either of the following criteria

$$a_{x,i} > k_g g \text{ and } u_i > \bar{u} + k_\sigma \sigma_u$$
$$a_{x,i} < -k_g g \text{ and } u_i < \bar{u} - k_\sigma \sigma_u \quad [5]$$

where k_g is a contant and σ is the standard deviation. Goring and Nikora (2002) proposed a value of k_g between 1 and 2 based upon experience. Cea et al. (2007)

modified this approach in two ways. First, they proposed different values of k_g for each component. Second, they proposed a more objective means of determining them by using the theoretical result of Donoho and Johnstone (1994) that for the expected maximum (λ) of N independent, normally-distributed, random variables, with zero mean and standard deviation σ can be defined as

$$\lambda = \sqrt{2\ln(N)} \quad [6]$$

Cea et al. (2007) then defined the values of k_g using:

$$k_{g,x} = \frac{\lambda \sigma_{a,x}}{g} \quad [7]$$

Cea et al. (2007) showed that the effects of k_σ in [5] were primarily to increase the proportion of the data that are filtered with respect to the value of k_σ that is chosen but they found relatively low sensitivity to k_σ and so ignored the right-hand terms in [5]. Thus, we applied the Cea et al. (2007) method. To check that the conclusions of Cea et al. (2007) applied to our data, we identified time series with abnormally high values of σ_u, σ_v, and σ_w compared with surrounding data and applied the modified form of [5]. In almost all cases, the time-series showed clear spikes; and a single application of [5] removed them. However, in a small number of cases there were spikes for adjacent times and the method tended to leave a single spike. Thus, we iterated the approach by removing spikes in the first iteration, recalculating the acceleration and then applying it a second time. Calculation of the spectral density function for those time-series tested showed that spike removal recovered the expected Kolmogorov scaling (i.e. a -5/3 slope between the spectral power and frequency).

Two issues may remain after spike removal. The first is how to replace those measurements identified as spikes. The second is that estimates derived from the time-series contain noise and estimates derived from the time-series need to be corrected for this (Voulgaris and Trowbridge, 1998; Blanckaert and Lemmin, 2006; Thomas et al., 2017)

First, following Cea et al. (2007), we did not interpolate values of velocity (or replace them with zero values) for those data points removed as spikes as we are interested in quantifying turbulent kinetic energy and the turbulent Reynolds stress tensor. These do not rely on time-dependent calculations but instantaneous values. Provided the number of spikes is small or the statistical distribution of true velocities labelled as spikes is similar to that of the full time-series, these parameters should not be biased.

Second, once spikes were removed, we used noise estimation methods after Thomas et al. (2017) which build on the fact that the ADV provides four beam velocities, duplicating the vertical components to give w_1 and w_2. Thomas et al. (2017) show that with a calibrated ADV probe and hence knowledge of the beam angles it is possible to determine how noise is propagated into both variance (i.e., $\overline{uv}$, $\overline{uw}$,$\overline{vw}$) and

covariance (i.e., $\overline{u^2}$, $\overline{v^2}$, $\overline{w^2}$) estimates and then to correct for it. This is important as the variance estimates are used to calculate the total turbulent kinetic energy and the variance and covariance estimates to calculate the turbulent Reynolds stress tensor. Following Thomas et al. (2017) we used the calibrated transformation matrix T provided by Nortek for our Vectrino. We calculated the sums of the cross-multiplied matrix elements to yield the noise multipliers for each variance and covariance measure. We combined these with the error in the variance between components w_1 and w_2 to remove the likely noise in each variance and covariance measure. As Thomas et al. (2017) found, the errors in the variance and covariance measures for the horizontal components were commonly larger than those for the other measures.

For the processed data for each ADV time-series, we extracted the Reynolds stress tensor; determined the turbulent kinetic energy; and undertook a quadrant analysis. The Reynolds stress tensor was defined as

$$\rho \begin{pmatrix} \overline{u'^2} & \overline{u'v'} & \overline{u'w'} \\ & \overline{v'^2} & \overline{v'w'} \\ & & \overline{w'^2} \end{pmatrix} \quad [8]$$

We defined *w*' by taking the average of the two vertical components *w*, then removing the mean to get *w*'. The turbulent kinetic energy, *k*, was defined as

$$k = \frac{1}{2}\left(\overline{u'^2} + \overline{v'^2} + \overline{w'^2}\right) \quad [9]$$

Research into the linkages between turbulent velocity fluctuations and sediment transport has emphasised the importance of interactions between horizontally and vertically directed flow accelerations and decelerations (e.g., Bennett and Best, 1995; Wu and Jiang, 2007; Paiement-Paradis et al., 2011; Dwivedi et al., 2011; Keylock et al., 2014). These can be represented as quadrants

$$\begin{aligned} &\text{Outward interactions} && [v'_h > 0] \cap [w' > 0] \cap \left[|v'_h w'| > H\sigma_{v'h}\sigma_w\right] \\ &\text{Ejections} && [v'_h < 0] \cap [w' > 0] \cap \left[|v'_h w'| > H\sigma_{v'h}\sigma_w\right] \\ &\text{Sweeps} && [v'_h > 0] \cap [w' < 0] \cap \left[|v'_h w'| > H\sigma_{v'h}\sigma_w\right] \\ &\text{Inward interactions} && [v'_h < 0] \cap [w' < 0] \cap \left[|v'_h w'| > H\sigma_{v'h}\sigma_w\right] \end{aligned} \quad [10]$$

where v_h is the horizontal velocity and *H* is the multiplier used to define significant events, taken here as 1 (Nezu and Nakagawa, 1993). This is a two-dimensional analysis. In a strongly three-dimensional flow it may be important to consider the two horizontal components of velocity (*u* and *v*) separately in an octant analysis (e.g., Keylock et al., 2014). However, in the straight flumes considered here, we determine a single component of horizontal velocity from $(u^2 + v^2)^{0.5}$ and determine v'_h from $v_h - \overline{v_h}$.

As the focus of our work was to quantify the long-term-evolution ecosystem engineering impacts of periphyton development, we present these data in the same way as the infiltration and streambed evolution experiments, focusing on their evolution through time at the scale of the experimental channels rather than the within-channel spatial patterns. We also undertake statistical comparisons of these distributions through time to quantify significant differences.

5.2.3 Results

5.2.3.1 DEM quality

We attempted to correct for the systematic deformations in our DEMs and for the effects of refraction at the air-water interface. Overall, our approach was able to reduce the mean errors (Figure 30a) in FA DEMs, producing DEMs without further evidence of systematic deformations (residual mean errors ranging from -0.001 to 0.001 m), except for JD217. Our approach also reduced the standard deviations of error (Figure 30b), though these reductions were less pronounced as compared to the means. The bathymetric corrections strongly reduced the mean errors (Figure 30c), but not the standard deviations (Figure 30d) that tended to increase after the correction. Based on our statistical analysis and visual inspection of our DEMs, we decided to flag as being of poor quality the FA DEMs of JD204, JD209, JD215, JD218, and JD231.

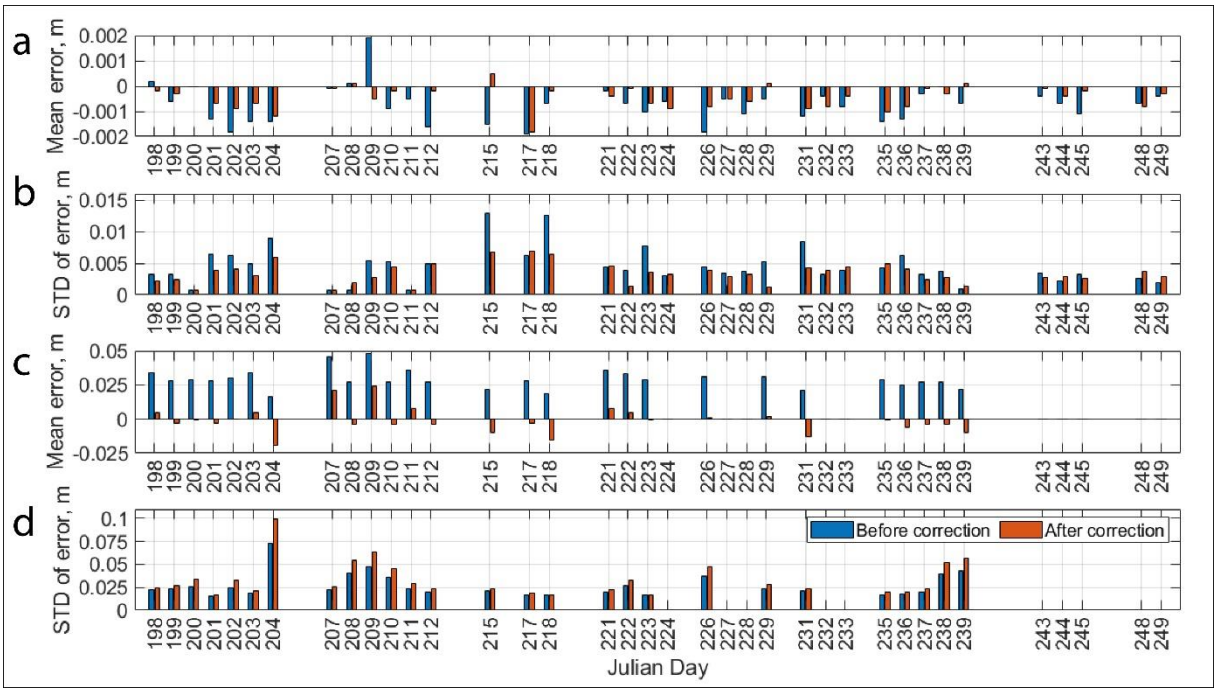

Figure 30: FA DEM quality in respect of the reference DEM (JD196), before and after systematic error and bathymetry corrections. a) Mean error before and after systematic error removal; b) Standard deviation of error before and after systematic error removal; c) Mean error before and after bathymetric correction; d) Standard deviation of error before and after bathymetric correction.

Similarly to FA DEMs, the mean errors in FB DEMs (Figure 31a) were reduced to within the range -0.001 to 0.001 m by correction, suggesting a successful removal of systematic deformations. The standard deviations of error (Figure 31b) were reduced, but this reduction was again less pronounced. As with the FA DEMs, the bathymetric correction reduced the mean errors in FB DEMs (Figure 31c), but had a minor impact on the standard deviations of error (Figure 31d) that were either enhanced or remained within the range prior to the corrections. Based on our statistical analysis and visual inspection of our DEMs, we decided to consider the DEMs of JD199, JD204, JD206, JD207, JD215, JD220, JD223, JD232, JD233 and JD238 as being of poor quality.

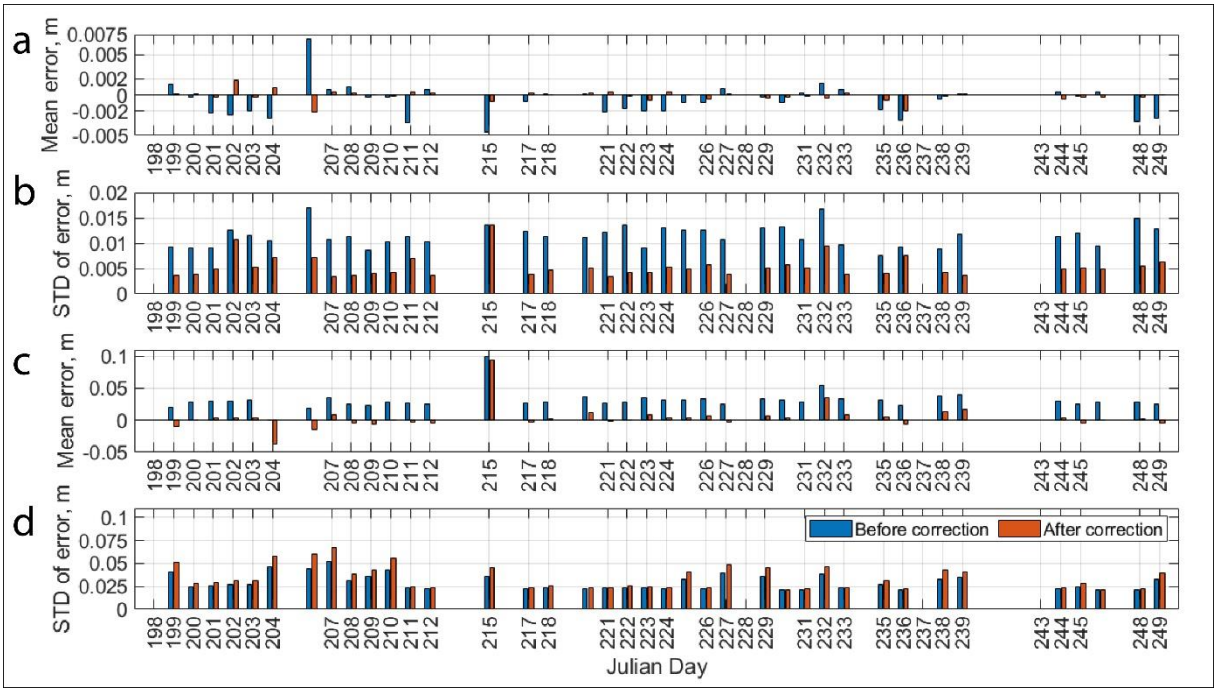

Figure 31: FB DEM quality in respect of the reference DEM (JD196), before and after systematic error and bathymetry corrections. a) Mean error before and after systematic error removal; b) Standard deviation of error before and after systematic error removal; c) Mean error before and after bathymetric correction; d) Standard deviation of error before and after bathymetric correction.

5.2.3.2 Modification of the streambed

Periphyton rapidly developed and covered the streambed of FA and FB (Figures 32 and 33). Between the beginning of the experiment (JD195) and the introduction of disturbances (i.e., JD224), the median roughness (Figures 32a and 33a) significantly (Mann-Kendall: $p < 0.05$) decreased by ~79% in FA (JD196: ± σ = 0.014 m; JD223: ± σ = 0.003 m) and by ~71% in FB (D196: ± σ = 0.017 m; JD222: ± σ = 0.005 m). In both cases, we noted that the roughness lengths substantially decreased until JD210, then entered a phase of quasi-steadiness in which the mean roughness lengths were 0.004 m (± σ = 0 m). During this initial phase, both flumes did not show significant differences in roughness evolution (Kruskal-Wallis: $p > 0.05$). Meantime, periphyton progressively filled the interstices of FA and FB (Figures 32b and 33b), and this was reflected in increases, yet non-significant (Mann-Kendall: $p > 0.05$), of the elevation lows of FA

(JD196, 90th percentile = 2453.66 m; JD223, 90th percentile = 2453.73 m) and of FB (JD196, 90th percentile = 2453.66 m; JD222, 90th percentile = 2453.74 m). Although coherent with the processes investigated, we found these are likely over-estimates, and reflected in differential noise in the data. As per the roughness lengths, during this first phase (i.e., before the disturbances) the flumes did not differ significantly between each other in terms of interstice filling (Kruskal-Wallis: $p > 0.05$).

Surprisingly, the introduction of disturbances in FA (from JD224 onwards) appeared to have little influence on the median roughness lengths (Figure 32a), which instead remained at a quasi-steady value (σ_{mean} = 0.003, ± σ = 0 m) until the end of the experiment. The trend had two exceptions, JD238 (± σ = 0.009 m) and JD239 (± σ = 0.006 m), which had greater median roughness lengths. These exceptions might be related to localized detachments of periphyton (see the upstream part of FA at JD239; Figure 32d), or to fluctuations of the periphyton mat at the time of image acquisition. We cannot exclude differences in DEM noise. The quasi steady pattern of FA was similar in FB (Figure 33a; σ_{mean} = 0.003, ± σ = 0 m) and we did not find significant differences (Kruskal-Wallis: $p > 0.05$) between the flumes. However, the results showed that FB experienced low magnitude fluctuations in bed roughness, and these likely related to the detachment of localized periphyton patches and the formation of holes on the periphyton carpet from JD224 onwards (Figure 33d)

As per the roughness, the introduction of disturbances did not modify the overall filling level (Figure 32b), which remained quasi-steady at ~2453.73 m (± σ = 0.002 m). There was an exception, JD238 (90th percentile = 2453.69 m), which experienced a drop that might explained by some localized detachments or by the fluctuations of the periphyton mat. As per FA, the interstices of FB (Figure 33b) remained at a quasi-steady level of ~2453.76 m (± σ = 0.001 m). Although both flumes experienced similar states of quasi-steadiness during this period, we found significant differences between the flumes (Kruskal-Wallis: $p < 0.05$), and those potentially related to the introduction of disturbances or by differences in periphyton morphology.

5.2.3.3 Infiltration rates

The infiltration rate was reduced in both flumes (Figures 32c and 33c) between the beginning and JD224 when we began to introduce disturbances into FA. We did not find statistical differences between the two trends (Kruskal-Wallis: $p > 0.05$). The infiltration rate in FA (Figure 32c) was significantly (Mann-Kendall: $p < 0.05$) reduced by ~88% between JD196 (0.17 l/s) and JD223 (0.02 l/s). Similarly, the rate in FB (Figure 33c) was reduced by ~84% between JD196 (0.19 l/s) and JD223 (0.03 l/s), and this reduction was also found to be significant (Mann-Kendall: $p < 0.05$).

The introduction of disturbances in FA appeared to have a slight impact on the infiltration rate (Figure 32c). In fact, we noted that after one day of dry conditions (JD225, 0.03 l/s), the infiltration increased by ~50% compared to JD223 (0.02 l/s), although it still remained ~82% less as compared to the beginning of the experiment. Similarly, after two days of dry conditions (JD231, 0.4 l/s), the infiltration increased by

~33% as compared to JD227 (0.03 l/s), but was still ~76% less as compared to JD196 (0.17 l/s). After three days of dry conditions (JD236, 0.03 l/s), the infiltration did not experience any increase as compared to JD232 (0.03 l/s), while it increased by ~33% between JD239 (0.03 l/s) and JD249 (0.04 l/s). Within this same period, the infiltration rate of FB was quasi steady ($mean_{infiltration}$ = 0.03 l/s, ± σ = 0 l/s), however we noted an increase of infiltration rate from JD232 (0.02 l/s) to JD238 (0.04 l/s). This increment might be explained by some detachments of some localized periphyton patches, and this was partly consistent with the slight increase in bed roughness (Figure 33a). Although we found some evidence of the impact of disturbances in FA and a slight increment in FB between JD232 and JD238, the two flumes did not show significant differences in their trends (Kruskal-Wallis: $p > 0.05$). Overall, the infiltration of FA was reduced by ~76% from JD196 (.0.17 l/s) and JD249 (0.4 l/s), and by ~84% from JD196 (0.19 l/s) to JD249 (0.03 l/s) in FB. Our results suggest that the infiltration related to the progressive filling of the interstices (FA: Pearson's correlation -0.58, $p < 0.01$; FB: Pearson's correlation -0.55, $p < 0.01$) and to the reduction of roughness (FA: Pearson's correlation 0.76, $p < 0.01$; FB: Pearson's correlation 0.85, $p < 0.01$).

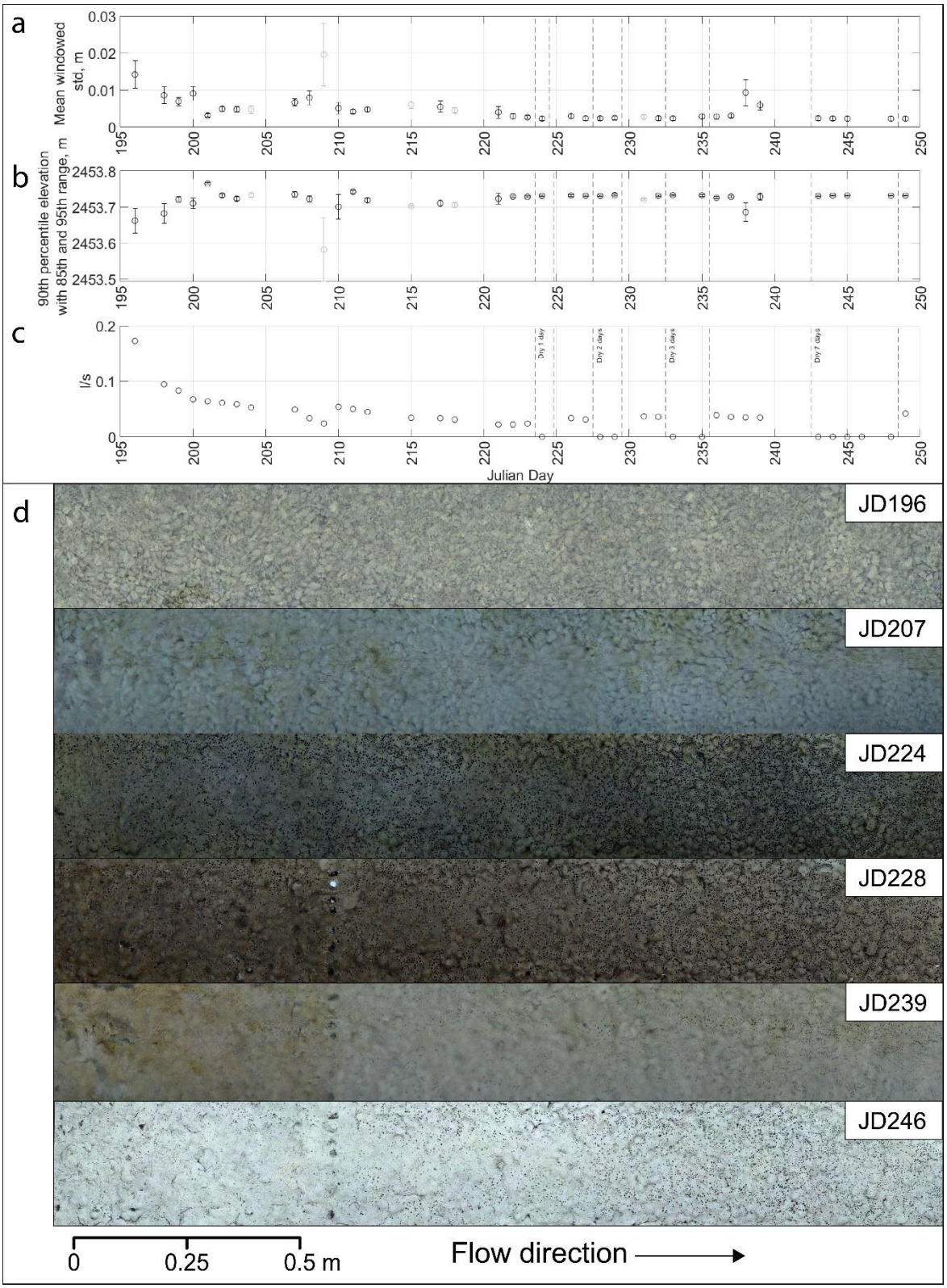

Figure 32: Streambed evolution of FA. a) Streambed roughness, expressed as the mean windowed standard deviations of the streambed elevations (m). Values computed from poor quality DEMs are marked in gray. b) Interstice filling, expressed as the elevations lows (m), presenting the 90th percentile and the 85th and 95th percentile range (where the percentile is counted from high to low elevations). Values computed from poor quality DEMs are marked in gray. c) Infiltration (l/s) evolution through time; d) Visual appreciation of the evolution of the streambed.

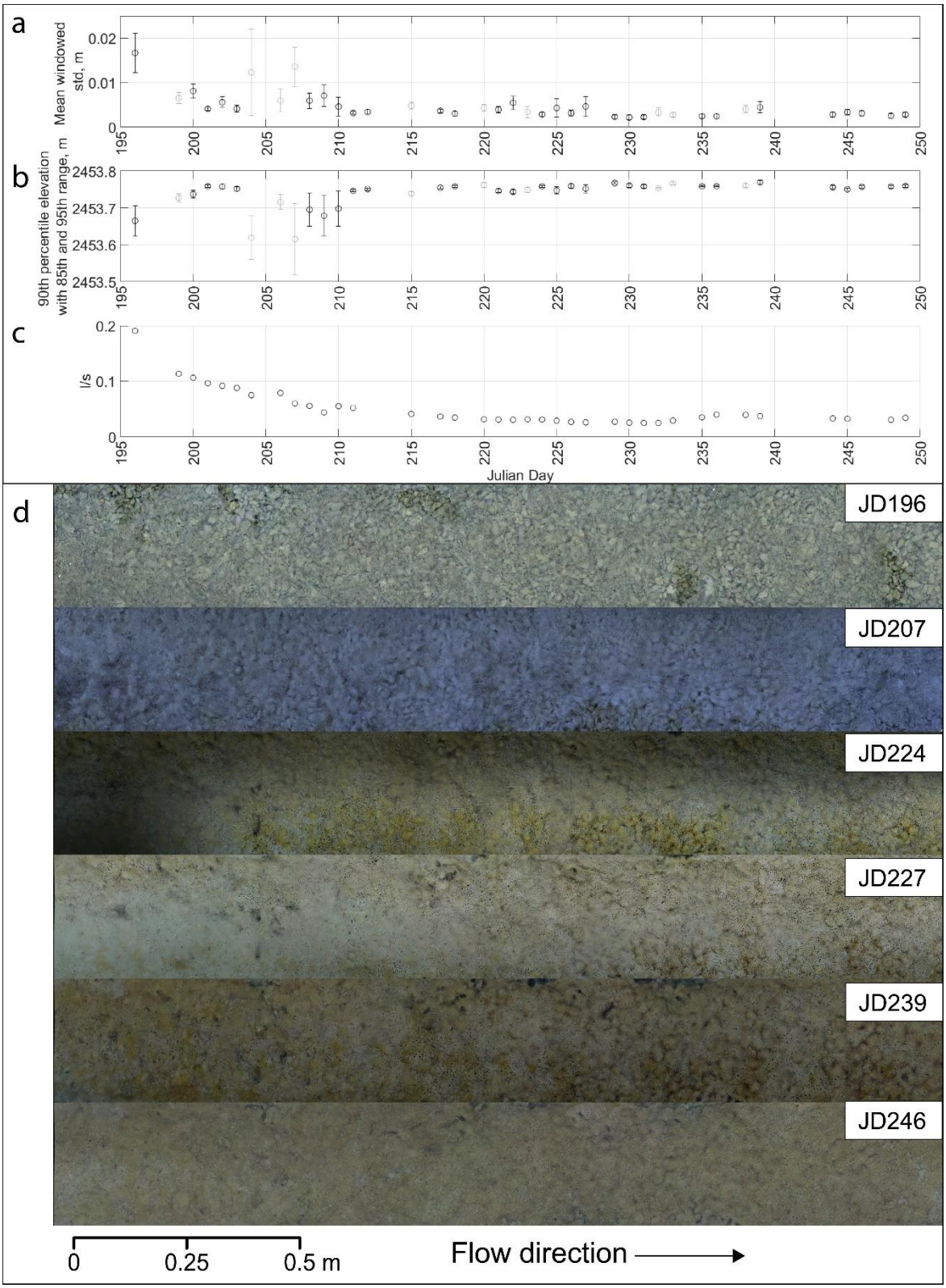

Figure 33: Streambed evolution of FB. a) Streambed roughness, expressed as the mean windowed standard deviations of the streambed elevations (m). Values computed from poor quality DEMs are marked in gray. b) Interstice filling, expressed as the elevations lows (m), presenting the 90th percentile and the 85th and 95th percentile range (where the percentile is counted from high to low elevations). Values computed from poor quality DEMs are marked in gray. c) Infiltration (l/s) evolution through time; d) Visual appreciation of the evolution of the streambed.

5.2.3.4 Hydraulics

In the first phase (i.e., before the introduction of disturbances in FA), periphyton development appeared to modify the near-bed turbulent structures in FA and FB. The median percentage of sweep and ejection events in FA (Figure 34a) was reduced by ~3 % from JD197 (64 %) to JD223 (62 %), but this was not statistically significant (Mann-Kendall: $p > 0.05$). In the same period, the ejections and sweeps in FB (Figure 35a) were significantly (Mann-Kendall: $p < 0.05$) reduced by 6 % (JD197: 65%; JD223: 61%). The turbulent structures in both flumes appeared to co-evolve during this initial phase, and no significant differences (Kruskal-Wallis: $p > 0.05$) were found between the two flumes in terms of ejection and sweep events. The median TKE of FA (Figure 34b) was significantly (Mann-Kendall: $p < 0.05$) reduced by ~61 % from JD197 ($1.21*10^{-4}$ m^2s^{-2}) to JD223 ($4.78*10^{-5}$ m^2s^{-2}). Similarly, the median TKE of FB (Figure 35b) was reduced by ~47 % from JD197 ($1.41*10^{-4}$ m^2s^{-2}) to JD223 ($7.53*10^{-5}$ m^2s^{-2}), but this reduction was not found statistically significant (Mann-Kendall: $p > 0.05$). Although both flumes experienced a reduction in TKE, the median TKE trends showed significant differences (Kruskal-Wallis: $p < 0.05$). These likely suggested differences in the periphyton morphologies, and thus in TKE.

The introduction of disturbances (from JD224 onwards) appeared to impact the turbulent structures in FA (Figure 34a), but only when desiccation was for longer than one day. We noted an increase between JD226 (54%) and JD230 (59%) and one more important between JD230 and JD236 (66%). The latter resulted in a percentage of ejection and sweep events greater than at the beginning of the experiment. Within this same period, the median percentage of ejection and sweep events in FB (Figure 35a) experienced a 2 % drop but this was not significant (Mann-Kendall: $p < 0.05$). The median percentages of ejection and sweep events during this period did not differ significantly (Kruskal-Wallis: $p > 0.05$) between the flumes, and this independently of the disturbances. Overall, from JD197 to JD238 (FA) / JD245 (FB) the median percentage decreased by ~17 % (Mann-Kendall: $p > 0.05$) in FA and by ~11% (Mann-Kendall: $p < 0.05$) in FB.

Our results showed that TKE of FA experienced an abrupt increase of ~222% after the introduction of the first disturbance, i.e. between JD223 ($4.78*10^{-5}$ m^2s^{-2}) and JD226 ($1.54*10^{-4}$ m^2s^{-2}). This increase was followed by a slight decrease in ejection or sweep events (Figure 34a), hence an increase in inward or outward interactions. However, after the JD226 event, the TKE started to drop again and reached $4.59*10^{-6}$ m^2s^{-2} on JD238. This reduction was however not significant (Mann-Kendall: $p > 0.05$). Within this same period, our results suggested a different behavior of the median TKE of FB (Figure 35b). In fact, from JD226 ($1.65*10^{-4}$ m^2s^{-2}) to JD245 ($7.52*10^{-5}$ m^2s^{-2}), TKE increased by ~50%, although this was not significant (Mann-Kendall: $p > 0.05$). Hence, the results suggested the TKE was characterized by two distinct phases, the first when TKE decreased (from JD197 to JD223) and the second when TKE increased (from JD223 to JD245). The increase in TKE between JD223 (i.e., the lowest level reached) and JD245 might relate to the roughness of the bed, which showed low

magnitude fluctuations within this period. The different evolutions in TKE were reflected in significant differences between the two trends (Kruskal-Wallis: $p < 0.05$).

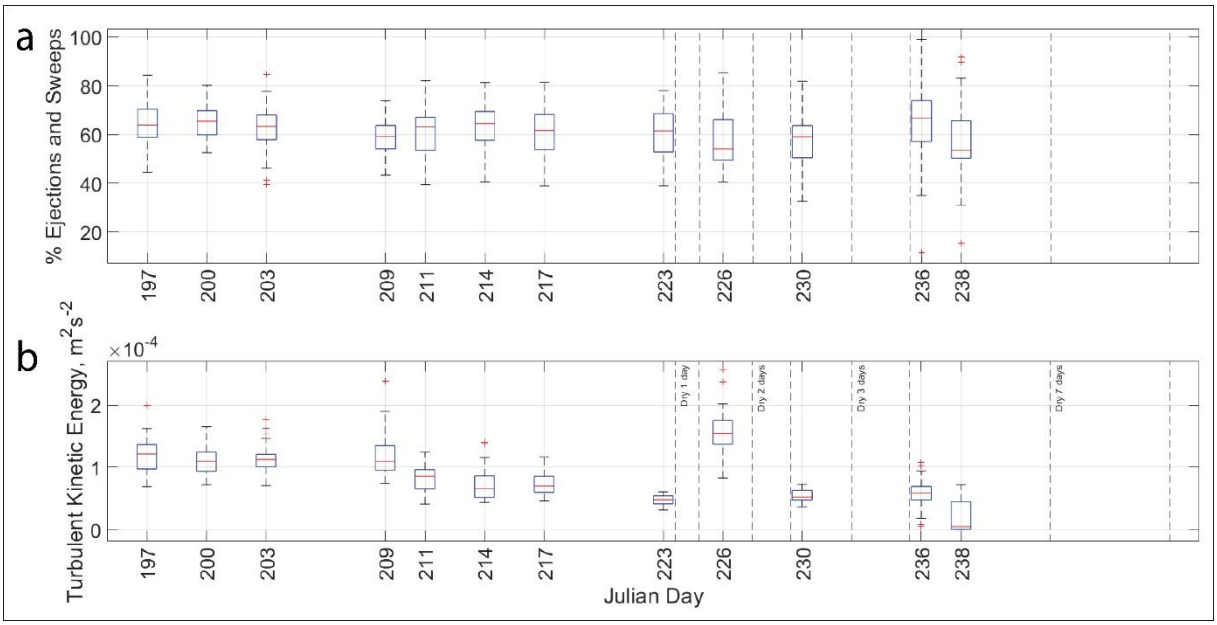

Figure 34: FA hydraulics. a) Percentage of ejection and sweep events at the near-bed layer. b) Turbulent kinetic energy TKE (m^2s^{-2}).

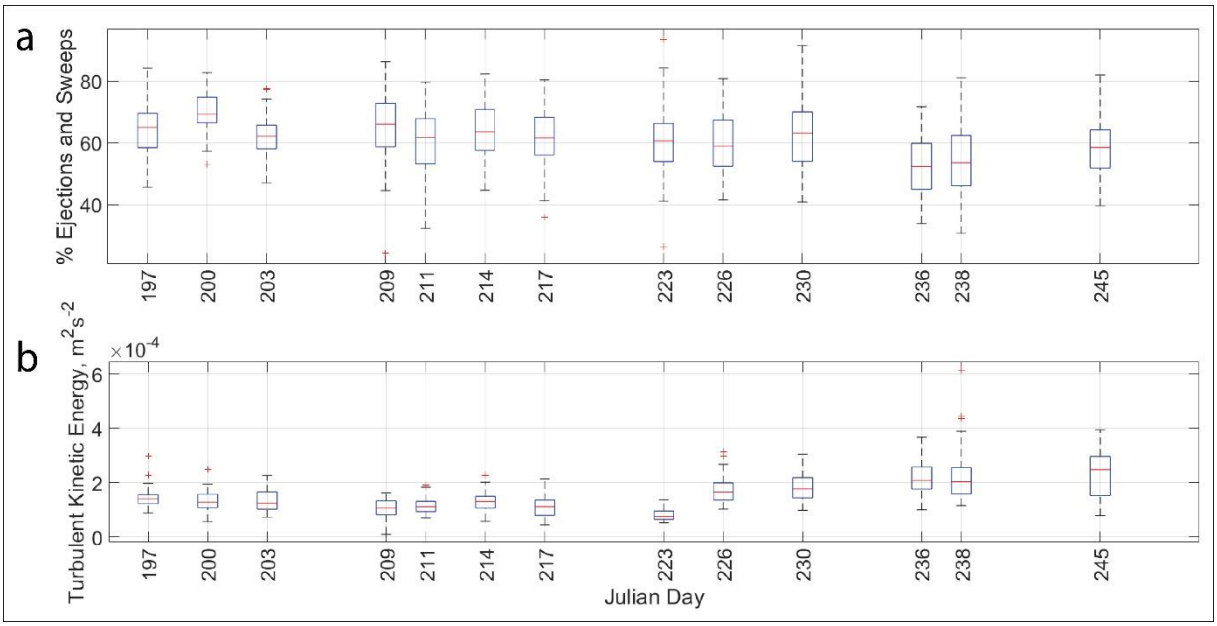

Figure 35: FB hydraulics. a) Percentage of ejection and sweep events at the near-bed layer. b) Turbulent kinetic energy TKE (m^2s^{-2}).

5.2.4 Discussion

5.2.4.1 Challenges and potential sources of errors

Flume experiments have been extensively used to investigate stream periphyton dynamics (e.g., Mulholland et al., 1994; Nikora et al., 1997, 1998; Hondzo and Wang, 2002; Battin et al., 2003a, b; Kazemifar et al., 2021). In this paper, we

installed a pair of outdoor flumes within an Alpine glacial forefield, and attempted to reproduce the hydraulic and environmental conditions of glacial floodplain tributaries. The functioning of the flumes and the running of the experiment in such an environment was a challenge and before we interpret the results we want to flag the errors that might have resulted.

Our flumes were fed by a hillslope tributary via a pipeline system, which emptied its water into a tank. The tank had two objectives: (1) it served as a sink for suspended sediments coming from the tributary in case of rain storm mobilization of fine sediment on the valley side walls; and (2) it attempted to maintain a constant hydraulic head and hence flume discharges. The hydraulic head was visually inspected several times during the day time, but never during the night-time. Overall, we could affirm that during the day time the head was almost constant through time but it obviously experienced some daily fluctuations (e.g., early in the morning compared to noon). Such fluctuations arose because of the fluctuations of the tributary discharge due to daily changes in air temperatures (i.e., increase or decrease of hillslope snowmelt) or because of the progressive shrinkage of the hydrological system (see Malard et al., 1999, Ward et al., 1999). In order to reduce the potential bias caused by the fluctuations of the flume discharges, we tried to collect the data always at the same time. We acknowledge the potential source of bias, but we argue that this uncontrolled variability also allowed periphyton to develop with the same conditions found in the floodplain tributaries.

The use of close-range digital or SfM photogrammetry in flume studies is well documented, and it typically involves a careful image acquisition design (e.g., Lane et al., 2001; Chandler et al., 2001; Butler et al., 2002; Kasprak et al., 2015; Morgan et al., 2017; Leduc et al., 2019). The use of a specific image acquisition geometry, which ultimately allows controlling image overlap and the overall DEM quality, is preferred and achieved via the use of camera supports (Lane et al., 2001; Chandler et al., 2001; Butler et al., 2002; Kasprak et al., 2015; Leduc et al., 2019). Due to the logistical complexity of our flume experiment, and the short windows of image capture (i.e., to ensure homogenous light conditions and avoid flume-wall related shadows), we collected the images manually, and those were captured by an operator that was changed on a periodical basis (i.e., depending on the people present at the base camp of the Otemma Glacier). However, it is now known that in SfM-MVS photogrammetry the use of standardized acquisition geometries, which must be adapted to the type of sensor used, produces more reliable and accurate DEMs by lowering the probability of producing systematic deformations (see James et al., 2020).

We attempted to overcome this crucial issue by using a good quality camera (O'Connor et al., 2017) and a dense network of GCPs (Chandler et al., 2001; Butler et al., 2002; Leduc et al., 2019; James et al., 2017, 2020). However, we note that the vertical and horizontal precisions of our control points were ±0.02 m and ±0.01 m respectively, which is greater than the precision one would expect for a millimetric study such as the one presented here. We acknowledge that the use of a total station would have led to much greater positioning precisions (Lane et al., 2001; Butler et al., 2002; Leduc et al., 2019). We decided to use references to compare the DEMs, and then used such results to spatially model the errors. Our results (Figures 30a, b and

31a, b) suggested that the systematic deformations were mostly removed, and the DEMs aligned with our references. Some random errors were still affecting the quality of our DEMs although their magnitude (typically below ± σ 0.005 m) was considered acceptable.

We also attempted to remove for the effect of refraction at the air-water interface (Fryer and Kniest, 1985; Westaway et al., 2000, 2001), which is known to produce erroneous bed elevations and hence roughness underestimates (Butler et al., 2002). We used the method proposed by Westaway et al. (2000, 2001), which produced acceptable results in terms of mean error (Figures 30c and 31c), but less in terms of standard deviation (Figures 30d and 31d). However, we reported results close to those proposed by Butler et al. (2002). We argue that the residual bias in our datasets was the result of the undulation of the water surface, which complicated the solution of the bathymetric correction (Westaway et al., 2000, 2001; Butler et al., 2002). *A posteriori*, it would have been useful to flatten the water surface at the time of image acquisition (Butler et al., 2002), but this would have been time-consuming and would have risked increasing near bed velocities so potentially impacting periphyton and its development.

5.2.4.2 Modification of the streambed and the near-bed hydraulics by periphyton

The periphyton developed very rapidly and covered the beds of our flumes (Figures. 32d and 33d), and this was reflected in the benthic interstices being filled by the mat (Figures 32b and 33b). Most of the filling occurred within the first 5 to 6 days of the experiments, as found in research in other environments (Cunningham et al., 1991). We found that the roughness decreased in both flumes within the same time-frame (Figures 32a and 33a). This finding is in agreement with some previous research (Godillot et al., 2001; Labiod et al., 2007; Fang et al., 2017), but in disagreement with others (Nikora et al.,1997, 1998) who found rougher beds after the development of periphyton. However, comparisons between studies remain difficult since the initial physical conditions (e.g., grain size, discharge, etc), and the study designs may differ.

We found that the evolution of the roughness length did not differ significantly between FA and FB, regardless of the introduction of disturbances in the form of dry conditions (Figures 32d and 36b). This suggested that although the periphyton progressively dried up in FA, it likely persevered its overall pre-disturbance morphology. A closer look at the roughness lengths of FB revealed a tendency to low magnitude fluctuations in roughness within a quasi-steady phase (Figure 33a, from JD224 to JD249), and these were likely related to the detachment and re-growth of localized periphyton patches (Figure 33d). However, we cannot exclude that these fluctuations were also a consequence of the buoyant nature of the periphyton due to the presence of air bubbles (Godillot et al., 2001; Labiod et al., 2007), as depicted by Figure 33d and Figure 36a. As per the roughness, the flumes did not differ in terms of streambed interstice filling before the introduction of disturbances. However, after the introduction we found significant differences between FA and FB. We therefore assumed that these differences related to differences in periphyton morphology or, most likely, to the introduction of disturbances in FA, and particularly to detachment of

biomass in FA from JD238 (Figure 32b, d). The detachment likely originated following the 3-day dry conditions, and it was tracked as a sudden roughness increase, but we noted that it was rapidly compensated the days after.

The infiltration of FA and FB was reduced significantly during the first part of the experiments (i.e., before the introduction of disturbances; Figures 32c and 33c), and the results reported here agreed with previous works both in terms of process duration and infiltration rate (Cunningham et al., 1991; Ragusa et al., 1994; Orr et al., 2009). Our results showed that the infiltration related to the progressive filling of the interstices and to the reduction of roughness. This is consistent with other studies that demonstrated that the accumulation of periphyton mats between the grains leads to clogging events and this reduces hyporheic exchanges (Cunningham et al., 1991; Battin and Sengschmitt, 1998; Thullner et al., 2002; Ibisch and Borchardt, 2002; Orr et al., 2009; Zhao et al., 2009; Gette-Bouvarot et al., 2014; Caruso et al., 2017). Surprisingly, we did not find significant differences in the infiltration rate between FA and FB once disturbances were introduced, and the total infiltration reduction was of ~76% and ~84% respectively. This result suggested that the introduction of disturbances had little influence on the overall rate at which water infiltrated into the sediments. This likely suggested that the periphyton mat of FA preserved its morphology although it progressively dried up. However, we noted that the infiltration rates in FA were typically higher the day after the disturbance ended (+50% after 1 day, +33% after 2 days, 0% after 3 days, and +33% after 7 days), although this increase was suddenly followed by a new decrease. This behavior reflected the presence of millimetric holes in the mat surface of the dried periphyton mat that originated from escape of air bubbles encapsulated within the mat before the disturbance (Figures 32d and 36). Thus, the subsequent sudden decreases in infiltration suggested that the organisms composing the mat survived the drought periods and returned to being photosynthetically active at a timescale of only hours after re-submergence. This trend is consistent with previous studies, notably in a similarly dry environment in Antarctica (Hawes and Howard-Williams, 1998; McKnight et al., 2007). It highlighted a concomitant process that we did not explore in this study. If the photosynthesis generated micro holes in the mat depend on the photosynthesis activity (i.e., light conditions versus dark conditions), it is possible that infiltration fluctuated daily, being lower when the periphyton continuously produced bubbles that filled the bubble-related micro holes (i.e., during the day time). Finally, but beyond the scope of this research, we highlight that the infiltration rate may be impacted by the grazing activity of benthic invertebrates (Ibisch and Borchardt, 2002) that are common in the tributaries we tried to mimic in this study, and this might adversely impact the process we have described here.

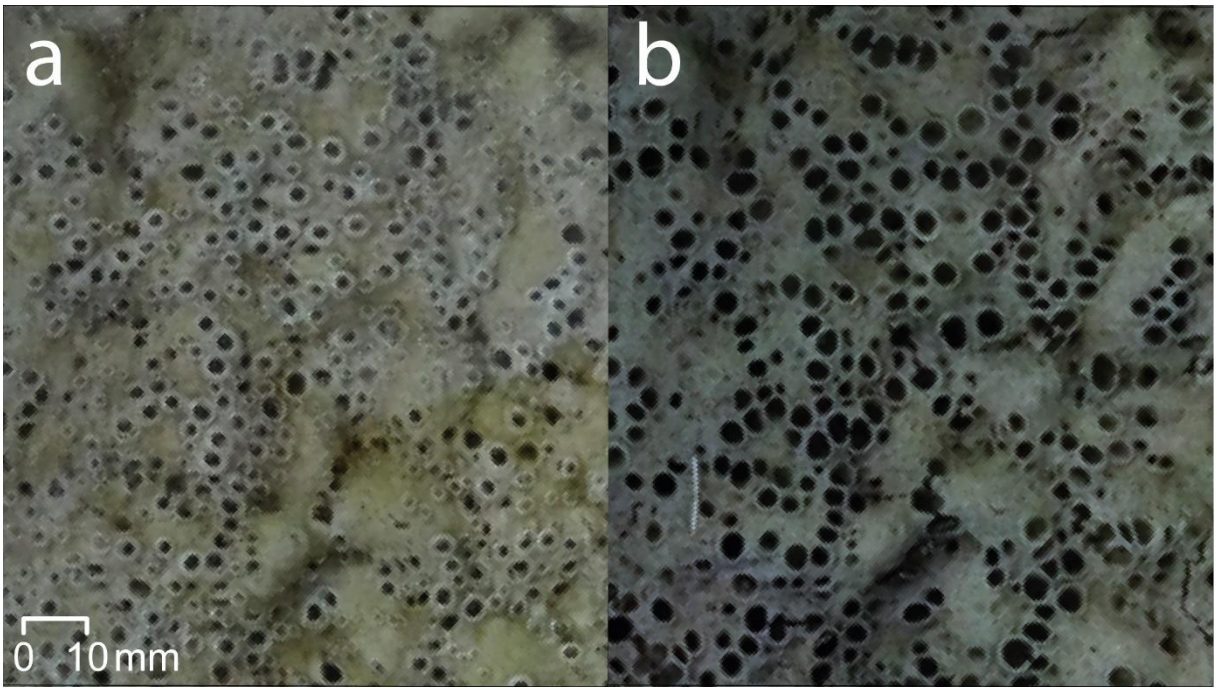

Figure 36: a) Periphyton active, producing air bubbles through photosynthesis in FA (JD223); b) Periphyton mat just after water was removed (JD224).

We also investigated how the development of periphyton modified near-bed turbulent structures (Figures 34 and 35). We found that the median percentages of ejection and sweep events were reduced in both flumes (Figures 34a and 35a), although this reduction was not found to be statistically significant in FA. In agreement with previous research (Reidenbach et al., 2010; Kazemifar et al., 2021), we attributed these reductions to the decrease in bed roughness (Figures 32a and 33a) due to the development of periphyton. Our results suggested that the development of periphyton also led to beds less prone to bursting processes. Sediment entrainment may be more likely in the presence of more ejections and sweeps (Bennet and Best, 1995; Dwivedi et al., 2011; Keylock et al., 2014), and this independently of changes in the shear stress (Shvidchenko and Pender, 2001). The introduction of disturbances in FA appeared to have a minor impact on ejections and sweeps, since after each dry event longer than one day the percentage of sweeps and ejections was slightly increased. However, such increases did not match any real increase in bed roughness (Figure 32a) at least at the data resolution we obtained here.

A more interesting view of the evolution of the near-bed turbulent structures was however provided by the TKE. In the first part of the experiments (i.e., before the introduction of the disturbances in FA), the median TKE diminished in both flumes (Figures 34b and 35b) in response of the bed becoming smoother (Figures 32a and 33a) due to the development of periphyton (Figures 32d and 33d). This behavior was found consistent with the study of Fang et al. (2017) that noted a decrease in TKE due to periphyton colonization. On the contrary, our results suggested that in the second part of the experiments (i.e., after the introduction of disturbances) the median TKE of FA and FB significantly diverged (Kruskal-Wallis: $p < 0.05$).

We reported an abrupt increase in FA (~222%) after the introduction of the first disturbance, and this was reflected in the ejection and sweep events being slightly decreased compared to JD223 and then again increased in JD230. This u-shaped trend between JD223 and JD230 might have suggested a more important contribution of inward and outward interactions on JD226, which are commonly the rarest events but which are recognized as being important as well (Nelson et al., 1995; Paiement-Paradis et al., 2011). This increase in TKE may have been related to a slight increase in roughness (Figure 32a) between JD224 (dry bed) and JD226 (re-submerged bed). From JD226 onwards, the TKE of FA dropped and reached its lowest level on JD238, although we did not find any new important decrease in bed roughness (Figure 32a), at least at data the resolution used here.

The TKE of FB instead increased in the second part of the experiment (Figure 35b), showing a pattern opposite to FA (Figure 34b). The results suggested that this increase was likely related to the roughness (Figure 33a), and particularly to its fluctuations caused by cycles of detachment and re-growth of periphyton (i.e., increase or decrease in roughness) and the formation of holes and cracks in the mat (Figure 33d). The detachment processes occurred in conditions of stability (e.g., shear stress), and thus presumably related to episodes of self-detachment after the peak biomass was attainted (Biggs, 1996) or because of the feeding activity of macrozoobenthos (Lamberti et al., 1987).

5.2.4.3 Implications for ecosystem engineering

The development of periphyton has been thought to promote primary succession in recently deglaciated floodplains (Miller and Lane, 2019; Roncoroni et al., 2019). These authors hypothesized the formation of an impermeable layer at the sediment surface that reduced vertical infiltration of water, so maintaining standing water; and reduced susceptibility of sediment to erosion. Roncoroni et al. (2023) followed periphyton development over an entire melt season and showed that periphyton development is limited to tributaries that flow over the most stable surfaces of glacial floodplains (i.e., terraces) due to high rates of stream erosion and deposition elsewhere. Such tributaries are commonly fed by snowmelt or ground water (Malard et al., 1999; Ward et al., 1999; Müller et al., 2022) and are substantially less harsh as compared to glacially-fed channels (Boix-Candell et al., 2021). Our findings confirm that the Miller and Lane (2019) and Roncoroni et al. (2019) hypotheses hold.

Periphyton develops and progressively covers the streambed. The experiments show that this is extremely rapid, making the bed smoother and filling benthic interstices over a few days. These changes have two major interrelated implications. On the one hand, the filling of the interstices clogs the streambed and significantly reduces the rate at which water infiltrates into the sediment also over a few days. This feedback is important in glacial floodplains that are both well-drained and water limited (Cooper, 1923; Matthews, 1992; Burga et al., 2010; Viles, 2012), and results in a more sustainable water supply to pioneer vegetation (Figure 37).

On the other hand, the development of periphyton modifies the near-bed turbulent layer by reducing the number of potentially adverse bursting events. We hypothesize that in such very stable channels this reduction has little effects on the sediment entrainment *per se*, but it likely has important effects in reducing the detachment of periphyton patches. This, in turn, provides a positive feedback by promoting the reduction of the infiltration rate.

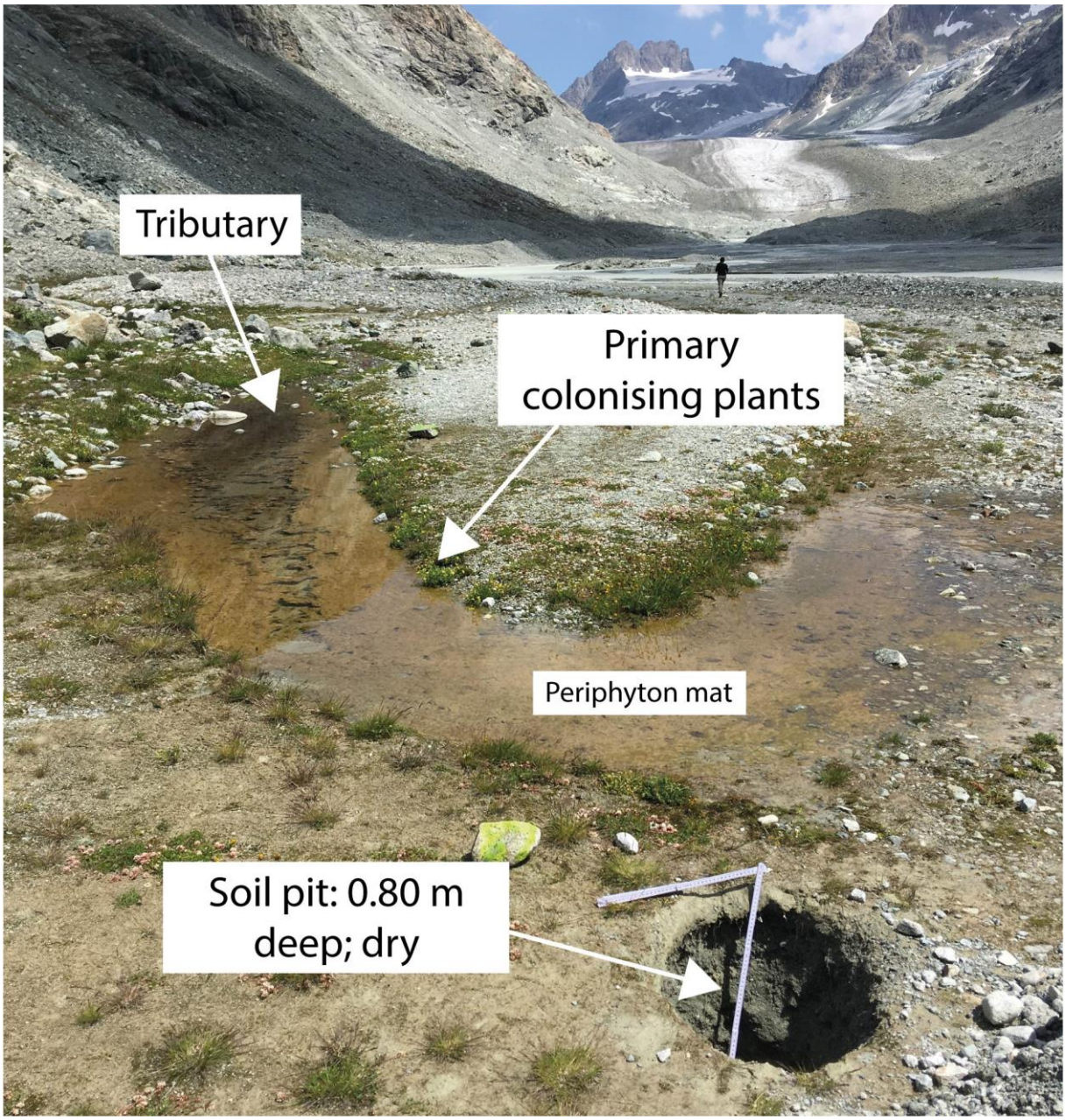

Figure 37: Image of a tributary flowing across a terrace upstream of the flume experiments showing a periphyton mat retaining tributary derived water at the surface and encouraging local plant colonization.

5.2.5 Conclusions

The modification of the streambed surface and of the hydraulic properties due to the colonization of periphyton was investigated with a set of outdoor flumes, and the

combination of DEM and near-bed hydraulic analysis. We can draw the following main conclusions. First, the development of periphyton effectively filled the benthic interstices, and as a result reduced local bed roughness (H1a). Contrary to our hypothesis (H1b), the introduction of disturbances, here in the form of non-permanent dry conditions (Roncoroni et al., 2023), had limited effects on the biogenic bed, which preserved its pre-disturbance morphology. Second, the development of periphyton modified near-bed coherent structures, and this resulted in a reduction of possible adverse bursting events in the first part of the experiments (H2a). Contrary to our hypothesis (H2b), the introduction of disturbances appeared to have little effects on the near-bed layer. However, for the case where the experiment continued without further disturbance the roughness increased which we attributed to maturing of the periphyton mat, and the apparent growth of streamer-like structures. Third, the filling of the sediment interstices clogged the streambed, and this had the result of reducing the rate at which water infiltrated into the sediment matrix (H3a). The introduction of disturbances might be expected to partly remove this feedback (H3b), but our findings suggested that the disturbances had only a marginal effect, with the undisturbed and disturbed flumes both maintaining low infiltration rates once periphyton had developed throughout the full experiment.

Our experiments were a logistical challenge, and we recognized the possible sources of bias related to the complexity of running outdoor flume experiments in such an extreme environment (i.e., the forefield of the Otemma Glacier). We also acknowledged that our findings may have reflected site-specific (e.g., water temperature, light conditions, etc.) and design-specific (e.g., grain size, flume slope, etc.) conditions that are difficult to replicate in other laboratory or outdoor studies. For these reasons, we call for new investigations that address the topic with different initial conditions and analytical approaches.

5.3 Chapter summary

This chapter provides the first quantitative evidence of the mechanisms relating to how periphyton development modifies the streambed properties of the tributary channels found on proglacial margin terraces. For the purposes of this chapter, flumes were installed near the Otemma glacier, and different data (including measures of infiltration through sediments, near-bed 3D velocities, photos) were collected and then processed. The data were found to be of good quality and the results coherent with the published literature, although some critical issues emerged during the analysis. The results presented here likely reflected the flume design (e.g., slope, discharge, grain-size, etc.) and the methodological approaches (e.g., close-range photogrammetry, roughness and interstice analysis, etc.) selected for the purposes of this chapter. For these reasons, the presence of biased and/or inflated results (e.g. roughness or hydraulic measures) could not be excluded. In this sense, the chapter lacks in providing a full explanation of the possible sources of error, and in analyzing the sensitiveness of the methods and how they contributed to the under- or over-estimation of the processes found here.

In acknowledging the critical issues of this chapter, the results tend to corroborate however the assumptions made by Miller and Lane (2019) and in Chapter 2. They show that periphyton decrease bed roughness, and this primarily by filling the benthic interstice space with biomass. These surface modifications had two main consequences. First, the bio-clogging leads to a decreased vertical hydraulic conductivity, and this regardless of the introduction of disturbances. Second, the bed smoothening modifies the bed coherent structures, and this results in a reduction of adverse bursting events and in the modification of the turbulent kinetic energy at the near-bed layer.

The results presented here suggest that the modification of the turbulent structures feeds back into periphyton development, which in turn favors more accumulation of biomass and hence promotes water retention at the surface. The latter is likely to facilitate the settling of pioneering vegetation in these extremely well-drained environments (Cooper, 1923; Matthews, 1992; Burga et al., 2010; Viles, 2012), and it might explain successional patterns that do not follow the classic chronosequence concept of vegetation development after deglaciation (Matthews, 1992). It was more difficult to establish the extent to which measured changes in turbulent kinetic energy significantly increased stability and the fact that periphyton do not develop where the rivers are dynamically active in these environments (Chapter 4) suggests that these hydraulic changes may not be that significant.

Chapter 6: Synthesis, limitations and perspectives

6.1 Synthesis

This PhD thesis had two main and interrelated goals: (1) to quantify periphyton development and its drivers in proglacial floodplains, with a particular focus on the melt-season; and (2) to investigate if and how periphyton promote primary succession via ecosystem engineering. Through the development of four main chapters, I attempted to reach the thesis goals. Here, I propose a synthesis of the main findings accordingly to the thesis research questions.

6.1.1 State of the knowledge and defining research questions

In the wide-ranging literature review proposed in Chapter 2, I summarized the present knowledge on biofilm dynamics in proglacial margins. The key lessons of this review serve as the basis for the development of this thesis, and are as follow.

The retreat of Alpine glaciers (Zemp et al., 2006; Sommer et al., 2020) has the consequence of creating extensive proglacial terrains (Carrivick et al., 2018) that become exposed to solar radiation and therefore open to ecological colonization (Chapin et al., 1994; Fastie, 1995; Kaufmann, 2001; Eichel, 2019). However, such colonization is made complicated by the unstable nature of proglacial environments (Marren, 2005; Heckmann et al., 2016; Bakker et al., 2019). This is particularly the case for the emerging stream systems that drain glacial floodplains. In fact, during the melt-season such systems experience continuous events of streambed reworking (Bakker et al., 2019) that are associated with high discharge and sediment supply rates (Nienow et al., 1998; Swift et al., 2005; Heckmann et al., 2016; Perolo et al., 2019). These events create a regime of disturbance that may adversely influence the development of benthic communities (Milner and Petts, 1994; Uehlinger et al., 1998, 2002, 2010; Burgherr and Ward, 2001). This regime is known to attenuate with distance from the glacier terminus, resulting in the increase of the benthic fauna diversity and abundance (Milner and Petts, 1994). Similarly, the disturbance regime fluctuates during the year, and there are periods of time when the conditions are less harsh for the development of the benthic communities, namely in late spring and autumn (Uehlinger et al., 1998, 2002, 2010; Burgherr and Ward, 2001). Thus, we have two dimensions: one that develops longitudinally, and the other that develops seasonally.

Glacial floodplains are also characterized by a heterogeneous assemblage of habitats (Ward et al., 1998), and these strongly develop laterally. The lateral dimension relates to non-glacial tributaries that provide less harsh environmental conditions during the melt season (Uehlinger et al., 1998; Burgherr et al., 2002; Boix-Canadell et al., 2021; Brandani et al., 2022). Such tributaries are fed by hillslope sources (Malard et al., 1999; Ward et al., 1999) and are often characterized by conditions of water transparency, hydrological and thermal stability (Boix-Canadell et al., 2021). These tributaries may flow over stable terraces (Marren and Toomath, 2013; 2014; Roussel

et al., 2018) that are disconnected from the glacial braided stream, and are rarely if never inundated by glacial water. This condition is thought to provide the most benign conditions for the development of periphyton during the melt-season (Miller and Lane, 2019).

The review led to a model that foresees the seasonal and spatial habitability of the periphyton habitat (Figure 5). Within the active floodplain (Figure 5b), habitability is thought to be high in spring and autumn (i.e., windows of opportunity; Uehlinger et al., 2002, 2010) and low during the rest of the year (except in winter if channels are not snow-covered). In the terrace zone (Figure 5c), habitability is likely to reach its maximum during the melt season because of both the presence of hillslope water and the absence of disturbances; whilst it is likely to be low during the winter because of the progressive shrinkage of the hillslope water sources (Malard et al., 1999; Ward et al., 1999) or because of the permanent snow cover.

Miller and Lane (2019) hypothesized a positive relationship between the presence of periphyton and the development of pioneer vegetation, and explained this by a reduction in water vertical infiltration due to the development of periphyton. The combination of the hypothesis of Miller and Lane (2019) and the habitability model (Figure 5) led to a second theoretical model that predicts the ontogeny of glacial floodplains (Figure 7). The model foresees that hillslope-fed channels on terraces are colonized by periphyton, which in turn increase sediment stability through biostabilization (Fang et al., 2014; Neumeier et al., 2006; Pivato et al., 2019), the availability of nutrients (Kaštovská et al., 2005; Schulz et al., 2013; Ciccazzo et al., 2016), and ultimately reduce water vertical infiltration (Miller and Lane, 2019). These feedbacks promote the development of pioneer vegetation, which further increases the stability of terraces. As the process progresses, more space is available for periphyton and pioneer vegetation and this has the result of straightening the stream system.

As Chapter 2 was built around theory and hypotheses, it opened up a number of critical questions that needed to be addressed. First, there was the need to quantify when and where periphyton develop in proglacial margins with a particular focus upon the melt season. Second, the knowledge of periphyton spatial and temporal dynamics unlocked the investigation of the periphyton habitat constraints, and hence the delineation of the areas where ecosystem engineering may effectively take place. Finally, this provided the boundaries for assessing the engineering effects of periphyton in glacial floodplains.

6.1.2 Where and when do biofilms develop in proglacial forefields during the melt-season?

Knowledge of the spatial and temporal development of biofilms is central for the understanding of the ecological functioning of recently-deglaciated floodplains. The traditional approach of acquiring such information is based upon the physical collection of biofilm samples (e.g., Uehlinger et al., 1998; 2010; Brandani et al., 2022). This approach can provide rich information on biofilm biomass and composition, but it has

limitations on the number of samples that one can acquire, thereby providing an approximation of biofilm dynamics in space and time.

An alternative approach to the traditional sampling strategies is satellite or airborne remote sensing, which may well provide information on biofilm biomass and composition (Méléder et al., 2003; Combe et al., 2005; Kazemipour et al., 2012; Benyoucef et al., 2014; Salvatore et al., 2020; Power et al., 2020) provided it has a suitable radiometric signature. Although this information is likely to be less rich as compared to physical samples, it has the advantage of providing greater spatial and/or temporal resolutions that are easier to integrate into analysis of the physical environment. The downside of satellite or airborne remote sensing is that high spatial resolutions are generally obtained at the detriment of high temporal resolutions (e.g., airborne), while high temporal resolutions are generally obtained at the detriment of high spatial resolutions (e.g., satellite). This downside is problematic in stream studies that need both high spatial and high temporal resolutions to appreciate stream processes (Carbonneau et al., 2004; Marcus and Fonstad, 2008; Woodget et al., 2015; Woodget and Austrums, 2017).This need is accentuated in Alpine glacial stream systems where processes can occur over a few centimeters or meters and over hours or days.

The need for very high spatial and temporal resolutions led to a critical thinking of how imagery had to be acquired to characterize the biofilm dynamics at appropriate resolutions, both in space and in time. The solution to this problem was in the use of low cost drones and SfM-MVS photogrammetry, and the application of logistic models to visible band ratios (Chapter 3). During summer 2020, daily RGB imagery of the floodplain of the Otemma glacier was acquired with a low cost drone (i.e., DJI Phantom 4 Pro). The images were processed through SfM-MVS photogrammetry following state-of-the-art photogrammetric techniques (James et al., 2017, 2020). The resultant orthomosaics were converted into visible band ratios from which it was possible to train a set of logistic models that delivered overall high performances (Tables 4, 5, and 6). Within the set of band ratios, the KANA index (Kawashima and Nakatani, 1998) had the best performance, and was therefore selected for the purpose of this research. The framework was found effective in mapping the presence of what we initially labelled biofilm in glacial floodplains, and this allowed for quantification at high temporal (daily over an entire melt-season) and spatial (cm-scale) resolutions of associated dynamics during the melt-season (Figure 20a). Chapter 3 also presented a map in November (Figure 20b), providing an overview of where biofilms appeared to developed during the autumn window of opportunity (Uehlinger et al., 2002, 2010).

However, in completing Chapter 3 and following subsequent attempts to relate results to chlorophyll-*a* (Figure 38), it was realized that the method presented and published was only capturing a subset of biofilms. In fact, this was suggested by the spatial match between the occupation map (Figure 20a) and the chlorophyll-*a* concentration map (Figure 38). Thus, after the publication of Chapter 3 we adopted a stricter definition of what we were mapping, referring to this from Chapter 4 onwards as periphyton.

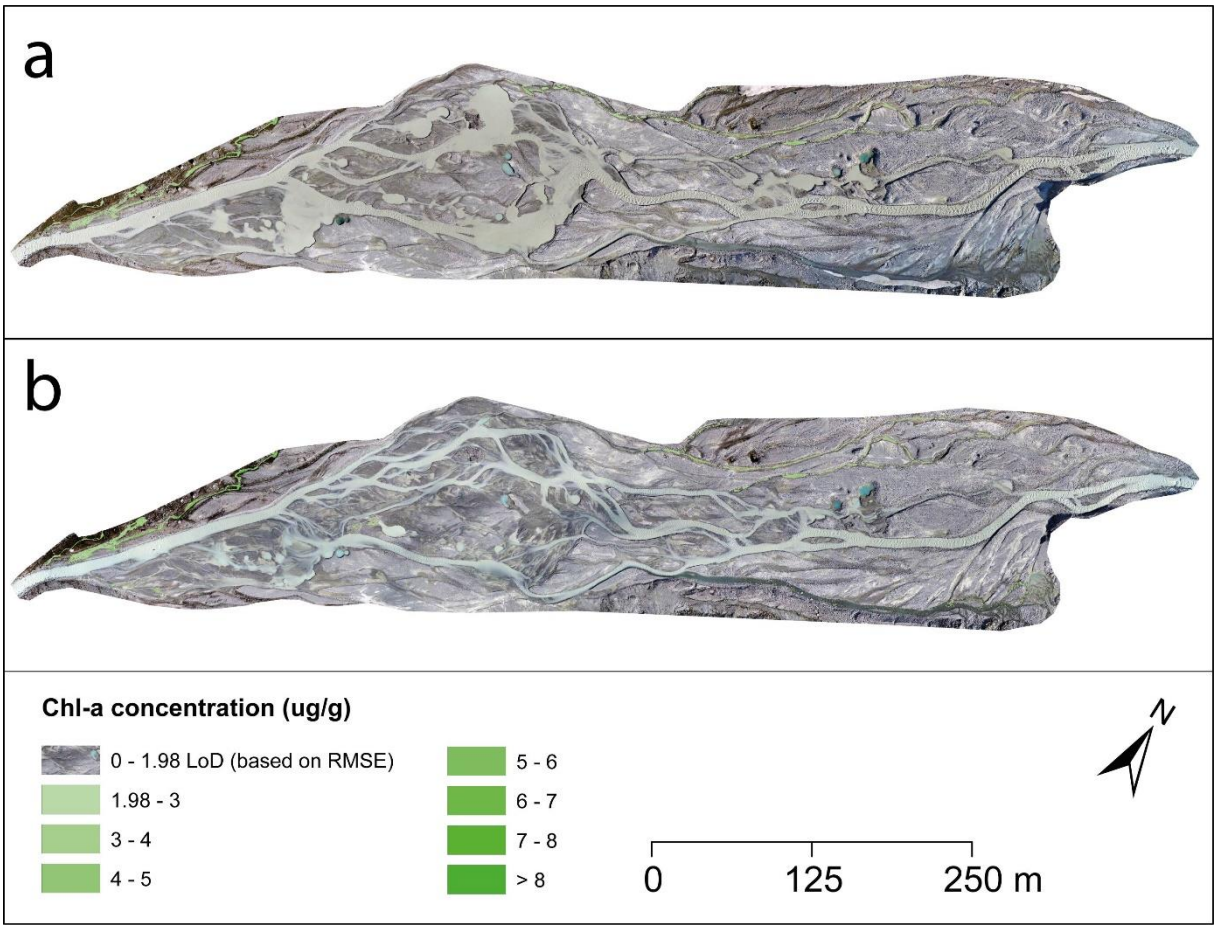

Figure 38: Chlorophyll-*a* concentrations (ug/g of dry sediments) on June 26 (a) and July 14 (b) 2020. Samples of colonized and uncolonized sediments were collected on June 26 and July 14 2020, and processed in laboratory to estimate the concentrations of chlorophyll-*a*. Results were linearly related to a visible band ratio (in this case the RCC, see Table 4), leading to a date-specific linear regression model that was then applied at the whole floodplain scale. The application of the model to different dates produced poor results, and it was decided to abandon the mapping of the chlorophyll-*a* concentrations.

The results presented in Chapter 3 demonstrated that periphyton effectively developed during the melt-season, and this development was important on hillslope-fed channels over the most stable zones of the floodplains (i.e., terraces). Those channels allowed periphyton to develop for long periods of time (i.e., for weeks) from June to late August (Figure 20a). The results also suggested that periphyton developed within the active floodplain during the melt-season, but this development was limited both in space and in time. In fact, the development within the active floodplain was typically of short duration (matter of days), and concentrated in shallow and small glacially-fed braids. In autumn (Figure 20b), periphyton development showed an opposite trend. Most of the development was concentrated within the active floodplain boundaries, reflecting the attenuation of the glacially-derived disturbances (Uehlinger et al., 2002, 2010). On the contrary, periphyton presence was strongly reduced over the terraces, and this reflected progressive within-summer contraction of the stream system that resulted in the exhaustion of hillslope water sources (Malard et al., 1998; Ward et al., 1998).

6.1.3 How is periphyton development related to habitat stability, stream morphodynamics, and access to water spatially and temporally at the scale of a representative proglacial braid plain?

As noted above, it is known that the harshness of glacial water and the associated regime of disturbances have a strong impact on the development of periphyton (Uehlinger et al., 1998, 2002, 2010; Miller and Lane, 2019; Brandani et al., 2022). This was further demonstrated by the findings of Chapter 3, which suggested that during the melt-season periphyton development was strongly connected with zones of high stability (i.e., terraces), away from the glacially-derived disturbances. However, Chapter 3 also demonstrated that within the most active floodplain there were periods of time, of short duration, when periphyton were effectively able to develop. These findings called for a better appreciation of the glacially-derived disturbances, the role of habitat stability and the access to water. Chapter 4 therefore provided a comprehensive analysis of the physical habitat of periphyton in an Alpine glacial floodplain, and this by taking advantage of the intensive photogrammetric processing of Chapter 3.

It was recognized that disturbance could have two elements: (1) physical disturbance by erosion and depositional processes; (2) physical disturbance where zones become inundated with harsh (cold, turbid) glacial streamwater. Following Lane and Richards (1997) and Bakker et al. (2019), the DEMs produced through SfM-MVS photogrammetry (see Section 3) were used to calculate rates of morphological reworking of the riverbed, defined as the time since the last stream reworking event. This led to an instability map covering the entire 2020 melt-season (Figure 22c). From the orthomosaics, the channels were digitized, and this allowed for the calculation for each floodplain zone of the days of submergence, either by glacial or non-glacial channels. This produced a submergence map covering the entire 2020 melt-season (Figure 22b). The analysis of the submergence map revealed that the geographical zonation made in Chapter 3 (i.e., active and stable zones) was inaccurate. Chapter 4 provided a better zonation that also accounted for zones where glacially-fed water intruded into the hillslope-fed channels; this was called the buffer zone. The glacially-fed channels of Figure 22b were then used into an analysis of the braiding characteristics (e.g., braiding intensity, number of dry bars, etc.) of the stream system (Hong and Davies, 1979; Mosley, 1982; Ashmore, 1988; Chew and Ashmore, 2001; Egozi and Ashmore, 2008). Finally, the physical habitat characteristics were linked to the periphyton map (Chapter 3, Figures 20a and 22a) for the analysis of the effects of glacially-derived disturbances, and the roles of habitat stability and access to water.

Periphyton presence was significant throughout the entire melt-season in the channels draining the terrace zone (Figure 22a), and this was possible due to the combination of water accessibility (Figure 22b) and habitat stability (Figure 22c). On the one hand, the presence was enhanced by the type of the water supply that there was hillslope-related (i.e., krenal and rhithral) and hence substantially less harsh as compared to glacial water (Ward et al., 1998; Uehlinger et al., 1998, 2002; Boix-Canadell et al., 2021). On the other hand, the absence of streambed reworking events due to the higher elevations of the terraces as compared to the glacially-fed stream

(Figure 27b) allowed for a constant periphyton presence. The results (Figure 28a) also suggested that water supply was progressively reduced from August onwards, leading to periphyton desiccation events. This process was consistent with the results Chapter 3 that found the terrace channels dry in autumn due to the shrinkage of the stream system (Malard et al., 1999, Ward et al., 1999).

In the buffer zone channels, periphyton development was important (Figure 22a), although it was not comparable to the terrace zone (Figure 23d). The results suggested that this difference was related to periodic changes in habitability due to the intrusion of glacial water (Figures 26 and 28b) leading to less suitable physical conditions (Figure 25a). The buffer zone was indeed at a slight lower elevation as compared to the terraces (Figure 25c), and that explained the periodic intrusions of glacial water. These results emphasized that the location of the hillslope-fed channels at the whole floodplain scale might be actually more important than the type of water that feeds those channels.

The development of periphyton in the active floodplain was spatially and temporally restricted (Figures 22a and 23d) due to the high frequency of disturbance, in the form of streambed reworking and channel shift events (Figure 22b, c), and the invariably turbid water of the braids. This regime led to the paradox that the active zone received a constant water supply that could have supported periphyton, but such supply was concurrently too harsh for the development of periphyton. With that being said, the results showed that in some localized braids periphyton developed for short periods of time (Figures 22a, 23d; and 28c). The analysis of the braiding characteristics revealed a relationship between the appearance of periphyton (Figure 28c) and the increase in braiding intensity (Figure 28e). The explanation was that as the number of braids increased, the likelihood of having channels hydraulically less harsh and shallower also increased (Ashmore, 1988; Warburton and Davies, 1994; Ashmore et al., 2011). This created short windows of opportunity for the development of periphyton within the active floodplain.

6.1.4 What are the mechanisms, rates and time-scales associated with these patterns and how does the development of periphyton feed back into glacial forefield habitability?

The development of periphyton is thought to engineer the environment of glacial floodplains (see Chapter 2), primarily by reducing the rate at which water infiltrates into the glaciogenic sediment matrix (Miller and Lane, 2019) due to the accumulation of biomass within the benthic interstice space (Battin and Sengschmitt, 1999; Ibisch and Borchardt, 2002; Gette-Bouvarot et al., 2014). This is likely to increase the water available to the pioneering vegetation in these extremely well drained environments (Cooper, 1923; Matthews, 1992; Burga et al., 2010; Viles, 2012). In addition to this process, research in other environments has demonstrated that the development of periphyton may reduce the susceptibility of the substrate to being eroded, either by increasing the critical bed shear stress (Neumeier et al., 2006; Le Hir et al., 2007; Gerbersdorf et al., 2008b, 2009a; Vignaga et al., 2013; Fang et al., 2014; Thom et al.,

2015; Pivato et al., 2019) or by the potential modification of the near-bed turbulent structures (Kazemifar et al., 2021).

The absence of disturbances is a critical condition for a long-term engineering effect that positively feeds back into the habitability of the floodplain. First, periphyton need time to develop and this time has to be longer than the time between two consecutive disturbances. Second, if the time interval between two disturbances is long enough for the periphyton to develop, but some disturbances occur periodically, this has the potential effect of returning the streambed to its pre-engineering condition.

The findings of Chapters 2 and 3 therefore suggested that the positive feedback associated with periphyton development is restricted to the terrace channels that are rarely, if never, flooded by glacial water. These are fed by hillslope water (i.e., krenal and rhithral) and characterized by very low level of suspended sediments and absence of major streambed dislodgment events (Malard et al., 1999; Ward et al., 1999; Boix-Canadell et al., 2021; Brandani et al., 2022). The progressive shrinkage of the terrace channels (see Chapter 3) is thought to be the sole disturbance that impacts periphyton in these channels, but it also coincides with the end of the vegetation growing season, and likely has a minor impact on the ecosystem engineering effect *per se*.

Ecosystem engineering was then investigated mechanistically in Chapter 5. For the purposes of this study, two twin flumes mimicking the conditions of the terrace channels were installed in the vicinity of the forefield of the Otemma glacier. Two experiments were conducted: in the first one, periphyton developed for 54 days at constant conditions; in the second one, periphyton developed for 28 days and then experienced disturbances in the form of desiccation events. Throughout the entire length of the experiment, the flumes were imaged for photogrammetric purposes, and subsequent analysis of the evolution of the streambed (i.e., roughness and interstice filling). On the same regular basis, data on the evolution of rate at which water infiltrated into the sediments were also collected. Finally, the near-bed 3D velocities were collected at regular intervals, and their post-processing led to the characterization of the evolution of the bursting processes and the turbulent kinetic energy.

Chapter 5 demonstrated that the colonization of periphyton modified the surficial streambed morphology (Figures 32 and 33). Periphyton rapidly filled the surficial interstice space with biomass, and this had the result of smoothening the bed. The changes in bed roughness were reflected into the modification of the near-bed turbulent structures (Figures 34 and 35), and particularly in the reduction of the likelihood of sediment-entraining bursting processes (i.e., sweep and ejection events; see Bennet and Best, 1995; Dwivedi et al., 2011; Keylock et al., 2014) that could have eroded the periphyton mat. The accumulation of biomass in the surficial interstice space (i.e., bio-clogging) also modified the hydraulic conductivity of the streambed (Figures 32c and 33c). The results of Chapter 5 demonstrated that water infiltration was strongly reduced (up to 84%) during the experiments, and this regardless of the introduction of disturbances.

The natural consequence of the bed becoming less hydraulically conductive is more water flowing at the surface (Figure 37). In environments that are extremely well-drained, such as glacial forefields, this process becomes relevant because vegetation has access to a more sustainable water supply during the growth season.

6.2 Limitations and perspectives

This thesis asked three main research questions (Chapter 1) that were supported by a detailed literature review in Chapter 2 and addressed in Chapters 3 through 5. However, this research has limitations that need to be addressed and these are discussed here.

The use of high resolution and high frequency remote sensing techniques (Chapters 2 and 3) allowed for precise detection of periphyton, and the study of the physical habitat constraints to periphyton development. The key insights of these studies substantially contributed to the understanding of the ecological functioning of recently-deglaciated floodplains, and I argue that the use of more traditional techniques (e.g., biological sampling) would have not allowed understanding the ecological and morphodynamic complexity of such environments, both in time and in space. That said, however, the results of this thesis remain largely dependent on and related to the study site, the floodplain of the Otemma glacier. Although the formation of glacial floodplains, and their morphodynamic behavior (e.g., braiding, terraces, etc), is a common response to retreating glaciers (Carrivick et al., 2018), site-related differences may still exist. These differences (e.g., glacier extent; floodplain altitude, slope, orientation and size; or the presence of a proglacial lake) may result in different environmental conditions and constraints, and hence in different patterns of periphyton development. Furthermore, the results presented here referred to a single melt-season (2020), and may not be representative of seasons with different climatic conditions that might result in a greater or smaller morphodynamic forcing. In this regard, advances in remote sensing, particularly in satellite imagery, may represent an opportunity for future studies. High spatial and temporal resolution imagery is rapidly becoming more available, and this might unlock studies over much larger spatial (e.g., the Alps) and temporal (i.e., inter-season) scales, provided that such resolutions can approach those proposed in this thesis.

The study also revealed a critical limit in what can be mapped using high resolution optical remote sensing. The wider context for the thesis was biofilms; but as discussed above, the optical (i.e., RGB) imagery only really maps periphyton so missing important parts of the biofilm community. This was only really appreciated fully when we tried to relate the optical remote sensing results to chlorophyll-*a* data (Figure 38) and it suggests that other sensors mounted on UAV type platforms might be needed to appreciate the fuller role of biofilms in this environment. As technology progresses, miniaturized multi- or hyper-spectral sensors become available to UAVs (Su and Chou, 2015, Kislik et al., 2018; Chabot et al., 2018; Song and Park, 2020; Taddia et al., 2020; Harrison et al., 2020), and they may provide substantial opportunities for the study of biofilm communities, delivering results that likely

approach the richness of traditional sampling techniques, but at higher spatial and temporal resolutions.

This thesis also provided the first quantitative evidence of the ecosystem engineering effects of periphyton in proglacial floodplains (Chapter 5), corroborating the hypothesis made by Miller and Lane (2019) and in Chapter 2. Although the results were found relevant, they provided an understanding that was deeply related to the design of the flume experiments, which was a broad approximation of the tributary channels. In fact, running of flumes in an Alpine glacial environment limited the number of initial conditions (e.g., grainsize, discharge, solar radiation, etc.) that might characterize the tributary channels and that have a critical impact on how periphyton develop in such environments. In this regard, there is the need of new studies that account for different initial conditions, and that could possibly validate the results proposed in this thesis.

The call for new studies, both in terms of spatial and temporal periphyton development and in terms of ecosystem engineering, would foster the understanding of the functioning of proglacial margins in the Alps and beyond, particularly with regard of the current global retreat of glaciers. Furthermore, new studies in different proglacial margins and particularly over multiple seasons would allow challenging the ontogeny model proposed in Chapter 2, which to date remains largely theoretical regardless of the results provided in Chapter 5.

7. Conclusions

This thesis aimed to quantify the presence of periphyton and the drivers that control periphyton development in proglacial floodplains, and to investigate how the development of periphyton promotes primary succession through ecosystem engineering. The findings of this thesis lead to the following conclusions.

The harsh environment of proglacial floodplains exerts a strong control on periphyton. During the melt season, the presence of both high discharges and high rates of sediment supply leads to the continuous reworking of the stream accommodation space, thereby limiting the development of periphyton. However, the findings of this thesis demonstrate that the magnitude and the spatial extent of disturbances are not homogenous, and zones of geomorphic stability exist during the melt-season. These zones may support periphyton development, but their spatial and temporal extent is strongly constrained by the type of stability that is found in the floodplain. In the most active floodplain (i.e., where the glacial stream develops braids), stability appears when the stream system is highly braided. This condition results in shallower channels with minimal bed load, and hence favors the development of periphyton. This development is however ephemeral since the braids evolve through time. The most stable conditions are found over terraces that are disconnected from the braiding stream. This disconnection makes the terraces dry, and the development of periphyton is only possible in the presence of hillslope-fed channels. If this condition is met, periphyton may develop throughout the entire melt season.

The development of periphyton in the terrace channels results in the modification of the streambed properties of these channels. This thesis demonstrates that periphyton can rapidly decrease the bed roughness by filling the benthic interstice space with biomass. This process has two important effects. First, the modification of the bed roughness may change the near-bed turbulent structures, thereby reducing the occurrence of adverse bursting processes that can lead to periphyton mat detachment and increasing the accumulation of biomass within the grains. Second, the biomass accumulated within the grains clogs the streambed, and reduces the sediment hydraulic conductivity. The consequence of the bed being clogged is more water flowing at the surface, which results in a more sustainable water supply for vegetation throughout the growing season in these extremely well-drained environments.

The findings of this thesis therefore contribute to the wider understanding of the ecological functioning of recently-deglaciated floodplains, and they open new research frontiers that need to be addressed for a full understanding of such systems. Such new research is needed to evaluate the extent to which these findings are transferable to other systems, and if the feedbacks (i.e., ecosystem engineering) associated with the development of periphyton effectively have a long-term positive effect on vegetation colonization and development in pro-glacial margins.

8. References

Aberle, J., & Smart, G. M. (2003). The influence of roughness structure on flow resistance on steep slopes. *Journal of Hydraulic Research*, *41*(3), 259–269. https://doi.org/10.1080/00221680309499971

Adamsen, F. J., Pinter, P. J., Barnes, E. M., LaMorte, R. L., Wall, G. W., Leavitt, S. W., & Kimball, B. A. (1999). Measuring Wheat Senescence with a Digital Camera. *Crop Science*, *39*(3), cropsci1999.0011183X003900030019x. https://doi.org/10.2135/cropsci1999.0011183X003900030019x

Alley, R. B., Cuffey, K. M., Evenson, E. B., Strasser, J. C., Lawson, D. E., & Larson, G. J. (1997). How glaciers entrain and transport basal sediment: Physical constraints. *Quaternary Science Reviews*, *16*(9), 1017–1038. https://doi.org/10.1016/S0277-3791(97)00034-6

Amos, C. L., Bergamasco, A., Umgiesser, G., Cappucci, S., Cloutier, D., DeNat, L., Flindt, M., Bonardi, M., & Cristante, S. (2004). The stability of tidal flats in Venice Lagoon—The results of in-situ measurements using two benthic, annular flumes. *Journal of Marine Systems*, *51*(1), 211–241. https://doi.org/10.1016/j.jmarsys.2004.05.013

An, C., Parker, G., Hassan, M. A., & Fu, X. (2019). Can magic sand cause massive degradation of a gravel-bed river at the decadal scale? Shi-ting River, China. *Geomorphology*, *327*, 147–158. https://doi.org/10.1016/j.geomorph.2018.10.026

Ashmore, P., Bertoldi, W., & Tobias Gardner, J. (2011). Active width of gravel-bed braided rivers. *Earth Surface Processes and Landforms*, *36*(11), 1510–1521. https://doi.org/10.1002/esp.2182

Ashmore, P. E. (1988). Bed load transport in braided gravel-bed stream models. *Earth Surface Processes and Landforms*, *13*(8), 677–695. https://doi.org/10.1002/esp.3290130803

Ashworth, P. J., & Ferguson, R. I. (1986). Interrelationships of Channel Processes, Changes and Sediments in a Proglacial Braided River. *Geografiska Annaler: Series A, Physical Geography*, *68*(4), 361–371. https://doi.org/10.1080/04353676.1986.11880186

Aufdenkampe, A. K., Mayorga, E., Raymond, P. A., Melack, J. M., Doney, S. C., Alin, S. R., Aalto, R. E., & Yoo, K. (2011). Riverine coupling of biogeochemical cycles between land, oceans, and atmosphere. *Frontiers in Ecology and the Environment*, *9*(1), 53–60. https://doi.org/10.1890/100014

Bakker, M., Antoniazza, G., Odermatt, E., & Lane, S. N. (2019). Morphological Response of an Alpine Braided Reach to Sediment-Laden Flow Events. *Journal of Geophysical Research: Earth Surface*. https://doi.org/10.1029/2018JF004811

Bao, N., Lechner, A. M., Fletcher, A., Mulligan, D., Mellor, A., & Bai, Z. (2012). Comparison of relative radiometric normalization methods using pseudo-invariant features for change detection studies in rural and urban landscapes. *Journal of Applied Remote Sensing*, *6*(1), 063578. https://doi.org/10.1117/1.JRS.6.063578

Bardgett, R. D., & Walker, L. R. (2004). Impact of coloniser plant species on the development of decomposer microbial communities following deglaciation. *Soil Biology and Biochemistry*, *36*(3), 555–559. https://doi.org/10.1016/j.soilbio.2003.11.002

Bardgett Richard D, Richter Andreas, Bol Roland, Garnett Mark H, Bäumler Rupert, Xu Xingliang, Lopez-Capel Elisa, Manning David A.C, Hobbs Phil J, Hartley Ian

R, & Wanek Wolfgang. (2007). Heterotrophic microbial communities use ancient carbon following glacial retreat. *Biology Letters*, *3*(5), 487–490. https://doi.org/10.1098/rsbl.2007.0242

Battin, T. J., Besemer, K., Bengtsson, M. M., Romani, A. M., & Packmann, A. I. (2016). The ecology and biogeochemistry of stream biofilms. *Nature Reviews Microbiology*, *14*(4), 251–263. https://doi.org/10.1038/nrmicro.2016.15

Battin, T. J., Kaplan, L. A., Denis Newbold, J., & Hansen, C. M. E. (2003). Contributions of microbial biofilms to ecosystem processes in stream mesocosms. *Nature*, *426*(6965), 439–442. https://doi.org/10.1038/nature02152

Battin, T. J., & Sengschmitt, D. (1999). Linking Sediment Biofilms, Hydrodynamics, and River Bed Clogging: Evidence from a Large River. *Microbial Ecology*, *37*(3), 185–196. https://doi.org/10.1007/s002489900142

Battin, T. J., Wille, A., Psenner, R., & Richter, A. (2004). Large-scale environmental controls on microbial biofilms in high-alpine streams. *Biogeosciences*, *1*(2), 159–171.

Bätz, N., Verrecchia, E. P., & Lane, S. N. (2015). Organic matter processing and soil evolution in a braided river system. *CATENA*, *126*, 86–97. https://doi.org/10.1016/j.catena.2014.10.013

Bengtsson, M. M., Wagner, K., Schwab, C., Urich, T., & Battin, T. J. (2018). Light availability impacts structure and function of phototrophic stream biofilms across domains and trophic levels. *Molecular Ecology*, *27*(14), 2913–2925. https://doi.org/10.1111/mec.14696

Bennett, S. J., & Best, J. L. (1995). Mean flow and turbulence structure over fixed, two-dimensional dunes: Implications for sediment transport and bedform stability. *Sedimentology*, *42*(3), 491–513. https://doi.org/10.1111/j.1365-3091.1995.tb00386.x

Benyoucef, I., Blandin, E., Lerouxel, A., Jesus, B., Rosa, P., Méléder, V., Launeau, P., & Barillé, L. (2014). Microphytobenthos interannual variations in a north-European estuary (Loire estuary, France) detected by visible-infrared multispectral remote sensing. *Estuarine, Coastal and Shelf Science*, *136*, 43–52. https://doi.org/10.1016/j.ecss.2013.11.007

Bertin, S., Groom, J., & Friedrich, H. (2017). Isolating roughness scales of gravel-bed patches. *Water Resources Research*, *53*(8), 6841–6856. https://doi.org/10.1002/2016WR020205

Bertoldi, W., Zanoni, L., & Tubino, M. (2009). Planform dynamics of braided streams. *Earth Surface Processes and Landforms*, *34*(4), 547–557. https://doi.org/10.1002/esp.1755

Biggs, B. J. F. (1996). 2—Patterns in Benthic Algae of Streams. In R. J. Stevenson, M. L. Bothwell, & R. L. Lowe (Eds.), *Algal Ecology* (pp. 31–56). Academic Press. https://doi.org/10.1016/B978-012668450-6/50031-X

Biggs, B. J. F., & Close, M. E. (1989). Periphyton biomass dynamics in gravel bed rivers: The relative effects of flows and nutrients. *Freshwater Biology*, *22*(2), 209–231. https://doi.org/10.1111/j.1365-2427.1989.tb01096.x

Biggs, B. J. F., Goring, D. G., & Nikora, V. I. (1998). Subsidy and stress responses of stream periphyton to gradients in water velocity as a function of community growth form. *Journal of Phycology*, *34*(4), 598–607. https://doi.org/10.1046/j.1529-8817.1998.340598.x

Biggs, B. J. F., Smith, R. A., & Duncan, M. J. (1999). Velocity and Sediment Disturbance of Periphyton in Headwater Streams: Biomass and

Metabolism. *Journal of the North American Benthological Society*, *18*(2), 222–241. https://doi.org/10.2307/1468462

Biggs, B. J. F., & Thomsen, H. A. (1995). Disturbance of Stream Periphyton by Perturbations in Shear Stress: Time to Structural Failure and Differences in Community Resistance. *Journal of Phycology*, *31*(2), 233–241. https://doi.org/10.1111/j.0022-3646.1995.00233.x

Bioucas-Dias, J. M., Plaza, A., Camps-Valls, G., Scheunders, P., Nasrabadi, N., & Chanussot, J. (2013). Hyperspectral Remote Sensing Data Analysis and Future Challenges. *IEEE Geoscience and Remote Sensing Magazine*, *1*(2), 6–36. https://doi.org/10.1109/MGRS.2013.2244672

Bishop, C. M., & Nasrabadi, N. M. (2006). *Pattern recognition and machine learning* (Vol. 4, No. 4, p. 738). New York: springer.

Blanckaert, K., & Lemmin, U. (2006). Means of noise reduction in acoustic turbulence measurements. *Journal of Hydraulic Research*, *44*(1), 3–17. https://doi.org/10.1080/00221686.2006.9521657

Bogen, J., Xu, M., & Kennie, P. (2015). The impact of pro-glacial lakes on downstream sediment delivery in Norway: the impact of pro-glacial lakes. *Earth Surface Processes and Landforms*, *40*(7), 942–952. https://doi.org/10.1002/esp.3669

Boix Canadell, M., Gómez-Gener, L., Ulseth, A. J., Clémençon, M., Lane, S. N., & Battin, T. J. (2021). Regimes of primary production and their drivers in Alpine streams. *Freshwater Biology*, *66*(8), 1449–1463. https://doi.org/10.1111/fwb.13730

Boogert, N. J., Paterson, D. M., & Laland, K. N. (2006). The Implications of Niche Construction and Ecosystem Engineering for Conservation Biology. *BioScience*, *56*(7), 570–578. https://doi.org/10.1641/0006-3568(2006)56[570:TIONCA]2.0.CO;2

Brandani, J., Peter, H., Busi, S. B., Kohler, T. J., Fodelianakis, S., Ezzat, L., Michoud, G., Bourquin, M., Pramateftaki, P., Roncoroni, M., Lane, S. N., & Battin, T. J. (2022). Spatial patterns of benthic biofilm diversity among streams draining proglacial floodplains. *Frontiers in Microbiology*, *13*. https://www.frontiersin.org/articles/10.3389/fmicb.2022.948165

Brasington, J., Langham, J., & Rumsby, B. (2003). Methodological sensitivity of morphometric estimates of coarse fluvial sediment transport. *Geomorphology*, *53*(3), 299–316. https://doi.org/10.1016/S0169-555X(02)00320-3

Brasington, J., Rumsby, B. T., & McVey, R. A. (2000). Monitoring and modelling morphological change in a braided gravel-bed river using high resolution GPS-based survey. *Earth Surface Processes and Landforms*, *25*(9), 973–990. https://doi.org/10.1002/1096-9837(200008)25:9<973::AID-ESP111>3.0.CO;2-Y

Breugem, W. P., Boersma, B. J., & Uittenbogaard, R. E. (2006). The influence of wall permeability on turbulent channel flow. *Journal of Fluid Mechanics*, *562*, 35–72. https://doi.org/10.1017/S0022112006000887

Brown, L. E., Hannah, D. M., & Milner, A. M. (2007). Vulnerability of alpine stream biodiversity to shrinking glaciers and snowpacks. *Global Change Biology*, *13*(5), 958–966. https://doi.org/10.1111/j.1365-2486.2007.01341.x

Brückner, M. Z. M., Schwarz, C., Coco, G., Baar, A., Boechat Albernaz, M., & Kleinhans, M. G. (2021). Benthic species as mud patrol—Modelled effects of bioturbators and biofilms on large-scale estuarine mud and morphology. *Earth*

Surface Processes and Landforms, *46*(6), 1128–1144. https://doi.org/10.1002/esp.5080

Burga, C. A., Krüsi, B., Egli, M., Wernli, M., Elsener, S., Ziefle, M., Fischer, T., & Mavris, C. (2010). Plant succession and soil development on the foreland of the Morteratsch glacier (Pontresina, Switzerland): Straight forward or chaotic? *Flora - Morphology, Distribution, Functional Ecology of Plants*, *205*(9), 561–576. https://doi.org/10.1016/j.flora.2009.10.001

Burgherr, P., & Ward, J. V. (2001). Longitudinal and seasonal distribution patterns of the benthic fauna of an alpine glacial stream (Val Roseg, Swiss Alps). *Freshwater Biology*, *46*(12), 1705–1721. https://doi.org/10.1046/j.1365-2427.2001.00853.x

Burgherr, P., Ward, J. V., & Robinson, C. T. (2002). Seasonal variation in zoobenthos across habitat gradients in an alpine glacial floodplain (Val Roseg, Swiss Alps). *Journal of the North American Benthological Society*, *21*(4), 561–575. https://doi.org/10.2307/1468430

Butler, J., Lane, S., Chandler, J., & Porfiri, E. (2002). Through-Water Close Range Digital Photogrammetry in Flume and Field Environments. *The Photogrammetric Record*, *17*(99), 419–439. https://doi.org/10.1111/0031-868X.00196

Carbonneau, P. E., Lane, S. N., & Bergeron, N. E. (2004). Catchment-scale mapping of surface grain size in gravel bed rivers using airborne digital imagery: MAPPING GRAIN SIZE IN GRAVEL BED RIVERS. *Water Resources Research*, *40*(7). https://doi.org/10.1029/2003WR002759

Carbonneau, P. E., Dugdale, S. J., Breckon, T. P., Dietrich, J. T., Fonstad, M. A., Miyamoto, H., & Woodget, A. S. (2020a). Adopting deep learning methods for airborne RGB fluvial scene classification. *Remote Sensing of Environment*, *251*, 112107. https://doi.org/10.1016/j.rse.2020.112107

Carbonneau, P. E., Belletti, B., Micotti, M., Lastoria, B., Casaioli, M., Mariani, S., G. Marchetti & Bizzi, S. (2020b). UAV-based training for fully fuzzy classification of Sentinel-2 fluvial scenes. *Earth surface processes and landforms*, *45*(13), 3120-3140. https://doi.org/10.1002/esp.4955

Cardinale, B. J., Gelmann, E. R., & Palmer, M. A. (2004). Net spinning caddisflies as stream ecosystem engineers: The influence of Hydropsyche on benthic substrate stability. *Functional Ecology*, *18*(3), 381–387. https://doi.org/10.1111/j.0269-8463.2004.00865.x

Carrivick, J. L., Heckmann, T., Turner, A., & Fischer, M. (2018). An assessment of landform composition and functioning with the first proglacial systems dataset of the central European Alps. *Geomorphology*, *321*, 117–128. https://doi.org/10.1016/j.geomorph.2018.08.030

Carter, N. (1932). A Comparative Study of the Alga Flora of Two Salt Marshes. Part I. *Journal of Ecology*, *20*(2), 341–370. JSTOR. https://doi.org/10.2307/2256083

Carter, N. (1933a). A Comparative Study of the Alga Flora of Two Salt Marshes. Part II. *Journal of Ecology*, *21*(1), 128–208. JSTOR. https://doi.org/10.2307/2255878

Carter, N. (1933b). A Comparative Study of the Alga Flora of Two Salt Marshes. Part III. *Journal of Ecology*, *21*(2), 385–403. JSTOR. https://doi.org/10.2307/2256588

Caruso, A., Boano, F., Ridolfi, L., Chopp, D. L., & Packman, A. (2017). Biofilm-induced bioclogging produces sharp interfaces in hyporheic flow, redox conditions, and microbial community structure. *Geophysical Research Letters*, *44*(10), 4917–4925. https://doi.org/10.1002/2017GL073651

Cea, L., Puertas, J., & Pena, L. (2007). Velocity measurements on highly turbulent free surface flow using ADV. *Experiments in Fluids*, *42*(3), 333–348. https://doi.org/10.1007/s00348-006-0237-3

Chabot, D., Dillon, C., Shemrock, A., Weissflog, N., & Sager, E. (2018). An Object-Based Image Analysis Workflow for Monitoring Shallow-Water Aquatic Vegetation in Multispectral Drone Imagery. *ISPRS International Journal of Geo-Information*, *7*(8), 294. https://doi.org/10.3390/ijgi7080294

Chandler, J. H., Shiono, K., Rameshwaren, P., & Lane, S. N. (2001). Measuring Flume Surfaces for Hydraulics Research Using a Kodak DCS460. *The Photogrammetric Record*, *17*(97), 39–61. https://doi.org/10.1111/0031-868X.00167

Chapin, F. S., Walker, L. R., Fastie, C. L., & Sharman, L. C. (1994). Mechanisms of Primary Succession Following Deglaciation at Glacier Bay, Alaska. *Ecological Monographs*, *64*(2), 149–175. https://doi.org/10.2307/2937039

Chen, X. D., Zhang, C. K., Zhou, Z., Gong, Z., Zhou, J. J., Tao, J. F., Paterson, D. M., & Feng, Q. (2017). Stabilizing Effects of Bacterial Biofilms: EPS Penetration and Redistribution of Bed Stability Down the Sediment Profile: EPS Penetration Down Sediment Profile. *Journal of Geophysical Research: Biogeosciences*, *122*(12), 3113–3125. https://doi.org/10.1002/2017JG004050

Cheng, H. D., Jiang, X. H., Sun, Y., & Wang, J. (2001). Color image segmentation: Advances and prospects. *Pattern Recognition*, *34*(12), 2259–2281. https://doi.org/10.1016/S0031-3203(00)00149-7

Chew, L. C., & Ashmore, P. E. (2001). Channel adjustment and a test of rational regime theory in a proglacial braided stream. *Geomorphology*, *37*(1), 43–63. https://doi.org/10.1016/S0169-555X(00)00062-3

Chicco, D., & Jurman, G. (2020). The advantages of the Matthews correlation coefficient (MCC) over F1 score and accuracy in binary classification evaluation. *BMC Genomics*, *21*(1), 6. https://doi.org/10.1186/s12864-019-6413-7

Ciccazzo, S., Esposito, A., Borruso, L., & Brusetti, L. (2016). Microbial communities and primary succession in high altitude mountain environments. *Annals of Microbiology*, *66*(1), 43–60. https://doi.org/10.1007/s13213-015-1130-1

Clifford, N. J., Richards, K. S., Brown, R. A., & Lane, S. N. (1995). Scales of Variation of Suspended Sediment Concentration and Turbidity in a Glacial Meltwater Stream. *Geografiska Annaler: Series A, Physical Geography*, *77*(1–2), 45–65. https://doi.org/10.1080/04353676.1995.11880428

Combe, J.-P., Launeau, P., Carrère, V., Despan, D., Méléder, V., Barillé, L., & Sotin, C. (2005). Mapping microphytobenthos biomass by non-linear inversion of visible-infrared hyperspectral images. *Remote Sensing of Environment*, *98*(4), 371–387. https://doi.org/10.1016/j.rse.2005.07.010

Cooper, W. S. (1923). The Recent Ecological History of Glacier Bay, Alaska: The Present Vegetation Cycle. *Ecology*, *4*(3), 223–246. https://doi.org/10.2307/1929047

Cordier, S., Adamson, K., Delmas, M., Calvet, M., & Harmand, D. (2017). Of ice and water: Quaternary fluvial response to glacial forcing. *Quaternary Science Reviews*, *166*, 57–73. https://doi.org/10.1016/j.quascirev.2017.02.006

Costerton, J. W., Lewandowski, Z., Caldwell, D. E., Korber, D. R., & Lappin-Scott, H. M. (1995). Microbial Biofilms. *Annual Review of Microbiology*, *49*(1), 711–745. https://doi.org/10.1146/annurev.mi.49.100195.003431

Crisp, D. T., & Carling, P. A. (1989). Observations on siting, dimensions and structure of salmonid redds. *Journal of Fish Biology*, *34*(1), 119–134. https://doi.org/10.1111/j.1095-8649.1989.tb02962.x

Cullis, J. D. S., Stanish, L. F., & McKnight, D. M. (2014). Diel flow pulses drive particulate organic matter transport from microbial mats in a glacial meltwater

stream in the McMurdo Dry Valleys. *Water Resources Research*, *50*(1), 86–97. https://doi.org/10.1002/2013WR014061

Cunningham, A. B., Characklis, W. G., Abedeen, F., & Crawford, D. (1991). *Influence of biofilm accumulation on porous media hydrodynamics* (world). ACS Publications; American Chemical Society. https://doi.org/10.1021/es00019a013

Curran, J. H., Loso, M. G., & Williams, H. B. (2017). Glacial conditioning of stream position and flooding in the braid plain of the Exit Glacier foreland, Alaska. *Geomorphology*, *293*, 272–288. https://doi.org/10.1016/j.geomorph.2017.06.004

Dade, W. B., Davis, J. D., Nichols, P. D., Nowell, A. R. M., Thistle, D., Trexler, M. B., & White, D. C. (1990). Effects of bacterial exopolymer adhesion on the entrainment of sand. *Geomicrobiology Journal*, *8*(1), 1–16. https://doi.org/10.1080/01490459009377874

Dawkins, R. (1982). *the extended phenotype: the gene as the unit of selection*. 39660. https://repository.library.georgetown.edu/handle/10822/548737

de Boer, P. L. de. (1981). Mechanical effects of micro-organisms on intertidal bedform migration*. *Sedimentology*, *28*(1), 129–132. https://doi.org/10.1111/j.1365-3091.1981.tb01670.x

de Winter, I. L., Storms, J. E. A., & Overeem, I. (2012). Numerical modeling of glacial sediment production and transport during deglaciation. *Geomorphology*, *167–168*, 102–114. https://doi.org/10.1016/j.geomorph.2012.05.023

Demars, B. O. L. (2019). Hydrological pulses and burning of dissolved organic carbon by stream respiration. *Limnology and Oceanography*, *64*(1), 406–421. https://doi.org/10.1002/lno.11048

Dietrich, J. T. (2017). Bathymetric Structure-from-Motion: Extracting shallow stream bathymetry from multi-view stereo photogrammetry. *Earth Surface Processes and Landforms*, *42*(2), 355–364. https://doi.org/10.1002/esp.4060

Donoho, D. L., & Johnstone, I. M. (1994). Ideal spatial adaptation by wavelet shrinkage. *Biometrika*, *81*(3), 425–455. https://doi.org/10.1093/biomet/81.3.425

Du, Y., Teillet, P. M., & Cihlar, J. (2002). Radiometric normalization of multitemporal high-resolution satellite images with quality control for land cover change detection. *Remote Sensing of Environment*, *82*(1), 123–134. https://doi.org/10.1016/S0034-4257(02)00029-9

Dwivedi, A., Melville, B. W., Shamseldin, A. Y., & Guha, T. K. (2011). Flow structures and hydrodynamic force during sediment entrainment. *Water Resources Research*, *47*(1). https://doi.org/10.1029/2010WR009089

Egli, P. E., Irving, J., & Lane, S. N. (2021). Characterization of subglacial marginal channels using 3-D analysis of high-density ground-penetrating radar data. *Journal of Glaciology*, *67*(264), 759–772. https://doi.org/10.1017/jog.2021.26

Egozi, R., & Ashmore, P. (2008). Defining and measuring braiding intensity. *Earth Surface Processes and Landforms*, *33*(14), 2121–2138. https://doi.org/10.1002/esp.1658

Egozi, R., & Ashmore, P. (2009). Experimental analysis of braided channel pattern response to increased discharge. *Journal of Geophysical Research: Earth Surface*, *114*(F2). https://doi.org/10.1029/2008JF001099

Eichel, J. (2019). Vegetation Succession and Biogeomorphic Interactions in Glacier Forelands. In T. Heckmann & D. Morche (Eds.), *Geomorphology of Proglacial Systems: Landform and Sediment Dynamics in Recently Deglaciated Alpine*

Landscapes (pp. 327–349). Springer International Publishing. https://doi.org/10.1007/978-3-319-94184-4_19

Fang, H., Shang, Q., Chen, M., & He, G. (2014). Changes in the critical erosion velocity for sediment colonized by biofilm. *Sedimentology*, *61*(3), 648–659. https://doi.org/10.1111/sed.12065

Fang, H. W., Lai, H. J., Cheng, W., Huang, L., & He, G. J. (2017). Modeling sediment transport with an integrated view of the biofilm effects. *Water Resources Research*, *53*(9), 7536–7557. https://doi.org/10.1002/2017WR020628

Fastie, C. L. (1995). Causes and Ecosystem Consequences of Multiple Pathways of Primary Succession at Glacier Bay, Alaska. *Ecology*, *76*(6), 1899–1916. https://doi.org/10.2307/1940722

Finn, D. S., Räsänen, K., & Robinson, C. T. (2010). Physical and biological changes to a lengthening stream gradient following a decade of rapid glacial recession: smaller glaciers, longer streams. *Global Change Biology*, *16*(12), 3314–3326. https://doi.org/10.1111/j.1365-2486.2009.02160.x

Flemming, B. W. (2002). Chapter Six Geographic distribution of muddy coasts. In T. Healy, Y. Wang, & J.-A. Healy (Eds.), *Proceedings in Marine Science* (Vol. 4, pp. 99–201). Elsevier. https://doi.org/10.1016/S1568-2692(02)80080-8

Flemming, H.-C., Strathmann, M., & Morales, C. F. L. (2007). Microbial Effects. In B. Westrich & U. Förstner (Eds.), *Sediment Dynamics and Pollutant Mobility in Rivers: An Interdisciplinary Approach* (pp. 343–378). Springer Berlin Heidelberg. https://doi.org/10.1007/978-3-540-34785-9_9

Flemming, H.-C., & Wingender, J. (2010). The biofilm matrix. *Nature Reviews Microbiology*, *8*(9), 623–633. https://doi.org/10.1038/nrmicro2415

Flemming, H.-C., Wingender, J., Szewzyk, U., Steinberg, P., Rice, S. A., & Kjelleberg, S. (2016). Biofilms: An emergent form of bacterial life. *Nature Reviews Microbiology*, *14*(9), 563–575. https://doi.org/10.1038/nrmicro.2016.94

Flemming, H.-C., & Wuertz, S. (2019). Bacteria and archaea on Earth and their abundance in biofilms. *Nature Reviews Microbiology*, *17*(4), 247–260. https://doi.org/10.1038/s41579-019-0158-9

Flynn, K., & Chapra, S. (2014). Remote Sensing of Submerged Aquatic Vegetation in a Shallow Non-Turbid River Using an Unmanned Aerial Vehicle. *Remote Sensing*, *6*(12), 12815–12836. https://doi.org/10.3390/rs61212815

Fonstad, M. A., Dietrich, J. T., Courville, B. C., Jensen, J. L., & Carbonneau, P. E. (2013). Topographic structure from motion: A new development in photogrammetric measurement. *Earth Surface Processes and Landforms*, *38*(4), 421–430. https://doi.org/10.1002/esp.3366

Fountain, A. G. (1996). Effect of Snow and Firn Hydrology on the Physical and Chemical Characteristics of Glacial Runoff. *Hydrological Processes*, *10*(4), 509–521. https://doi.org/10.1002/(SICI)1099-1085(199604)10:4<509::AID-HYP389>3.0.CO;2-3

Francoeur, S. N., & Biggs, B. J. F. (2006). Short-term Effects of Elevated Velocity and Sediment Abrasion on Benthic Algal Communities. *Hydrobiologia*, *561*(1), 59–69. https://doi.org/10.1007/s10750-005-1604-4

Freeman, C., & Lock, M. A. (1995). The biofilm polysaccharide matrix: A buffer against changing organic substrate supply? *Limnology and Oceanography*, *40*(2), 273–278. https://doi.org/10.4319/lo.1995.40.2.0273

Frey, B., Bühler, L., Schmutz, S., Zumsteg, A., & Furrer, G. (2013). Molecular characterization of phototrophic microorganisms in the forefield of a receding

glacier in the Swiss Alps. *Environmental Research Letters*, *8*(1), 015033. https://doi.org/10.1088/1748-9326/8/1/015033

Fryer, J. G., & Kniest, H. T. (1985). Errors in Depth Determination Caused by Waves in Through-Water Photogrammetry. *The Photogrammetric Record*, *11*(66), 745–753. https://doi.org/10.1111/j.1477-9730.1985.tb01326.x

Füreder, L. (1999). High alpine streams: Cold habitats for insect larvae. In R. Margesin & F. Schinner (Eds.), *Cold-Adapted Organisms* (pp. 181–196). Springer Berlin Heidelberg. https://doi.org/10.1007/978-3-662-06285-2_10

Gabbud, C., Robinson, C. T., & Lane, S. N. (2019). Summer is in winter: Disturbance-driven shifts in macroinvertebrate communities following hydroelectric power exploitation. *Science of The Total Environment*, *650*, 2164–2180. https://doi.org/10.1016/j.scitotenv.2018.09.180

Gerbersdorf, S. U., Manz, W., & Paterson, D. M. (2008a). The engineering potential of natural benthic bacterial assemblages in terms of the erosion resistance of sediments. FEMS microbiology ecology, 66(2), 282-294. https://doi.org/10.1111/j.1574-6941.2008.00586.x

Gerbersdorf, S. U., Jancke, T., Westrich, B., & Paterson, D. M. (2008b). Microbial stabilization of riverine sediments by extracellular polymeric substances. *Geobiology*, *6*(1), 57–69. https://doi.org/10.1111/j.1472-4669.2007.00120.x

Gerbersdorf, S. U., Westrich, B., & Paterson, D. M. (2009a). Microbial Extracellular Polymeric Substances (EPS) in Fresh Water Sediments. *Microbial Ecology*, *58*(2), 334–349. https://doi.org/10.1007/s00248-009-9498-8

Gerbersdorf, S. U., Bittner, R., Lubarsky, H., Manz, W., & Paterson, D. M. (2009b). Microbial assemblages as ecosystem engineers of sediment stability. Journal of Soils and Sediments, 9, 640-652. https://doi.org/10.1007/s11368-009-0142-5

Gerbersdorf, S. U., & Wieprecht, S. (2015). Biostabilization of cohesive sediments: Revisiting the role of abiotic conditions, physiology and diversity of microbes, polymeric secretion, and biofilm architecture. *Geobiology*, *13*(1), 68–97. https://doi.org/10.1111/gbi.12115

Germanoski, D., & Schumm, S. A. (1993). Changes in Braided River Morphology Resulting from Aggradation and Degradation. *The Journal of Geology*, *101*(4), 451–466. https://doi.org/10.1086/648239

Gette-Bouvarot, M., Mermillod-Blondin, F., Angulo-Jaramillo, R., Delolme, C., Lemoine, D., Lassabatere, L., Loizeau, S., & Volatier, L. (2014). Coupling hydraulic and biological measurements highlights the key influence of algal biofilm on infiltration basin performance. *Ecohydrology*, *7*(3), 950–964. https://doi.org/10.1002/eco.1421

Gimbert, F., Tsai, V. C., Amundson, J. M., Bartholomaus, T. C., & Walter, J. I. (2016). Subseasonal changes observed in subglacial channel pressure, size, and sediment transport: SUBGLACIAL HYDROLOGY FROM SEISMIC NOISE. *Geophysical Research Letters*, *43*(8), 3786–3794. https://doi.org/10.1002/2016GL068337

Gitelson, A. A., Kaufman, Y. J., Stark, R., & Rundquist, D. (2002). Novel algorithms for remote estimation of vegetation fraction. *Remote Sensing of Environment*, *80*(1), 76–87. https://doi.org/10.1016/S0034-4257(01)00289-9

Godillot, R., Caussade, B., Ameziane, T., & Capblancq, J. (2001). Interplay between turbulence and periphyton in rough open-channel flow. *Journal of Hydraulic Research*, *39*(3), 227–239. https://doi.org/10.1080/00221680109499826

Goring, D. G., & Nikora, V. I. (2002). Despiking Acoustic Doppler Velocimeter Data. *Journal of Hydraulic Engineering*, *128*(1), 117–126. https://doi.org/10.1061/(ASCE)0733-9429(2002)128:1(117)

Grant, J., & Gust, G. (1987). Prediction of coastal sediment stability from photopigment content of mats of purple sulphur bacteria. *Nature*, *330*(6145), 244. https://doi.org/10.1038/330244a0

Gurnell, A. (2014). Plants as river system engineers. *Earth Surface Processes and Landforms*, *39*(1), 4–25. https://doi.org/10.1002/esp.3397

Gurnell, A. M., & Petts, G. E. (2002). Island-dominated landscapes of large floodplain rivers, a European perspective. *Freshwater Biology*, *47*(4), 581–600. https://doi.org/10.1046/j.1365-2427.2002.00923.x

Harrison, L. R., Legleiter, C. J., Overstreet, B. T., Bell, T. W., & Hannon, J. (2020). Assessing the potential for spectrally based remote sensing of salmon spawning locations. *River Research and Applications*, *36*(8), 1618–1632. https://doi.org/10.1002/rra.3690

Harvey, A. H., Gallagher, J. S., & Sengers, J. M. H. L. (1998). Revised Formulation for the Refractive Index of Water and Steam as a Function of Wavelength, Temperature and Density. *Journal of Physical and Chemical Reference Data*, *27*(4), 761–774. https://doi.org/10.1063/1.556029

Hastings, A., Byers, J. E., Crooks, J. A., Cuddington, K., Jones, C. G., Lambrinos, J. G., Talley, T. S., & Wilson, W. G. (2007). Ecosystem engineering in space and time. *Ecology Letters*, *10*(2), 153–164. https://doi.org/10.1111/j.1461-0248.2006.00997.x

Hawes, I., & Howard-Williams, C. (1998). Primary Production Processes in Streams of the Mcmurdo Dry Valleys, Antarctica. In *Ecosystem Dynamics in a Polar Desert: The Mcmurdo Dry Valleys, Antarctica* (pp. 129–140). American Geophysical Union (AGU). https://doi.org/10.1029/AR072p0129

Heckmann, T., McColl, S., & Morche, D. (2016). Retreating ice: Research in pro-glacial areas matters. *Earth Surface Processes and Landforms*, *41*(2), 271–276. https://doi.org/10.1002/esp.3858

Hodgkins, R. (1996). Seasonal trend in suspended-sediment transport from an Arctic glacier, and implications for drainage-system structure. *Annals of Glaciology*, *22*, 147–151. https://doi.org/10.3189/1996AoG22-1-147-151

Holland, A. F., Zingmark, R. G., & Dean, J. M. (1974). Quantitative evidence concerning the stabilization of sediments by marine benthic diatoms. *Marine Biology*, *27*(3), 191–196. https://doi.org/10.1007/BF00391943

Hondzo, M., & Wang, H. (2002). Effects of turbulence on growth and metabolism of periphyton in a laboratory flume. *Water Resources Research*, *38*(12), 13-1-13–19. https://doi.org/10.1029/2002WR001409

Hong, L. B., & Davies, T. R. H. (1979). A study of stream braiding. *GSA Bulletin*, *90*(12_Part_II), 1839–1859. https://doi.org/10.1130/GSAB-P2-90-1839

Horner, R. R., & Welch, E. B. (1981). Stream Periphyton Development in Relation to Current Velocity and Nutrients. *Canadian Journal of Fisheries and Aquatic Sciences*, *38*(4), 449–457. https://doi.org/10.1139/f81-062

Horner, R. R., Welch, E. B., Seeley, M. R., & Jacoby, J. M. (1990). Responses of periphyton to changes in current velocity, suspended sediment and phosphorus concentration. *Freshwater Biology*, *24*(2), 215–232. https://doi.org/10.1111/j.1365-2427.1990.tb00704.x

Hotaling, S., Hood, E., & Hamilton, T. L. (2017). Microbial ecology of mountain glacier ecosystems: Biodiversity, ecological connections and implications of a warming

climate: Microbial ecology of mountain glaciers. *Environmental Microbiology*, *19*(8), 2935–2948. https://doi.org/10.1111/1462-2920.13766

House, R. A., & Boehne, P. L. (1986). Effects of Instream Structures on Salmonid Habitat and Populations in Tobe Creek, Oregon. *North American Journal of Fisheries Management*, *6*(1), 38–46. https://doi.org/10.1577/1548-8659(1986)6<38:EOISOS>2.0.CO;2

Howard, A. D., Keetch, M. E., & Vincent, C. L. (1970). Topological and Geometrical Properties of Braided Streams. *Water Resources Research*, *6*(6), 1674–1688. https://doi.org/10.1029/WR006i006p01674

Hoyle, J. T., Kilroy, C., Hicks, D. M., & Brown, L. (2017). The influence of sediment mobility and channel geomorphology on periphyton abundance. *Freshwater Biology*, *62*(2), 258–273. https://doi.org/10.1111/fwb.12865

Ibisch, R. B., & Borchardt, D. (2002). Effects of periphyton biomass and suspended solids on river bed permeability and hyporheic oxygen balances. *SIL Proceedings, 1922-2010*, *28*(4), 1875–1879. https://doi.org/10.1080/03680770.2001.11901954

Jacobsen, D., Milner, A. M., Brown, L. E., & Dangles, O. (2012). Biodiversity under threat in glacier-fed river systems. *Nature Climate Change*, *2*(5), 361–364. https://doi.org/10.1038/nclimate1435

James, M. R., Antoniazza, G., Robson, S., & Lane, S. N. (2020). Mitigating systematic error in topographic models for geomorphic change detection: Accuracy, precision and considerations beyond off-nadir imagery. *Earth Surface Processes and Landforms*, *45*(10), 2251–2271. https://doi.org/10.1002/esp.4878

James, M. R., & Robson, S. (2014). Mitigating systematic error in topographic models derived from UAV and ground-based image networks. *Earth Surface Processes and Landforms*, *39*(10), 1413–1420. https://doi.org/10.1002/esp.3609

James, M. R., Robson, S., d'Oleire-Oltmanns, S., & Niethammer, U. (2017). Optimising UAV topographic surveys processed with structure-from-motion: Ground control quality, quantity and bundle adjustment. *Geomorphology*, *280*, 51–66. https://doi.org/10.1016/j.geomorph.2016.11.021

Johnson, M. F., Reid, I., Rice, S. P., & Wood, P. J. (2009). Stabilization of fine gravels by net-spinning caddisfly larvae. *Earth Surface Processes and Landforms*, *34*(3), 413–423. https://doi.org/10.1002/esp.1750

Jones, C. G., Lawton, J. H., & Shachak, M. (1994). Organisms as Ecosystem Engineers. *Oikos*, *69*(3), 373–386. JSTOR. https://doi.org/10.2307/3545850

Jones, C. G., Lawton, J. H., & Shachak, M. (1997). Positive and Negative Effects of Organisms as Physical Ecosystem Engineers. *Ecology*, *78*(7), 1946–1957. https://doi.org/10.1890/0012-9658(1997)078[1946:PANEOO]2.0.CO;2

Kasprak, A., Wheaton, J. M., Ashmore, P. E., Hensleigh, J. W., & Peirce, S. (2015). The relationship between particle travel distance and channel morphology: Results from physical models of braided rivers. *Journal of Geophysical Research: Earth Surface*, *120*(1), 55–74. https://doi.org/10.1002/2014JF003310

Kaštovská, K., Elster, J., Stibal, M., & Šantrůčková, H. (2005). Microbial Assemblages in Soil Microbial Succession After Glacial Retreat in Svalbard (High Arctic). *Microbial Ecology*, *50*(3), 396–407. https://doi.org/10.1007/s00248-005-0246-4

Kaufmann, R. (2001). Invertebrate Succession on an Alpine Glacier Foreland. *Ecology*, *82*(8), 2261–2278. https://doi.org/10.1890/0012-9658(2001)082[2261:ISOAAG]2.0.CO;2

Kawashima, S., & Nakatani, M. (1998). An Algorithm for Estimating Chlorophyll Content in Leaves Using a Video Camera. *Annals of Botany*, *81*(1), 49–54. https://doi.org/10.1006/anbo.1997.0544

Kazemifar, F., Blois, G., Aybar, M., Perez Calleja, P., Nerenberg, R., Sinha, S., Hardy, R. J., Best, J., Sambrook Smith, G. H., & Christensen, K. T. (2021). The Effect of Biofilms on Turbulent Flow Over Permeable Beds. *Water Resources Research*, *57*(2), e2019WR026032. https://doi.org/10.1029/2019WR026032

Kazemipour, F., Launeau, P., & Méléder, V. (2012). Microphytobenthos biomass mapping using the optical model of diatom biofilms: Application to hyperspectral images of Bourgneuf Bay. *Remote Sensing of Environment*, *127*, 1–13. https://doi.org/10.1016/j.rse.2012.08.016

Keylock, C. J., Lane, S. N., & Richards, K. S. (2014). Quadrant/octant sequencing and the role of coherent structures in bed load sediment entrainment. *Journal of Geophysical Research: Earth Surface*, *119*(2), 264–286. https://doi.org/10.1002/2012JF002698

Kislik, C., Dronova, I., & Kelly, M. (2018). UAVs in Support of Algal Bloom Research: A Review of Current Applications and Future Opportunities. *Drones*, *2*(4), 35. https://doi.org/10.3390/drones2040035

Kulessa, B., Booth, A. D., Hobbs, A., & Hubbard, A. L. (2008). Automated monitoring of subglacial hydrological processes with ground-penetrating radar (GPR) at high temporal resolution: Scope and potential pitfalls. *Geophysical Research Letters*, *35*(24). https://doi.org/10.1029/2008GL035855

Kumar, L., Skidmore, A. K., & Knowles, E. (1997). Modelling topographic variation in solar radiation in a GIS environment. *International Journal of Geographical Information Science*, *11*(5), 475–497. https://doi.org/10.1080/136588197242266

Labiod, C., Godillot, R., & Caussade, B. (2007). The relationship between stream periphyton dynamics and near-bed turbulence in rough open-channel flow. *Ecological Modelling*, *209*(2), 78–96. https://doi.org/10.1016/j.ecolmodel.2007.06.011

Lamberti, G. A., Ashkenas, L. R., Gregory, S. V., & Steinman, A. D. (1987). Effects of Three Herbivores on Periphyton Communities in Laboratory Streams. *Journal of the North American Benthological Society*. https://doi.org/10.2307/1467219

Lane, S. N., Bakker, M., Gabbud, C., Micheletti, N., & Saugy, J.-N. (2017). Sediment export, transient landscape response and catchment-scale connectivity following rapid climate warming and Alpine glacier recession. *Geomorphology*, *277*, 210–227. https://doi.org/10.1016/j.geomorph.2016.02.015

Lane, S. N., Chandler, J. H., & Porfiri, K. (2001). Monitoring River Channel and Flume Surfaces with Digital Photogrammetry. *Journal of Hydraulic Engineering*, *127*(10), 871–877. https://doi.org/10.1061/(ASCE)0733-9429(2001)127:10(871)

Lane, S. N., Gentile, A., & Goldenschue, L. (2020). Combining UAV-Based SfM-MVS Photogrammetry with Conventional Monitoring to Set Environmental Flows: Modifying Dam Flushing Flows to Improve Alpine Stream Habitat. *Remote Sensing*, *12*(23), 23. https://doi.org/10.3390/rs12233868

Lane, S. N., & Nienow, P. W. (2019). Decadal-Scale Climate Forcing of Alpine Glacial Hydrological Systems. *Water Resources Research*, *55*(3), 2478–2492. https://doi.org/10.1029/2018WR024206

Lane, S. N., & Richards, K. S. (1997). Linking River Channel Form and Process: Time, Space and Causality Revisited. *Earth Surface Processes and Landforms*, *22*(3), 249–260. https://doi.org/10.1002/(SICI)1096-9837(199703)22:3<249::AID-ESP752>3.0.CO;2-7

Lane, S. N., Richards, K. S., & Chandler, J. H. (1996). Discharge and sediment supply controls on erosion and deposition in a dynamic alluvial channel. *Geomorphology*, *15*(1), 1–15. https://doi.org/10.1016/0169-555X(95)00113-J

Lane, S. N., Westaway, R. M., & Murray Hicks, D. (2003). Estimation of erosion and deposition volumes in a large, gravel-bed, braided river using synoptic remote sensing. *Earth Surface Processes and Landforms*, *28*(3), 249–271. https://doi.org/10.1002/esp.483

Launeau, P., Méléder, V., Verpoorter, C., Barillé, L., Kazemipour-Ricci, F., Giraud, M., Jesus, B., & Le Menn, E. (2018). Microphytobenthos Biomass and Diversity Mapping at Different Spatial Scales with a Hyperspectral Optical Model. *Remote Sensing*, *10*(5), 716. https://doi.org/10.3390/rs10050716

Lavandier, P., & Décamps, H. (1984). Estaragne. In B. A. Whitton (Ed.) Ecology of Europeanrivers (pp. 237– 264). Oxford: Blackwell Scientific Publications.

Lawton, J. H., & Jones, C. G. (1993). Linking species and ecosystem perspectives. *Trends in Ecology & Evolution*, *8*(9), 311–313. https://doi.org/10.1016/0169-5347(93)90236-I

Le Hir, P., Monbet, Y., & Orvain, F. (2007). Sediment erodability in sediment transport modelling: Can we account for biota effects? *Continental Shelf Research*, *27*(8), 1116–1142. https://doi.org/10.1016/j.csr.2005.11.016

Leduc, P., Peirce, S., & Ashmore, P. (2019). Short communication: Challenges and applications of structure-from-motion photogrammetry in a physical model of a braided river. *Earth Surface Dynamics*, *7*(1), 97–106. https://doi.org/10.5194/esurf-7-97-2019

Leopold, L. B., Wolman, M. G., & Miller, J. P. (1964). *Fluvial processes in geomorphology*. https://pubs.er.usgs.gov/publication/70185663

Liu, Y., Yano, T., Nishiyama, S., & Kimura, R. (2007). Radiometric correction for linear change-detection techniques: Analysis in bi-temporal space. *International Journal of Remote Sensing*, *28*(22), 5143–5157. https://doi.org/10.1080/01431160701268954

Louhaichi, M., Borman, M. M., & Johnson, D. E. (2001). Spatially Located Platform and Aerial Photography for Documentation of Grazing Impacts on Wheat. *Geocarto International*, *16*(1), 65–70. https://doi.org/10.1080/10106040108542184

Luce, J. J., Cattaneo, A., & Lapointe, M. F. (2010). Spatial patterns in periphyton biomass after low-magnitude flow spates: Geomorphic factors affecting patchiness across gravel–cobble riffles. *Journal of the North American Benthological Society*, *29*(2), 614–626. https://doi.org/10.1899/09-059.1

Luce, J. J., Lapointe, M. F., Roy, A. G., & Ketterling, D. B. (2013). The effects of sand abrasion of a predominantly stable stream bed on periphyton biomass losses: effects of sand abrasion of a stable stream bed on periphyton biomass losses. *Ecohydrology*, *6*(4), 689–699. https://doi.org/10.1002/eco.1332

Mair, D., Nienow, P., Sharp, M. J., Wohlleben, T., & Willis, I. (2002). Influence of subglacial drainage system evolution on glacier surface motion: Haut Glacier d'Arolla, Switzerland. *Journal of Geophysical Research*, *107*(B8). https://doi.org/10.1029/2001JB000514

Maizels, J. (2002). 9—Sediments and landforms of modern proglacial terrestrial environments. In J. Menzies (Ed.), *Modern and Past Glacial Environments* (pp. 279–316). Butterworth-Heinemann. https://doi.org/10.1016/B978-075064226-2/50012-X

Malard, F., Tockner, K., & Ward, J. V. (1999). Shifting Dominance of Subcatchment Water Sources and Flow Paths in a Glacial Floodplain, Val Roseg, Switzerland. *Arctic, Antarctic, and Alpine Research*, *31*(2), 135–150. https://doi.org/10.1080/15230430.1999.12003291

Mancini, D., & Lane, S. N. (2020). Changes in sediment connectivity following glacial debuttressing in an Alpine valley system. *Geomorphology*, *352*, 106987. https://doi.org/10.1016/j.geomorph.2019.106987

Mancini, D., Roncoroni, M. and Lane, S.N. (in preparation, a). UAV- SfM photogrammetry of braided river morphodynamics using heuristic representation of inundated zones.

Mancini, D., Nicholas, A., Roncoroni, M. and Lane, S.N. (in preparation, b). Morphodynamic shredding of subglacial export by proglacial forefield in a context of rapid glacier retreat.

Mancini, D., Dietze, M., Muller, T., Jenkin, M., Miesen, F., Roncoroni, M., Nicholas, A. and Lane, S.N. (in review). Rapid shredding of subglacial sediment export signal by proglacial forefields. Geophysical Research Letters - Earth Surface.

Mao, L., & Carrillo, R. (2017). Temporal dynamics of suspended sediment transport in a glacierized Andean basin. *Geomorphology*, *287*, 116–125. https://doi.org/10.1016/j.geomorph.2016.02.003

Mao, L., Comiti, F., Carrillo, R., & Penna, D. (2019). Sediment Transport in Proglacial Rivers. In T. Heckmann & D. Morche (Eds.), *Geomorphology of Proglacial Systems* (pp. 199–217). Springer International Publishing. https://doi.org/10.1007/978-3-319-94184-4_12

Marcus, W. A., & Fonstad, M. A. (2008). Optical remote mapping of rivers at sub-meter resolutions and watershed extents. *Earth Surface Processes and Landforms*, *33*(1), 4–24. https://doi.org/10.1002/esp.1637

Mariotti, G., & Fagherazzi, S. (2012). Modeling the effect of tides and waves on benthic biofilms. *Journal of Geophysical Research: Biogeosciences*, *117*(G4). https://doi.org/10.1029/2012JG002064

Marren, P. M. (2002). Glacier margin fluctuations, Skaftafellsjökull, Iceland: Implications for sandur evolution. *Boreas*, *31*(1), 75–81. https://doi.org/10.1111/j.1502-3885.2002.tb01057.x

Marren, P. M. (2005). Magnitude and frequency in proglacial rivers: A geomorphological and sedimentological perspective. *Earth-Science Reviews*, *70*(3), 203–251. https://doi.org/10.1016/j.earscirev.2004.12.002

Marren, P. M., & Toomath, S. C. (2013). Fluvial adjustments in response to glacier retreat: Skaftafellsjökull, Iceland. *Boreas*, *42*(1), 57–70. https://doi.org/10.1111/j.1502-3885.2012.00275.x

Marren, P. M., & Toomath, S. C. (2014). Channel pattern of proglacial rivers: Topographic forcing due to glacier retreat. *Earth Surface Processes and Landforms*, *39*(7), 943–951. https://doi.org/10.1002/esp.3545

Matthews, J. A. (1992). *The Ecology of Recently-deglaciated Terrain: A Geoecological Approach to Glacier Forelands*. Cambridge University Press.

McKnight, D. M., Tate, C. M., Andrews, E. D., Niyogi, D. K., Cozzetto, K., Welch, K., Lyons, W. B., & Capone, D. G. (2007). Reactivation of a cryptobiotic stream ecosystem in the McMurdo Dry Valleys, Antarctica: A long-term geomorphological experiment. *Geomorphology*, *89*(1–2), 186–204. https://doi.org/10.1016/j.geomorph.2006.07.025

Méléder, V., Launeau, P., Barillé, L., & Rincé, Y. (2003). Microphytobenthos assemblage mapping by spatial visible-infrared remote sensing in a shellfish

ecosystem. *Comptes rendus biologies*, *326*(4), 377–389. https://doi.org/10.1016/S1631-0691(03)00125-2
Meyer, G. E., & Neto, J. C. (2008). Verification of color vegetation indices for automated crop imaging applications. *Computers and Electronics in Agriculture*, *63*(2), 282–293. https://doi.org/10.1016/j.compag.2008.03.009
Meyer G. E., T. Mehta, M. F. Kocher, D. A. Mortensen, & A. Samal. (1998). Textural imaging and discriminant analysis for distinguishingweeds for spot spraying. *Transactions of the ASAE*, *41*(4), 1189–1197. https://doi.org/10.13031/2013.17244
Mianaei, S. J., & Keshavarzi, A. R. (2010). Study of near bed stochastic turbulence and sediment entrainment over the ripples at the bed of open channel using image processing technique. *Stochastic Environmental Research and Risk Assessment*, *24*(5), 591–598. https://doi.org/10.1007/s00477-009-0346-7
Milan, D. J., Heritage, G. L., Large, A. R. G., & Fuller, I. C. (2011). Filtering spatial error from DEMs: Implications for morphological change estimation. *Geomorphology*, *125*(1), 160–171. https://doi.org/10.1016/j.geomorph.2010.09.012
Miller, H. R., & Lane, S. N. (2019). Biogeomorphic feedbacks and the ecosystem engineering of recently deglaciated terrain. *Progress in Physical Geography: Earth and Environment*, *43*(1), 24–45. https://doi.org/10.1177/0309133318816536
Milner, A. M., Brown, L. E., & Hannah, D. M. (2009). Hydroecological response of river systems to shrinking glaciers. *Hydrological Processes*, *23*(1), 62–77. https://doi.org/10.1002/hyp.7197
Milner, A. M., & Petts, G. E. (1994). Glacial rivers: Physical habitat and ecology. *Freshwater Biology*, *32*(2), 295–307. https://doi.org/10.1111/j.1365-2427.1994.tb01127.x
Montgomery, D. R., Buffington, J. M., Peterson, N. P., Schuett-Hames, D., & Quinn, T. P. (1996). Stream-bed scour, egg burial depths, and the influence of salmonid spawning on bed surface mobility and embryo survival. *Canadian Journal of Fisheries and Aquatic Sciences*, *53*(5), 1061–1070. https://doi.org/10.1139/f96-028
Moon, T. (2017). Saying goodbye to glaciers. *Science*, *356*(6338), 580–581. https://doi.org/10.1126/science.aam9625
Moore, J. W. (2006). Animal Ecosystem Engineers in Streams. *BioScience*, *56*(3), 237–246. https://doi.org/10.1641/0006-3568(2006)056[0237:AEEIS]2.0.CO;2
Morgan, J. A., Brogan, D. J., & Nelson, P. A. (2017). Application of Structure-from-Motion photogrammetry in laboratory flumes. *Geomorphology*, *276*, 125–143. https://doi.org/10.1016/j.geomorph.2016.10.021
Mosley, M. P. (1982). Analysis of the effect of changing discharge on channel morphology and instream uses in a Braided River, Ohau River, New Zealand. *Water Resources Research*, *18*(4), 800–812. https://doi.org/10.1029/WR018i004p00800
Mulholland, P. J., Steinman, A. D., Marzolf, E. R., Hart, D. R., & DeAngelis, D. L. (1994). Effect of periphyton biomass on hydraulic characteristics and nutrient cycling in streams. *Oecologia*, *98*(1), 40–47. https://doi.org/10.1007/BF00326088
Müller, T., Lane, S. N., & Schaefli, B. (2022). Towards a hydrogeomorphological understanding of proglacial catchments: An assessment of groundwater storage and release in an Alpine catchment. *Hydrology and Earth System Sciences*, *26*(23), 6029–6054. https://doi.org/10.5194/hess-26-6029-2022

Müller, T., Roncoroni, M., Mancini, D., Lane, S.N. and Schaefli, B. (in review). Current and future role of meltwater-groundwater dynamics in a proglacial Alpine outwash plain. EGUsphere, 1-34.

Nelson, J. M., Shreve, R. L., McLean, S. R., & Drake, T. G. (1995). Role of Near-Bed Turbulence Structure in Bed Load Transport and Bed Form Mechanics. *Water Resources Research*, *31*(8), 2071–2086. https://doi.org/10.1029/95WR00976

Neumann, A. C., Gebelein, C. D., & Scoffin, T. P. (1970). The Composition, Structure and Erodability of Subtidal Mats, Abaco, Bahamas. *Journal of Sedimentary Research*, *40*(1). http://archives.datapages.com/data/sepm/journals/v38-41/data/040/040001/0274.htm

Neumeier, U., Lucas, C. H., & Collins, M. (2006). Erodibility and erosion patterns of mudflat sediments investigated using an annular flume. *Aquatic Ecology*, *40*(4), 543–554. https://doi.org/10.1007/s10452-004-0189-8

Nezu, I., & Nakagawa, H. (1993). Turbulence in open-channel flows. Routledge.

Niederdorfer, R., Besemer, K., Battin, T. J., & Peter, H. (2017). Ecological strategies and metabolic trade-offs of complex environmental biofilms. *Npj Biofilms and Microbiomes*, *3*(1), 21. https://doi.org/10.1038/s41522-017-0029-y

Nienow, P., Sharp, M., & Willis, I. (1998). Seasonal changes in the morphology of the subglacial drainage system, Haut Glacier d'Arolla, Switzerland. *Earth Surface Processes and Landforms*, *23*(9), 825–843. https://doi.org/10.1002/(SICI)1096-9837(199809)23:9<825::AID-ESP893>3.0.CO;2-2

Nikora, V. I., & Goring, D. G. (1998). ADV Measurements of Turbulence: Can We Improve Their Interpretation? *Journal of Hydraulic Engineering*, *124*(6), 630–634. https://doi.org/10.1061/(ASCE)0733-9429(1998)124:6(630)

Nikora, V. I., Goring, D. G., & Biggs, B. J. F. (1997). On stream periphyton-turbulence interactions. *New Zealand Journal of Marine and Freshwater Research*, *31*(4), 435–448. https://doi.org/10.1080/00288330.1997.9516777

Nikora, V. I., Goring, D. G., & Biggs, B. J. F. (1998). A Simple Model of Stream Periphyton-Flow Interactions. *Oikos*, *81*(3), 607. https://doi.org/10.2307/3546782

Nikora, V. I., Goring, D. G., & Biggs, B. J. F. (2002). Some observations of the effects of micro-organisms growing on the bed of an open channel on the turbulence properties. *Journal of Fluid Mechanics*, *450*. https://doi.org/10.1017/S0022112001006486

O'Connor, J., Smith, M. J., & James, M. R. (2017). Cameras and settings for aerial surveys in the geosciences: Optimising image data. *Progress in Physical Geography: Earth and Environment*, *41*(3), 325–344. https://doi.org/10.1177/0309133317703092

Orr, C. H., Clark, J. J., Wilcock, P. R., Finlay, J. C., & Doyle, M. W. (2009). Comparison of morphological and biological control of exchange with transient storage zones in a field-scale flume. *Journal of Geophysical Research: Biogeosciences*, *114*(G2). https://doi.org/10.1029/2008JG000825

Paiement-Paradis, G., Marquis, G., & Roy, A. (2011). Effects of turbulence on the transport of individual particles as bedload in a gravel-bed river. *Earth Surface Processes and Landforms*, *36*(1), 107–116. https://doi.org/10.1002/esp.2027

Paterson, D., & Daborn, G. (1991). Sediment Stabilisation by Biological Action. In D. H. Peregrine & J. H. Loveless (Eds.), *Developments in Coastal Engineering* (pp. 111–120). University of Bristol.

Paterson, D. M. (1989). Short-term changes in the erodibility of intertidal cohesive sediments related to the migratory behavior of epipelic diatoms. *Limnology and Oceanography*, *34*(1), 223–234. https://doi.org/10.4319/lo.1989.34.1.0223

Paterson, D. M. (1994). Microbiological mediation of sediment structure and behaviour. In L. J. Stal & P. Caumette (Eds.), *Microbial Mats* (pp. 97–109). Springer Berlin Heidelberg.

Perolo, P., Bakker, M., Gabbud, C., Moradi, G., Rennie, C., & Lane, S. N. (2019). Subglacial sediment production and snout marginal ice uplift during the late ablation season of a temperate valley glacier. *Earth Surface Processes and Landforms*, *44*(5), 1117–1136. https://doi.org/10.1002/esp.4562

Peterson, C. G. (1996). Response of Benthic Algal Communities to Natural Physical Disturbance. In *Algal Ecology* (pp. 375–402). Elsevier. https://doi.org/10.1016/B978-012668450-6/50042-4

Piqué, G., Vericat, D., Sabater, S., & Batalla, R. J. (2016). Effects of biofilm on river-bed scour. *Science of The Total Environment*, *572*, 1033–1046. https://doi.org/10.1016/j.scitotenv.2016.08.009

Pivato, M., Carniello, L., Moro, I., & D'Odorico, P. (2019). On the feedback between water turbidity and microphytobenthos growth in shallow tidal environments. *Earth Surface Processes and Landforms*, *44*(5), 1192–1206. https://doi.org/10.1002/esp.4567

Polvi, L. E., & Sarneel, J. M. (2018). Ecosystem engineers in rivers: An introduction to how and where organisms create positive biogeomorphic feedbacks. *Wiley Interdisciplinary Reviews: Water*, *5*(2), e1271. https://doi.org/10.1002/wat2.1271

Power, S. N., Salvatore, M. R., Sokol, E. R., Stanish, L. F., & Barrett, J. E. (2020). Estimating microbial mat biomass in the McMurdo Dry Valleys, Antarctica using satellite imagery and ground surveys. *Polar Biology*, *43*(11), 1753–1767. https://doi.org/10.1007/s00300-020-02742-y

Raab, T., Krümmelbein, J., Schneider, A., Gerwin, W., Maurer, T., & Naeth, M. A. (2012). Initial Ecosystem Processes as Key Factors of Landscape Development—A Review. *Physical Geography*, *33*(4), 305–343. https://doi.org/10.2747/0272-3646.33.4.305

Ragusa, S. R., de Zoysa, D. S., & Rengasamy, P. (1994). The effect of microorganisms, salinity and turbidity on hydraulic conductivity of irrigation channel soil. *Irrigation Science*, *15*(4), 159–166. https://doi.org/10.1007/BF00193683

Ramezan, C. A., Warner, T. A., Maxwell, A. E., & Price, B. S. (2021). Effects of training set size on supervised machine-learning land-cover classification of large-area high-resolution remotely sensed data. *Remote Sensing*, *13*(3), 368. https://doi.org/10.3390/rs13030368

Reichman, O. J., & Seabloom, E. W. (2002a). The role of pocket gophers as subterranean ecosystem engineers. *Trends in Ecology & Evolution*, *17*(1), 44–49. https://doi.org/10.1016/S0169-5347(01)02329-1

Reichman, O. J., & Seabloom, E. W. (2002b). Ecosystem engineering: A trivialized concept?: Response from Reichman and Seabloom. *Trends in Ecology & Evolution*, *17*(7), 308. https://doi.org/10.1016/S0169-5347(02)02512-0

Reidenbach, M. A., Limm, M., Hondzo, M., & Stacey, M. T. (2010). Effects of bed roughness on boundary layer mixing and mass flux across the sediment-water interface. *Water Resources Research*, *46*(7). https://doi.org/10.1029/2009WR008248

Richards, K. S. (1982). *Rivers: Form and process in alluvial channels*. London ; New York : Methuen. https://trove.nla.gov.au/version/31361403

Riihimaki, C. A., MacGregor, K. R., Anderson, R. S., Anderson, S. P., & Loso, M. G. (2005). Sediment evacuation and glacial erosion rates at a small alpine

glacier. *Journal of Geophysical Research*, *110*(F3). https://doi.org/10.1029/2004JF000189

Roncoroni, M., Brandani, J., Battin, T. I., & Lane, S. N. (2019). Ecosystem engineers: Biofilms and the ontogeny of glacier floodplain ecosystems. *Wiley Interdisciplinary Reviews: Water*, *6*(6). https://doi.org/10.1002/wat2.1390

Roncoroni, M., & Lane, S. N. (2019). A framework for using small Unmanned Aircraft Systems (sUASs) and SfM photogrammetry to detect salmonid redds. *Ecological Informatics*, *53*, 100976. https://doi.org/10.1016/j.ecoinf.2019.100976

Roncoroni, M., Mancini, D., Kohler, T. J., Miesen, F., Gianini, M., Battin, T. J., & N. Lane, S. (2022). Centimeter-scale mapping of phototrophic biofilms in glacial forefields using visible band ratios and UAV imagery. *International Journal of Remote Sensing*, *0*(0), 1–35. https://doi.org/10.1080/01431161.2022.2079963

Roncoroni, M., Mancini, D., Miesen, F., Müller, T., Gianini, M., Ouvry, B., Clémençon, M., Lardet, F., Battin, T. J., & Lane, S. N. (2023). Decrypting the stream periphyton physical habitat of recently deglaciated floodplains. *Science of The Total Environment*, *867*, 161374. https://doi.org/10.1016/j.scitotenv.2022.161374

Rothman, D. H., & Forney, D. C. (2008). Response to Comment on 'Physical Model for the Decay and Preservation of Marine Organic Carbon'. *Science*, *319*(5870), 1616–1616. https://doi.org/10.1126/science.1148678

Rott, E., Cantonati, M., Füreder, L., & Pfister, P. (2006). Benthic Algae in High Altitude Streams of the Alps – a Neglected Component of the Aquatic Biota. *Hydrobiologia*, *562*(1), 195–216. https://doi.org/10.1007/s10750-005-1811-z

Roussel, E., Marren, P. M., Cossart, E., Toumazet, J.-P., Chenet, M., Grancher, D., & Jomelli, V. (2018). Incision and aggradation in proglacial rivers: Post-Little Ice Age long-profile adjustments of Southern Iceland outwash plains. *Land Degradation & Development*, *29*(10), 3753–3771. https://doi.org/10.1002/ldr.3127

Rydgren, K., Halvorsen, R., Töpper, J. P., & Njøs, J. M. (2014). Glacier foreland succession and the fading effect of terrain age. *Journal of Vegetation Science*, *25*(6), 1367–1380. https://doi.org/10.1111/jvs.12184

Saberioon, M. M., Amin, M. S. M., Anuar, A. R., Gholizadeh, A., Wayayok, A., & Khairunniza-Bejo, S. (2014). Assessment of rice leaf chlorophyll content using visible bands at different growth stages at both the leaf and canopy scale. *International Journal of Applied Earth Observation and Geoinformation*, *32*, 35–45. https://doi.org/10.1016/j.jag.2014.03.018

Salvatore, M. R., Borges, S. R., Barrett, J. E., Sokol, E. R., Stanish, L. F., Power, S. N., & Morin, P. (2020). Remote characterization of photosynthetic communities in the Fryxell basin of Taylor Valley, Antarctica. *Antarctic Science*, *32*(4), 255–270. https://doi.org/10.1017/S0954102020000176

Schmidt, H., Thom, M., King, L., Wieprecht, S., & Gerbersdorf, S. U. (2016). The effect of seasonality upon the development of lotic biofilms and microbial biostabilisation. *Freshwater Biology*, *61*(6), 963–978. https://doi.org/10.1111/fwb.12760

Schmidt S.K, Reed Sasha C, Nemergut Diana R, Stuart Grandy A, Cleveland Cory C, Weintraub Michael N, Hill Andrew W, Costello Elizabeth K, Meyer A.F, Neff J.C, & Martin A.M. (2008). The earliest stages of ecosystem succession in high-elevation (5000 metres above sea level), recently deglaciated soils. *Proceedings of the Royal Society B: Biological Sciences*, *275*(1653), 2793–2802. https://doi.org/10.1098/rspb.2008.0808

Schott, J. R., Salvaggio, C., & Volchok, W. J. (1988). Radiometric scene normalization using pseudoinvariant features. *Remote Sensing of Environment*, *26*(1), 1–16. https://doi.org/10.1016/0034-4257(88)90116-2

Schroeder, T. A., Cohen, W. B., Song, C., Canty, M. J., & Yang, Z. (2006). Radiometric correction of multi-temporal Landsat data for characterization of early successional forest patterns in western Oregon. *Remote Sensing of Environment*, *103*(1), 16–26. https://doi.org/10.1016/j.rse.2006.03.008

Schulz, S., Brankatschk, R., Dümig, A., Kögel-Knabner, I., Schloter, M., & Zeyer, J. (2013). The role of microorganisms at different stages of ecosystem development for soil formation. *Biogeosciences*, *10*(6), 3983–3996. https://doi.org/10.5194/bg-10-3983-2013

Schumm, S. A., & Lichty, R. W. (1965). Time, space, and causality in geomorphology. *American Journal of Science*, *263*(2), 110–119. https://doi.org/10.2475/ajs.263.2.110

Scoffin, T. P. (1970). The Trapping and Binding of Subtidal Carbonate Sediments by Marine Vegetation in Bimini Lagoon, Bahamas. *Journal of Sedimentary Research*, *40*(1). http://archives.datapages.com/data/sepm/journals/v38-41/data/040/040001/0249.htm

Shields, A. (1936). Anwendung der Aehnlichkeitsmechanik und der Turbulenzforschung auf die Geschiebebewegung. PhD Thesis Technical University Berlin.

Shvidchenko, A. B., & Pender, G. (2001). Macroturbulent structure of open-channel flow over gravel beds. *Water Resources Research*, *37*(3), 709–719. https://doi.org/10.1029/2000WR900280

Simon, A., & Collison, A. J. C. (2002). Quantifying the mechanical and hydrologic effects of riparian vegetation on streambank stability. *Earth Surface Processes and Landforms*, *27*(5), 527–546. https://doi.org/10.1002/esp.325

Singer, G., Besemer, K., Schmitt-Kopplin, P., Hödl, I., & Battin, T. J. (2010). Physical Heterogeneity Increases Biofilm Resource Use and Its Molecular Diversity in Stream Mesocosms. *PLOS ONE*, *5*(4), e9988. https://doi.org/10.1371/journal.pone.0009988

Smart, G., Aberle, J., Duncan, M., & Walsh, J. (2004). Measurement and analysis of alluvial bed roughness. *Journal of Hydraulic Research*, *42*(3), 227–237. https://doi.org/10.1080/00221686.2004.9728388

Soluk, D. A., & Richardson, J. S. (1997). The Role of Stoneflies in Enhancing Growth of Trout: A Test of the Importance of Predator-Predator Facilitation within a Stream Community. *Oikos*, *80*(2), 214–219. JSTOR. https://doi.org/10.2307/3546588

Sommer, C., Malz, P., Seehaus, T. C., Lippl, S., Zemp, M., & Braun, M. H. (2020). Rapid glacier retreat and downwasting throughout the European Alps in the early 21st century. *Nature Communications*, *11*(1), 1. https://doi.org/10.1038/s41467-020-16818-0

Song, B., & Park, K. (2020). Detection of Aquatic Plants Using Multispectral UAV Imagery and Vegetation Index. *Remote Sensing*, *12*(3), 387. https://doi.org/10.3390/rs12030387

Song, C., & Woodcock, C. E. (2003). Monitoring forest succession with multitemporal Landsat images: Factors of uncertainty. *IEEE Transactions on Geoscience and Remote Sensing*, *41*(11), 2557–2567. https://doi.org/10.1109/TGRS.2003.818367

Spears, B. M., Saunders, J. E., Davidson, I., & Paterson, D. M. (2008). Microalgal sediment biostabilisation along a salinity gradient in the Eden Estuary, Scotland:

Unravelling a paradox. *Marine and Freshwater Research*, *59*(4), 313–321. https://doi.org/10.1071/MF07164

Stal, L. J. (2003). Microphytobenthos, their Extracellular Polymeric Substances, and the Morphogenesis of Intertidal Sediments. *Geomicrobiology Journal*, *20*(5), 463–478. https://doi.org/10.1080/713851126

Statzner, B., Arens, M.-F., Champagne, J.-Y., Morel, R., & Herouin, E. (1999). Silk-producing stream insects and gravel erosion: Significant biological effects on critical shear stress. *Water Resources Research*, *35*(11), 3495–3506. https://doi.org/10.1029/1999WR900196

Stoodley, P., Sauer, K., Davies, D. G., & Costerton, J. W. (2002). Biofilms as Complex Differentiated Communities. *Annual Review of Microbiology*, *56*(1), 187–209. https://doi.org/10.1146/annurev.micro.56.012302.160705

Stott, T., Nuttall, A.-M., & Biggs, E. (2014). Observed run-off and suspended sediment dynamics from a minor glacierized basin in south-west Greenland. *Geografisk Tidsskrift-Danish Journal of Geography*, *114*(2), 93–108. https://doi.org/10.1080/00167223.2013.862911

Su, T.-C., & Chou, H.-T. (2015). Application of Multispectral Sensors Carried on Unmanned Aerial Vehicle (UAV) to Trophic State Mapping of Small Reservoirs: A Case Study of Tain-Pu Reservoir in Kinmen, Taiwan. *Remote Sensing*, *7*(8), 10078–10097. https://doi.org/10.3390/rs70810078

Suga, K., Matsumura, Y., Ashitaka, Y., Tominaga, S., & Kaneda, M. (2010). Effects of wall permeability on turbulence. *International Journal of Heat and Fluid Flow*, *31*(6), 974–984. https://doi.org/10.1016/j.ijheatfluidflow.2010.02.023

Swift, D. A., Nienow, P. W., Hoey, T. B., & Mair, D. W. F. (2005). Seasonal evolution of runoff from Haut Glacier d'Arolla, Switzerland and implications for glacial geomorphic processes. *Journal of Hydrology*, *309*(1), 133–148. https://doi.org/10.1016/j.jhydrol.2004.11.016

Swift, D. A., Nienow, P. W., Spedding, N., & Hoey, T. B. (2002). Geomorphic implications of subglacial drainage configuration: Rates of basal sediment evacuation controlled by seasonal drainage system evolution. *Sedimentary Geology*, *149*(1–3), 5–19. https://doi.org/10.1016/S0037-0738(01)00241-X

Taddia, Y., Russo, P., Lovo, S., & Pellegrinelli, A. (2020). Multispectral UAV monitoring of submerged seaweed in shallow water. *Applied Geomatics*, *12*(1), 19–34. https://doi.org/10.1007/s12518-019-00270-x

Tamminga, A., Hugenholtz, C., Eaton, B., & Lapointe, M. (2015). Hyperspatial Remote Sensing of Channel Reach Morphology and Hydraulic Fish Habitat Using an Unmanned Aerial Vehicle (UAV): A First Assessment in the Context of River Research and Management: remote sensing using uavs. *River Research and Applications*, *31*(3), 379–391. https://doi.org/10.1002/rra.2743

Thom, M., Schmidt, H., Gerbersdorf, S. U., & Wieprecht, S. (2015). Seasonal biostabilization and erosion behavior of fluvial biofilms under different hydrodynamic and light conditions. *International Journal of Sediment Research*, *30*(4), 273–284. https://doi.org/10.1016/j.ijsrc.2015.03.015

Thomas, R. E., Schindfessel, L., McLelland, S. J., Creëlle, S., & Mulder, T. D. (2017). Bias in mean velocities and noise in variances and covariances measured using a multistatic acoustic profiler: The Nortek Vectrino Profiler. *Measurement Science and Technology*, *28*(7), 075302. https://doi.org/10.1088/1361-6501/aa7273

Thompson, A. (1988). *Historical development of the proglacial landforms of Svinafellsjokull and Skaftafellsjokull, southeast Iceland*.

Thompson, A., & Jones, A. (1986). Rates and causes of proglacial river terrace formation in southeast Iceland: An application of lichenometric dating techniques. *Boreas*, *15*(3), 231–246. https://doi.org/10.1111/j.1502-3885.1986.tb00928.x

Thorne, P. D., Williams, J. J., & Heathershaw, A. D. (1989). In situ acoustic measurements of marine gravel threshold and transport. *Sedimentology*, *36*(1), 61–74. https://doi.org/10.1111/j.1365-3091.1989.tb00820.x

Thullner, M., Zeyer, J., & Kinzelbach, W. (2002). Influence of Microbial Growth on Hydraulic Properties of Pore Networks. *Transport in Porous Media*, *49*(1), 99–122. https://doi.org/10.1023/A:1016030112089

Tolhurst, T. J., Gust, G., & Paterson, D. M. (2002). The influence of an extracellular polymeric substance (EPS) on cohesive sediment stability. In J. C. Winterwerp & C. Kranenburg (Eds.), *Proceedings in Marine Science* (Vol. 5, pp. 409–425). Elsevier. https://doi.org/10.1016/S1568-2692(02)80030-4

Tucker, C. J. (1979). Red and photographic infrared linear combinations for monitoring vegetation. *Remote Sensing of Environment*, *8*(2), 127–150. https://doi.org/10.1016/0034-4257(79)90013-0

Uehlinger, U., Malard, F., & Ward, J. V. (2003). Thermal patterns in the surface waters of a glacial river corridor (Val Roseg, Switzerland). *Freshwater Biology*, *48*(2), 284–300. https://doi.org/10.1046/j.1365-2427.2003.01000.x

Uehlinger, U., Robinson, C. T., Hieber, M., & Zah, R. (2010). The physico-chemical habitat template for periphyton in alpine glacial streams under a changing climate. *Hydrobiologia*, *657*(1), 107–121. https://doi.org/10.1007/s10750-009-9963-x

Uehlinger, U., Tockner, K., & Malard, F. (2002). Ecological windows in glacial stream ecosystems. *Eawag News [Engl. Ed.]*, *54*, 20–21.

Uehlinger, U., Zah, R., & H.R., B. (1998). The Val Roseg project: Temporal and spatial patterns of benthic algae in an Alpine stream ecosystem influenced by glacier runoff. In *IAHS-AISH Publication* (Vol. 248, p. 424).

Valentine, K., Mariotti, G., & Fagherazzi, S. (2014). Repeated erosion of cohesive sediments with biofilms. *Advances in Geosciences*, *39*, 9-14. https://doi.org/10.5194/adgeo-39-9-2014

van Rijn Leo C. (2007). Unified View of Sediment Transport by Currents and Waves. I: Initiation of Motion, Bed Roughness, and Bed-Load Transport. *Journal of Hydraulic Engineering*, *133*(6), 649–667. https://doi.org/10.1061/(ASCE)0733-9429(2007)133:6(649)

Vignaga, E. (2012). The effect of biofilm colonization on the stability of non-cohesive sediments. (Doctoral dissertation). University of Glasgow.

Vignaga, E., Sloan, D. M., Luo, X., Haynes, H., Phoenix, V. R., & Sloan, W. T. (2013). Erosion of biofilm-bound fluvial sediments. *Nature Geoscience*, *6*(9), 770–774. https://doi.org/10.1038/ngeo1891

Viles, H. A. (2012). Microbial geomorphology: A neglected link between life and landscape. *Geomorphology*, *157–158*, 6–16. https://doi.org/10.1016/j.geomorph.2011.03.021

Voulgaris, G., & Trowbridge, J. H. (1998). Evaluation of the Acoustic Doppler Velocimeter (ADV) for Turbulence Measurements*. *Journal of Atmospheric and Oceanic Technology*, *15*(1), 272–289. https://doi.org/10.1175/1520-0426(1998)015<0272:EOTADV>2.0.CO;2

Warburton, J., & Davies, T. (1994). Variability of bedload transport and channel morphology in a braided river hydraulic model. *Earth Surface Processes and Landforms*, *19*(5), 403–421. https://doi.org/10.1002/esp.3290190503

Ward, J., Burgherr, P., Gessner, M., Malard, F., Robinson, C., Tockner, K., Uehlinger, U., & Zah, R. (1998). The Val Roseg project: Habitat heterogeneity and connectivity gradients in a glacial flood-plain system. In *IAHS Publication* (Vol. 248, p. 432).

Ward, J. V. (1994). Ecology of alpine streams. *Freshwater Biology*, *32*(2), 277–294. https://doi.org/10.1111/j.1365-2427.1994.tb01126.x

Ward, J. V., Malard, F., Tockner, K., & Uehlinger, U. (1999). Influence of ground water on surface water conditions in a glacial flood plain of the Swiss Alps. *Hydrological Processes*, *13*(3), 277–293. https://doi.org/10.1002/(SICI)1099-1085(19990228)13:3<277::AID-HYP738>3.0.CO;2-N

Westaway, R. M., Lane, S. N., & Hicks, D. M. (2000). The development of an automated correction procedure for digital photogrammetry for the study of wide, shallow, gravel-bed rivers. *Earth Surface Processes and Landforms*, *25*(2), 209–226. https://doi.org/10.1002/(SICI)1096-9837(200002)25:2<209::AID-ESP84>3.0.CO;2-Z

Westaway, R. M., Lane, S. N., & Hicks, D. M. (2001). Remote sensing of clear-water, shallow, gravel-bed rivers using digital photogrammetry. *Photogrammetric Engineering and Remote Sensing*, *67*(11), 1271–1281.

Westoby, M. J., Brasington, J., Glasser, N. F., Hambrey, M. J., & Reynolds, J. M. (2012). 'Structure-from-Motion' photogrammetry: A low-cost, effective tool for geoscience applications. *Geomorphology*, *179*, 300–314. https://doi.org/10.1016/j.geomorph.2012.08.021

Widdows, J., Brinsley, M. D., Salkeld, P. N., & Lucas, C. H. (2000). Influence of biota on spatial and temporal variation in sediment erodability and material flux on a tidal flat (Westerschelde, The Netherlands). *Marine Ecology Progress Series*, *194*, 23–37. https://doi.org/10.3354/meps194023

Wilcock, P. R., Kenworthy, S. T., & Crowe, J. C. (2001). Experimental study of the transport of mixed sand and gravel. *Water Resources Research*, *37*(12), 3349–3358. https://doi.org/10.1029/2001WR000683

Woebbecke, D. M., G. E. Meyer, K. Von Bargen, & D. A. Mortensen. (1995). Color Indices for Weed Identification Under Various Soil, Residue, and Lighting Conditions. *Transactions of the ASAE*, *38*(1), 259–269. https://doi.org/10.13031/2013.27838

Woodget, A. S., & Austrums, R. (2017). Subaerial gravel size measurement using topographic data derived from a UAV-SfM approach. *Earth Surface Processes and Landforms*, *42*(9), 1434–1443. https://doi.org/10.1002/esp.4139

Woodget, A. S., Carbonneau, P. E., Visser, F., & Maddock, I. P. (2015). Quantifying submerged fluvial topography using hyperspatial resolution UAS imagery and structure from motion photogrammetry. *Earth Surface Processes and Landforms*, *40*(1), 47–64. https://doi.org/10.1002/esp.3613

Wright, J. P., & Jones, C. G. (2004). Predicting Effects of Ecosystem Engineers on Patch-Scale Species Richness from Primary Productivity. *Ecology*, *85*(8), 2071–2081. https://doi.org/10.1890/02-8018

Wu, F.-C., & Jiang, M.-R. (2007). Numerical Investigation of the Role of Turbulent Bursting in Sediment Entrainment. *Journal of Hydraulic Engineering*, *133*(3), 329–334. https://doi.org/10.1061/(ASCE)0733-9429(2007)133:3(329)

Xu, F., Gao, Z., Jiang, X., Shang, W., Ning, J., Song, D., & Ai, J. (2018). A UAV and S2A data-based estimation of the initial biomass of green algae in the South Yellow Sea. *Marine Pollution Bulletin*, *128*, 408–414. https://doi.org/10.1016/j.marpolbul.2018.01.061

Yallop, M. L., de Winder, B., Paterson, D. M., & Stal, L. J. (1994). Comparative structure, primary production and biogenic stabilization of cohesive and non-cohesive marine sediments inhabited by microphytobenthos. *Estuarine, Coastal and Shelf Science*, *39*(6), 565–582. https://doi.org/10.1016/S0272-7714(06)80010-7

Zemp, M., Haeberli, W., Hoelzle, M., & Paul, F. (2006). Alpine glaciers to disappear within decades? *Geophysical Research Letters*, *33*(13). https://doi.org/10.1029/2006GL026319

Zhao, L., Zhu, W., & Tong, W. (2009). Clogging processes caused by biofilm growth and organic particle accumulation in lab-scale vertical flow constructed wetlands. *Journal of Environmental Sciences*, *21*(6), 750–757. https://doi.org/10.1016/S1001-0742(08)62336-0

Zika, U., & Peter, A. (2002). The introduction of woody debris into a channelized stream: Effect on trout populations and habitat. *River Research and Applications*, *18*(4), 355–366. https://doi.org/10.1002/rra.677

Zumsteg, A., Luster, J., Göransson, H., Smittenberg, R. H., Brunner, I., Bernasconi, S. M., Zeyer, J., & Frey, B. (2012). Bacterial, Archaeal and Fungal Succession in the Forefield of a Receding Glacier. *Microbial Ecology*, *63*(3), 552–564. https://doi.org/10.1007/s00248-011-9991-8

9. Supplementary materials

Supplementary Material SM1: Results of the PIF normalization date (mmdd) by date and band by band for Group 1 (reference 14 July). $RMSE_{before}$ refers to the errors of the non-normalized orthomosaics compared to the master one, while $RMSE_{after}$ refers to the errors after the normalization occurred.

Channel (+date)	R^2	*p*-value	Slope	y-intercept	$RMSE_{before}$	$RMSE_{after}$
0626 Red	0.93	0.00	0.81	43.68	17.28	11.01
0626 Green	0.93	0.00	0.82	41.27	16.93	11.48
0626 Blue	0.96	0.00	0.81	40.05	23.08	9.98
0627 Red	0.89	0.00	0.84	50.47	28.45	14.17
0627 Green	0.86	0.00	0.81	50.27	25.69	16.03
0627 Blue	0.94	0.00	1.04	17.69	25.65	12.76
0628 Red	0.91	0.00	0.83	45.32	21.17	12.93
0628 Green	0.88	0.00	0.80	47.87	21.72	14.87
0628 Blue	0.94	0.00	1.06	12.28	23.68	12.47
0630 Red	0.91	0.00	0.81	47.09	20.80	12.94
0630 Green	0.89	0.00	0.81	45.66	20.80	14.03
0630 Blue	0.94	0.00	1.01	17.14	21.85	12.50
0701 Red	0.95	0.00	0.93	26.45	16.97	9.43
0701 Green	0.95	0.00	0.94	21.57	15.24	9.35
0701 Blue	0.91	0.00	0.92	24.28	21.08	15.10
0702 Red	0.87	0.00	0.82	45.70	21.84	15.37
0702 Green	0.87	0.00	0.82	44.63	21.86	15.84
0702 Blue	0.92	0.00	1.09	8.73	24.67	14.37
0704 Red	0.87	0.00	0.83	38.94	19.15	15.23
0704 Green	0.87	0.00	0.82	39.41	19.08	15.34
0704 Blue	0.76	0.00	0.87	30.29	29.34	24.91
0705 Red	0.96	0.00	0.87	30.32	11.97	8.26
0705 Green	0.96	0.00	0.87	29.89	11.83	8.36
0705 Blue	0.96	0.00	0.86	31.76	18.97	9.81
0706 Red	0.91	0.00	1.16	-20.30	17.13	12.83
0706 Green	0.91	0.00	1.13	-16.07	15.66	12.89
0706 Blue	0.94	0.00	1.21	-32.89	15.37	12.52
0707 Red	0.96	0.00	0.92	19.21	10.32	8.23
0707 Green	0.96	0.00	0.92	20.21	10.44	8.55
0707 Blue	0.98	0.00	0.88	24.29	13.18	6.87
0708 Red	0.95	0.00	0.89	26.51	12.11	9.38
0708 Green	0.94	0.00	0.89	23.99	12.07	10.18
0708 Blue	0.97	0.00	0.89	21.77	13.36	9.19
0709 Red	0.81	0.00	1.07	7.00	27.13	18.62
0709 Green	0.81	0.00	1.00	13.70	23.40	18.83
0709 Blue	0.90	0.00	1.44	-53.26	21.98	15.61
0710 Red	0.96	0.00	1.18	-29.08	11.65	8.23
0710 Green	0.97	0.00	1.15	-25.13	9.49	7.24
0710 Blue	0.98	0.00	1.13	-22.63	9.65	6.61
0712 Red	0.91	0.00	0.87	31.89	16.55	12.77
0712 Green	0.91	0.00	0.87	31.80	16.67	12.99
0712 Blue	0.93	0.00	1.12	-2.85	18.83	13.32
0715 Red	0.90	0.00	0.98	22.76	23.55	13.41
0715 Green	0.90	0.00	0.95	23.00	20.39	13.57
0715 Blue	0.90	0.00	1.27	-27.32	20.32	15.77
0718 Red	0.93	0.00	1.02	-1.18	11.84	11.65
0718 Green	0.93	0.00	1.05	-7.74	11.49	11.23
0718 Blue	0.75	0.00	0.90	8.99	26.25	25.27
0719 Red	0.96	0.00	1.07	-12.93	9.09	8.63
0719 Green	0.96	0.00	1.08	-14.86	8.80	8.19
0719 Blue	0.97	0.00	1.06	-10.93	9.19	8.48

Supplementary Material SM2: Results of the PIF normalization date (mmdd) by date and band by band for Group 2 (reference 26 July). $RMSE_{before}$ refers to the errors of the non-normalized orthomosaics compared to the master one, while $RMSE_{after}$ refers to the errors after the normalization occurred.

Channel (+date)	R2	p-value	Slope	y-intercept	RMSEbefore	RMSEafter
0721 Red	0.87	0.00	0.94	30.53	27.54	18.19
0721 Green	0.84	0.00	0.95	26.98	26.71	18.53
0721 Blue	0.96	0.00	1.27	-14.77	23.66	14.86
0723 Red	0.95	0.00	0.90	26.98	14.89	11.02
0723 Green	0.93	0.00	0.91	23.14	14.95	12.25
0723 Blue	0.98	0.00	1.14	-5.82	15.82	10.91
0725 Red	0.96	0.00	0.90	23.06	12.81	10.36
0725 Green	0.94	0.00	0.91	20.40	12.95	11.17
0725 Blue	0.98	0.00	1.12	-6.65	14.66	11.27
0727 Red	0.95	0.00	1.00	-1.49	10.91	10.97
0727 Green	0.95	0.00	0.99	0.84	10.35	10.17
0727 Blue	0.98	0.00	0.97	-1.77	10.96	9.64
0729 Red	0.95	0.00	0.95	17.75	15.16	11.56
0729 Green	0.92	0.00	0.97	16.18	16.54	12.69
0729 Blue	0.97	0.00	1.19	-12.77	18.46	13.22
0730 Red	0.98	0.00	1.01	0.12	7.63	7.23
0730 Green	0.98	0.00	1.03	-2.41	8.33	7.32
0730 Blue	0.99	0.00	1.06	-6.35	8.91	7.95
0731 Red	0.96	0.00	1.01	-1.37	10.21	10.09
0731 Green	0.96	0.00	1.03	-3.14	10.19	9.85
0731 Blue	0.98	0.00	1.03	-8.78	11.42	9.88
0801 Red	0.94	0.00	1.06	-4.46	14.01	11.85
0801 Green	0.92	0.00	1.07	-4.52	14.92	12.89
0801 Blue	0.97	0.00	1.08	-15.17	15.19	12.72
0802 Red	0.96	0.00	1.00	2.26	10.51	10.28
0802 Green	0.95	0.00	1.04	-4.34	11.16	10.68
0802 Blue	0.98	0.00	1.08	-10.48	12.23	10.68
0803 Red	0.82	0.00	0.84	44.11	28.62	21.27
0803 Green	0.75	0.00	0.86	38.75	28.90	23.06
0803 Blue	0.95	0.00	1.64	-56.92	33.14	16.43
0806 Red	0.96	0.00	1.04	-6.86	10.29	10.07
0806 Green	0.96	0.00	1.07	-11.88	10.01	9.61
0806 Blue	0.98	0.00	1.02	-6.63	11.24	10.03
0807 Red	0.93	0.00	0.96	6.11	13.08	12.82
0807 Green	0.93	0.00	0.97	6.06	12.69	12.53
0807 Blue	0.98	0.00	0.93	3.34	13.47	11.44
0810_Red	0.87	0.00	0.96	20.61	22.65	18.51
0810 Green	0.82	0.00	0.95	21.96	23.90	19.53
0810 Blue	0.93	0.00	1.00	2.70	19.05	19.01
0811 Red	0.93	0.00	0.99	4.89	13.78	13.49
0811 Green	0.92	0.00	0.94	7.71	13.68	12.90
0811 Blue	0.86	0.00	1.49	-89.14	44.31	28.02
0812 Red	0.95	0.00	1.08	-18.68	12.55	11.32
0812 Green	0.97	0.00	1.02	-14.31	12.90	8.08
0812 Blue	0.91	0.00	1.37	-84.54	45.18	22.46
0814 Red	0.94	0.00	0.94	16.65	13.73	11.99
0814 Green	0.93	0.00	0.98	8.86	13.86	12.52
0814 Blue	0.97	0.00	1.19	-17.53	16.94	12.02
0816_Red	0.95	0.00	1.08	-10.85	12.03	10.75
0816 Green	0.93	0.00	1.12	-17.54	13.36	12.11
0816 Blue	0.98	0.00	1.11	-20.19	15.41	11.08
0817 Red	0.90	0.00	0.91	30.61	22.46	15.91
0817 Green	0.86	0.00	0.94	24.83	22.78	17.58
0817 Blue	0.83	0.00	1.17	-14.90	31.68	30.07
0818 Red	0.91	0.00	0.97	14.85	17.52	14.90

0818 Green	0.88	0.00	1.00	8.18	18.29	15.91
0818 Blue	0.84	0.00	1.22	-28.26	32.58	29.83
0819_Red	0.50	0.00	0.77	64.64	46.61	35.57
0819 Green	0.50	0.00	0.80	55.30	41.83	32.88
0819 Blue	0.90	0.00	1.14	-15.94	24.59	23.00
0820 Red	0.92	0.00	0.96	9.37	14.73	14.52
0820 Green	0.91	0.00	0.96	9.27	14.19	13.93
0820 Blue	0.94	0.00	0.95	-0.82	19.48	17.89
0821 Red	0.87	0.00	1.00	10.83	21.02	18.46
0821 Green	0.82	0.00	1.03	6.40	22.70	19.76
0821_Blue	0.94	0.00	1.09	-10.38	19.03	17.94

Supplementary Material SM3: Results of the PIF normalization date (mmdd) by date and band by band for Group 3 (reference 14 July). $RMSE_{before}$ refers to the errors of the non-normalized orthomosaics compared to the master one, while $RMSE_{after}$ refers to the errors after the normalization occurred.

Channel (+date)	R2	p-value	Slope	y-intercept	RMSDbefore	RMSDafter
0823 Red	0.96	0.00	0.93	15.87	9.65	8.89
0823 Green	0.96	0.00	0.95	11.03	8.82	8.47
0823 Blue	0.95	0.00	1.02	-7.19	12.42	11.61
0824 Red	0.93	0.00	0.92	12.81	11.98	11.02
0824 Green	0.93	0.00	0.94	8.51	11.82	11.22
0824 Blue	0.97	0.00	0.89	11.33	11.03	8.51
0825 Red	0.91	0.00	1.00	14.66	18.82	12.66
0825 Green	0.93	0.00	1.02	8.31	15.79	11.37
0825 Blue	0.95	0.00	1.17	-20.16	14.19	11.64
0826 Red	0.95	0.00	0.97	2.56	10.50	9.57
0826 Green	0.95	0.00	0.99	-1.49	9.88	9.57
0826 Blue	0.97	0.00	0.95	3.36	10.05	8.91
0827 Red	0.94	0.00	0.99	-0.28	10.84	10.71
0827 Green	0.94	0.00	1.01	-3.07	10.24	10.13
0827 Blue	0.95	0.00	0.97	0.59	12.00	11.57
0902 Red	0.87	0.00	0.95	7.97	15.89	15.69
0902 Green	0.88	0.00	0.97	3.93	14.84	14.65
0902 Blue	0.89	0.00	1.16	-25.23	18.47	16.99
0903 Red	0.75	0.00	0.95	28.88	30.22	21.46
0903 Green	0.87	0.00	0.98	10.55	17.22	15.46
0903 Blue	0.92	0.00	1.02	-5.39	14.36	14.06
0904 Red	0.93	0.00	0.88	21.47	12.67	11.39
0904 Green	0.94	0.00	0.92	14.60	11.37	10.69
0904 Blue	0.97	0.00	0.91	11.77	9.79	8.43
0908_Red	0.95	0.00	0.92	11.66	10.89	9.70
0908 Green	0.97	0.00	0.93	9.11	9.37	8.01
0908 Blue	0.96	0.00	0.88	15.95	12.70	10.49
0910 Red	0.94	0.00	0.92	26.31	16.28	10.30
0910 Green	0.94	0.00	0.95	15.72	12.38	10.16
0910 Blue	0.95	0.00	1.03	-4.19	11.44	11.24
0913 Red	0.94	0.00	0.95	14.84	11.73	10.50
0913 Green	0.95	0.00	0.96	11.46	10.42	9.21
0913 Blue	0.94	0.00	1.00	3.09	12.65	12.09

Supplementary Material SM4: Logistic regressions for Groups 1 and 3.

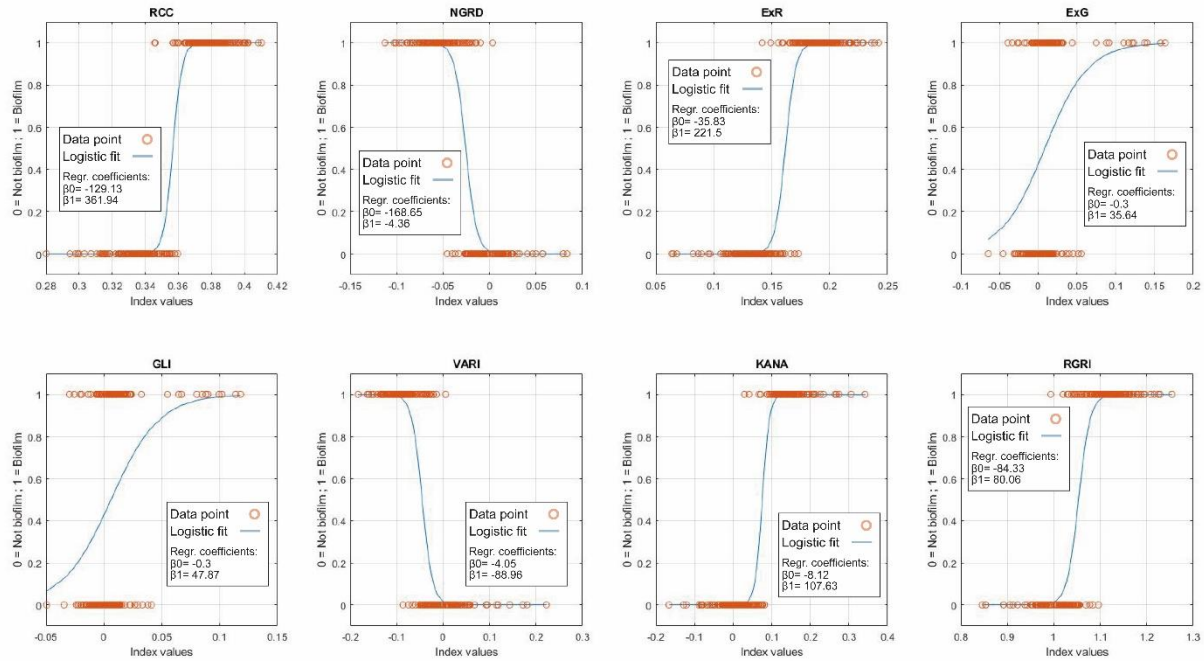

Supplementary Material SM5: Logistic regressions of Group 2.

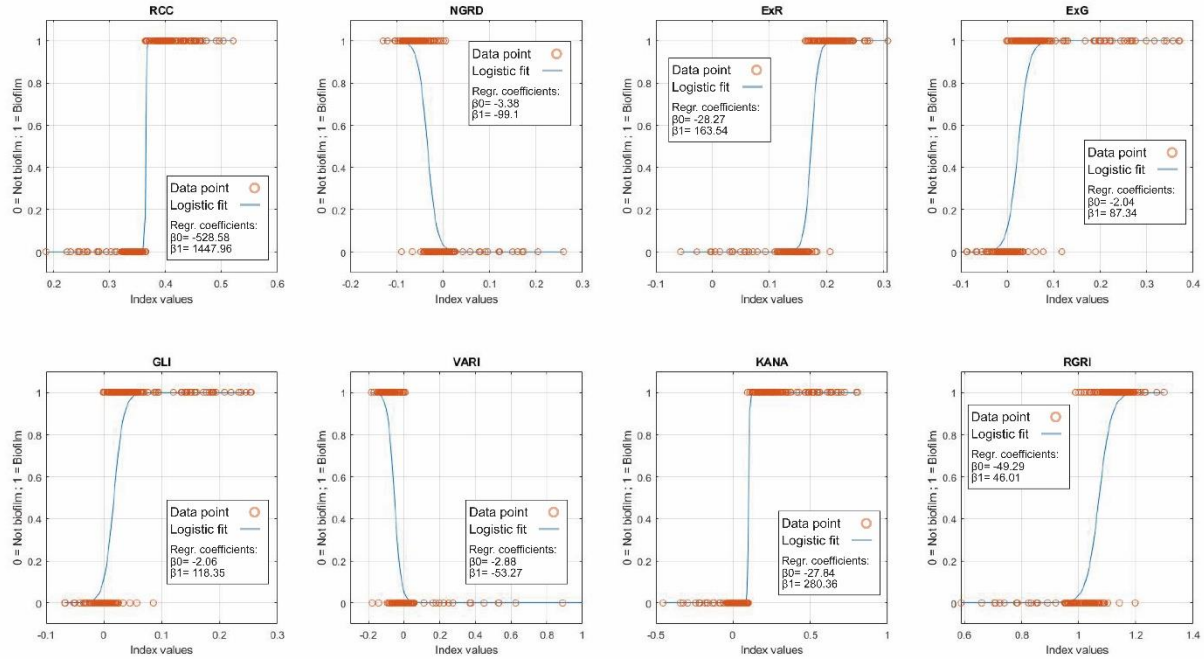

Supplementary Material SM6: Logistic regressions for Group 4.

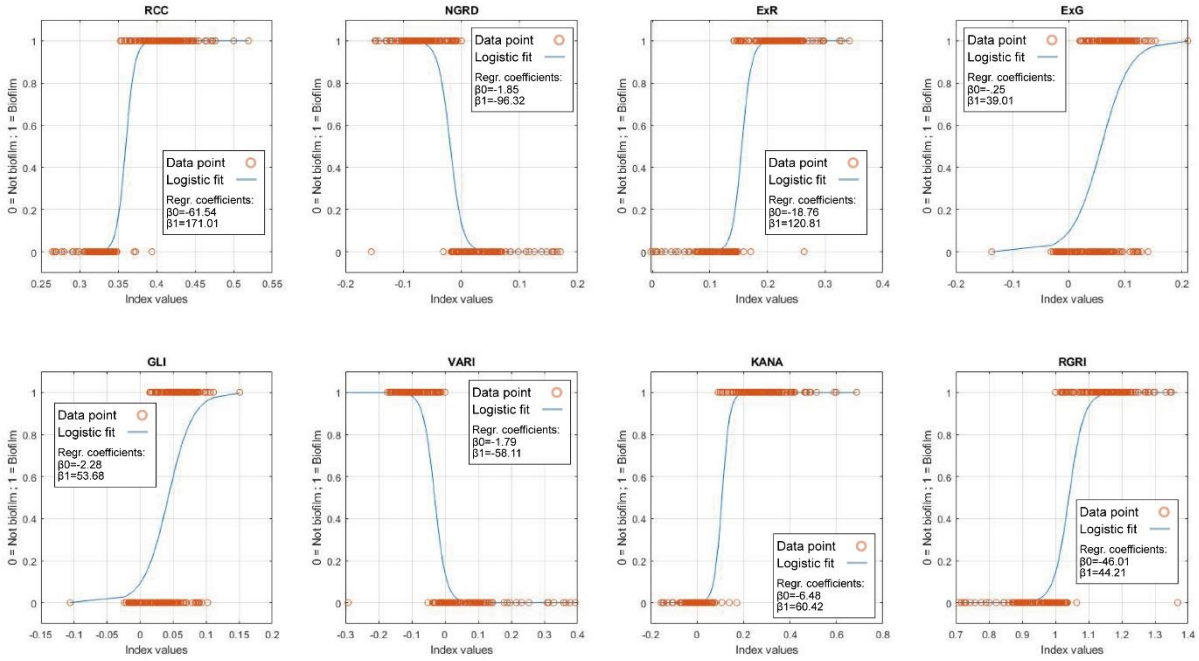

Supplementary Material SM7: Limits of Detection (m)

DoD Date (*mdd*)	LoD95%	DoD Date (*mdd*)	LoD95%
627_626	0.06	802_801	0.09
628_627	0.09	803_802	0.09
630_628	0.10	806_803	0.09
701_630	0.09	807_806	0.09
702_701	0.09	810_807	0.12
704_702	0.09	811_810	0.13
705_704	0.09	812_811	0.11
706_705	0.09	814_812	0.11
707_706	0.09	816_814	0.11
708_707	0.09	817_816	0.10
709_708	0.08	818_817	0.10
710_709	0.10	819_818	0.11
712_710	0.10	820_819	0.11
714_712	0.08	821_820	0.12
715_714	0.08	823_821	0.11
718_715	0.08	824_823	0.11
719_718	0.08	825_824	0.11
721_719	0.08	826_825	0.12
723_721	0.08	827_826	0.11
725_723	0.10	902_827	0.11
726_725	0.10	903_902	0.12
727_726	0.09	904_903	0.12
729_727	0.09	908_904	0.13
730_729	0.09	910_908	0.13
731_730	0.09	913_910	0.12
801_731	0.09		

Supplementary Material SM8: Summary statistics for the three geographical areas (active, buffer, and stable)

	Mean	Q25	Q50	Q75	Q95
Active					
Occupation (in %)	12.1	7.5	10.0	13.8	21.9
Submergence (in %)	35.7	0.0	32.5	61.9	100.0
Unstable (in %)	10.2	0.0	5.1	16.1	36.5
Buffer					
Occupation (in %)	30.9	10.6	25.0	49.4	70.6
Submergence (in %)	45.9	1.9	43.1	85.6	100.0
Unstable (in %)	17.2	0.0	12.7	26.1	56.0
Stable					
Occupation (in %)	38.8	18.8	35.6	53.1	85.6
Submergence (in %)	4.1	0.0	0.0	0.0	2.5
Unstable (in %)	0.0	0.0	0.0	0.0	0.0

Supplementary Material SM9: Summary statistics (surfaces) for the three geographical areas (active, buffer, and stable)

	Total Surface (m2)	Total occupied surface (m2)	Total submerged surface (m2)	Total unstable surface (m2)
Active	55830.7	56.4	39174.6	34477.4
Buffer	6085.0	221.6	4776.3	4481.9
Stable	49148.8	713.1	4929.2	0.0

Supplementary Material SM10: Active floodplain periphyton frequencies
Periphyton frequency in relation to submergence and instability rates.

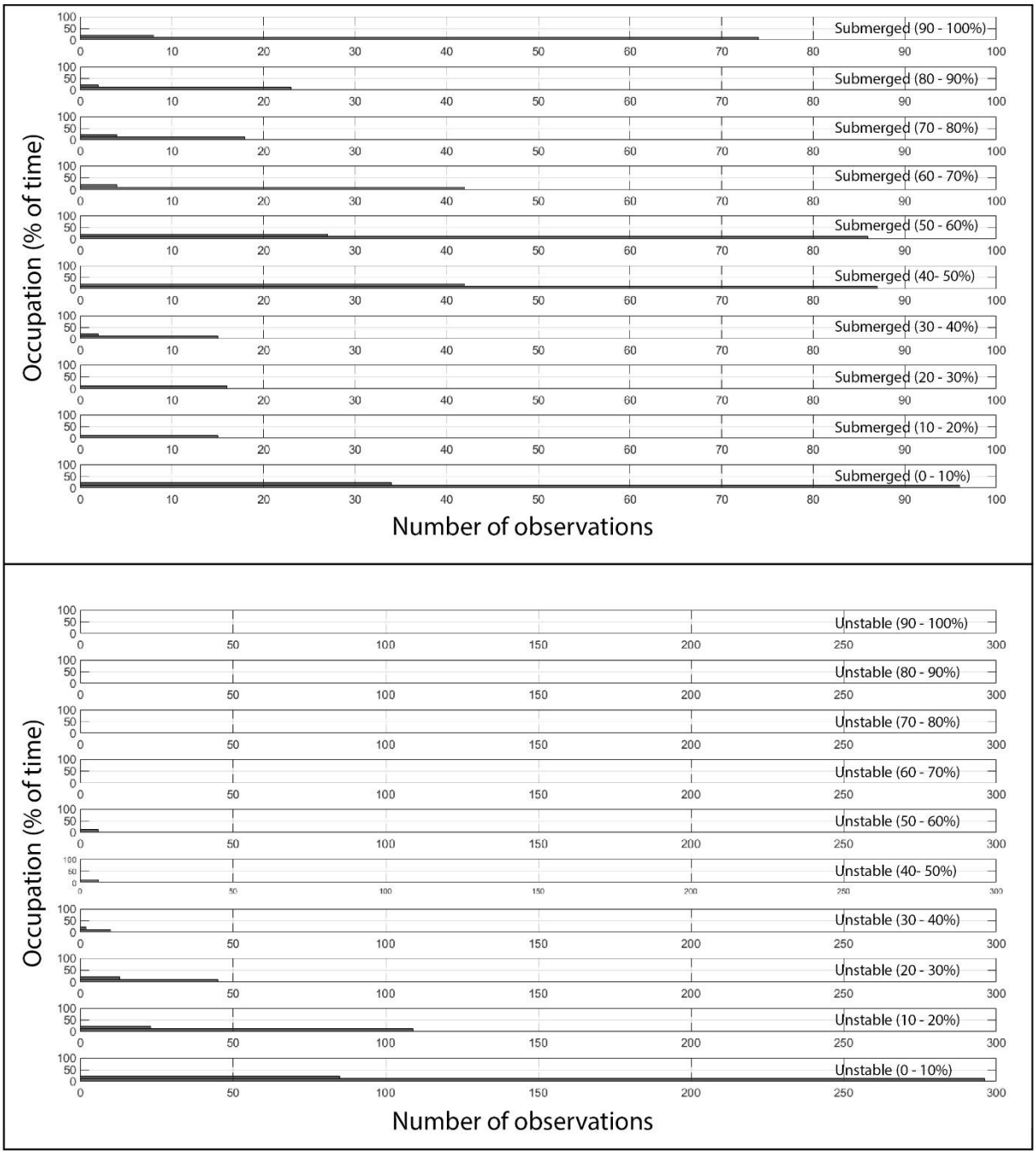

Supplementary Material SM11: Buffer floodplain periphyton frequencies
Periphyton frequency in relation to submergence and instability rates.

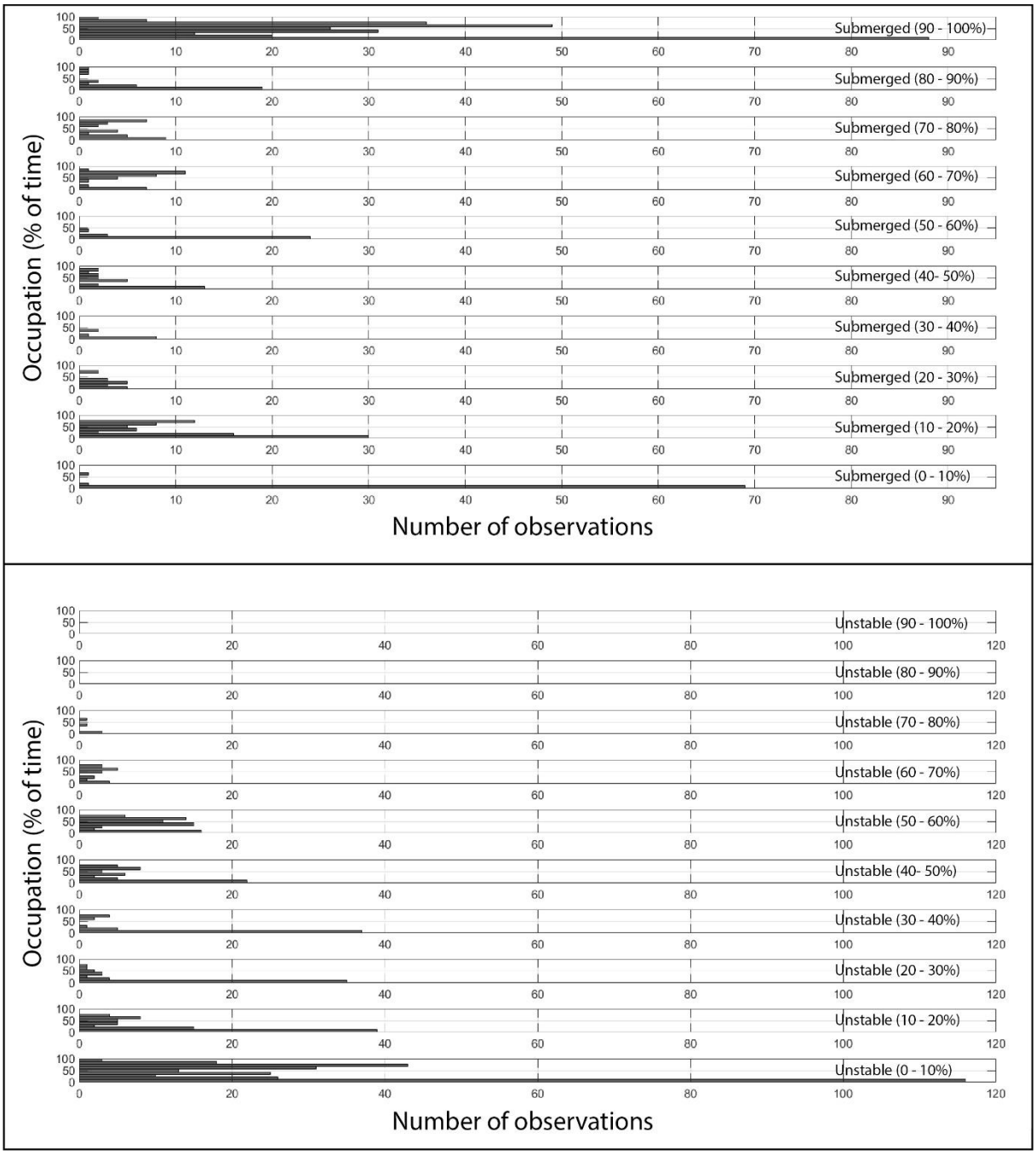

Supplementary Material SM12: Buffer floodplain periphyton frequencies, glacial water
Periphyton frequency in relation to submergence of glacial water

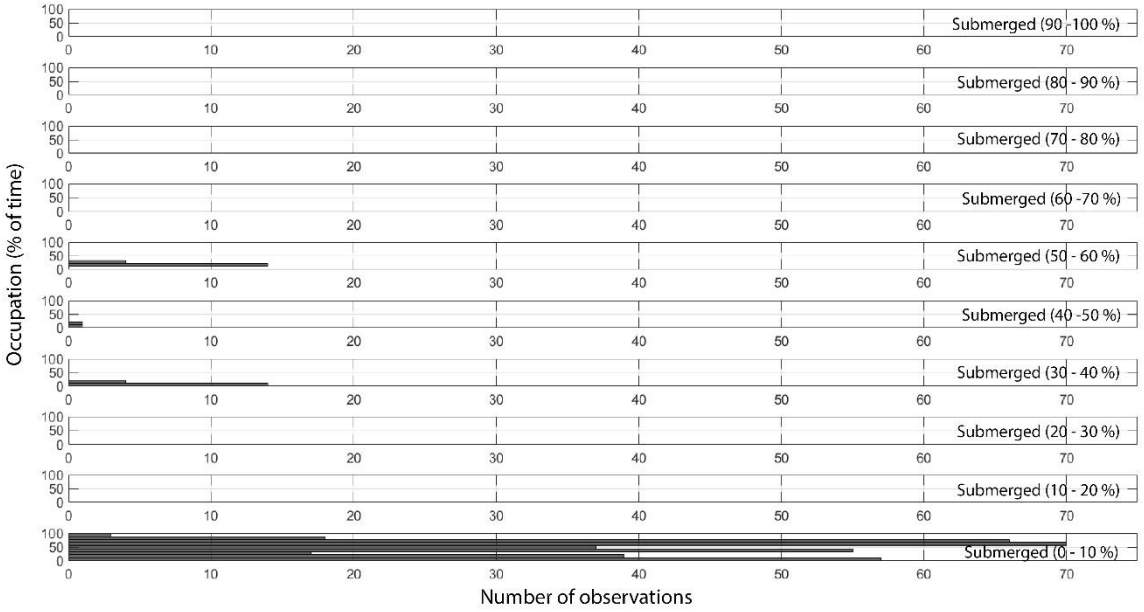

Supplementary Material SM13: Stable floodplain periphyton frequencies
Periphyton frequency in relation to submergence rates.